EPOXY + LIQUID CRYSTALLINE EPOXY COREACTED NETWORKS

Prakaipetch Punchaipetch, B.S., M.S.

Dissertation Prepared for the Degree of

DOCTOR OF PHILOSOPHY

UNIVERSITY OF NORTH TEXAS

December 2000

APPROVED:

Nandika Anne D'Souza, Major Professor
Witold Brostow, Major Professor
William E. Acree, Committee Member
Teresa Golden, Committee Member
Michael Kozak, Committee Member
Richard Reidy, Committee Member
Bruce Gnade, Committee Member and Chair of the Department of Materials Science
C. Neal Tate, Dean of the Robert B. Toulouse School of Graduate Studies

Acknowledgments

I would like to express sincere gratitude towards my advisors; Professor Nandika Anne D'Souza and Professor Witold Brostow for the opportunities and their patient guidance. Their support, encouragement, and teaching throughout the research are highly appreciated. I am indebted to Dr. D'Souza's hospitality. Her generous support and inspiration help to lead me with high confidence in my research and personnel life.

Advice and suggestion from my doctoral committee, Professor Bruce Gnade, Professor Micheal Kozak, and Professor Richard Reidy are highly appreciated. I appreciate the help from Professor Teresa Golden for serving on my committee and helping with the X-ray diffraction studies. I would like to give sincere thanks to Professor William E. Acree for serving on my committee and allowing me to use the optical microscope in his laboratory.

I would like to acknowledge Veronica Ambrogi, Dr. Marta Giamberini, and Professor Cosimo Carfagna for their help in synthesis portion of my dissertation. I had a wonderful experience working with Veronica during the summer of 1998. I would like to further acknowledge Prof. Tom Smith and his research group for the pultrusion sample preparation.

I appreciate the discussions on technical information about thermal characterization with Dr. Kevin P. Mernard. Moreover, I thank David Garrett for his help with the SEM experiments. I would like to thank Peter Butzloff for helping me with RDS

testing and for our useful discussions. I would like to acknowledge Dr. Gales Homes for his interesting suggestions on this research. I would like to thank Dr. Magdalena Jaklewicz and Dr. Pablo Montamatini for their help in testing the pultrusion samples.

My thanks to Yangdong Chang, Joe Boclair, and Alejandro Hernandez-Luna, all colleagues in LAPOM, Mechanical Mechanics Research groups, and my Thai friends for their wonderful friendship and assistance.

Financial support from the State of Texas Advanced Technology Program (Project # 003594-077) and the Advance Research Program (Project # 003594-0075) is gratefully acknowledged. Thanks also for funding from Welch Foundation.

Last but not least, I deeply thank my family for their love, understanding, support, and patience. Moreover, the friendship never-ending support, and encouragement from Boonyarach Kitiyanan is appreciative.

TABLE OF CONTENTS

LIST OF TABLES

LIST OF ILLUSTRATIONS

CHAPTER 1

INTRODUCTION

Epoxies are widely utilized for coatings and structural applications, adhesives and composites for microelectronic encapsulants. These materials have a large number of advantages including: low thermal expansivity, good dimensional stability, low dielectric constant, low density, good resistance to environment and heat, ease of processability, and relatively low costs. Epoxy resins which are cured under high temperature conditions have high glass transition temperatures and high moduli. The high modulus with low shrinkage makes them widely used as matrices for composite applications [1-3]. High annual consumption of epoxies as aerospace and spacecraft composites, electronic component encapsulations, laminated circuit boards and adhesives.

Epoxy resins constitute a class of thermoset polymers with a high crosslink density of covalent networks. Crosslink density is defined as the number of polymer chain segments between crosslinks. This value is approximately 10^{27} strands/m^3 for a conventional epoxy. This value is fairly high compared with elastomers a crosslink density of about 10^{26} strands/m^3 [4-6]. The dense crosslinks lead to high *glass transition temperatures* (T_g), superior thermal resistance and good mechanical performance. These materials do not melt, but decompose upon application of heat. However, an increase in crosslink density causes low fracture toughness. Therefore, there are many efforts to improve mechanical properties of epoxy resins. The details are provided in Chapter 2.

The style of this dissertation follows *Polymer*

Molecular reinforcement through in-situ polymerization of liquid crystalline epoxies (LCEs) and a non-liquid crystalline epoxy has been investigated. We considered the effects of coreacting an epoxy with a reactive monomer LC epoxy in these terms. The increasing demand for lightweight, high performance materials has stimulated considerable research. Polymeric LC epoxy resins are expensive. Thus, in spite of their advantageous properties, they are not widely used. Therefore, one of the objectives of the present dissertation was an investigation of the potential impact of a low concentration of an epoxy LC on the properties of epoxy resins. This approach has the potential for toughening epoxy resins without affecting T_g of the materials.

In chapter 2, an overview of information pertinent for the work at hand has been provided. A review of extant toughening methods of epoxy resins has been presented. More detailed information on LC epoxies is discussed in Chapter 3. The synthesis, reaction mechanism, and characterization results for three kinds of LCEs are also reported. Three LCEs; diglycidyl ether of 4,4'-dihydroxybiphenol (DGE-DHBP) and digylcidyl ether of 4-hydroxyphenyl-4"-hydroxybiphenyl-4'-carboxylate (DGE-HHC), were synthesized and blended with diglycidyl ether of bisphenol F (DGEBP-F) and subsequently cured with an anhydride and amine curing agents.

The time-temperature-transformation (TTT) diagrams of curing behavior of LCEs are reported in Chapter 4. The curing kinetics of LCEs and a non-LC epoxy blends are presented in Chapter 5. Curing kinetics were determined using differential scanning calorimetry (DSC). Parameters for autocatalytic curing kinetics of both pure monomers

and blended systems were determined. The effect of LC constituent on curing kinetics was studied.

The miscibility study, based on the solubility parameter, and the detection of T_g is presented in Chapter 6. The glass transitions were evaluated as a function of composition using DSC and dynamic mechanical analysis (DMA). The effect of curing conditions on the secondary transition results is also discussed.

Chapter 7 addresses with the mechanical properties of a LC epoxy + commercial non-LC epoxy blend system. The testing methods, based on the concepts of plain stress and plain strain, are reported. The effects of molecular reinforcement of DGEBP-F by DGE-DHBP and DGE-HHC were investigated. The concentration of liquid crystalline moiety affects mechanical properties. Tensile, impact and fracture toughness tests results are evaluated. Scanning electron microscopy of the fracture surfaces shows changes in failure mechanisms compared to the pure components. The results indicate that the mechanical properties of the blended samples are improved already at low concentration by weight of the LCE added to epoxy resin. The mechanism of crack propagation in the sub-fracture surface zone of cured LCE, non-LCE and modified system are studied.

Modified epoxy developed in this work was used as the matrix for glass fiber composites. The effect of glass fibers on curing kinetics was investigated and used as a basis for processing to prepare composite samples. Furthermore, results pertaining to the mechanical behavior of the modified epoxy composites under various service conditions are presented in Chapter 8. Finally, the summary of this work and suggestions for future work are presented in Chapter 9.

CHAPTER 2

LITERATURE REVIEW

There are many efforts to improve mechanical properties of epoxy resins reported in the literature. Each method provides a different magnitude of improvement, but might also introduce some undesirable properties. These problems will be discussed below.

1) Toughening mechanisms for polymers

Toughened polymers constitute a growing area of research. New thermoplastics as well as thermosets are being developed to provide improvement in properties so as to meet specific service requirements. There are several methods of toughening epoxy resins and other polymers [7-15]; the most important are:

1.1 *Chemical modification and formation of interpenetrating polymer networks*. The structure of epoxy main chains or curing agents can be modified by flexible or rigid structures depending on the application. Moreover, simultaneous curing of the epoxy resin with rubbery networks e.g. polyurethane, to form an interpenetrating network (IPN) has been applied to improve toughness of epoxies [13]. D'Souza and coworkers showed that IPNs formed through a simultaneous reaction of an epoxy and polyisocyanate monomer in the presence of a single curing agent increased fracture toughness [14].

1.2 *Promotion of crazing* [15]. Crazing is an effective process of toughening loosely crosslinked and uncrosslinked polymers. The "crazes" are formed during irreversible volume expansion creating highly strained in fibrillar microcrack structures. Crazes are generated at the imperfection point in the polymer matrix by the presence of a

hydrostatic or dilatational component of the stress tensor. Multiple crazing can sustain loads between crack faces and generate yielding as a toughening mechanism.

1.3 *Introduction of localized or bulk shear yielding* [15]. Increasing the molecular weight of an epoxy monomer increases cross-link density. This increase in turn promotes toughening through the shear yielding mechanism in some polymers.

1.4 *Macroporous (void-filled) thermosets.* These materials can be produced by chemically induced phase separation during curing. Low boiling point liquids, which are added to the network, introduce phase separation. The liquids evaporate when heating the material above the T_g of the polymer.

1.5 *Multiphase or second phase toughening mechanism.* This process is an effective way to produce high toughness epoxies. Introduction of functionalized reactive rubbers and thermoplastics are two common approaches.

1.5.1 Rubber toughening

Rubber is incorporated into a polymer matrix, typically 5-20 % by weight, as the dispersed phase. This idea has been applied to reactive rubbers like carboxyl, amine or epoxy terminated butadiene acrylonitrile (CTBN, ATBN, or ETBN) [16-19]. The other elastomeric modifiers studied include acrylates [20-21], poly(oxypropylene amines) [22-23], and polysiloxane copolymers [8]. The fracture toughness of modified epoxy resins is typically higher than that of unmodified ones. However, the blends show adverse effects in decreased upper use temperatures, lower stiffness and strength [24-26]. Furthermore, the rubber toughening approach of thermosets fails in high temperature applications.

Toughening of such blends involves a chemically induced phase separation process [10]. One starts from a single homogeneous phase of rubber and host matrix. A low molecular weight liquid rubber, which can dissolve in the epoxy resin, is usually first blended and dispersed into the epoxy matrix. However, the components separate out during the curing process. The degree of chemical interaction between the resin and rubber particles, as well as the rubber particle sizes, affect the interfacial adhesion and the toughness performance.

1.5.2 Thermoplastics toughening

The modification of epoxies with thermoplastics provides an alternative approach which avoids the problems seen in toughening epoxies by rubber. Important properties such as modulus, yield stress, and glass transition are not adversely affected by the addition of a modifier. However, toughening epoxies with thermoplastics presents significant problems in processing due to large viscosity differences between the thermoplastic and epoxy. Epoxy resins blends, with non-modified thermoplastics such as poly(ether sulfone) and poly(ether imide), have been studied by Bucknall [27] and Diamont [28]. No significant improvement was reported. In contrast, thermoplastics with reactive terminal groups have been found to improve the fracture toughness while having little affect on other properties [29-32].

As we learn from the above information, the ideal epoxy matrix should have a high glass transition temperature and simultaneously a high toughness. Kinloch also supports the need to develop tough thermosets without sacrificing high glass transition temperatures for high performance applications [10]. Light weight, high performance and

high T_g epoxy resins can serve important applications as matrices for aerospace and integrated electronic circuit industries.

2) Liquid crystals

Liquid crystals (LCs) serve a variety of applications due to their unique properties resulting from their rigid, strong dipoles, and easily polarizable molecular structures. They provide intermediate properties between those of isotropic liquids (flow properties) and crystalline solid phases (anisotropic properties); see Figure 2.1. Molecules of a crystal are regularly arranged in a three dimensional lattice while the centers of gravity of molecules in a liquid do not exhibit repetitive order.

The liquid crystalline behavior was first reported by Friedrich who observed the transition of cholesteryl benzoate in 1888 (from ref. [33]). He found a material which could change from a hazy liquid to a clear transparent liquid at a specific temperature. The hazy liquid had birefringent (anisotropic) properties. An early theoretical model of LCs was proposed by Onsanger in 1949 [34], a second model by Flory in 1956 [35]. Flory suggested that the rigid rod polymers display an anisotropic LC phase at specific critical concentration depending on the aspect ratio (length-to-width ratio) of the rigid molecules. The *mesogenic* units must be linear with high aspect ratio. The typical mesogenic group consist of at least two aromatic or cycloaliphatic rings connected in the *para* positions. Robinson reported that the phase behavior of a polyglutamates solution followed the Flory theory [36]. This type of LC is referred as *lyotropic* liquid crystal. The critical concentration C* is related to the aspect ratio *x*, according to Flory, as follows:

$$C^* = \frac{8}{x}(1 - \frac{2}{x}) \tag{2-1}$$

Thermotropic liquid crystals are another category of LCs. The LC phase in these materials is stable within a certain temperature range. The first melt processable LC was synthesized by Cottis in 1972 [37]. This copolyester, based on p-hydroxybenzoic acid and biphenol terephthalate, was later commercialized under the trade name of Xydar. Hsiao and coworkers [38] found that the liquid crystallinity of some materials can be induced by pressure. Brostow proposed to name such materials *barotropic* liquid crystals [39].

The *degree of order (s)* of LCs is an important factor to quantify their order behavior:

$$s = \frac{1}{2}(3 < \cos^2 \theta > -1) \tag{2-2}$$

Here θ is the angle between a monomer liquid crystal (MLC) molecule or a polymer liquid crystal (PLC) rigid sequence and a preferred direction (*director, ñ*). s is the average quantity for the material as represented by the brackets. Thus, s equals zero in the case of a completely isotropic system while in a perfectly aligned system s equals 1. A typical order parameter of LC is in the range of 0.3 - 0.9. The order parameter in LCs is dependent on temperature; s decreases as the temperature increases and drops to zero at the clearing temperature T_C, also called the isotropization temperature T_I. As LCs are heated up, they may undergo several phase transitions with decreasing values of the order parameter s, eventually becoming an isotropic liquid; see Figure 2.2.

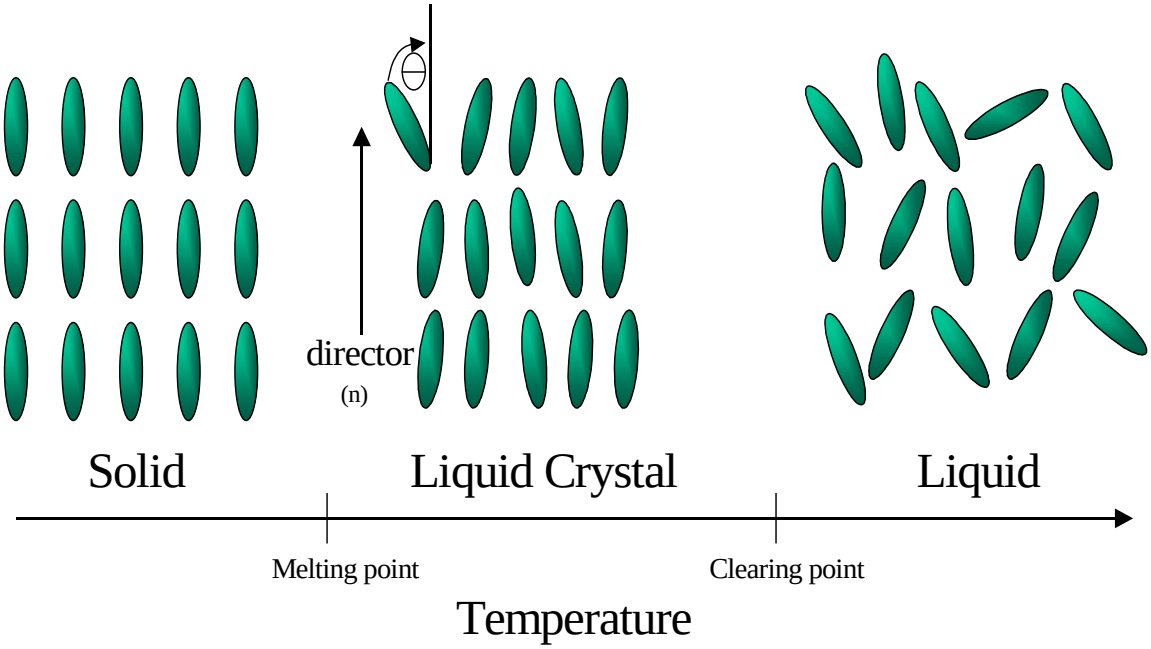

Figure 2.1 Schematic of comparison of solid, liquid crystal, and liquid states

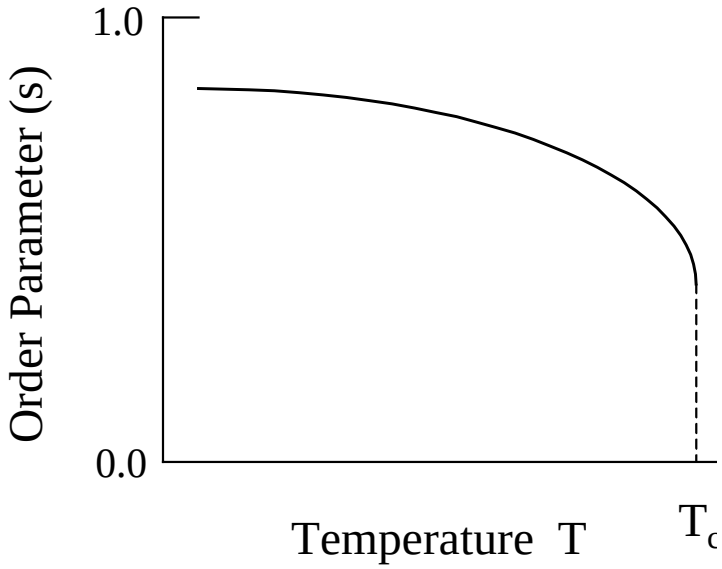

Figure 2.2 Schematic of the order parameters as a function of temperature T; (T_c is the clearing temperature).

2.1 Polymer liquid crystals

Polymer liquid crystals (PLCs) constitute one type of LC that is important in industrial applications [39-42]. PLC are long chain molecules obtained from the polymerization of *monomer liquid crystals (MLCs)*. The directional structure of PLCs is related to their rigidity. Variation of the chains average fraction which belong to the rigid LC sequences strongly affect their anisotropic properties. The longer the LC units, the more oriented they become in shearing, electric, and magnetic fields [40,43, 44].

The molecular order in each type of LC is different and can be divided into 3 main types (Figure 2.3). In a *nematic* mesophase LC, there is an approximate molecular alignment. Such materials do not exhibit positional order but have long range molecular order. The chains in a nematic domain have significant freedom to move both laterally and longitudinally. Thus, these materials have relatively low melting points compared to other types of PLCs.

In a *smectic* mesophase LC there is a high degree of molecular alignment with a high degree of molecular order. Smectics exhibit both long range molecular orientational order and 1- or 2-dimensional positional order. There are at least 10 subtypes of smectic PLCs, namely; normal smectic PLCs: S_A, S_B, S_E and tilted smetic PLCs: S_C, S_I, S_F, S_J, S_G, S_H, and S_K.

A *cholesteric* mesophase LC is composed of nematic mesogenic molecules containing a chiral center which produce intermolecular forces that favor alignment between molecules at a slight angle to one another. These mesophase are characterized by their multilayer structure.

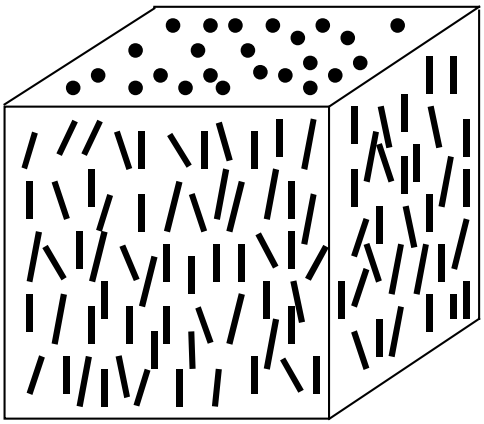

Nematic

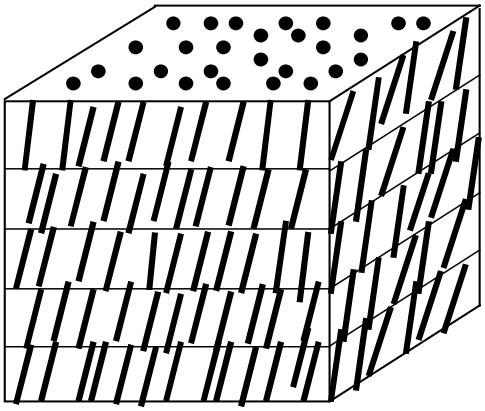

Smectic

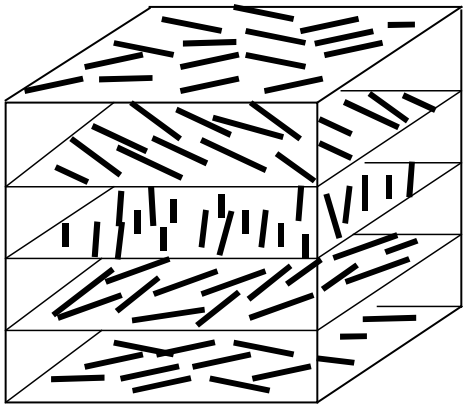

Cholesteric

Figure 2.3 Schematic of three main types of liquid crystal phases; after [45].

2.2 Blends of thermotropic liquid crystals with thermoplastics

There has been considerable interest in blending thermotropic longitudinal PLCs with other thermoplastics [39, 46-49]. Longitudinal PLCs are those in which the LC units are located in the main chains and oriented along the chain backbone [39]. The idea of blending PLCs with thermoplastics can be related to *heterogeneous composites (HCs)* in which the matrix component is macroscopically reinforced by rigid fibers. The mechanical performance of HCs is improved compared with pure thermoplastics matrices. However, the differences in fibers and matrices often cause problems at the interphase. Fiber pullout and delamination are widely found as the cause of failure of HCs.

The idea of *molecular composites* has been developed [50-51]. The degree of reinforcement depends on the structure of the PLCs used. The need for light weight materials with high performance is one of the driving forces for the materials development. The weight reduction capability with high performance of *in situ composites*, formed under appropriate conditions in one step, is one of their advantages. The dispersed PLC phase deforms into a fribrillar form and acts as a reinforcing phase in a single step process.

The choice of thermoplastics and thermotropic LCs affects the properties of the resulting blends. One factor to be considered is the level of interphasic interaction achieved by the specific chemical structure of the blend materials. The principle of “like to like” structure has been used to choose the blend’s components. For example, phenyl and ester groups are the most typical functional groups in aromatic polyesters. These

groups should also be found in the thermoplastics, so that the blends have the same groups from both components. Studies on blends of PLCs, e.g. of copolymers of polyethylene terephthalate with p-(acetoxybenzoic acid) (PET/PHB) with polyethylene terephthalate were reported by several research groups [52, 53]. PLC blends containing some other thermoplastics namely polystyrene [54], polysulphone [55], polycarbonate [56], polybutylene terephthalate [57-58] have also been studied.

2.3 Liquid crystalline networks

Thermoplastic longitudinal PLCs have many advantages including excellent mechanical properties, good thermal stability, and low viscosity under shear force. However, these materials have high processing temperatures. Another drawback can be anisotropy properties, undesirable in some applications. This led to the development of PLC networks which contain frozen-in LC domains.

PLC networks can be obtained by the following methods. The first is to simultaneously polymerize and crosslink reactive monomers. The monomer can be of the polyaddition or polycondensation type. An example of the former type of monomer is the group of diacrylates [59-68]. The polycondensation type monomers can be obtained by capping the end of mesogenic groups with reactive groups. The rigid component might be biphenyl, phenyl benzoate, methyl stilbene, or naphthyl, etc, which are endcapped with reactive glycidyl [69-72], acetylene [73-75], cyanate [76-79], or amine [80-82] groups. The second method consists of the preparation of LC networks from reactive oligomers. Networks with LC properties are formed after curing [83-85]. Due to rigid rod-like properties, these networks display LC molecular orientation, along with other desirable

properties. For example, one might achieve a mesophase alignment in a highly oriented network, along with an increase in thermal stability

PLC networks can be divided into two main types, *LC thermosets (LCTs*) and *LC elastomers (LCEMs)*, according to their crosslink density. LC thermosets are networks with high crosslink density and high concentration of mesogenic units in the structure. In contrast, LCEMs exhibit low crosslink density (lower than 10 %) and low fractions of rod-like groups in the network structure. The lightly crosslinked LCEMs, with outstanding optical properties, can be used for non-linear optics, waveguides, optical switches, polarizers, and polymer dispersed liquid crystals (PDLCs) while the highly crosslinked LCTs can be used as advanced adhesives and matrices for high performance composites and microelectronics [86-89].

2.4 Liquid crystalline epoxies (LCEs)

There is an interest in PLC thermosets because of the combination of desirable properties from a thermoset and a PLC [90]. LC epoxy resins are thermosets that have been studied for at least a decade [91-93]. These materials combine the advantages of both PLCs and epoxies, resulting in their ability to be used in novel applications such as matrices for advanced composites, and in electronic packaging [94-95]. As compared to ordinary epoxies, crosslinked epoxy PLCs have higher fracture toughness [93, 96]. This can be explained by their approximately overall isotropic properties, combined with localized anisotropy. The inhomogeneties of LC structure lead to the deviation of crack propagation from straight lines and, thus, an increase in fracture toughness.

Carfagna and coworkers [97] used a LCE as a matrix to prepare PDLCs instead of non-LC epoxy resins. Micron sized LC droplets were prepared and dispersed in the LCE matrix. The LC droplet can be switched between on and off states upon applying an electrical or magnetic field. They found that the T_g and the electro-optical response were improved, compared with a non-LC epoxy system. A lower driving voltage and shorter switching time were found. Moreover, a reduction in the angular dependence of light scattering in the on-state was observed.

Barclay and coworkers [98] studied the effect of magnetic and mechanical alignment on the orientation of LC epoxies during curing. They found that the influence of a magnetic field can increase the order parameter from 0.13 to 0.57 - as measured by X-ray diffraction. Moreover, a substantial reduction of thermal expansivity in the direction parallel to the applied field direction was observed compared with randomly oriented networks.

2.5 Blends of thermotropic PLCs with epoxy resins

Carfagna and coworkers [99] studied the use of PLC fibers for increasing the toughness of an epoxy resin. A PLC blended with polyarylates was extruded into fibers and introduced into an epoxy resin. This mixture was cured. Results show an increase in toughness over unmodified fiber composites. The addition of 2 % by weight of PLC increased fracture toughness of the blends by about 20 %. They explained that PLC fibers act as crack stoppers to the fracture force. Moreover, T_g of the blends shows that there is a fair compatibility between these two polymers.

3) Fracture mechanics

3.1 Molecular fracture of thermosets and thermoplastics

Mechanical properties of a material are determined by its response to the applied stress. The breakage of either primary, secondary bonds, or both are involved when the materials are fractured. For a thermoset, fracture involves the breaking of primary covalent bonds at the crack tip. In the case of thermoplastics, sliding between chains or entanglements might be the dominant fracture mechanism. The crystal portions in a semicrystalline polymer can also act as anchor points for applied stress. The strength of a polymeric material depends on the density of main chain bonds crossing the fracture plane.

3.2 Background of fracture mechanics

There are two requirements which have to be fulfilled at the crack tip before the fracture can take place. Firstly, enough fractured energy must be provided to the system. Secondly, the local stress at crack tip must be greater than the cohesive strength of material.

The first requirement has been derived from the first law of thermodynamics by Griffith [100]. Figure 2.4 represents the schematic of a through thickness crack in a wide plate. For a crack in an infinitively wide plate, the change in the potential energy associated with the introduction of a crack is given by:

$$U = U_0 + 4aB\gamma_s - \frac{\pi\sigma^2 a^2 B}{E'} \qquad (2\text{-}3)$$

where U is the potential energy with a crack while U_o is the potential energy without a crack, σ is the applied stress, a is half of the crack length, B is thickness, E' represents modulus of elasticity, which is equal to $E/(1-\nu^2)$ (ν = poison ratio) in the condition of plane strain, and γ_s is the specific surface energy.

The differential equation for the potential energy U with respect to the crack length leads to the equilibrium condition as:

$$2\gamma_s = \frac{\pi\sigma^2 a}{E'} \tag{2-4}$$

However, the condition described in Eq. (2-4) is not stable and the crack still grows. We can rearrange the equation to obtain the applied stress in this condition as follows:

$$\sigma = \sqrt{\frac{2E'\gamma_s}{\pi a}} \tag{2-5}$$

The second condition requires that the local stress at the crack tip is larger than the cohesive strength of material. The cohesive strength is given by:

$$\sigma_c = \sqrt{\frac{E'\gamma_s}{a_o}} \tag{2-6}$$

where σ_c is the cohesive strength and a_o is the interatomic spacing.

The maximum stress at the elliptical crack tip in a wide plate is given by

$$\sigma_{\max} = 2\sigma\sqrt{\frac{a}{\rho}} \tag{2-7}$$

where ρ represents the radius of curvature at the crack tip.

The maximum stress must be higher than the cohesive strength of the materials in order to produce the fracture. Therefore, the following condition is provided:

$$\sigma_{\max} > \sigma_c \tag{2-8}$$

$$2\sigma\sqrt{\frac{a}{\rho}} > \sqrt{\frac{E'\gamma_s}{a_o}} \tag{2-9}$$

$$\sigma > \sqrt{\frac{E'\gamma_s\rho}{4aa_o}} \tag{2-10}$$

With the combination of stress prediction (Eq. 2-10) and energy requirements (Eq. 2-5), one obtains

$$\sqrt{\frac{E'\gamma_s\rho}{4aa_o}} = \sqrt{\frac{2E'\gamma_s}{\pi a}} \tag{2-11}$$

In the condition of plane strain, this equation is reduced to

$$\rho = \frac{8a_o}{\pi(1-\nu^2)} \approx 3a_o \tag{2-12}$$

Therefore, the condition of $\rho = 3a_o$ represents a critical measure of the notch root radius. Figure 2.5 is the schematic of required stress necessary to satisfy both the energy requirement and the stress requirement as a function of radius of curvature at the crack tip. For the values of $\rho < 3a_o$ fracture mechanics may be employed while for $\rho > 3a_o$, a stress concentration factor approach is necessary.

The crack introduced in test specimens is important to ensure validity of the result. The crack must be sufficiently sharp to ensure that a minimum value of toughness

is obtained. Details on sample size and the required testing condition for a valid results will be discussed further in Chapter 7. In the current standard method to determine fracture toughness of material [101], a precrack, introduced by tensile fatigue, is required to ensure the sufficient sharp radius at the crack tip.

There are three modes of loading that can be applied to a crack, labeled from I to III. In mode I (opening), the principal symmetric load is applied normal to the crack plane. In mode II (in-plane shear), the principal loading tends to slide one crack face with respect to the other. For mode III (out-of-plane shear), the shearing force is provided in an out-of-plane manner. Figure 2.6 presents three modes of loading that can be applied to a crack.

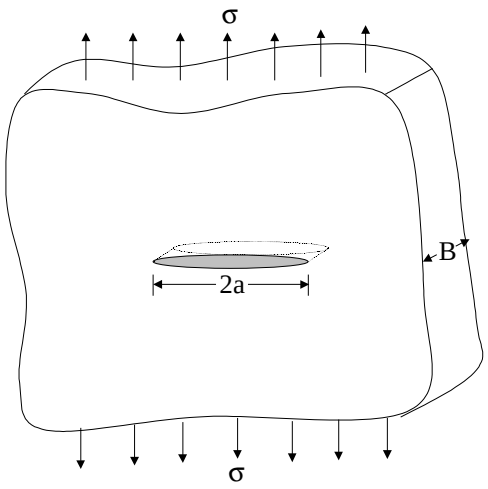

Figure 2.4 Through-thickness crack in an infinitely wide plate

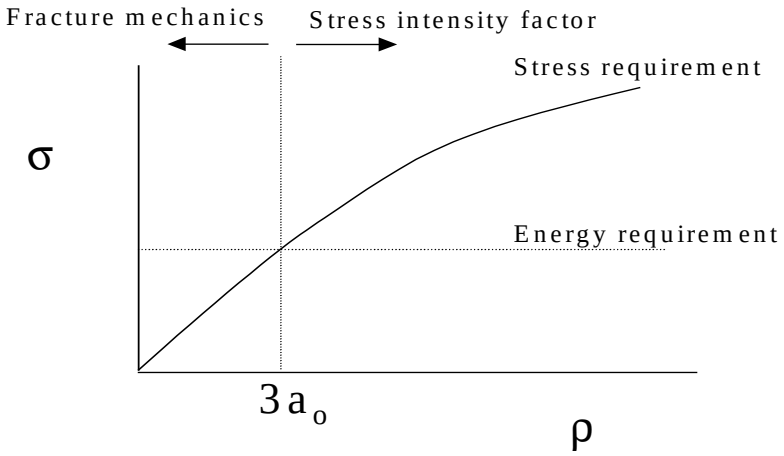

Figure 2.5 Schematic of required stress as a function of radius of curvature

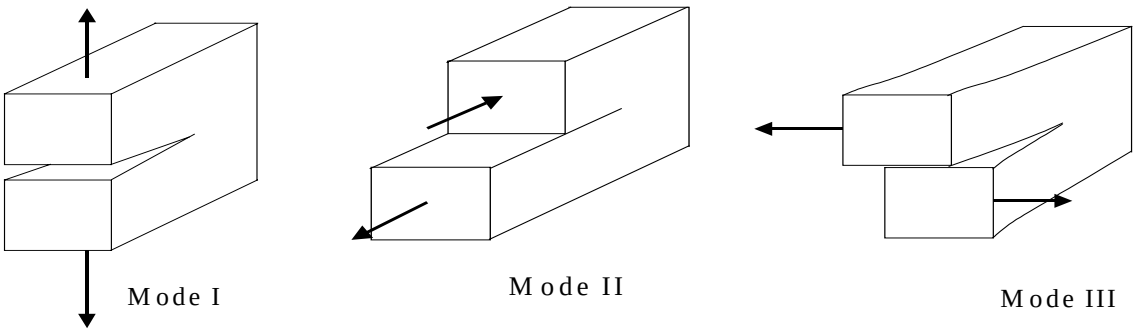

Figure 2.6 Three loading modes that can be applied to a crack

CHAPTER 3

SYNTHESIS AND CHARACTERIZATION OF LIQUID CRYSTALLINE EPOXY RESINS

1) Introduction

1.1 Review of liquid crystalline networks

The initial idea of utilizing a mesogenic phase to form an ordered network was proposed by Herz in 1964. He studied the free radical polymerization of 11- sodium styrylundecanoate and water system by using divinylbenzene as a crosslinking agent. A film with permanently locked-in molecular organization was obtained [102]. In 1969, Blumstein studied the quasi-smectic mesophase of polar molecules by using tetraethylene glycol dimethacrylate as the crosslinking agent [103].

The first LC thermosets were prepared by Strzelecki and Liebert in 1973. They crosslinked a diacrylated MLC in its LC state. The resulting network possessed the same molecular orientation as the monomer. They concluded that the mesogenic groups are locked into the crosslink structures upon curing [104]. Furthermore, Blumstein studied the effect of a magnetic field on the curing reaction of the same acrylate LCT. They have found substantial orientation of LC molecules in the network [105]. Finkelmann and coworkers prepared the first LC elastomer from side chain PLCs (LC sequences in side chains) in 1981. The crosslinking reaction locked the rigid molecules into an elastomer network [106].

De Gennes, as well as Wander and coworkers, developed [107-110] theoretical models of LC systems after monomer crosslinking. They suggested that crosslinked nematic LCs can produce remarkable properties including a discontinuous stress-strain relationship, different from behavior of non-LC networks. For the non-LC network, the molecular shape changes when stress is applied. However, the molecular shape in a nematic LC network can change spontaneously upon transition from the isotropic to the nematic phase. Furthermore, application of mechanical stress to an LC network can weaken the first order transition and increase the transition temperature. This is related to the development of some nematic order in response to a weak external applied field. The discontinuity in the nematic order will occur as the field is increased, provided of course that the temperature is not higher than the clearing temperature.

According to de Gennes' theories, there are three main regions in the relationship of stress vs. strain (Figure 3.1), and order parameter vs. strain (Figure 3.2) for LCEs. This behavior has been found in longitudinal and side chain nematic and smectic LCEs [111-114]. In stage A, we have the usual linear elastic relationship between stress and strain. A small amount of strain can induce stress in the polydomain elastomer. In stage B, the transition of polydomains to monodomains takes place with a change in optical properties. The plateau relationship of stress vs. strain is found while a dramatic increase of s is seen. In stage C, the modulus of the material is increased again, but the change is insignificant.

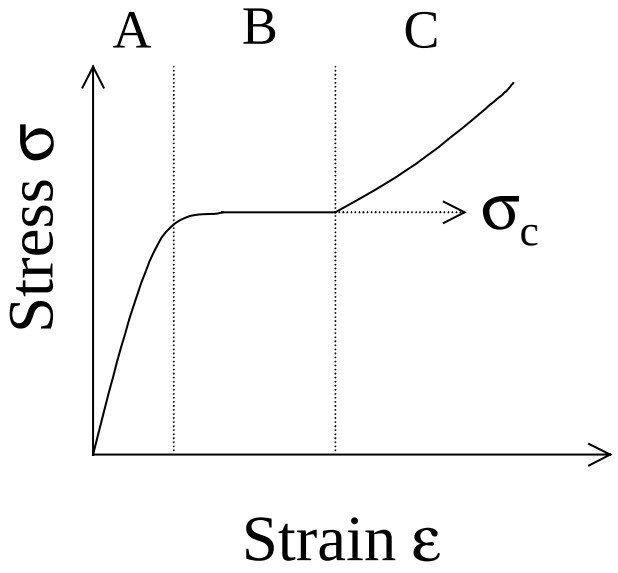

Figure 3.1 The schematic of stress vs. strain according to de Gennes theory

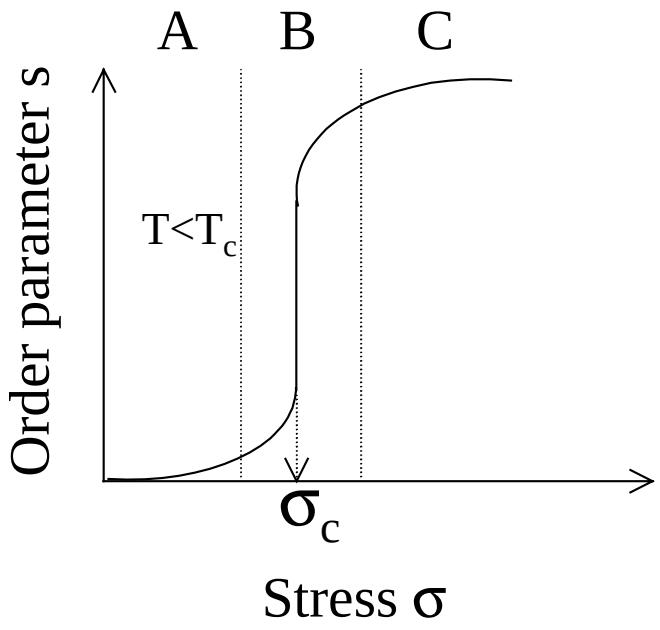

Figure 3.2 The schematic of the order parameter vs. stress according to de Gennes theory

1.2 Review of liquid crystalline epoxies

Liquid crystalline epoxy (LCE) networks are an important area of research, given their potential use in a number of applications such as electronics, advanced composites, and non-linear optics.

LC epoxy thermosets were first developed in industry. The first patent on LCE was claimed in Japan in 1984 [115], followed by Bayer AG [116-118] and Dow Chemical Company [119, 120]. However, only limited information from these patents is available. There has been growing interest in the study of LCEs to understand their remarkable behavior. The synthesis, development of texture, mechanical properties and influence of curing conditions have been examined for a number of LCEs [94, 121-133].

There are many factors affecting the physical properties of cured LCEs, including the nature and stability of mesogenic units of LCEs, the nature of curing agents, and the curing temperature. The performance of cured LCEs can be molecular engineered by varying these parameters for different applications. Work on densely crosslinked and lightly crosslinked rigid rod epoxy resins during the past decade resulted in a better understanding of the behavior of LCEs. Examples of LCEs with rigid structures are shown in Table 3.1 while examples of LCEs with semi-rigid structures are presented in Table 3.2. Behavior of rigid rods in the network is different from the networks obtained from random coil linkages. This is due to the change in the entropic contribution to network deformation and stress relief.

Table 3.1 Examples of rigid monomer liquid crystalline epoxies

Liquid crystalline epoxy	References
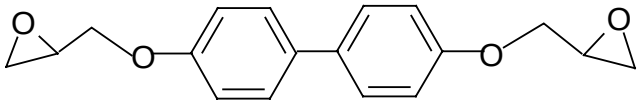	134, 135, 136
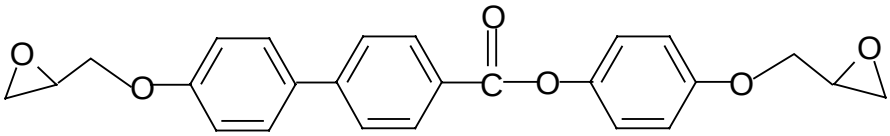	137
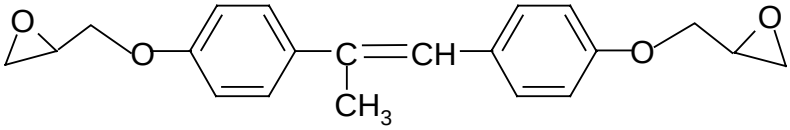	130, 131, 132, 133, 134, 138, 139, 140
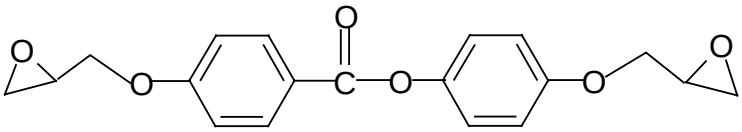	88, 141, 142
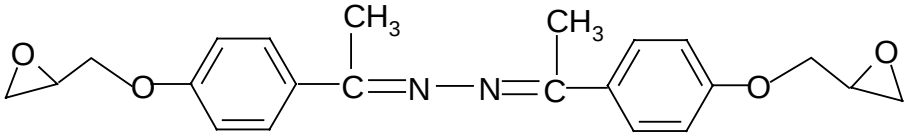	143
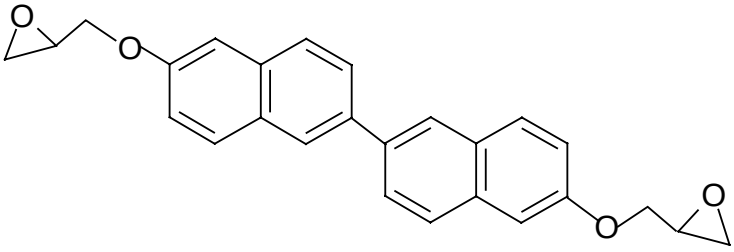	143

Table 3.2 The example of semi-rigid monomer liquid crystalline epoxies

Liquid crystalline epoxy	References
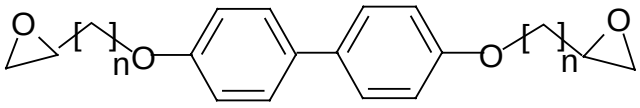 n=3,4,6	144
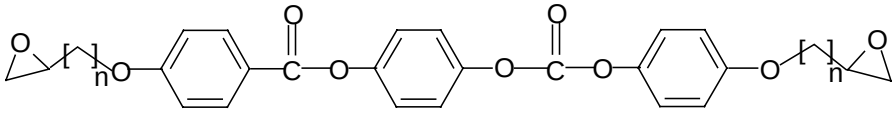 n=4,6	127, 144
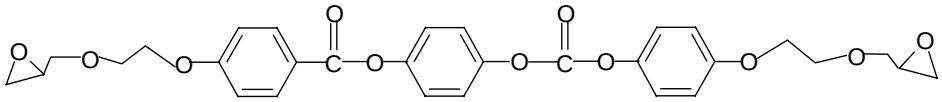	144, 145, 146, 147
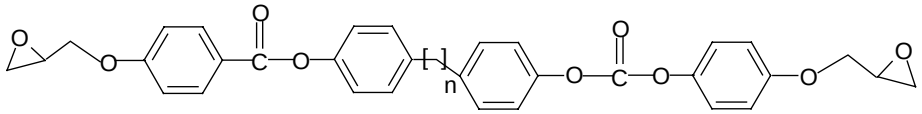 n=8-9	127
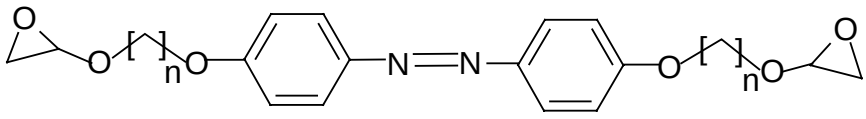 n=6	148

1.3 Description of LCE resin synthesized in this work

There are three types of LC epoxy resins which were synthesized for this study. They include digylcidyl ether of 4,4'-dihydroxybiphenol (DGE-DHBP), digylcidyl ether of 4-hydroxyphenyl-4"-hydroxybiphenyl-4'-carboxylate (DGE-HHC) and digylcidyl ether of 4,4'-dihydroxy-α-methylstilbene (DGE-DHMS). LCEs are capable of forming LC phases during curing. For monomer LCEs, the structures consist of different lengths of mesogenic units which are encapped with glycidyl groups. These end reactive groups can react further with a curing agent and form three-dimensional networks. This chapter is devoted to the synthesis of three LCEs and their characterization - so as to understand their properties before curing, blending and mechanical testing.

2) Synthesis of LCEs

2.1 An overview of the synthesis procedures

The LCEs were synthesized and purified for the purpose of blending them with a non-LC epoxy. The raw materials and solvents for synthesis were obtained from Aldrich Chemical Company. The materials were used as received – unless a statement to the contrary is given below. The materials were prepared in laboratory scale glass reactors according to the procedure described in the literature [137, 149].

2.2 Characterization

The synthesized products were dried for 48 hours at 70^{o}C under vacuum, ground and then characterized by the following methods.

Differential scanning calorimetry (DSC) (Perkin Elmer DSC-7) was used to observe thermal transition temperatures. Dynamic scans were conducted from 25-250^{o}C at 10 K/min.; the samples were cooled to 25^{o}C at the rate 10 K/min. N_2 was used as the purge gas with the flow rate of 20 mL/min. Heating and cooling cycles were conducted to locate the LC phase transition and melting temperatures. The temperature scale of the DSC apparatus was calibrated with an indium standard.

The polarized optical microscope (POM) used was a Zeiss Axioplan equipped with a camera and Ernst Leitz heating stage. LC phase transitions were observed during heating and curing and compared with the results from DSC. The synthesized products were put on a glass slide, covered and pressed to make a thin layer before being observed under a microscope.

Fourier-transform infrared spectroscopy (FT-IR) (Perkin Elmer) was used to determine the functional groups in the product. The powder sample and dried KBr were finely mixed and pressed into a KBr pellet. Spectra were recorded at the resolution of 4 cm^{-1} with 40 scans. The peak assignments were obtained and compared based on standard peaks [150].

X-ray diffraction (XRD) was used to determine liquid crystalline characteristics and d-spacing. The measurement was conducted on a Siemens D-500 diffractometer using Cu(Kα) radiation. The tube source was operated at 40 kV and 30 mA with the scanning speed of 1^{o}/min and sample interval of 0.05^{o}.

2.3 Synthesis of diglycidyl ether of 4,4'-dihydroxybiphenol (DGE-DHBP)

The schematic for the preparation of DGE-DHBP is shown in Figure 2.3. DGE-DHBP was synthesized by endcapping the hydroxyl groups of biphenol with epichlorohydrin in the presence of sodium hydroxide.

Biphenol (80 g, 0.43 mol), distilled water (74 mL), isopropanol (263 mL) and epichlorohydrin (340 mL, 4.32 mol) were added into a four necked 1 liter round bottom flask, equipped with a magnetic strirrer, thermometer, and addition funnel. The mixture was heated to 90 ^{o}C. After the temperature reached 90 ^{o}C, 75 mL NaOH solution (NaOH 37.2 g in 152 mL water) was added dropwise for 1 hour. The mixture was reacted for 1 additional hour. The reaction was stopped and the water layer removed with a pipette. The remaining 75 mL NaOH solution was added dropwise for 1 hour, and the water layer removed. After completion, the precipitated product was washed with isopropanol and filtered through a funnel until dried. 400 mL dioxane was used to reprecipitate the product. $MgSO_4$ was added to absorb water and removed with filter paper. The solution was kept for precipitation overnight in a refrigerator. The product was filtered and dried in the oven at 70 ^{o}C for 48 hours. The product has about 85 % yield.

The proposed reaction mechanism is shown in Figure 3.4. The reaction initiator is NaOH which produces phenolate anion. These reactive groups can react with glycidyl groups and create the nucleophilic ring opening at the primary carbon of epichlorohydrin. The dehydrohalogenation reaction result in the epoxide group as shown.

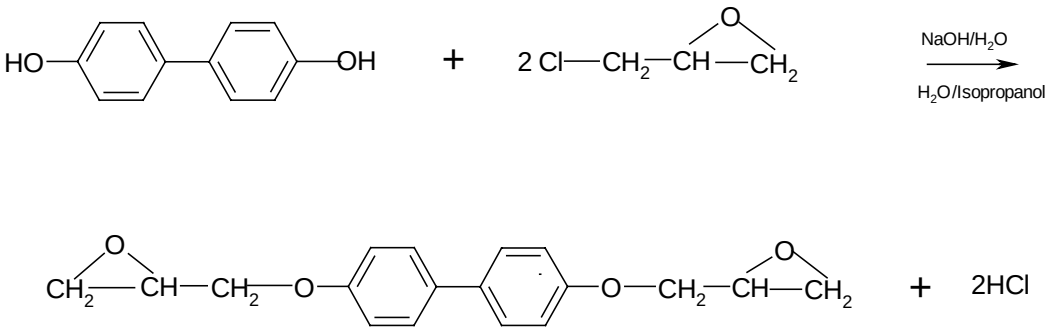

Figure 3.3 Reaction scheme for diglycidyl ether of 4,4'-dihydroxybiphenol synthesis

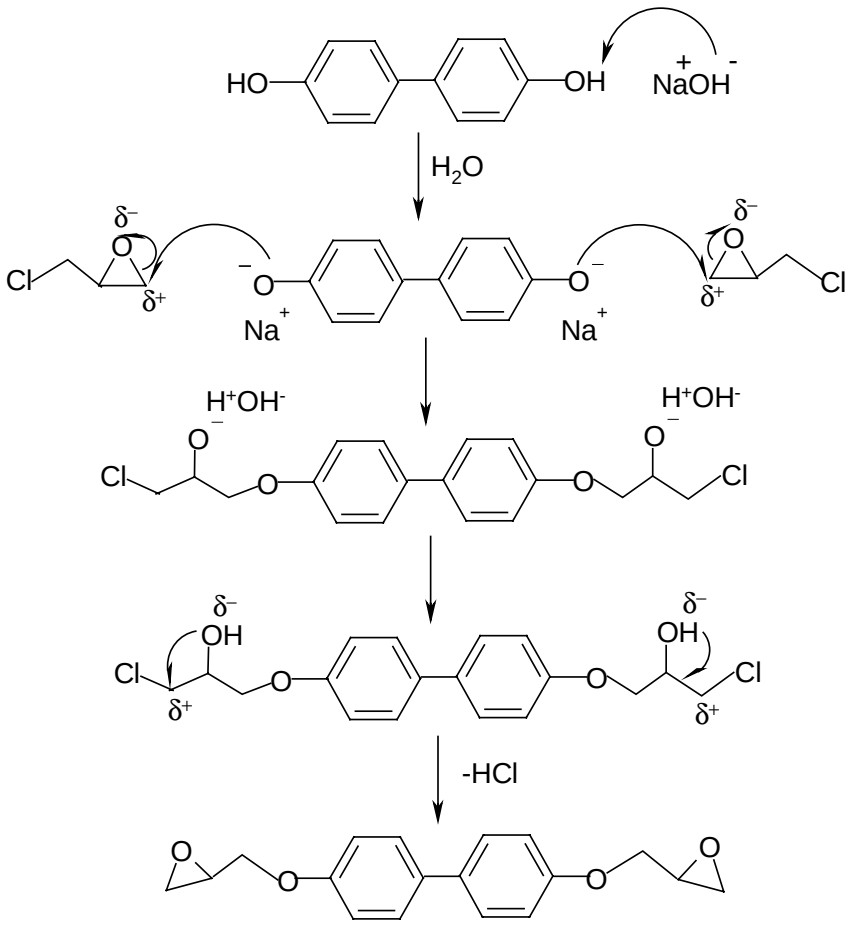

Figure 3.4 Reaction mechanism for digylcidyl ether of 4,4'-dihydroxybiphenol synthesis

2.3.1 Characterization

The DSC thermogram of the synthesized DGE-DHBP is presented in Figure 3.5. It reveals a first transition at 135 ^{o}C followed by the melting point at 158 ^{o}C. The heats of transition are 20.5 and 73.7 J/g, respectively. Upon cooling to room temperature a double peak is recorded with two maxima at 140 and 149 ^{o}C, as also previously observed by Carfagna and his colleagues [134]. Polarized optical micrograph shows no change in the appearance of LC texture on low temperature transition. The crystal melts and at the same time becomes isotropic upon heating to 158 ^{o}C. The LC phase has not been found for the uncured sample. Figures 3.6 and 3.7 show the change while heating the DGE-DHBP respectively at 25 and 120 ^{o}C. The texture at 120 ^{o}C, while the sample was cooled, is presented in Figure 3.8. The crystal is formed when the sample is further cooled down (Figure 3.9). We note the results of Hefner [151] who earlier reported the absence of the LC phase earlier. Grebowicz [128] suggested the first peak at 135 ^{o}C corresponds to the melting of metastable crystals. The functional groups of the product were checked by FT-IR (Figure 3.10). The peak at 915 cm^{-1}, which represents the absorption related to the asymmetric stretch of epoxy ring, was monitored. This peak was also examined in the cured samples to resolve the amount of epoxy left in the system. Assignment of the spectrum is shown in Table 3.3. X-ray spectrum and respective assignments are shown in Figure 3.11 and Table 3.4. There are two major diffraction patterns. The diffraction at 2θ = 6.02 (d = 14.22) represents the intermolecular correlation while the diffraction from layer spacing is found around 2θ = 19 (d = 4.5).

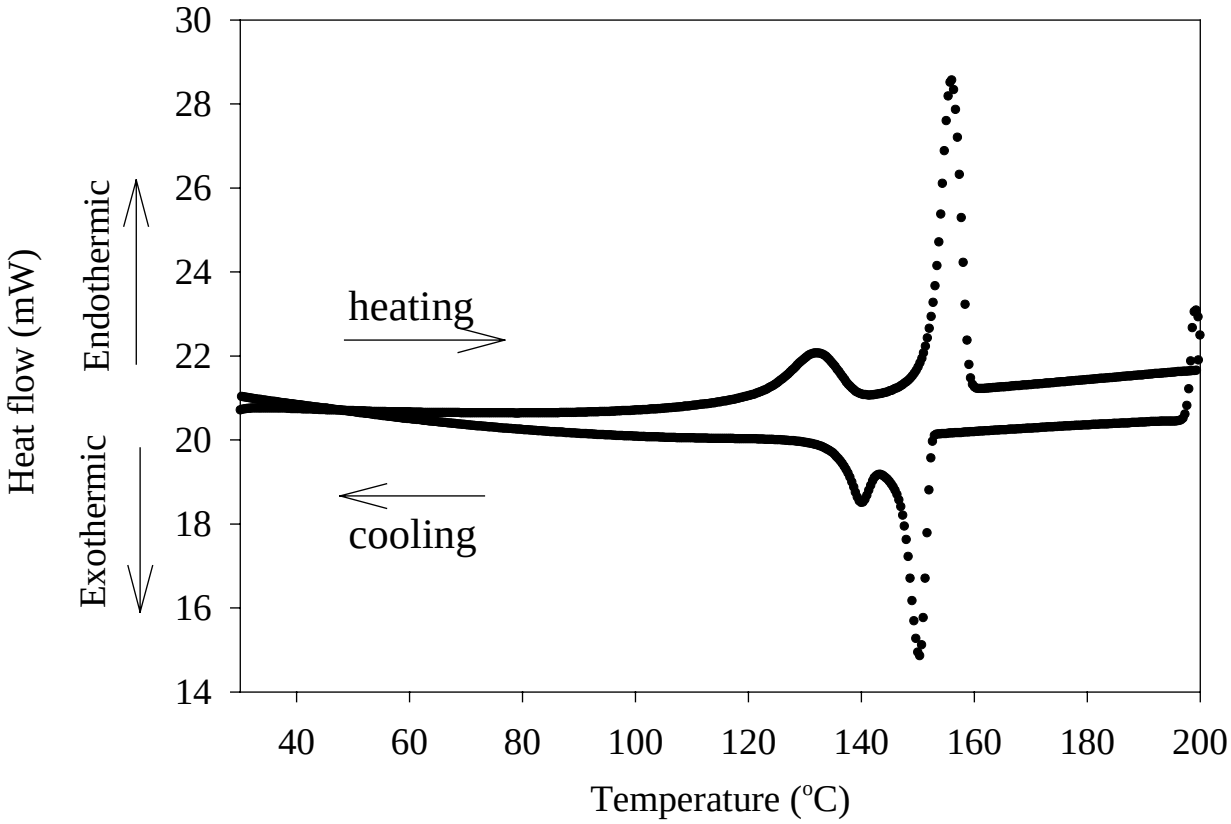

Figure 3.5 DSC thermogram of DGE-DHBP

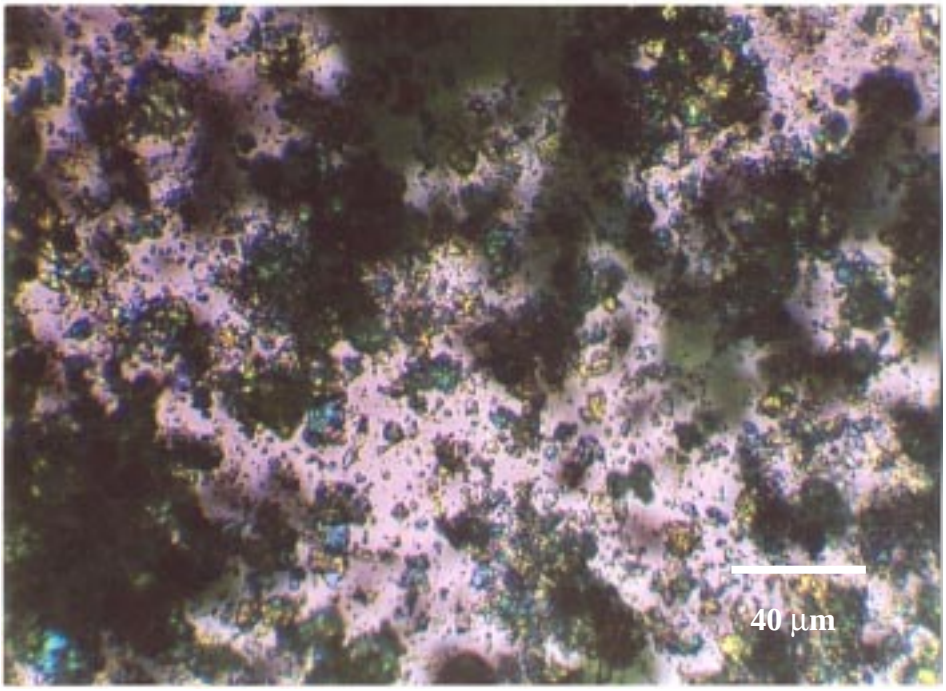

Figure 3.6 Optical microscopy of DGE-DHBP at 25 ^{o}C

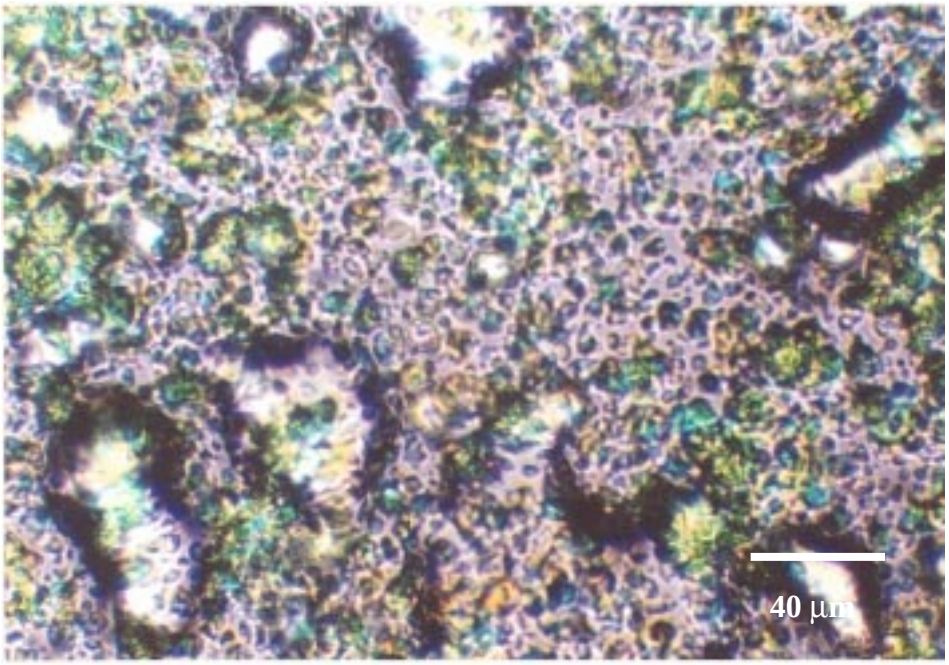

Figure 3.7 Optical microscopy of DGE-DHBP at 120 ^{o}C

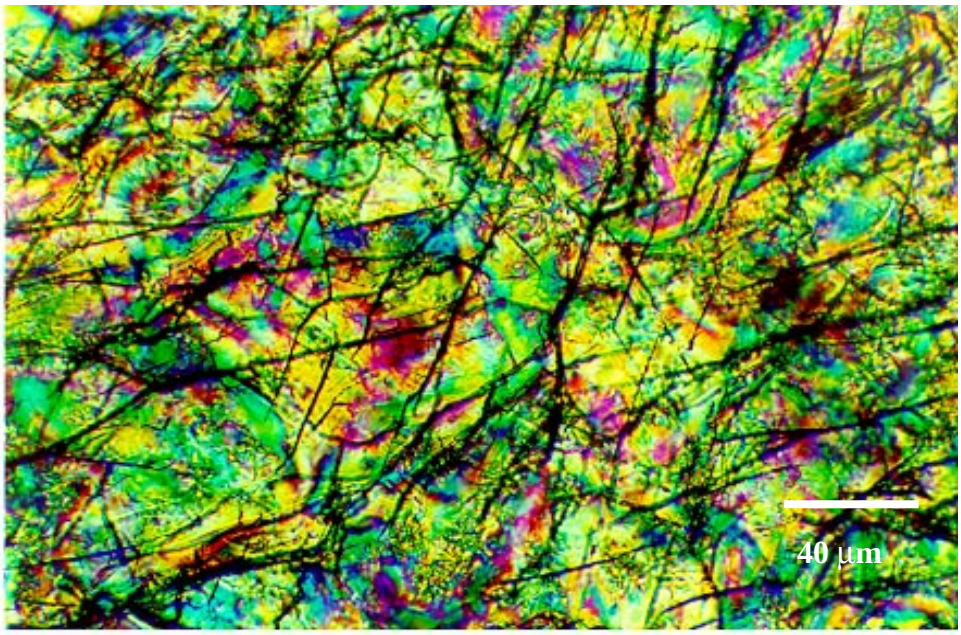

Figure 3.8 Optical microscopy of DGE-DHBP while cooling at 120 ^{o}C

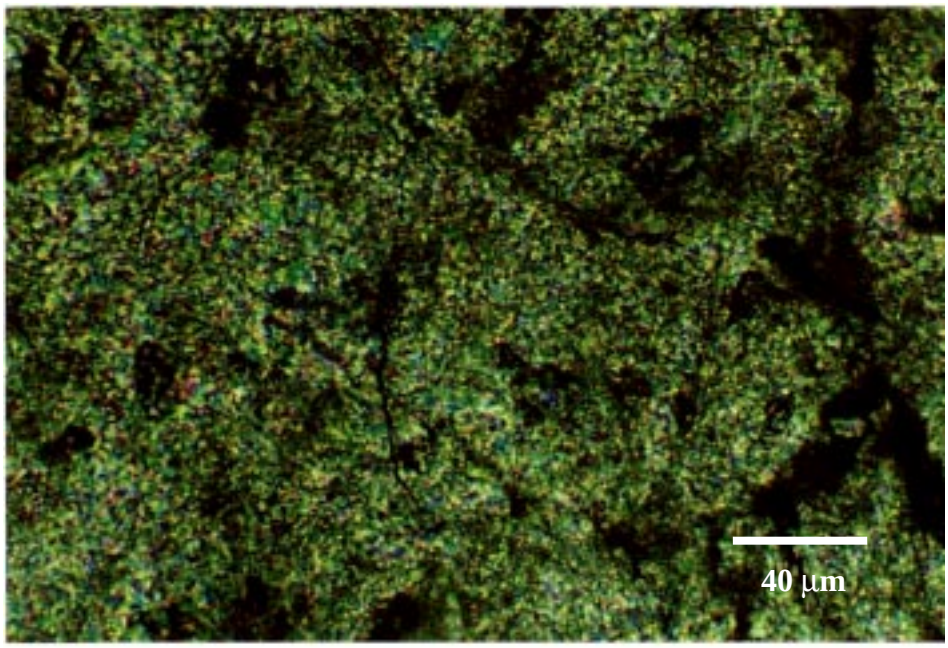

Figure 3.9 Optical microscopy of DGE-DHBP while cooling to 100 ^{o}C

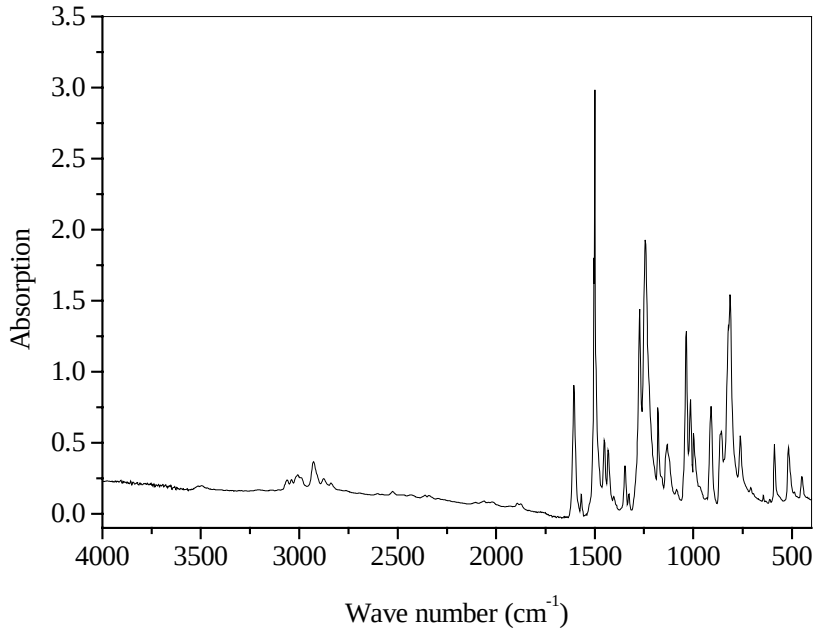

Figure 3.10 FT-IR spectra of synthesized DGE-DHBP

Table 3.3 Assignment of infrared spectrum of DGE-DHBP

Functional groups	Wave number (cm^{-1})
C-H aromatic	2870-3000
C=C olefinic	1605
C=C aryl	1500
C-O-C	1179, 1132, 1085
C-O-C epoxy	916, 863
1,4 disubstituted aromatic	813
Biphenyl	587, 517, 449

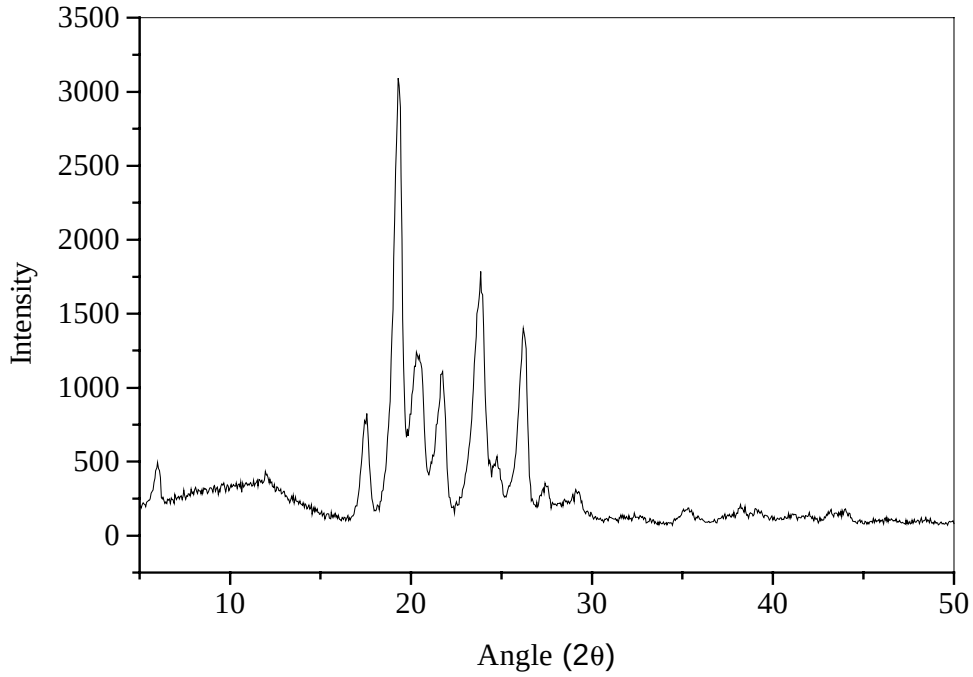

Figure 3.11 X-ray spectrum of DGE-DHBP

Table 3.4 X-ray assignment of DGE-DHBP to d-spacing

2θ	d (Å)
6.02	14.66
17.69	5.01
19.46	4.56
20.48	4.33
20.72	4.28
21.89	4.06
24.02	3.70
26.39	3.37

2.4 Synthesis of diglycidyl ether of (4-hydroxyphenyl-4"-hydroxybiphenyl-4'-carboxylate) (DGE-HHC)

The synthesis procedure of DGE-HHC consists of two main steps. The first is the preparation of 4-hydroxyphenyl-4"-hydroxybiphynyl-4'-carboxylate (HHC) with hydroxy end groups. The second step is the functionalization of the glycidyl groups at both ends of the mesogenic groups.

Hydroxydiphenyl carboxylic acid (15 g, 0.069 mol) and hydroquinone (39 g, 0.360 mol) were added into a four-necked 1 liter round bottom flask equipped with a heating mantle, nitrogen sweep, thermometer, and nitrogen trap in the first step. The reaction mixture was kept at 270 ^{o}C for 1 hour. After the completion of the reaction, the mixture was poured into a beaker filled with distilled water. The product was stirred in the water for 30 minutes and then filtered. The solid was recrystallized with ethanol and one tablespoon of activated carbon was added to the reaction mixture. After the solid was filtered out, the solution was kept in the refrigerator overnight. The crystal obtained was filtered and dried in the oven at 70 ^{o}C for 24 hours.

The compound obtained from the first step was terminated by the following method. HCC (8.14 g, 0.027 mol) epichlorohydrin (63 mL, 0.82 mol), and tetrabutyl ammonium chloride (0.18 g, 6.50×10^{-4} mol) were added to the four-necked 1 liter round bottom flask equipped with a thermometer, magnetic stirrer, nitrogen sweep, condenser, and nitrogen trap. The reaction was kept at 60 ^{o}C for 16 hours. Afterwards, the pressure in the flask was reduced to 0.3 atm. 45 weight % of NaOH solution was added dropwise to the reaction. The reaction was performed at 65 ^{o}C for 5 hours and the epichlorohydrin

was removed from the system by vacuum. The product obtained was dissolved in 300 mL acetonitrile. NaCl from the reaction was filtered out and 300 mL methanol was added to the solution. The mixture was kept overnight in the refrigerator, filtered and dried in the oven for 30 hours at 70 ^{o}C.

The reaction schematic is shown in Figure 3.12. The proposed reaction mechanism is shown in Figures 3.13 and 3.14. In the first step, the hydroquinone attacks the carbonium ion of the resonance structure of hydroxydiphenyl carboxylic acid. The loss of water produces DHMS as a stable product. In the second step, the glycidyl groups are terminated in the place of hydroxyl groups involved in the reaction with epichlorohdrin. Tetrabutylammonium chloride is used as the catalyst for the reaction.

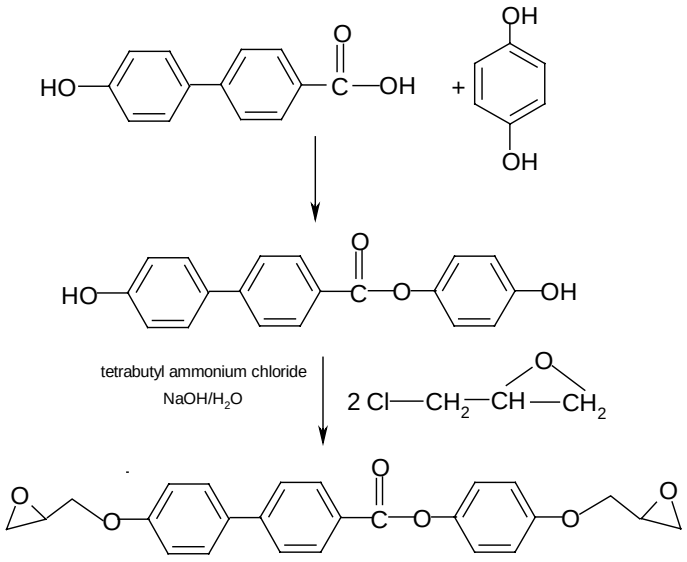

Figure 3.12 Reaction schematic for DGE-HHC synthesis

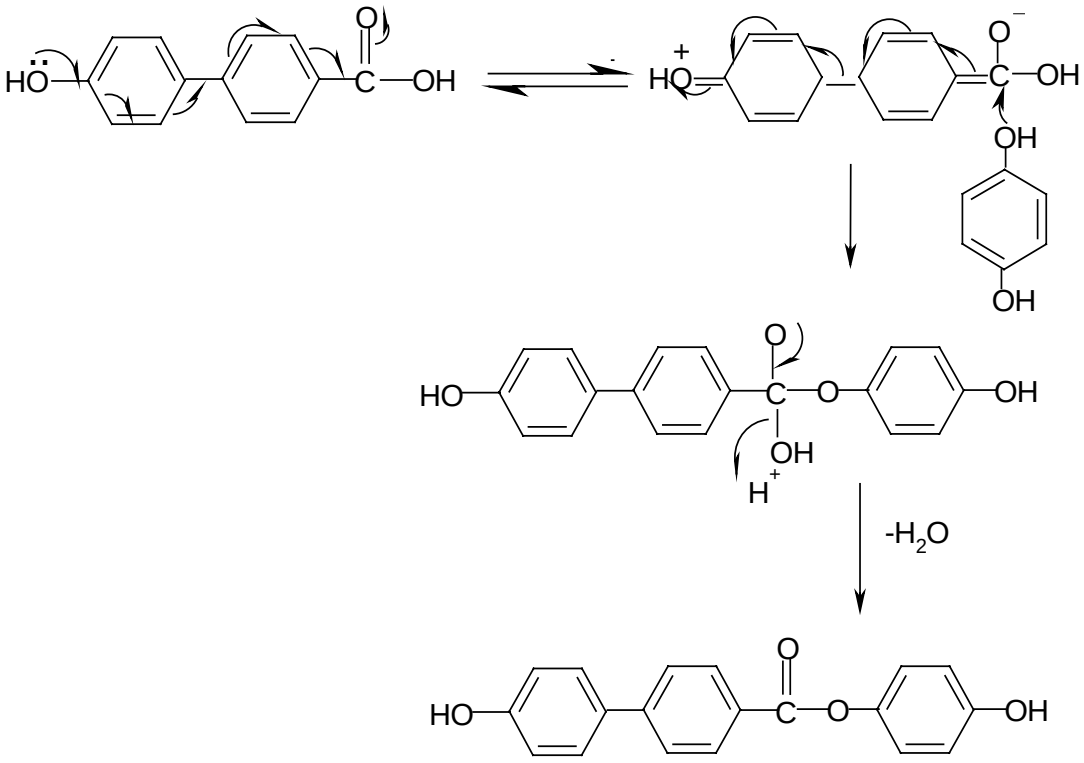

Figure 3.13 Proposed mechanism of synthesis of 4-hydroxyphenyl-4”-hydroxybiphenyl-4’-carboxylate (HHC) (step I)

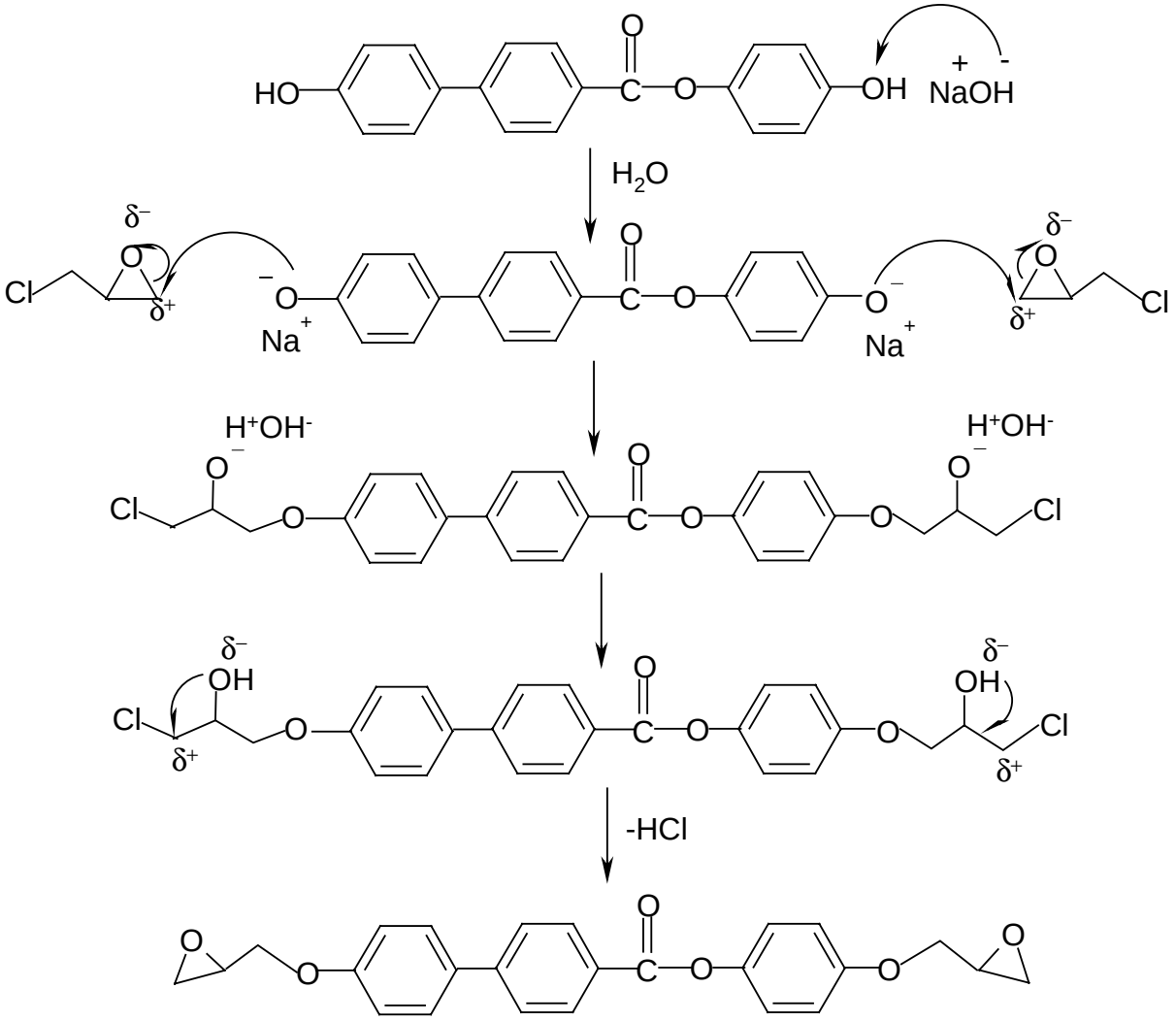

Figure 3.14 Proposed mechanism of synthesis of diglycidyl of 4-hydroxyphenyl-4”-hydroxybiphenyl-4’-carboxylate (DGE-HHC) (step II)

2.4.1 Characterization

The DSC thermogram of the synthesized HHC is presented in Figure 3.15. It reveals a melting transition at 293 ^{o}C with the heat of fusion ΔH_f = 161.9 J/g in the first heating run. The crystallization peak was recorded during cooling at 280 ^{o}C.

The thermogram of DGE-HHC is shown in Figure 3.16. The enantiotropic LC characteristic is found. In the first heating, the melting peak at 121 ^{o}C with ΔH_f = 31.8 J/g and the nematic-isotropic transition was found at 192 ^{o}C with the heat of transition of 0.36 J/g.. The cooling run indicates a small LC transition in the range of 120-190 ^{o}C.

Polarized optical microscopy shows that DGE-HHC is an enantiotropic LC in which the LC phase occurs in both heating and cooling processes. The anisotropic nature of the LC leads to the birefringence. The LC phase is found in the range of 130-210 ^{o}C. In the first heating, DGE-HHC melts at 120 ^{o}C with the formation of birefringence (Figure 3.17). The small scale schlieren texture and birefringence area coexist at 130 ^{o}C - as shown in Figure 3.18. The LC droplet is formed around 220 ^{o}C (Figure 3.19). The center of each nematic droplet represents a point defect. Formation of the schlieren texture [152] follows. The schlieren texture is the nonuniformity of local director. The nematic schlieren structure seen at 50 ^{o}C is shown in Figure 3.20. A disclination point and a disclination brush are shown in the picture. The disclination brushes are observed when director is parallel or perpendicular to the polarizer.

The functional groups of the product were checked by FT-IR measurement (Figure 3.21); the assignment of spectrum is provided in Table 3.5. The dominant peak is

found at 1778 cm^{-1}; it represents the absorption related to stretching of the carbonyl group.

X-ray spectrum and the respective assignment of DGE-HHC are shown in Figure 3.22 and Table 3.6. As compared to DGE-DHBP (d = 14), the d-spacing is approximately double for DGE-HHC (d = 27). Thus, the latter has a longer mesogenic unit.

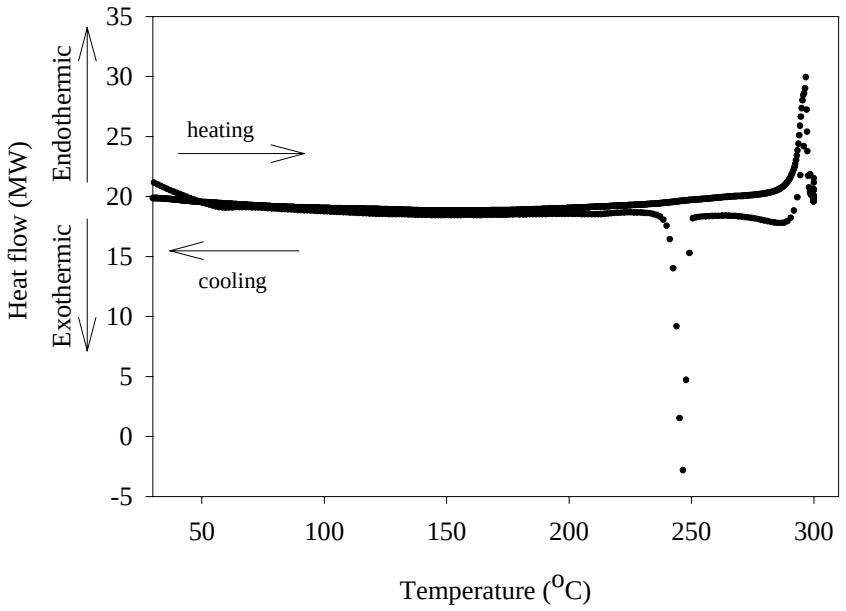

Figure 3.15 DSC thermogram of HHC

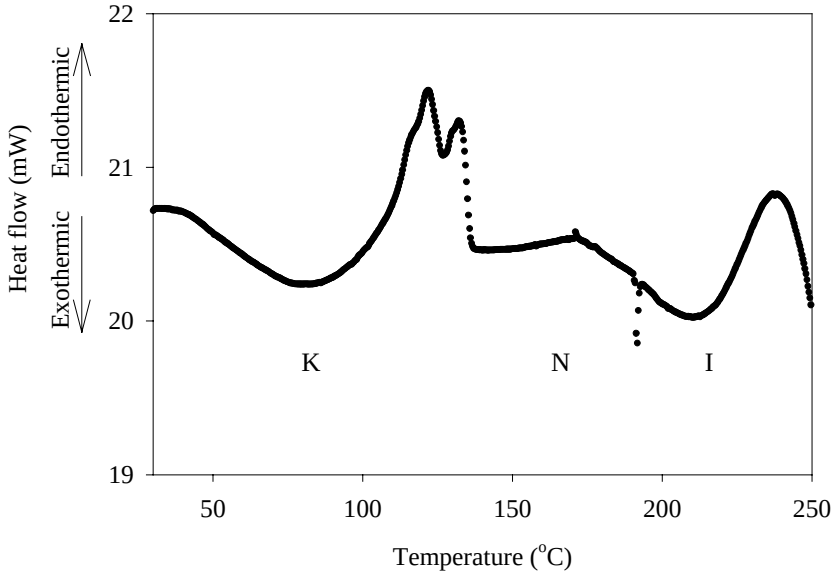

Figure 3.16 DSC thermogram of DGE-HHC

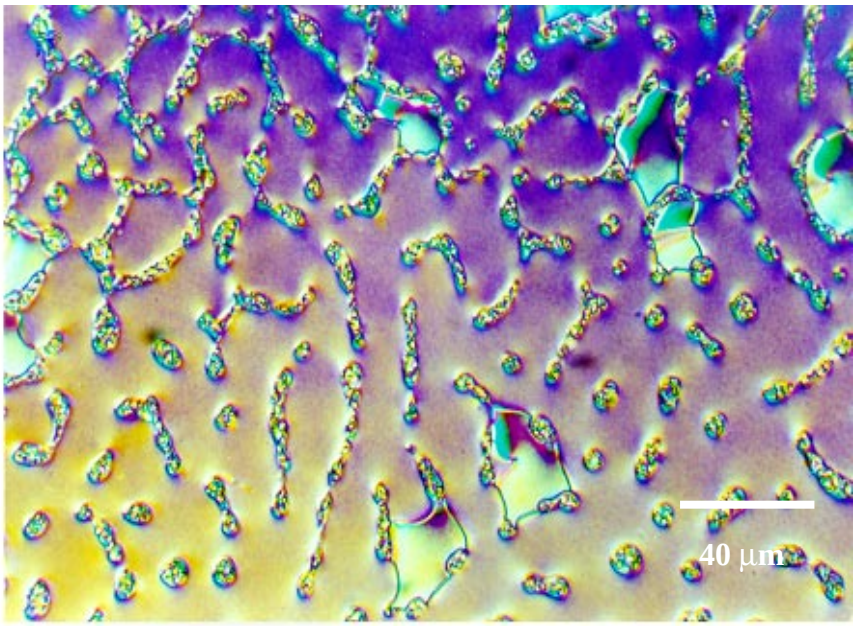

Figure 3.17 Small scale schlieren texture and birefringence obtained during heating DGE-HHC at 120 ^{o}C under polarizing optical microscope

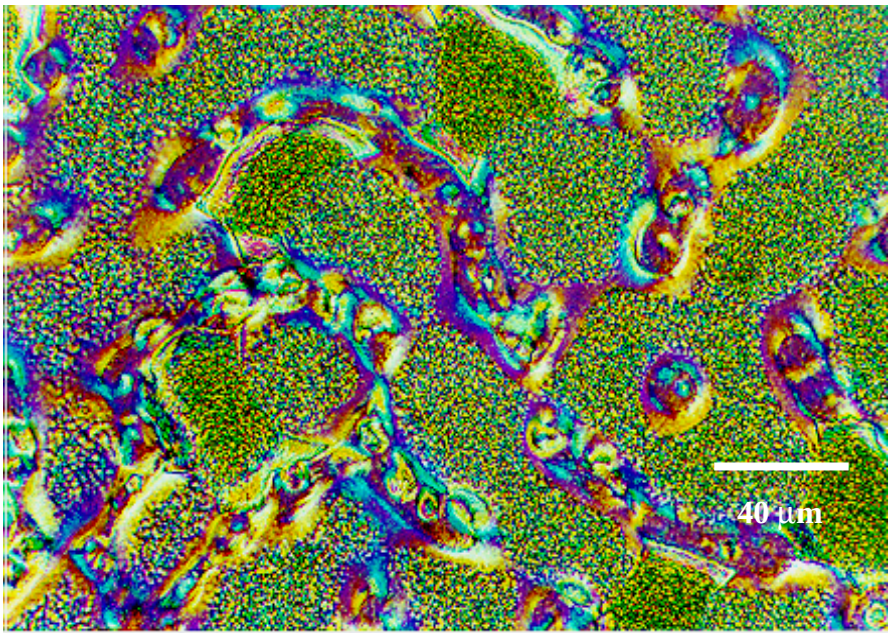

Figure 3.18 Small scale schlieren texture and birefringence obtained during heating DGE-HHC at 130 ^{o}C under polarizing optical microscope

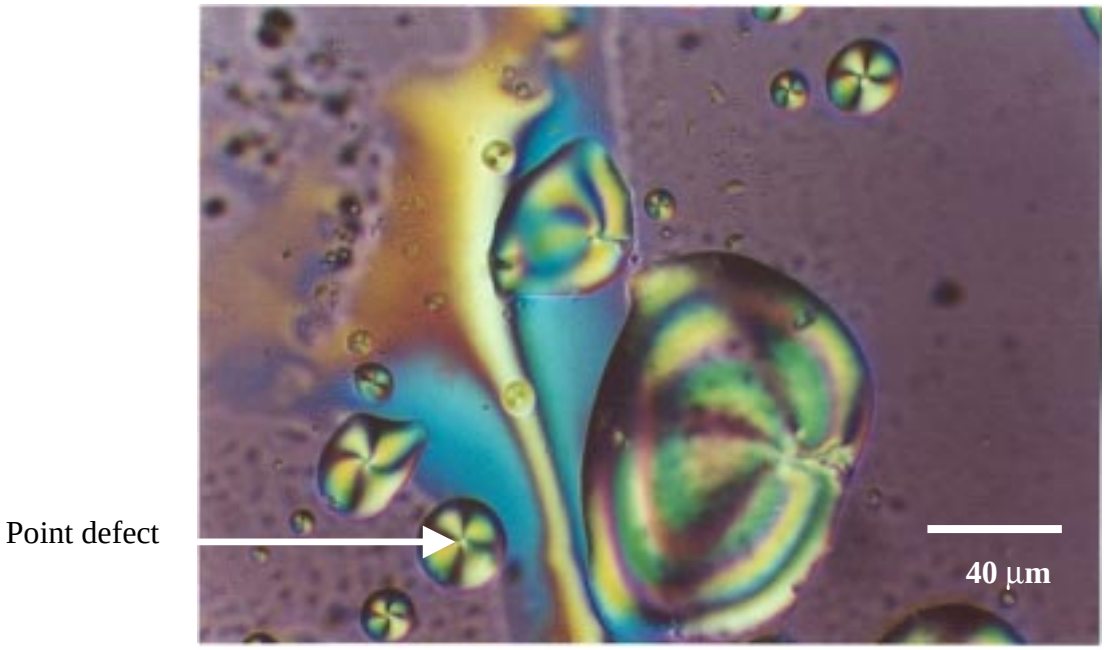

Figure 3.19 A droplet of schlieren texture obtained during heating DGE-HHC at 220 ^{o}C under polarizing optical microscope

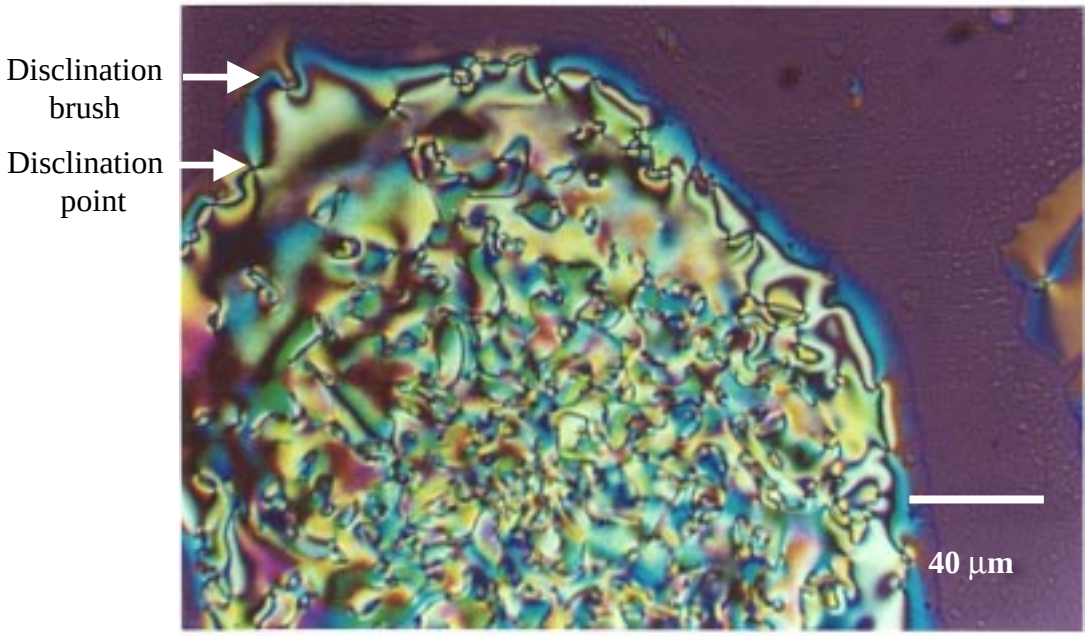

Figure 3.20 A large scale schlieren texture obtained during cooling DGE-HHC under a polarizing optical microscope

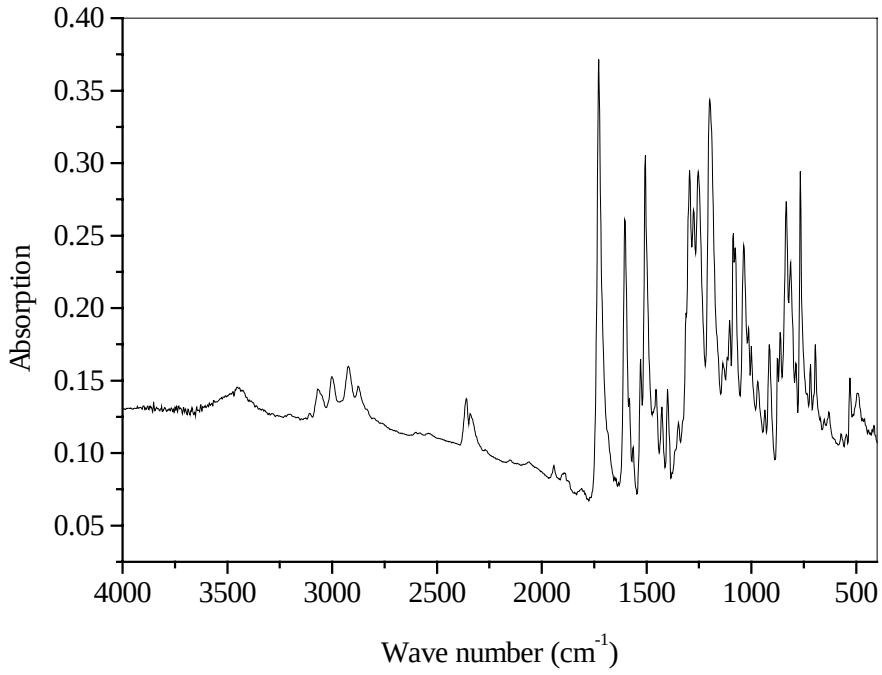

Figure 3.21 FT-IR spectra of DGE-HHC

Table 3.5 Assignment of infrared spectrum of DGE-HHC

Functional groups	Wave number (cm^{-1})
C-H aromatic	2870-3000
C=O stretching	1775
C=C olefinic	1603
C=C aryl	1506
C-O-C	1275, 1253, 1198
C-O-C epoxy	916, 863
1,4 disubstituted aromatic	813

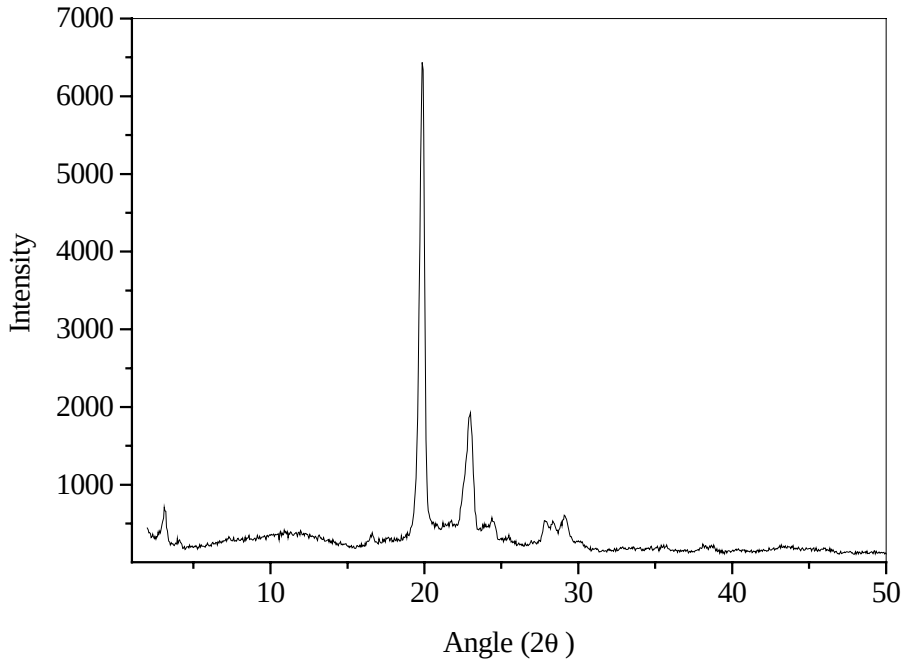

Figure 3.22 X-ray spectrum of DGE-HHC

Table 3.6 The assignment of X-ray peak

2θ	d (Å)
3.15	27.80
19.90	4.46
23.10	3.85
27.86	3.20

2.5 Synthesis of diglycidyl ether of 4,4'-dihydroxy-α-methylstibene (DGE-DHMS).

There are two steps to the synthesis of DGE-DHMS. In the first we prepare 4,4'-dihydroxy-α-methylstilbene (DHMS) with hydroxy end groups while in the second step we encap the the glycidyl groups at both ends of these mesogenic groups.

Phenol (68.0 g, 0.72 mol), chloroacetone (28.9 g, 0.31 mol), and dichloromethane (40.8 mL) were added into a four-necked 1 liter round bottom flask equipped with a magnetic stirrer, addition funnel and thermometer in the first step. The reaction mixture was cooled to -10 ^{o}C in a bath of NH_4Cl and dry ice. The mixture was stirred until a clear solution was obtained. Concentrated sulfuric acid (20 mL) was added dropwise slowly to the solution. The temperature of the reacting mixture was carefully controlled in the range from – 5 to – 10 ^{o}C. After completion of the acid addition, the mixture was continuously reacted for 2 hours to obtain a viscous orange paste. The reaction mixture was washed repeatedly with a mixture of ice and water until the pH of the product was between 6 and 7. The product was recrystallized from a mixture of water and ethanol and precipitated at room temperature overnight. The product was washed with a mixture of water and ethanol until a pH close to 7 was achieved. The product was allowed to precipitate again at room temperature overnight, filtered and dried in the oven at 70 ^{o}C for 24 hours.

In the second step, the DHMS product was endcapped with epichlorohydrin in the presence of sodium hydroxide as following. DHMS (58 g), distilled water (54 mL), isopropanol (191 mL) and epichlorohydrin (248 mL) were added into a four-necked 1

liter round bottom flask, equipped with a magnetic strirrer, thermometer, and addition funnel. The mixture was controlled at 90 ^{o}C while adding 55 mL NaOH solution (NaOH 27 g in water 110 mL) dropwise for 1 hour. The mixture was reacted further for 1 hour. The reaction was stopped and the water layer was removed by pipette. The remaining 55 mL NaOH solution was added dropwise, reacted for 1 hour, and the water layer removed. After completion, the precipitated product was washed with isopropanol and filtered by funnel until dried. Then 400 mL dioxane was used to reprecipitate the product. $MgSO_4$ was added to absorb water and was removed with filter paper. The solution was precipitated from 300 mL cold distilled water. 300 mL cold methanol was added to the white solid product. The product was filtered through a Buechner funnel and washed 3 times with distilled water. The product was dried in the oven at 70 ^{o}C for 48 hours.

The overall schematic of the synthesis of DGE-DHMS is shown in Figure 3.23. The proposed mechanism of the synthesis of DHMS is shown in Figure 3.24. To produce DHMS, the hydrogen ions from the acid first attack the carbonyl groups of chloroacetone to produce quarternary ions. The intermediate product further reacts with phenol via Sn_1 reaction and leaves chloride ions. The conjugation structure drives the reaction to form methylstilbene as a stable structure. In the epoxidation step, the mechanism is the same as discussed in Section 2.3.

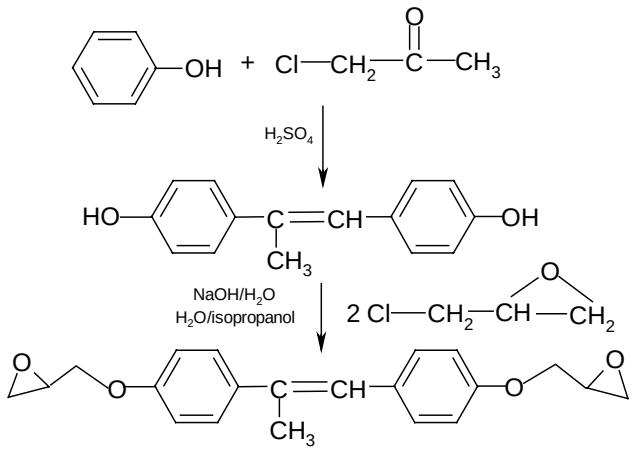

Figure 3.23 Reaction schematic for DGE-DHMS synthesis

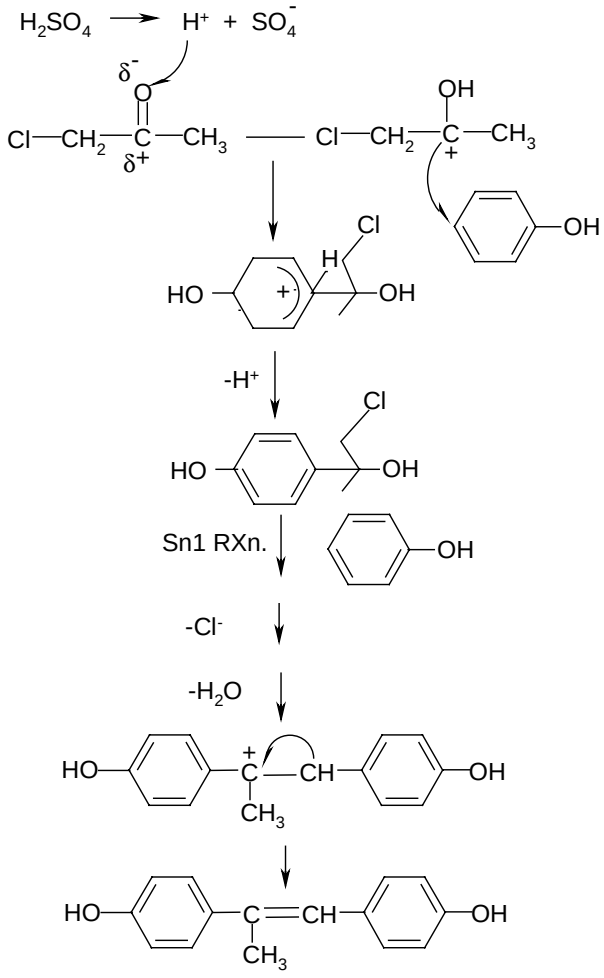

Figure 3.24 The mechanism of DHMS synthesis

2.5.1 Characterization

Figure 3.25 presents the DSC thermogram of DHMS. The heating cycle shows a melting peak at 192 ^{o}C and a crystallization peak at 156 ^{o}C during the cooling cycle. The DSC thermogram of the synthesized DGE-DHMS is shown in Figure 3.26. In the first heating, the melting transition is observed at 126 ^{o}C with the heat of transition equal to 92 J/g. Two transitions are found during the cooling stage. The isotropic-nematic transition is found at 106 ^{o}C with the heat of transition of 1.75 J/g; the nematic-crystal transition appears at 65 ^{o}C with the heat of transition of 42 J/g.

Polarized optical microscopy confirms the DSC result that DGE-DHMS is a monotropic LC upon cooling to the range 60-105 ^{o}C. DGE-DHMS melts and becomes isotropic during the first heating at 126 ^{o}C. During cooling, an abrupt LC formation began at 106 ^{o}C. The LC texture began to develop at 105 ^{o}C, as shown in Figure 3.27. The texture of the nematic thread-like type is presented in Figure 3.28. The LC texture develops from microdomains and grows into a crystal form as shown in Figure 3.29. Furthermore, the cooling leads to the crystal formation (Figure 3.30).

The functional groups of the product were checked by FT-IR spectrum (Figure 3.31) with the assignment of spectrum given in Table 3.7. The dominant peak is found at 1609 cm^{-1} and represents the absorption related to stretching of the C=C double bond.

The X-ray spectrum and respective peak assignment are presented in Figure 3.32 and in Table 3.8. The diffraction pattern shows lower d-spacing compared to DGE-DHBP and DGE-HHC since DGE-DHMS does not contain biphenyl groups. However, the double bond at the center creates an oriented structure.

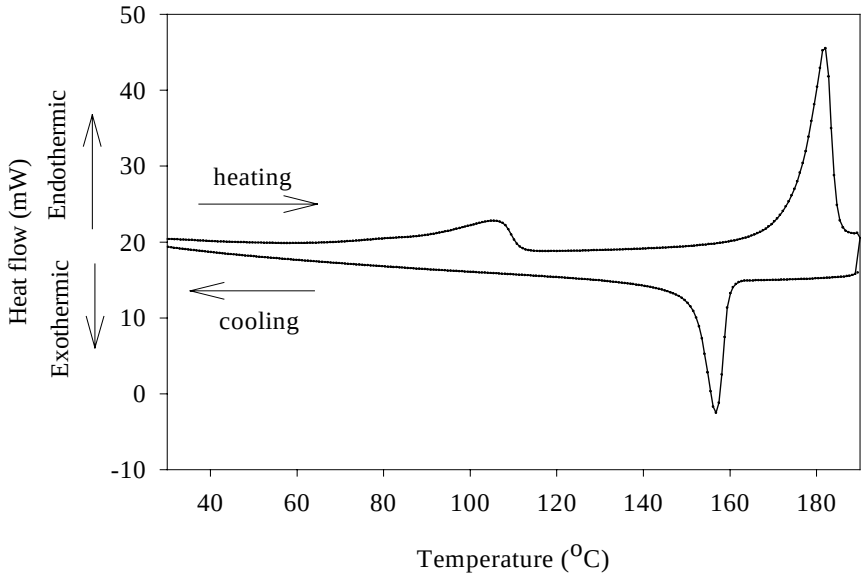

Figure 3.25 DSC thermogram of DHMS

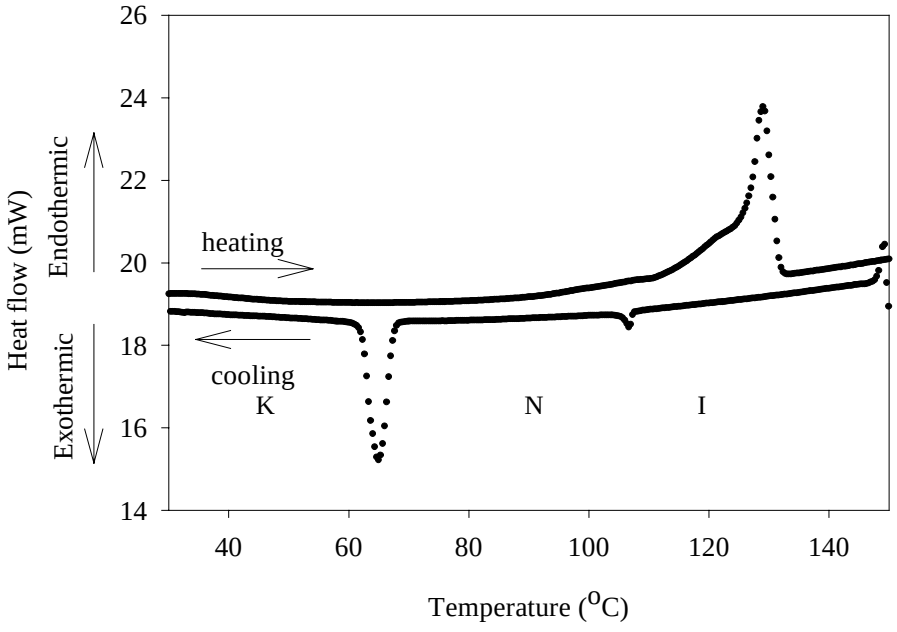

Figure 3.26 DSC thermogram of DGE-DHMS

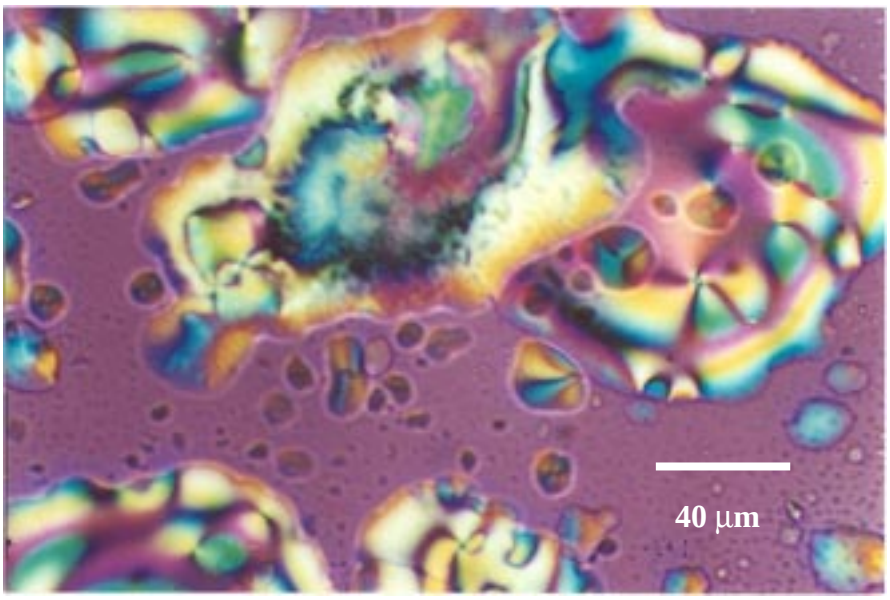

Figure 3.27 The beginning of birefringence of DGE-DHMS observed with optical microscope

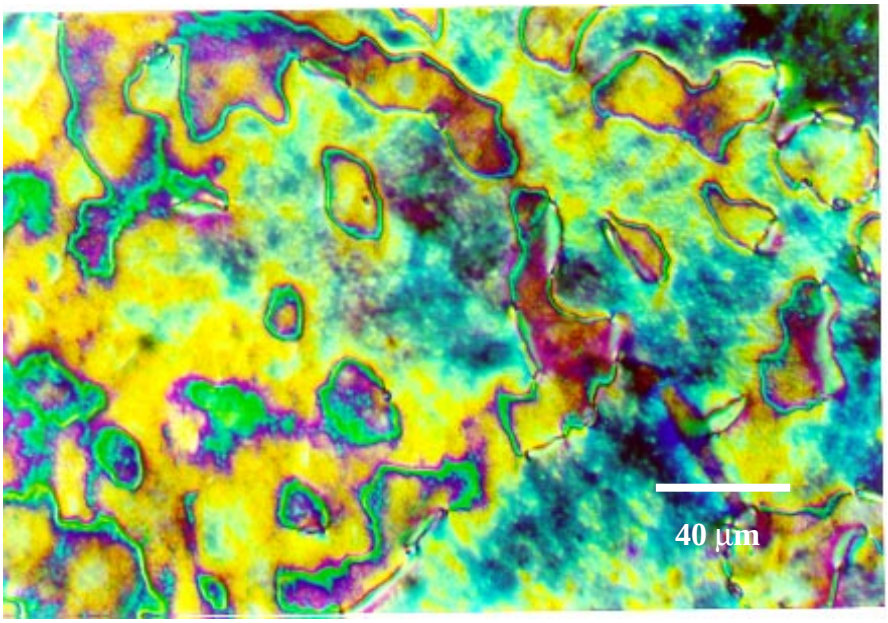

Figure 3.28 Nematic thread-like texture of DGE-DHMS observed under optical microscope at 100 ^{o}C

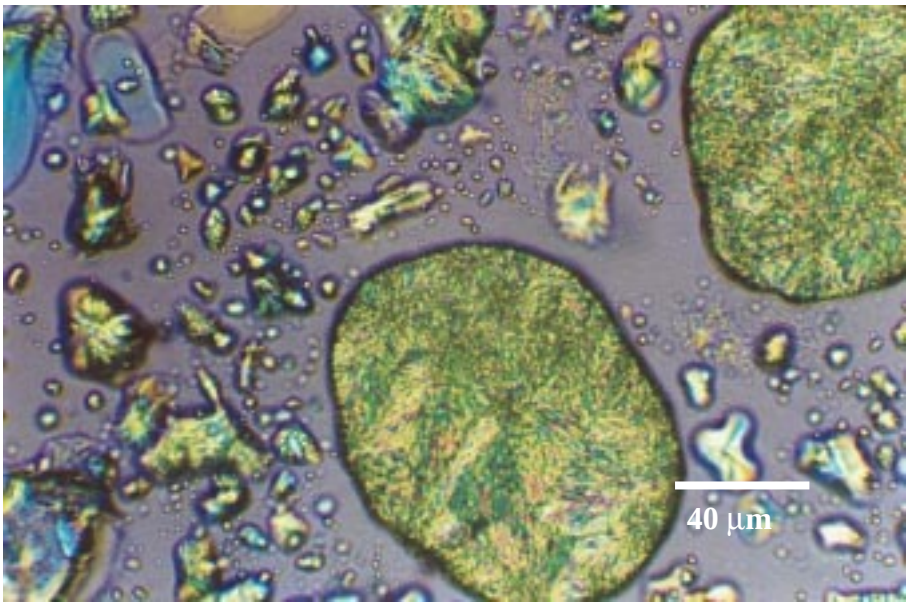

Figure 3.29 Optical microscopy of DGE-DHMS observed under POM at 90 ^{o}C

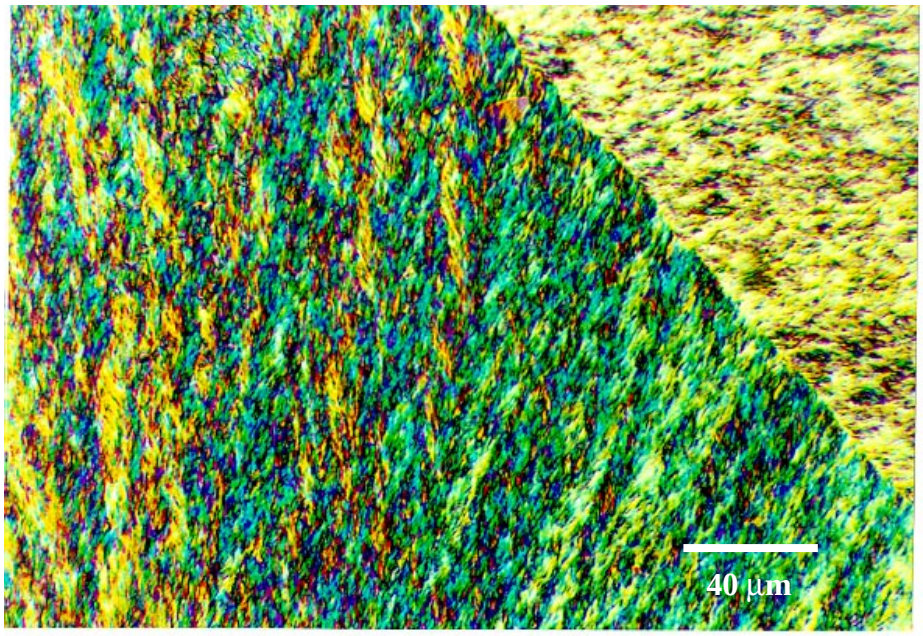

Figure 3.30 Optical microscopy of DGE-DHMS observed under POM at 60 ^{o}C

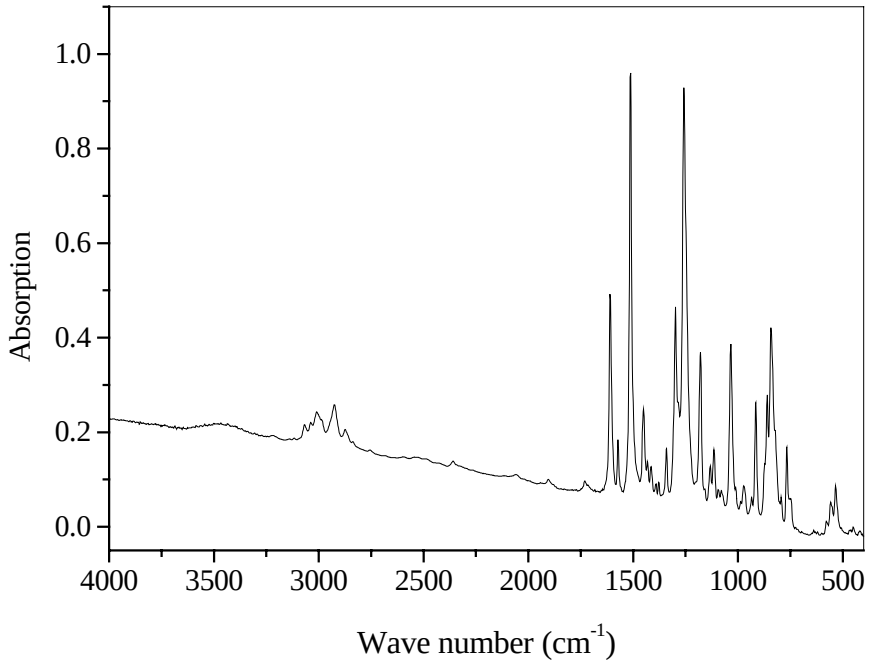

Figure 3.31 FT-IR spectrum of DGE-DHMS

Table 3.7 Assignment of infrared spectrum of DGE-DHMS

Functional groups	Wave number
C-H aromatic	2870-3000
C=C olefinic	1609, 1572
C=C aryl	1513
C-O-C	1179, 1132, 1085
C-O-C epoxy	916, 863
1,4 disubstituted aromatic	813

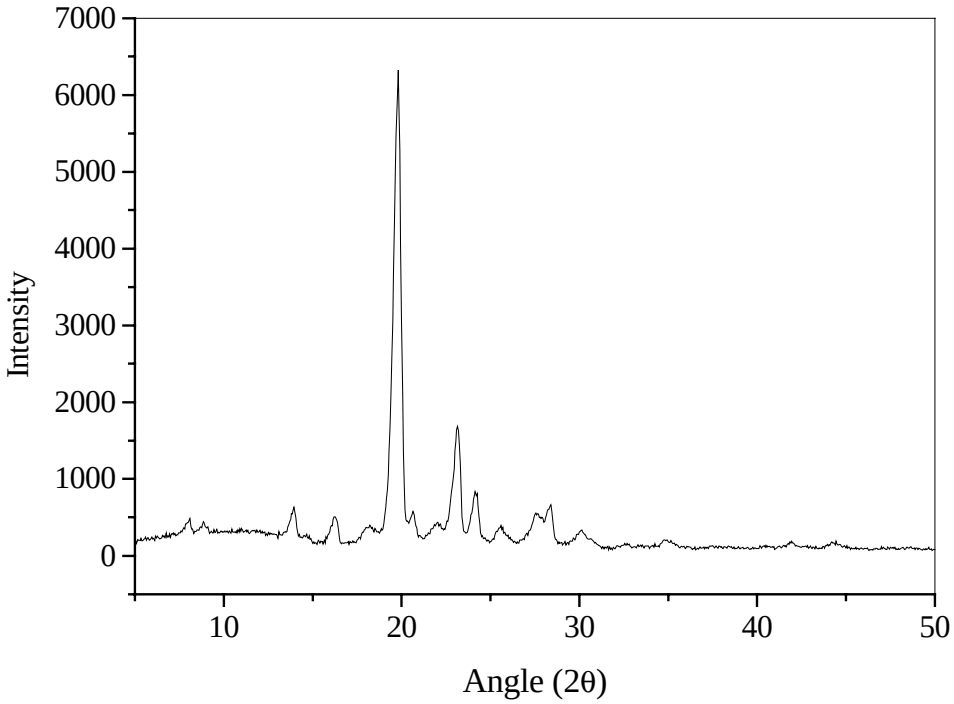

Figure 3.32 X-ray spectrum of DGE-DHMS

Table 3.8 The assignment of X-ray spectrum

2θ	d (Å)
8.10	11.33
8.85	11.04
13.95	6.35
16.21	5.46
19.80	4.48
23.15	3.84
24.15	3.68
27.55	3.23
28.39	3.14

CHAPTER 4

CURING AND BLENDING OF LIQUID CRYSTALLINE EPOXY WITH NON LIQUID CRYSTALLINE EPOXY

1) Introduction

1.1 Curing of Liquid Crystalline Epoxy Resins

The mechanical properties of cured LC epoxy networks are varied and depend on the following parameters: nature of mesogenic units and their length in epoxy monomers, nature of curing agents, and curing conditions. Normally, longer mesogenic units lead to an increased stability of the LC phase. However, chemical structures also affect the behavior. The nature of curing agents provides several mechanisms of curing. Curing conditions highly affect the properties of cured LCEs as well.

The network formation reaction of LCEs involves two main mechanisms, namely "chain extension" as well as "crosslinking" - different from conventional non-LCEs. Therefore, the classic theory of LC phase formation by Warner [153] needs to be modified to include the effect of chain extension of LCEs which can increase LC interactions and also increase the stability of the LC mesophase.

1.2 Time-temperature-transformation diagram

The isothermal time-temperature-transformation (TTT) cure diagram proposed by Gillham relates the time and temperature of curing to the state of cured resins [154-157]. The diagram is a useful tool to optimize properties of cured material. The curing of epoxies is complex and involves the linear growth of main chains, growing of branch

chains and the formation of a three-dimensional network. Figure 4.1 is the schematic of the TTT diagram for a curing thermoset.

Gelation and vitrification are important phenomena found during isothermal cure of epoxy resins. The gelation point involves the initial formation of an infinite crosslinked polymer, so the epoxy cannot be processed after this point. The vitrification point corresponds to the transition of liquid or rubbery state into the glassy state; it can occur at any stage during cure.

Three glass transitions shown in the picture are T_{go}, the glass transition temperature of the unreacted material; ${}_{gel}T_g$, the temperature at which gelation and vitrification occur simultaneously; $T_{g\infty}$, the glass transition temperature of a fully cured network. At temperatures below T_{go}, the curing reaction is slow since the material is in the glassy state. When the system is cured between the T_{go} and ${}_{gel}T_g$, the reaction will occur without gelation until its increasing T_g meets the cure temperature (${}_{gel}T_g = {}_{gel}T_{cure}$). After that point, diffusion controls the process. At cure temperatures between ${}_{gel}T_g$ and $T_{g\infty}$, the viscous liquid changes to a viscous fluid and rubber, and to glass. The material first gels and then vitrifies. At temperatures above $T_{g\infty}$, the material is in the rubbery state after gelation unless there are other reactions, including thermal degradation or oxidative crosslinking. Polymer degradation is the normal step in ceramics manufacturing or in carbon-carbon composites [158].

The diagram of rubber-modified epoxy is shown in Figure 4.2. The curing process involves changes in morphology from a homogeneous to a heterogeneous phase to form rubber particles. The separation range is shown close to the gelation range.

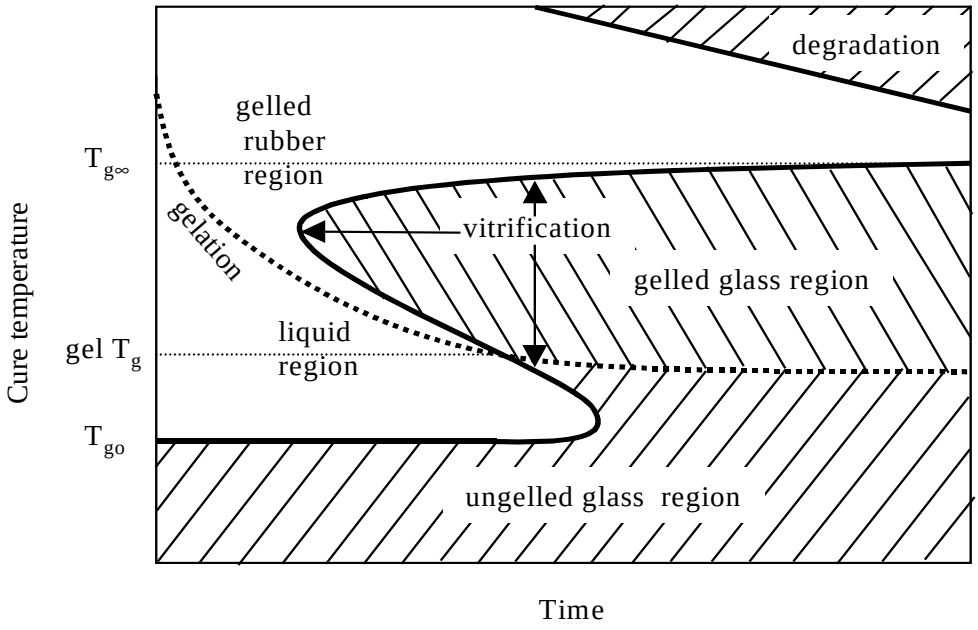

Figure 4.1 Schematic of isothermal time-temperature-transformation diagram for thermoset curing (after [154-156])

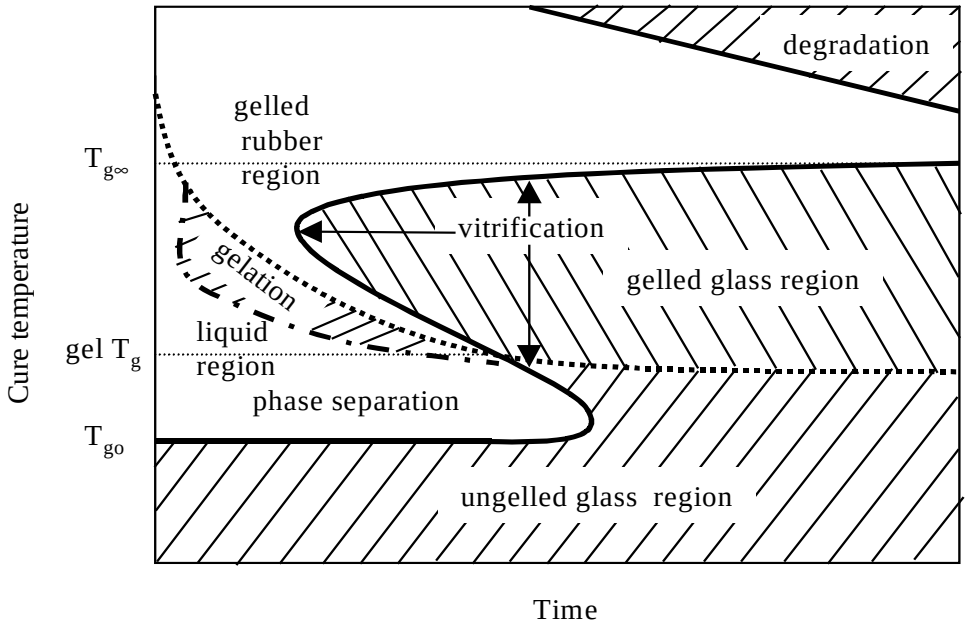

Figure 4.2 Schematic of isothermal time-temperature-transformation diagram for curing of a rubber-modified thermoset (after [154-156])

The TTT diagram of liquid crystalline and isotropic phase is a useful tool to understand the phase transformations of LC networks. In crosslinking of LCEs with amine curing, the mesophase is developed during the initial stage of curing. The epoxy monomer and the curing agent react to form a linear polymer and then the liquid crystalline phase is stabilized during gelation of the network [159]. The effect of time and temperature of curing, therefore, needs to be clearly understood.

Lin and Yee [160] studied the TTT diagram of DGE-DHMS with aniline adduct of the DGE-DHMS (difunctional amine) and sulfanilamide (tetrafunctional amine). They found the S-curve characteristics which correspond to the LC transformation of isotropic to nematic phase in the case of a difunctional amine. The smectic phase was found for a tetrafunctional amine system. The S-shape is the result of interaction between LCEs and curing agents.

The TTT diagram of DGE-DHMS with 4,4'-methylene dianiline has been observed by Ortiz and Ober [161] and involves transition temperatures of smectic, nematic LC and isotropic phases. They found that the LC transformation took place in the range of 10 to 25 minutes of cure time at each temperature. Wide angle X-ray diffraction was used to confirm the existence of the LC phase.

Crosslinking reactions of LCEs with several types of curing agents were studied. Therefore, POM and DSC were used to determine the time-temperature-transformation (TTT) diagram by observing isothermal cure in all systems. This information will be used later to cure LCEs to obtain desired properties.

2) Materials

Four main kinds of epoxy resins were chosen for this study (Table 4.1). The DGE-DHBP, DGE-HHC and DGE-DHMS are the LCEs. The synthesis procedures are presented in Chapter 3. LCEs have different properties compared with non-LC epoxy since the curing reaction of LCE locks the LC sequences in a three-dimensional network. The non-LC epoxy resin used in this study is a low viscosity diglycidyl ether of bisphenol F (DGEBP-F) obtained from Shell (EPON862®). DGEBP-F forms an isotropic network upon curing. There is no mesogenic unit in the structure; instead it has kinked structure. A schematic comparing the chemical structures of all epoxies is shown in Figure 3.3. For monomer LCEs, the structures contain mesogenic units of different lengths which are encapped with glycidyl groups. These end reactive groups can react further with the curing agent and form a three-dimensional network. The para-substituted benzene rings in LCES, which are elongated and arranged parallel to one another, act like mesogenic units.

Table 4.2 shows the physical properties of three curing agents used in this study. Methyltetrahydro-phthalic anhydride (MTHPA) (Lindride-6) pre-catalyzed by benzyl triethyl ammonium chloride (BTEAC) was chosen since it will be further used for composite applications. Two amine curing agents, 2,4-diaminotoluene (DAT) and diaminodiphenyl sulfone (DDS) were obtained from Aldrich Chemical Co. DAT is an asymmetric molecule while DDS is a symmetric one. Consequences of this difference will be discussed later. DDS is the standard curing agent used for high temperature applications in military and aerospace industries.

Table 4.1 Comparison of physical properties and schematic of shape for all epoxy resins

Structure	MW	EEP	T_m (^oC)	T_{NI} (^oC)	ML* (Å)
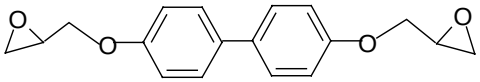 Digylcidyl ether of 4,4'-dihydroxybiphenol (DGE-DHBP)	298	166	153	-	7.2
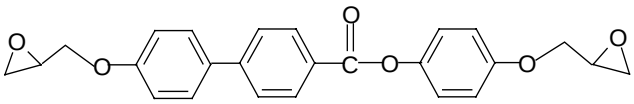 Digylcidyl ether of 4-hydroxyphenyl-4"-hydroxybiphenyl-4'-carboxylate (DGE-HHC)	418	211	121	220	13.5
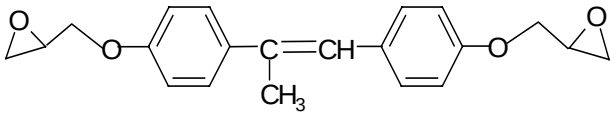 Digylcidyl ether of 4,4'-dihydroxy-α-methylstilbene (DGE-DHMS).	338	185	129	106	9.2
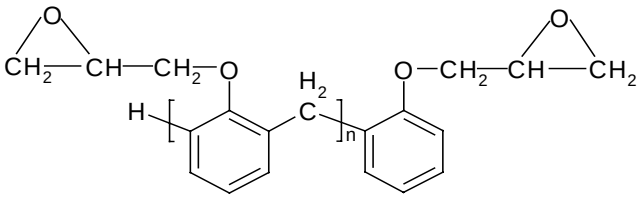 diglycidyl ether of bisphenol F (DGEBP-F)	342	168	-	-	-

Note : MW = molecular weight, EEP = epoxide equivalence weight, T_m = melting temperature, T_{NI} = nematic-isotropic transition temperature, ML = mesogenic unit length * (after [93])

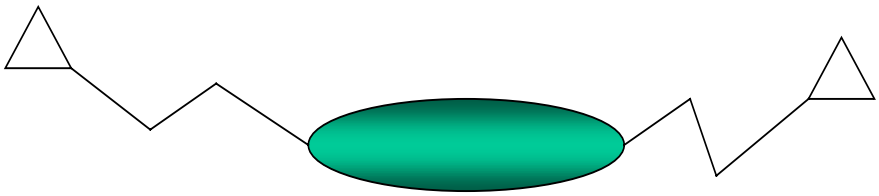

digylcidyl ether of 4,4’-dihydroxybiphenol (DGE-DHBP)

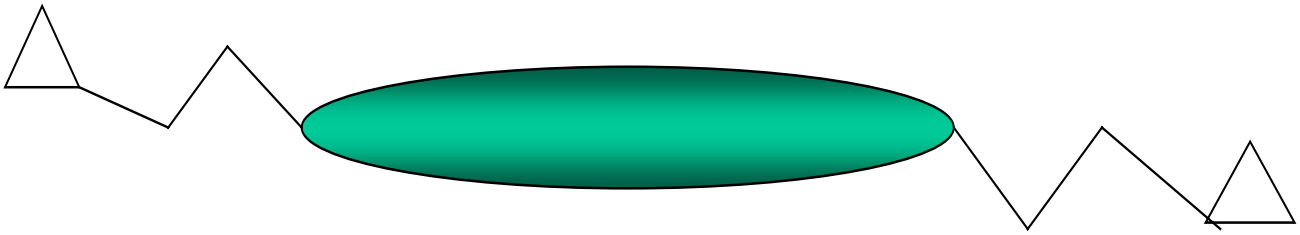

digylcidyl ether of 4-hydroxyphenyl-4”-hydroxybiphenyl-4’-carboxylate (DGE-HHC)

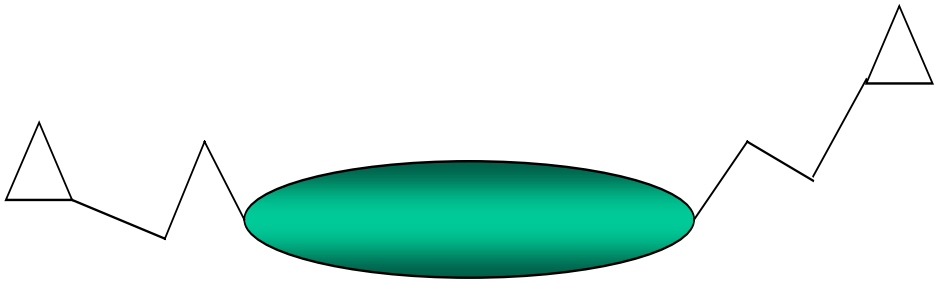

digylcidyl ether of 4,4’-dihydroxy-α-methylstilbene (DGE-DHMS).

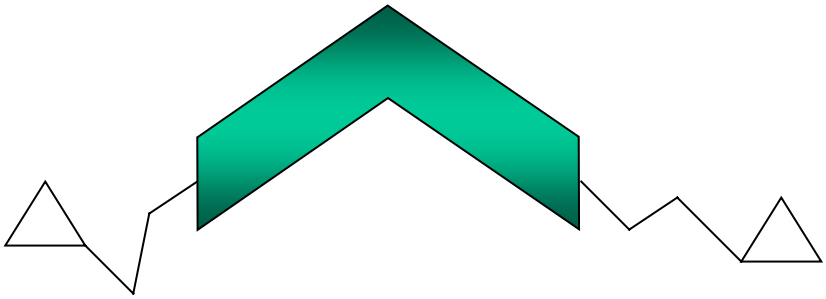

diglycidyl ether of bisphenol F (DGEBP-F)

Figure 4.3 Schematics of molecular shapes of both LCEs and non-LCEs

Table 4.2 Physical properties of the curing agents

Structure/name	MW	T_m	EW
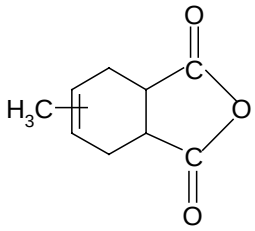 Methyltetrahydrophthalic anhydride (MTHPA)	168	-	168
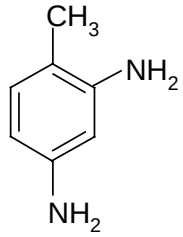 2,4-diaminotoluene (DAT)	122	98	31
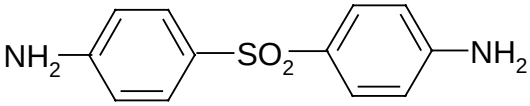 Diaminodiphenyl sulfone (DDS)	248	176	62

Note : MW = molecular weight, EW = equivalence weight, T_m = melting temperature

3) Curing mechanisms

3.1 Mechanism of anhydride curing

Mechanisms of catalyzed curing of epoxies with cyclic anhydrides are complex since several competing reactions can occur and involve an anionic mechanism suggested by Fisher [162]. In this case a tertiary amine, which is used as a Lewis base, is added to accelerate the curing reaction. The reaction is supposed to occur via the formation of a zwitterion. A tertiary amine first reacts with the anhydride group to create the carboxylate zwitterion group [$R'_3N^{\oplus}$-CO CO-$O^{\ominus}$]. The reactive groups can react further with an epoxide. Tanaka and Kaki [163] suggested that a tertiary amine in the form of hydroxylate [$R_3N^{\oplus}CH_2$-$CH(CH_2R')O^{\ominus}$] can also react with anhydride groups. The continuation of these alternating reactions produces a polyester. Therefore, the addition esterification and etherification via ionic living polymerization are the major mechanisms. The proposed curing mechanism is shown in Figure 4.4.

Methyl tetrahydrophthalic anhydride (MTHPA) was chosen for this study due to its potential to increase the flexibility and ductility of epoxy. Potential applications include electrical casting, encapsulation, and impregnation. The epoxy curing reaction with MTHPA is slightly exothermic, resulting in low shrinkage and a stress-free system. These qualities are pertinent for good electrical insulation and are retained under moderate to high operating temperatures. Good thermal stability is important for electrical applications. MTHPA is prepared as a eutectic mixture of regio- and stereo-isomers by Diels-Alder reaction between isoprene and maleic anhydride.

Step I: Initiation

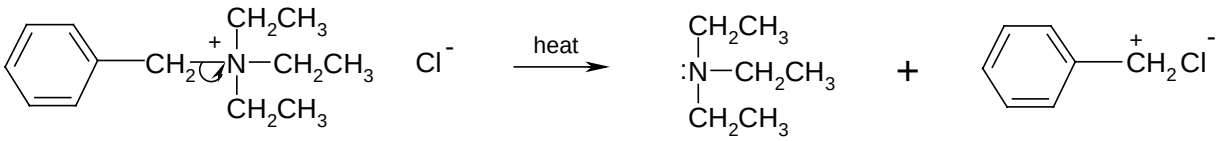

benzyltriethylammonium chloride (BTEAC) | triethyl amine | benzyl chloride

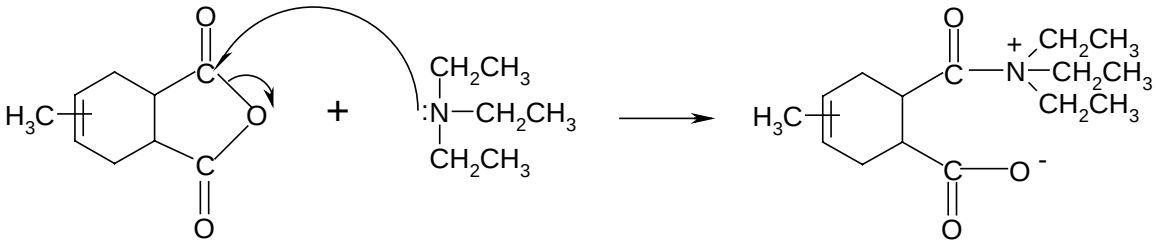

methyltetrahydrophtalic anhydride

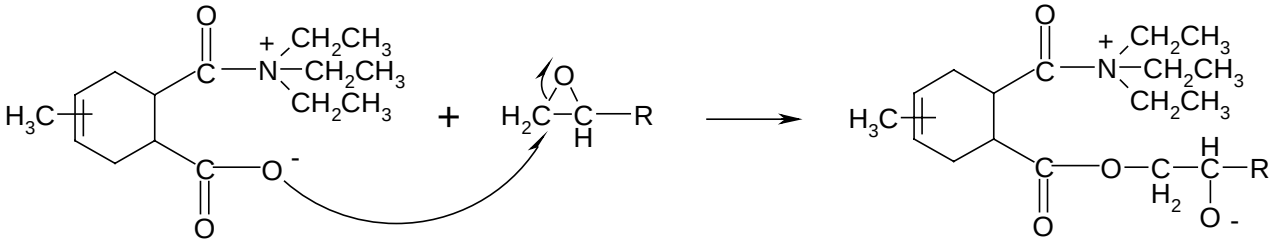

I | **II**

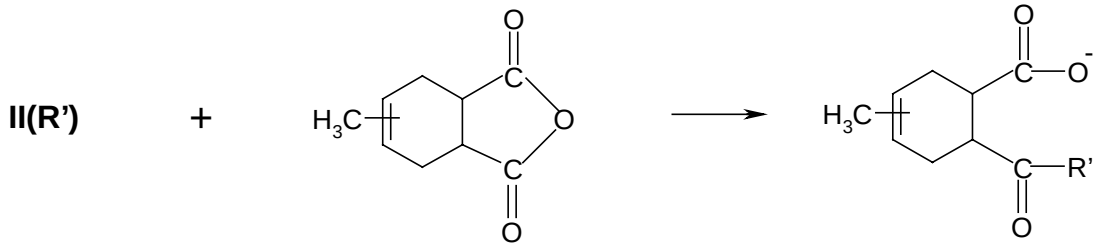

II(R')

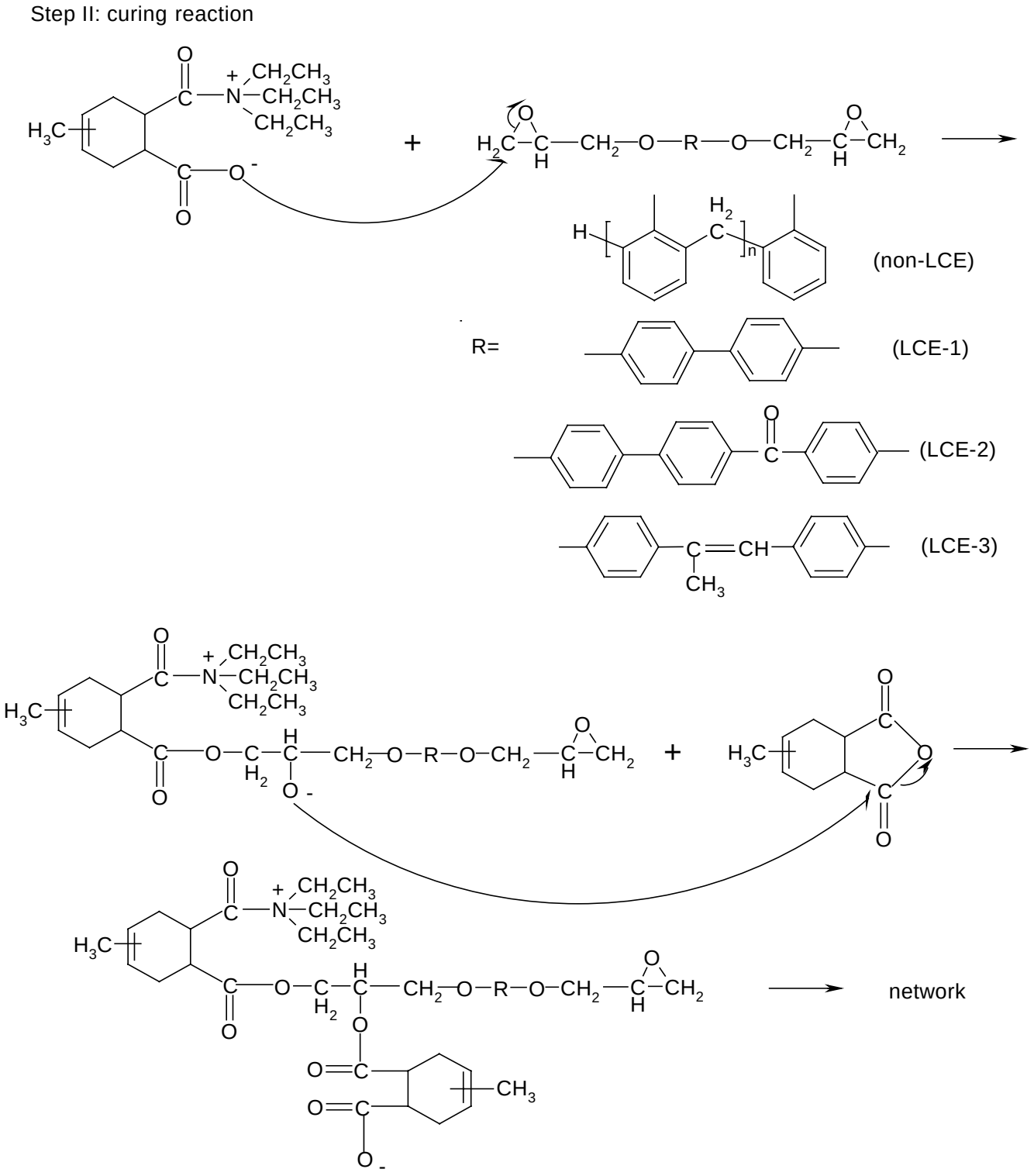

Figure 4.4 Reaction mechanism for curing epoxy resins by anhydride curing agents

3.2 Mechanism of amine curing

The epoxy ring is a highly strained structure with unbalanced charges. Therefore, it can react with a variety of curing agents. Amine curing agents are widely used. Curing of epoxy-amine systems involve four possible reactions, namely 1) reaction of primary amine with epoxy; 2) reaction of secondary amine with epoxy; 3) reaction of hydroxyl groups with epoxy (etherification reaction); and 4) reaction of the homopolymer with epoxy. The homopolymer is found only in Lewis acid or base catalyst systems hence it can be neglected in this case [164-165].

The reaction of an amine hardener involves the opening of the epoxide group to form an alcohol without any by-product formation. The secondary amine is further reacted with another epoxy group. Hydroxyl groups can react with epoxide groups and act like self-catalysts since they create new hydroxyl groups as they react. Therefore, the reaction proceeds in the autocatalytic mode. The schematic of the first three reactions is shown in Figure 4.5.

The reaction rate constant (k) for each step of the reaction is different. The reactivity of primary amine (k_1) is the dominant reaction. Normally, k_1 is higher than the reactivity of the secondary amine (k_2). This is the result of steric hindrance and reduced mobility. The ratio of k_2/k_1 has been reported = 0.67 for oxirane and N-(2-hydroxyethyl)amine or oxirane and N,N-bis(2-hydroxyethyl)amine [166], and equals 0.49 for 1,2-epoxypropane and n-butylamine [167]. The reaction constant of etherification (k_3) is also lower than k_1. Moacanin et al. [168] reported that k_3 is about 10 times lower than k_1 as observed from DSC and FT-IR. The study of Morgan and

coworkers [169] indicates that the primary amine-epoxide reaction is dominant at the early stages of cure until all primary amine is consumed. The hydroxyl-epoxide reaction is then dominant at the later stages of the cure.

The mechanism for the hydroxyl group accelerating the amine-epoxide reaction was suggested by Shechter et al. [170-171]. They found that the hydroxyl groups generated during the reaction, or provided by addition of solvent (water, isopropyl alcohol, phenol), accelerate the amine-glycidyl ether reaction via a concerted termolecular reaction mechanism. The hydroxyl groups present in the epoxy resin also serve as catalysts for the reaction. This is confirmed by Desek and Bleha [172], Riccardi and Williams [173], and Simon and Gillham [174]. Therefore, in the system with excess amine or at the stochiometric concentration, reactions 1) and 2) are dominant while reaction 3) can be neglected. In contrast, the etherification cannot be ignored when excess epoxide is presented in the reaction. The schematic of this mechanism is presented in Figure 4.6.

Smith [175] proposed the mechanism of hydrogen formation through transition complexes, referring to the work of Parker [176] and Eastman [177-178] as shown in Figure 4.7. The hydrogen bond is formed between the oxygen of the epoxide and the hydrogen of the donor (step I). The next step is the opening of epoxy ring through termolecular hydrogen-bonded transition complexes (step II). This is the rate determining step. The reaction is completed by the rapid displacement of the proton (step III).

1) Reaction of primary amine with epoxy

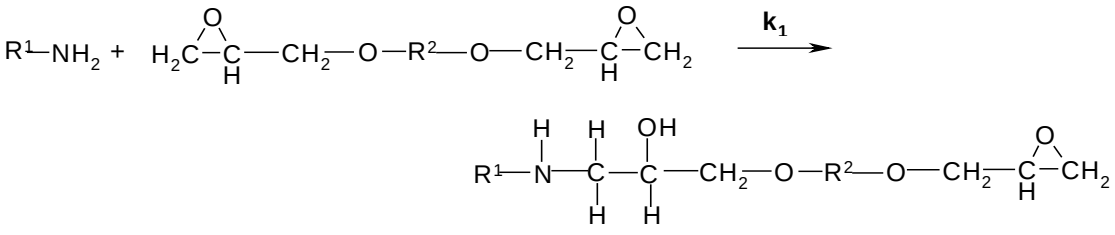

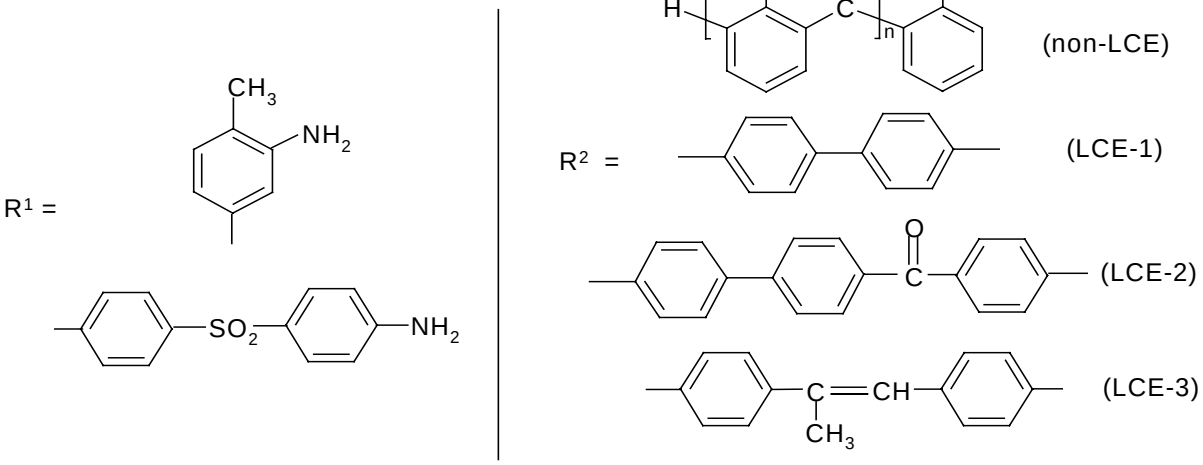

2) Reaction of secondary amine with epoxy

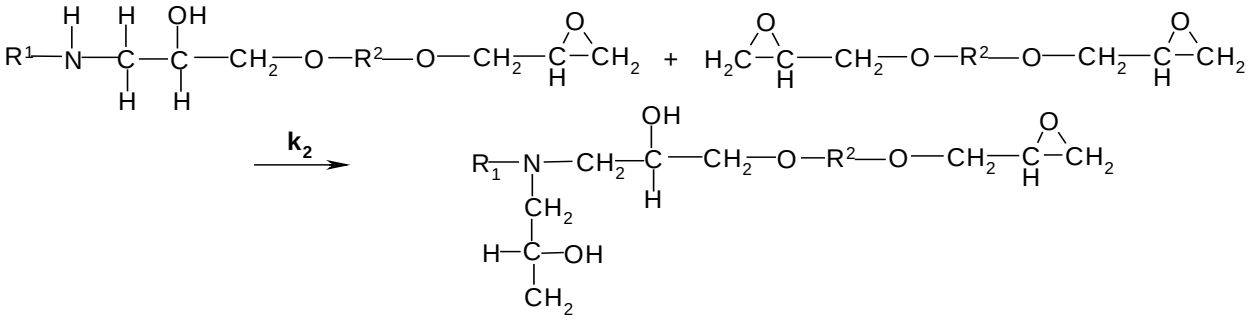

3) Reaction of hydroxyl with epoxy

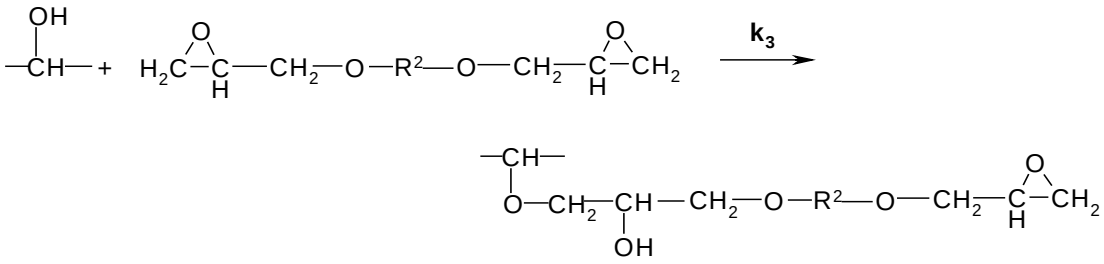

Figure 4.5 Reaction mechanism for curing epoxy resins by amine curing agents

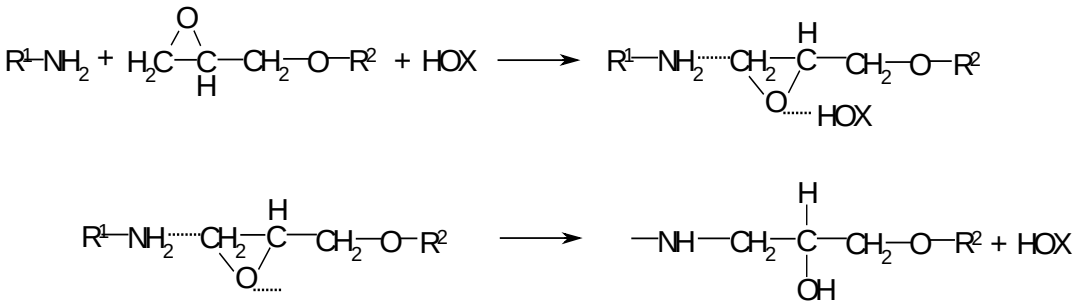

Figure 4.6 Mechanism of hydrogen bond formation via termolecular reaction mechanism

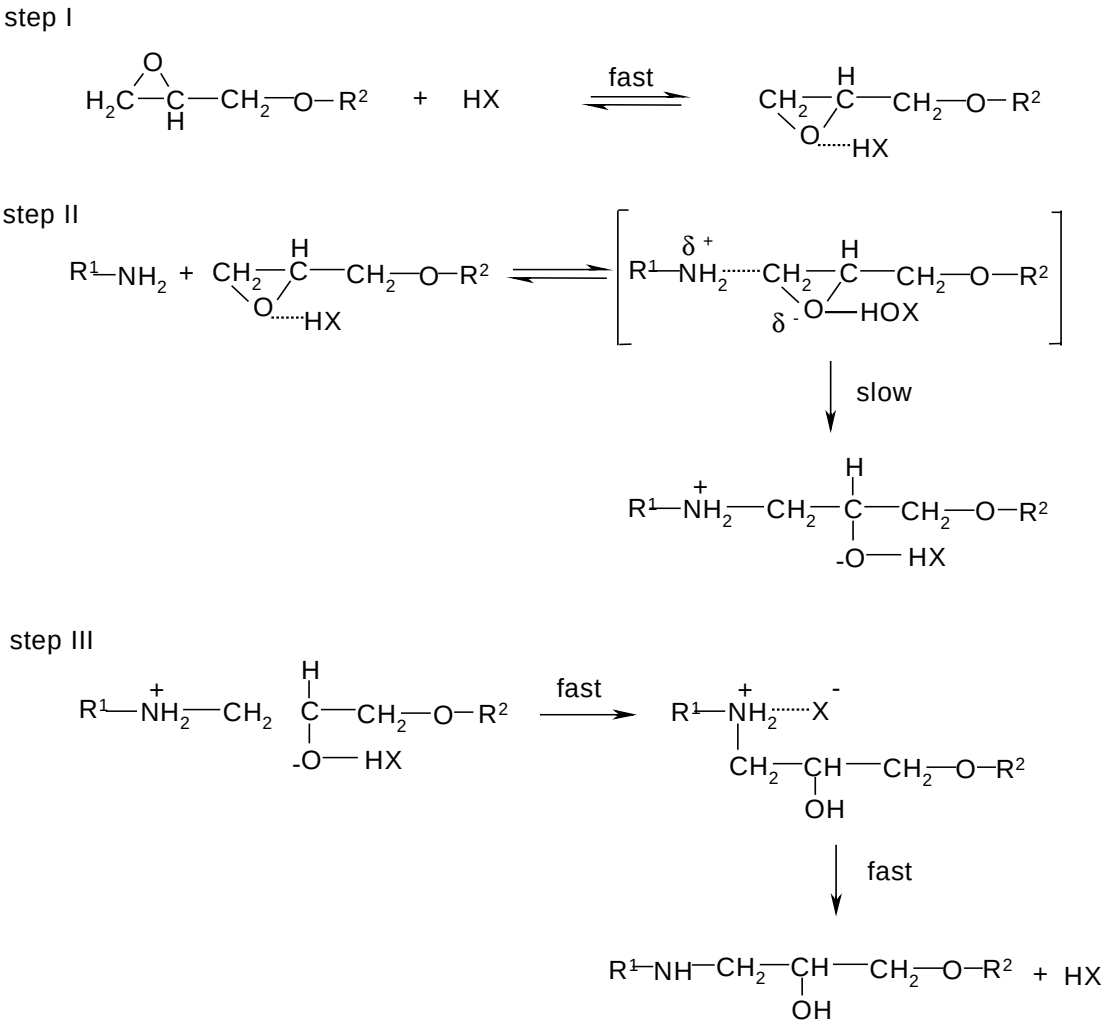

Figure 4.7 Mechanism of hydrogen bond formation via hydrogen complex

4) Experimental

Differential scanning calorimetry (DSC) (Perkin Elmer DSC-7) was applied to observe thermal transition temperatures (melting point and curing enthalpy) of cured samples. The epoxy resin and curing agent were mixed well in the stoichiometric ratio and samples of 5-10 grams were placed in a high pressure sealed steel pan. Dynamic scans were conducted from 25 to 350 ^{o}C at 10 K/min., then the samples were cooled down to 25^{o}C at the rate of 10 K/min. N_2 was used as the purge gas with a flow rate of 20 mL/min.

The polarized optical microscope used was a Zeiss Axioplan equipped with a photographic camera and an Ernst Leitz heating stage. LC phase transitions were observed and compared with the results from DSC. The heating and cooling cycle was conducted to observe LC phase transition and melting temperatures to create the TTT diagram of curing. The final structure of cured LCEs with each curing agent was investigated. The optical microscope provides the information in a microscale. To determine the TTT diagram, the isothermal experiment was performed to detect the onset point of isotropic to liquid crystalline transition.

X-ray diffraction (XRD) was used to determine liquid crystalline characteristics of the cured sample. XRD results help in the confirmation of the LC phase presence since diffraction results provide information about long range order on the nanometer scale. The measurements were conducted on a Siemens D-500 diffractometer with Cu(K_α) radiation. The X-ray tube was operated at 40 kV and 30 mA, with a scanning speed of 1^{o}/min and a sample interval of 0.05^{o}.

Fourier transform infrared spectroscopy (FT-IR) was used to determine the functional groups in the cured product. Ground samples from cured epoxy and dried KBr were finely mixed and pressed into a KBr pellet. The spectra were recorded at the resolution of 4 cm^{-1}, with 40 scans to obtain absorbtion spectra.

DGE-DHBP and MTHPA were chosen for further study since their cure properties are suitable for using as matrices for composites. Result obtained for composites made from these matrices are presented in Chapter 8.

5) Results

5.1 Dynamic DSC results

The results of dynamic DSC experiments to observe the endothermic and exothermic transitions are presented in Table 4.3. The endothermic peak which represents melting was used as the reference temperature for melt mixing. To prepare a homogeneous mixture for curing, the stochiometric ratio of each LCE and curing agent was first ground and mixed homogeneously to ensure completeness of the reaction. The mixtures were melted before curing. The melting transition was observed as an endothermic reaction. The curing transition was analyzed. The DSC data are used as the guideline to observe LC transformations by POM.

The first small endothermic peaks which are found in the DDS system are caused by small amount of crystalline material from DDS. The heat of fusion (ΔH_f) of this peak is found at 80 ^oC with about 3 % ΔH_f compared to the pure DDS. This was also reported by Morgan [179].

Table 4.3 The comparison of transition peaks from DSC

Stoichiometric Component of	Endothermic T (ΔH_m) ^oC (J/g)	Exothermic ΔT (ΔH) ^oC (J/g)
DGE-DHBP + MTHPA	114 (53)	125-250 (367)
DGE-DHBP + DAT	88 (65)	100-150 (334)
DGE-DHBP + DDS	82 (3) 140 (99)	155-320 (653)
DGE-HCC + MTHPA	117 (62)	140-220 (250)
DGE-HCC + DAT	91 (111)	100-150 (165)
DGE-HCC + DDS	82 (3) 124 (19) 153 (37)	160-240 (178) 240-300 (51)
DGE-DHMS + MTHPA	-	110-225 (662)
DGE-DHMS + DAT	90 (14)	100-150 (253)
DGE-DHMS + DDS	81 (3) 124 (46)	140-250 (405) 250-276 (55)

Note : Endothermic peak (melting) was reported as the peak temperature T, ^oC

Exothermic peak (curing) was reported as a range of temperatures ΔT, ^oC

Enthalpies of endothermic and exothermic reactions were obtained by integration of areas under the curve of ΔH, J/g

5.2 TTT diagram

The structure of each LCE and the curing agent affect the character of the TTT diagram. Results reflect intermolecular interactions and anisotropic chain conformations. Table 4.4 lists the observed final LC textures of each system. The TTT diagram is a useful guideline for further curing. Curing conditions can be controlled to provide desirable LC characteristics.

Each system shows a different character of the S-curve depending on the thermodynamics of curing and the intermolecular interactions in the reacting systems. The curing process can introduce more order into the network system since the curing reaction of LCEs involves both chain extension and crosslinking. The chain extension reaction can enhance the molecular anisotropy, providing an increase in LC stability. Therefore, curing the sample in the nematic phase can lead to a smectic-like network, while curing the sample in the isotropic phase can lead to a nematic network.

Figure 4.8 shows the TTT diagram of isothermal cure of DGE-DHBP by DAT. S-curve phase diagrams are found. The change of birefringence occurs in the time period between 8-20 minutes. The TTT diagram of DGE-DHMS and DAT is presented in Figure 4.9. Curing conditions allow a smectic mesophase formation.

The final structures of cured LCEs were observed by optical microscopy. We found that most systems were stable in the nematic phase, except DGE-DHMS + DAT, which is stable in the smectic phase. For the cured sample of DGE-DHBP + MTHPA, coexistence of isotropic and nematic phase was observed (Figure 4.10). The example of a nematic phase formed by the DGE-DHBP + DDS system is shown in Figure 4.11. A

small scale nematic schlieren texture was formed. Another sample of the nematic mesophase of DGE-HHC + MTHPA system is shown in Figure 4.12.

A smectic phase is found in the system of DGE-DHMS and DAT. The nematic thread-like texture is also observed for this system (Figure 4.13). Figure 4.14 shows the region where both nematic and smectic phases were found. The smectic mesophase, where the molecular long axis are parallel, in addition to layering of the molecules, is presented in Figure 4.15.

X-ray diffractometry was used to confirm smectic phase formation. Figure 4.16 shows the X-ray spectrum of cured DGE-DHMS and DAT. The first peak at $2\theta = 4.6^{o}$ (d = 19 Å) corresponds to the interlayer spacing. The second peak at $2\theta = 20.20^{o}$ (d = 4.3 Å) corresponds to the layer spacing.

The observed smectic liquid crystalline DGE-DHMS + DAT phase absent in DDS can be explained in terms of asymmetrical active amine groups of DAT. The unequal reactivity can promote chain extension prior to the crosslinking reaction. In the initial stages of reaction, the primary amine reaction with epoxy groups is dominant. The chain extension reaction introduces an increase in molecular weight of the product. At about 60 % of curing, the reaction of the secondary amine becomes dominant and leads to the crosslinking reaction. A study of asymmetrical tetra-functional amine (sulfanilamide) on curing DGE-DHMS also found this effect [160].

Table 4.4 The final liquid crystalline phases observed by POM from each epoxy and curing agent system

Cured product of	Final liquid crystalline phase from POM
DGE-DHBP + MTHPA	Isotropic + Nematic
DGE-DHBP + DAT	Nematic
DGE-DHBP + DDS	Nematic
DGE-HCC + MTHPA	Nematic
DGE-HCC + DAT	Nematic
DGE-HCC + DDS	Nematic
DGE-DHMS + MTHPA	Nematic
DGE-DHMS + DAT	Nematic + Smectic
DGE-DHMS + DDS	Nematic

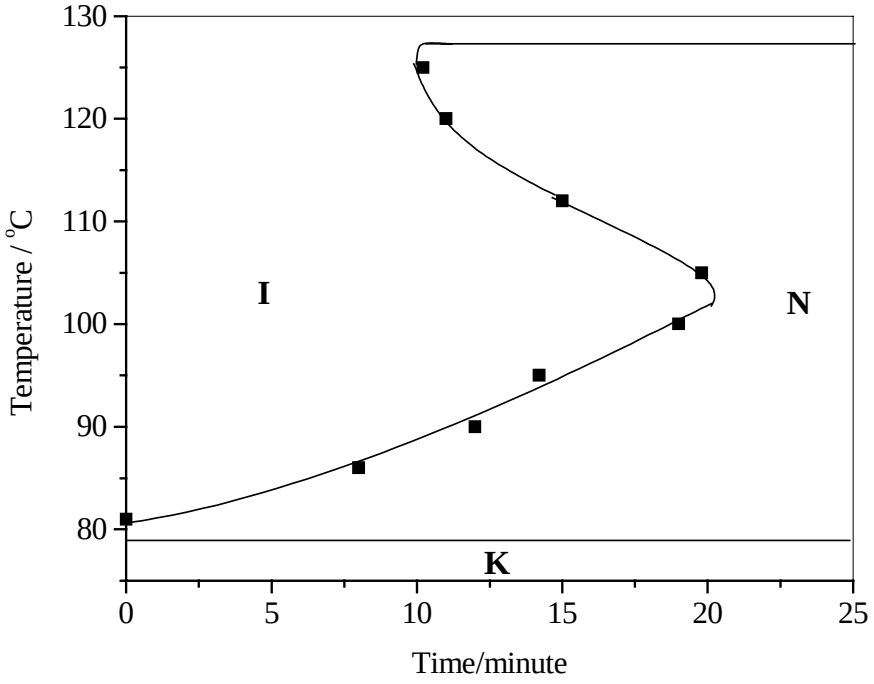

Figure 4.8 TTT diagram of isothermal cure of DGE-DHBP with DAT

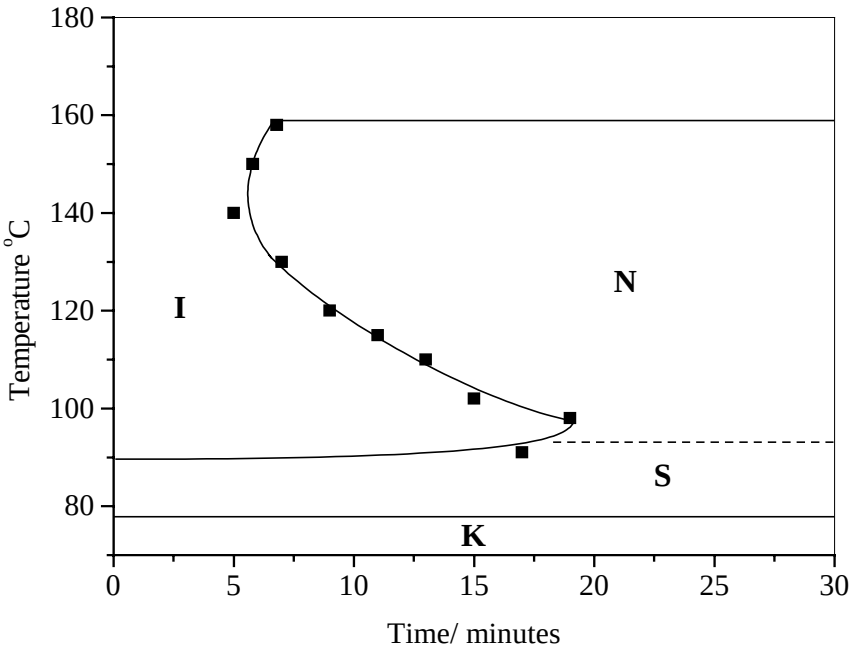

Figure 4.9 TTT diagram of isothermal cure of DGE-DHMS with DAT

Note K:crystal; I:isotropic; N:nematic; S:smectic

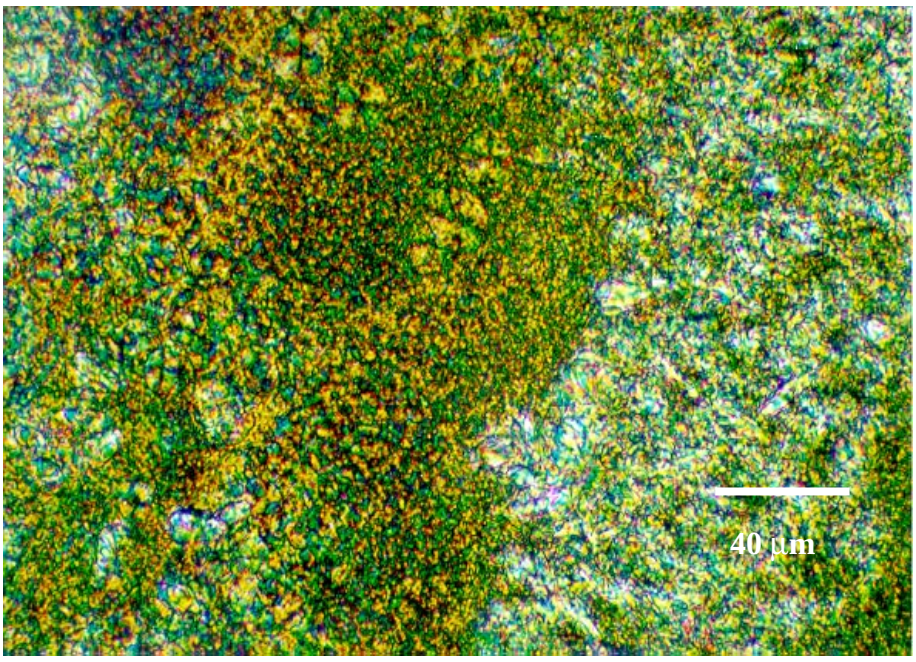

Figure 4.10 Optical microscopy of nematic phase of cured DGE-DHBP + MTHPA

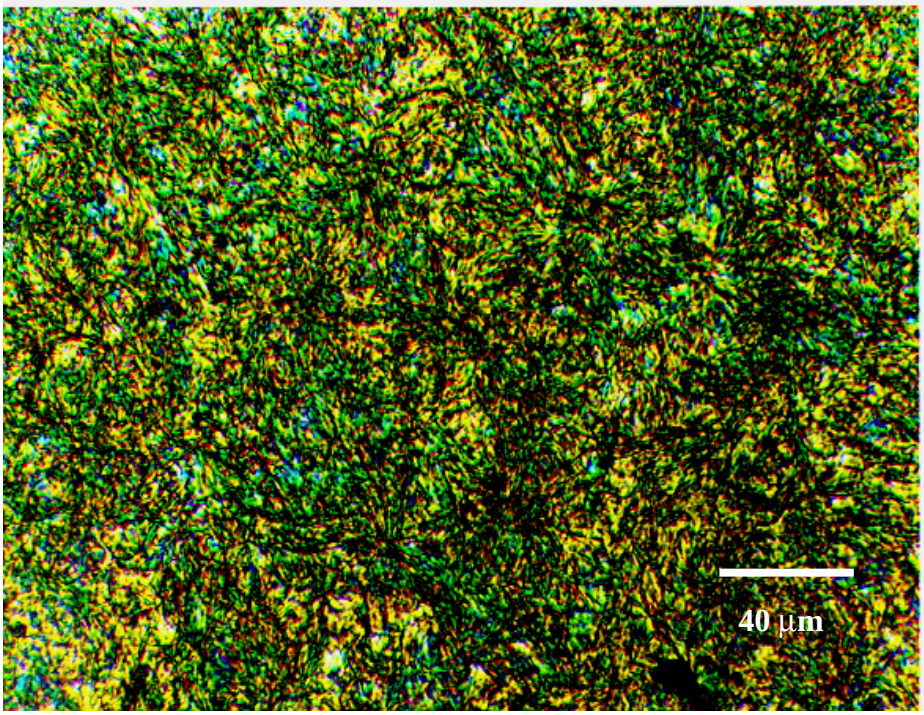

Figure 4.11 Optical microscopy of nematic phase of cured DGE-DHBP + DDS

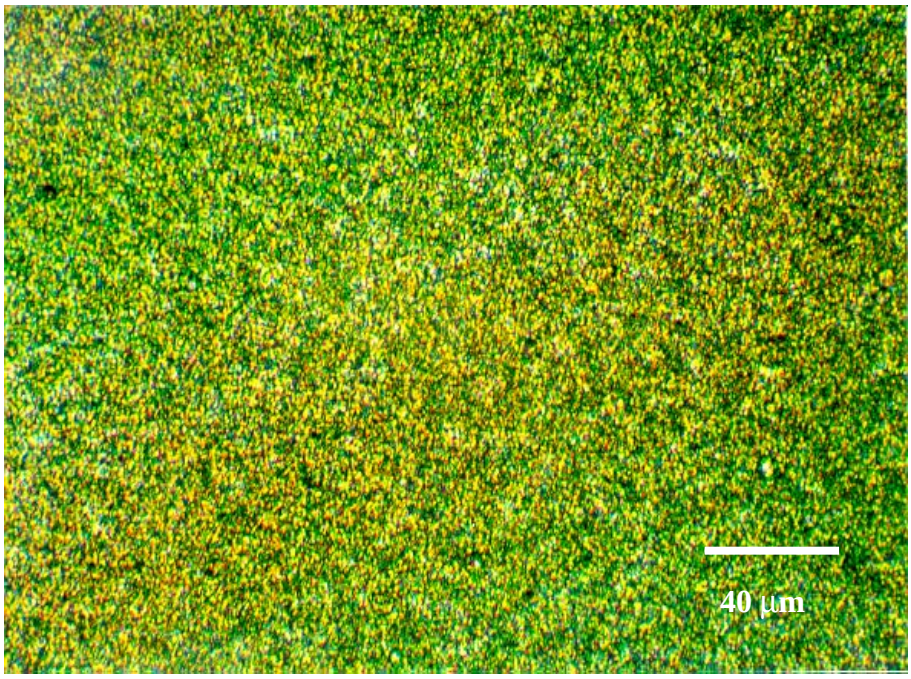

Figure 4.12 Optical microscopy of cured nematic phase of DGE-HHC + MTHPA

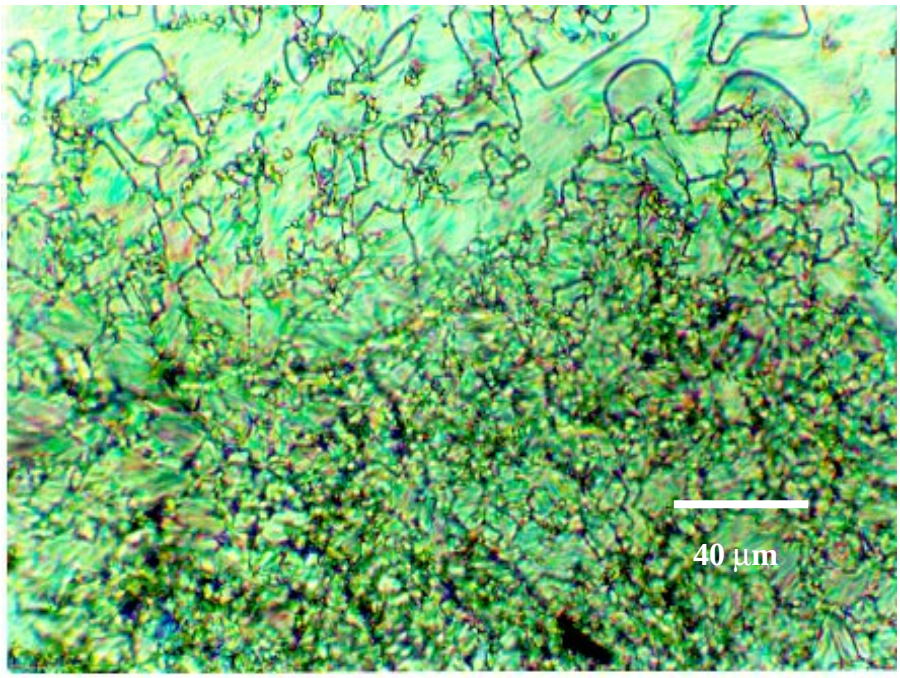

Figure 4.13 Optical microscopy of the nematic thread-like phase of DGE-DHMS and DAT

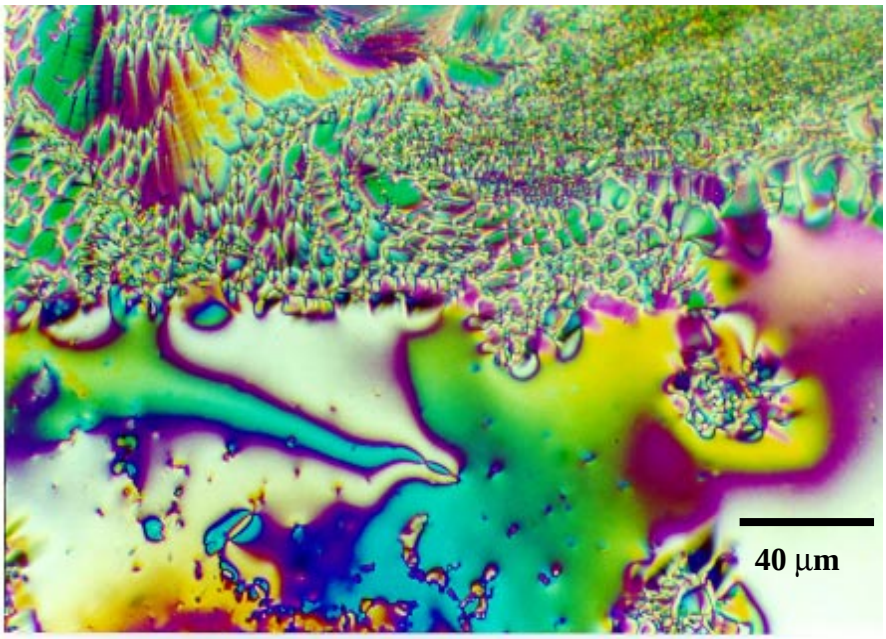

Figure 4.14 Optical microscopy of the transition region between schlieren texture and the smectic phase of DGE-DHMS and DAT

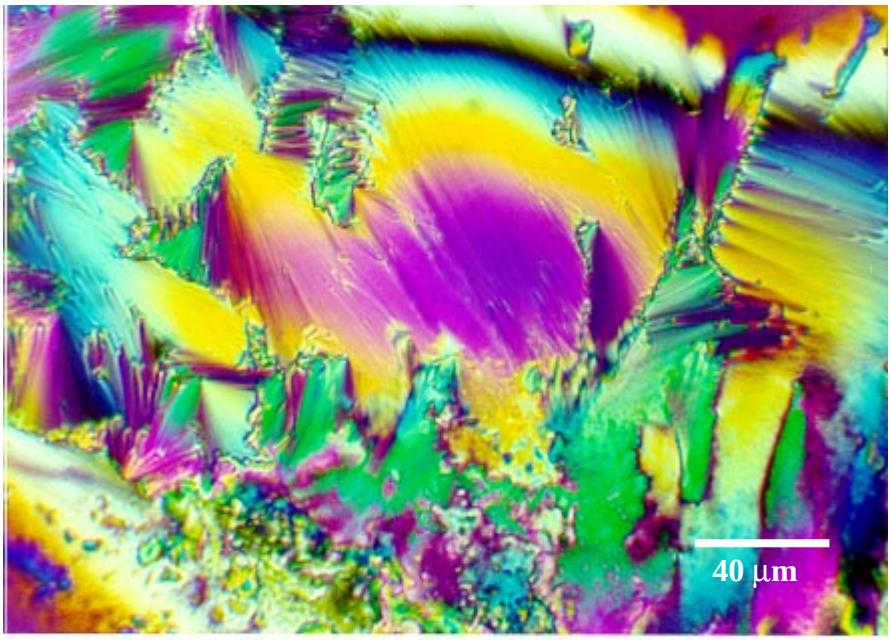

Figure 4.15 Optical microscopy of fan-like smectic phase of DGE-DHMS and DAT

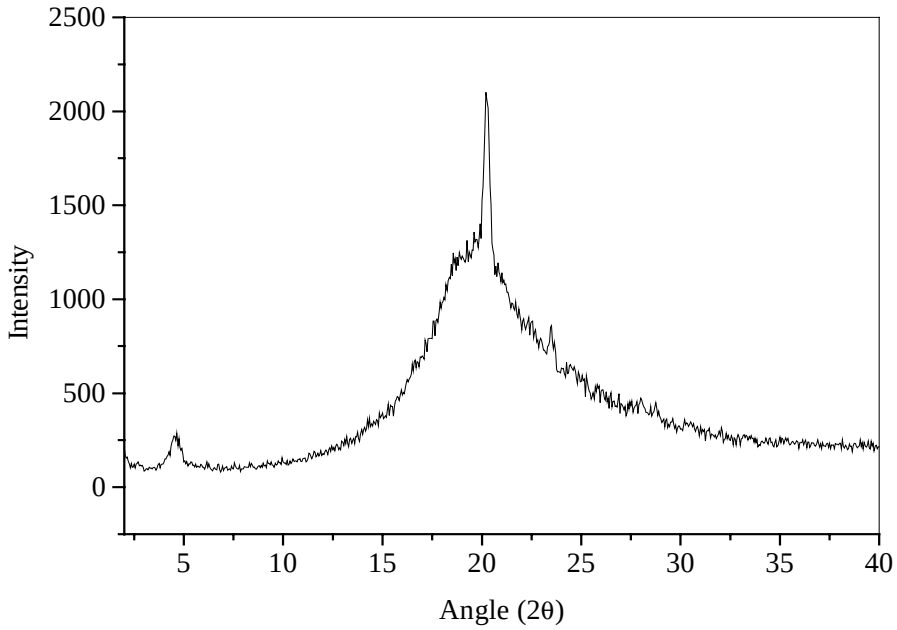

Figure 4.16 X-ray diffraction of cured DGE-DHMS and DAT

5.3 ***FT-IR results***

Figure 4.17 presents the comparison of results for cured and uncured DGE-DHBP and DGEBP-F. The peaks at 915 cm^{-1} and 896 cm^{-1} which represent asymmetric stretching of glycidyl groups were compared to determine the amount of epoxy left in the system.

The FT-IR spectra of pure epoxy and each of the DGE-DHBP + DGEBP-F systems cured with MTHPA (Figure 4.18) were compared. No absorption at 915 cm^{-1} was found for the cured sample, indicating there is no reactive epoxy left in the samples. As the concentration of DGE-DHBP in the sample increases, the intensity at 823 cm^{-1}, which corresponding to the 1,4-disubstituted aromatic groups increases, in contrast to the peak decrease at 754 cm^{-1} (1,2-disubstituent). Moreover, the characteristic peaks of aromatic C=C stretching at 1506 and 1603 cm^{-1} changes from a doublet to a single sharp peak. The peak at 2800-3000 cm^{-1} is attributed to the bending mode of the aliphatic C-H bond, and the peak above 3000 cm^{-1} is assigned to the bending mode of the aromatic C-H bond.

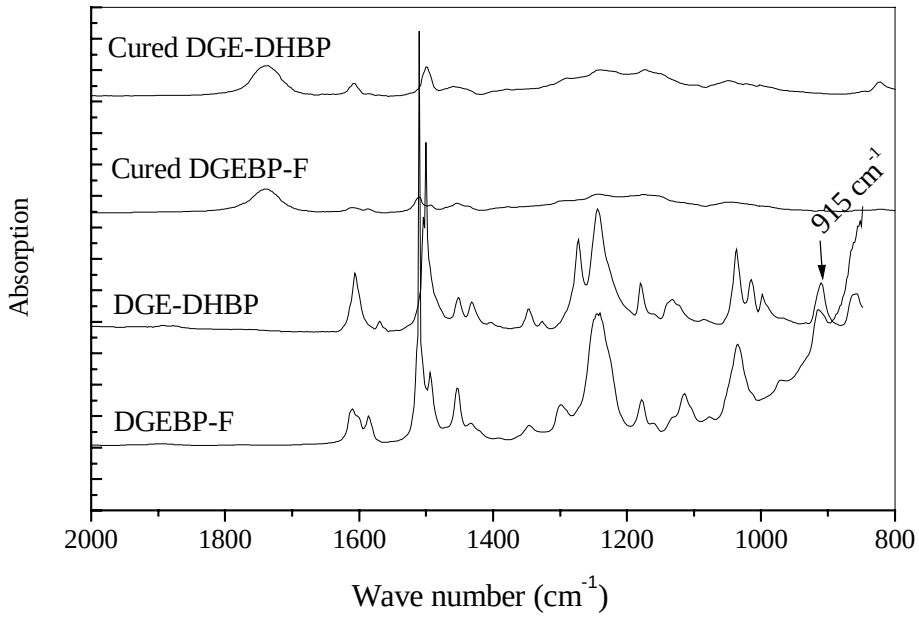

Figure 4.17 FT-IR spectrum of uncured and cured DGE-DHBP and DGEBP-F

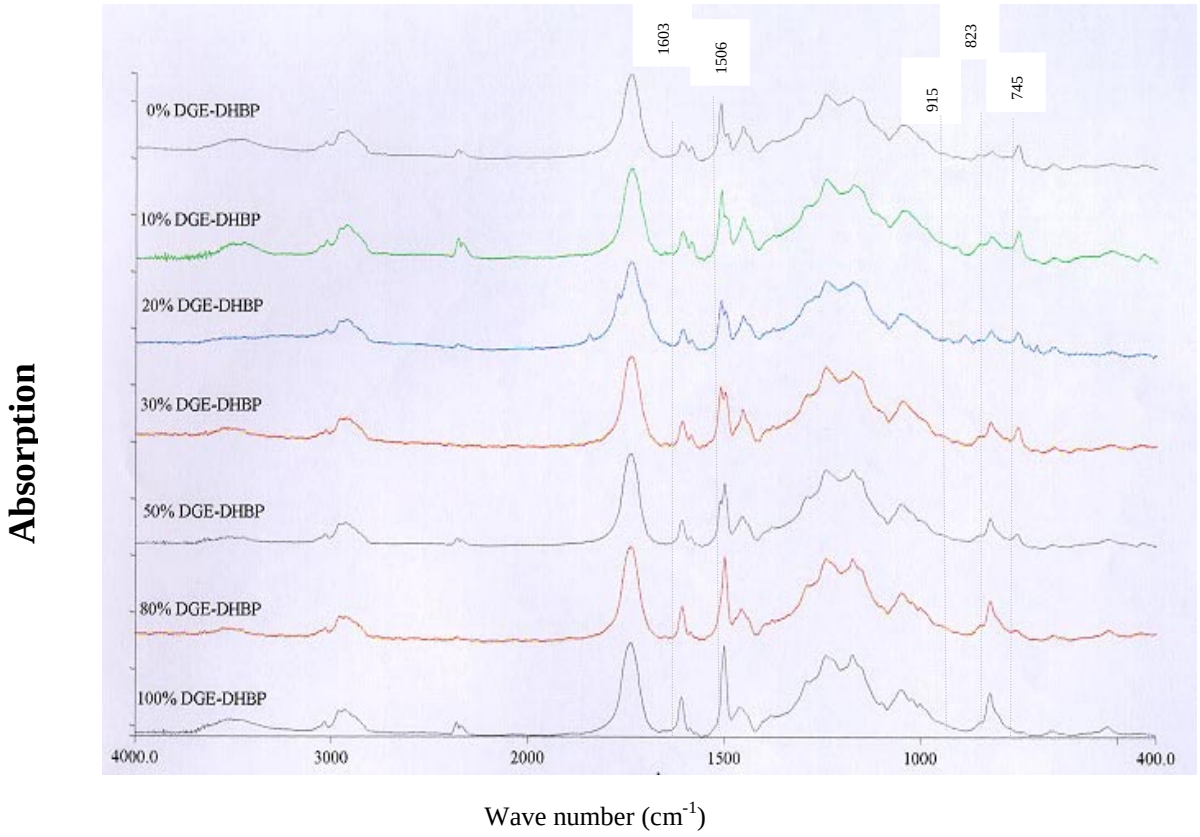

Figure 4.18 FT-IR spectrum of cured DGEBP-F + DGE-DHBP with MTHPA

6) Concluding remarks

The structure of epoxide resins determines their physical and chemical properties. The mesogenic units in LCEs provide the chain extension reaction prior to the crosslinking reaction and results in enhancing LC phase stability of cured LCEs. TTT diagram of cured LCEs have been obtained by using polarized optical microscope and X-ray diffractometry. The TTT diagram of LCEs also shows S-shaped as well as the diagram of non-LCEs. In case of LCEs, this diagram provides the phase stability information of the anisotropic phases. There are two main factors which affect the characteristics of the diagram. The first parameter is the molecular interaction between epoxy and curing agent. Moreover, the LC phase is stable only in the certain temperature range. Thus, the thermal perturbation is also affect the shape of the diagram. The range of time and temperature to cure LCE should, therefore, be carefully chosen to obtain the desirable LC phase.

The choice of curing agents affects the final LC phase texture. The anhydride curing agents provide a higher probability of crosslinking reaction compared with chain extension reaction and causes a lower stability of LC phase formation. In contrast, tetra-functional amines provide the opportunity of chain extension to the product and might enhance the LC phase stability. Moreover, the asymmetric functionality also apparently strengthens the LC phase stability.

FT-IR results confirm the completeness of the curing reaction and is seen as the disappearance of the epoxide groups at 915 cm^{-1} for the cured samples and in the curing kinetics results.

CHAPTER 5

CURING KINETICS OF MODIFIED AND UNMODIFIED EPOXY

1) Introduction

Curing kinetics of epoxy resins are important to the manufacturing process since kinetic parameters affect mechanical and physical performance. The understanding of the curing mechanism and kinetics is therefore the first essential step in the relationship evaluation between processing, morphology and mechanical properties of cured epoxy resins.

There are many methods to monitor curing of epoxy resins, including the direct measurement of reactive species concentration, indirect estimation of the extent of chemical reaction, and measurement of changes in physical and mechanical properties. However, the full interpretation of curing should be based on monitoring concentrations of reactive groups, as well as other properties.

Gel permeation chromatography and nuclear magnetic resonance (NMR) have been used to determine the degree of branching in partially cured epoxies [180181]. The chemical shift from proton and carbon NMR [182-183] and magic angle spinning NMR can be used to study the curing reactions of epoxy resins [184]. The magic angle spinning technique is used for solid samples.

The intensity of FT-IR functional groups is directly related to the concentration of reactive species and can be used to monitor the curing process. The spectrum bands at 4,535 cm^{-1} (2.2 μm) and 915 cm^{-1} (10.9 μm) which are assigned to the epoxy group have

been used to measure epoxy concentrations during curing. Measurements of near infrared absorption offer advantages because of strong absorption with less complicated spectra. Therefore, the peak overlapping problem can be avoided. Details of the application of FT-IR for curing are discussed by Lee and Neville [185] and also by Hadad [186].

Rheological properties of epoxies can be used to monitor the curing process. Changes of structure from viscous liquid to a rigid glassy solid can be clearly detected as rheological changes. For example, the real part of the shear modulus (G') goes from zero at the beginning of the cure to about 3 GPa as the cure progresses. The *in situ* monitoring of rheological properties can be done using microdielectrometry sensors [187]. The application of rheological properties to monitor curing of epoxy was proposed by Macosko [188]. Verchére and coworkers [189] studied the curing of epoxies by comparing several methods. The extent of cure was obtained from shear viscosity using a concentric cylinder viscometer and FT-IR spectra, size exclusion chromatography, and DSC. Mijovic et al. [190] studied the chemorheological model by combining viscosity and DSC measurements.

As curing reaction progresses, the shear viscosity of the resin increases and is difficult to monitor. The complex modulus and its components can be measured more accurately from the torsional braid analysis (TBA) techniques. TBA has been applied by Gillham and coworkers for this purpose [191]. Dynamic mechanical Analysis (DMA) can be used to measured changes of the complex modulus G* as a function of frequency or temperature.

2) Kinetics of Curing: Models

DSC is extensively used for investigating the curing reactions of thermoset polymers. Kinetics can be characterized with DSC by measuring the heat generated during the curing reaction as a function of temperature and time. The extent of curing reaction may be determined by measuring the total area of the reaction peak. The basic assumption of DSC kinetic measurements is that the heat flow is proportional to the change in the extent of the reaction:

$$\dot{\alpha} = \frac{d\alpha}{dt} = \frac{1}{H_{tot}} \frac{dH}{dt} \tag{5-1}$$

where dH/dt represents the rate of heat generation during the curing reaction. H_{tot} is the overall heat of reaction and α is the extent of reaction while $d\alpha/dt$ is the rate of the reaction.

Several different kinetic models have been used to characterize curing of epoxy resins by relating the chemical reactions to time, temperature and extent of cure [192]. The simplest expression is the n^{th} order model, namely

$$\frac{d\alpha}{dt} = k(1-\alpha)^n \tag{5-2}$$

where n is the reaction order, and k represents the rate constant. In turn, one often represents k by an Arrhenius type formula:

$$k = k_0 \exp(-E_a / RT) \tag{5-3}$$

where k_o is the Arrhenius frequency factor, E_a is the activation energy, R is the gas constant and T is absolute temperature.

2.1 Isothermal model

The isothermal thermogram of a n^{th} order reaction predicts the maximum reaction rate at the time equal to zero. However, this model cannot be applied to the entire reaction because of complex cure mechanisms. The existence of impurities or catalysts in amine or anhydride curing agents does not necessarily preclude the reaction following the autocatalytic model; however, more complex mechanisms are also possible [193]. If an isothermal process characterized by a thermogram shows a maximum reaction rate at some point other than the start of the reaction, an autocatalytic model given below (Eq. 5-4) has been found to be more appropriate to investigate kinetic parameters.

Prime [193] pointed out the curing of a thermoset was not limited to one chemical reaction. Two or more consecutive curing reactions are possible, as investigated by Lau [194]. He found the cure of amine systems at room temperature proceeded first according to combined n^{th} order and autocatalytic models, then predominantly by the autocatalytic model. Finally, the reaction becomes diffusion controlled as T_g increased to 10-15 ^oC above the curing temperature.

In this study, kinetic parameters were calculated based on a two parameter autocatalytic model. Kamal et al. [195-196] proposed a generalized model which provides a description of curing to the onset of the vitrification point as follows:

$$\frac{d\alpha}{dt} = (k_1 + k_2\alpha^m)(1-\alpha)^n \qquad (5\text{-}4)$$

where k_1 is the externally catalyzed rate constant, and k_2 is the autocatalyzed rate constant with Arrhenius temperature dependency.

The curing reaction of commercial epoxy resins with hardener involves the conversion of a liquid or fluid mixture into a solid network. As the curing reaction progresses, the glass transition T_g of the network gradually increases until the onset of the vitrification point, where T_g approaches the curing temperature, T_c. As the difference between T_c and T_g becomes small, the reaction is changed from chemically controlled kinetics into a diffusion controlled mechanism due to the rapidly decreasing molecular mobility of the network.

The cure mechanism is assumed to be the same for the entire temperature range investigated. Therefore, the constant k_1 is calculated using the initial reaction rate at t = 0 from the intercept of the isothermal thermogram. Consequently, Eq. (5-4) is simplified to

$$\left.\frac{d\,\alpha}{dt}\right|_{t\,=\,o} \;=\; k_1 \tag{5-5}$$

2.2 Dynamic Model

Multiple-heating rate methods are isoconversional and allow estimation of activation energies from the relationship between the heating rate and temperature to attain constant conversion.

Ozawa [197-198] proposed the model which relates the activation energy E, the heating rate φ and the isoconversional temperature based on the assumption that the frequency factor A, E and f(α) are independent of temperature:

$$\int_0^{\alpha_m} \frac{d\alpha}{f(\alpha)} = A\int_{t_0}^{t_m} e^{-E/RT}dt = \frac{A}{\varphi}\int_{T_0}^{T_m} e^{-E/RT}dt \tag{5-6}$$

$$\cong \frac{A}{\varphi}\int_0^{T_m} e^{-E/RT}\,dT \cong \frac{AE}{\varphi R}\,p(E/RT_m) \tag{5-7}$$

The degree of cure (α_m), time (t_m) and temperature (T_m) pertain to the same specific point. In this case, the conversion point is chosen. The term p(E/RT) is the approximation solution, which was tabulated by Doyle [199]. Further, we have

$$\log\ p(E/RT_m) \cong -2.15 - 0.4567\ E/RT_m \tag{5-8}$$

Therefore, activation energy can be estimated from the following relationship:

$$E \cong \frac{-R}{0.4567}\frac{\Delta \log \varphi}{\Delta(1/T_m)} \equiv -\frac{R}{1.052}\frac{\Delta \ln \varphi}{\Delta(1/T_m)} \tag{5-9}$$

Kinetics can be investigated by dynamic experiments at different heating rates and analyzed using the Kissinger method [200]. The activation energy can be calculated from the following equation:

$$\frac{d[\ln(\varphi/T_m^2)]}{d[1/T_m]} = -\frac{E}{R} \tag{5-10}$$

where φ represents dT/dt or the heating rate, and T_m is the peak temperature.

3) Experimental

3.1 Differential Scanning Calorimetry (DSC)

The DGEBP-F and ground DGE-DHBP were mixed in a 1:1 weight ratio. Then, MTHPA was added in the equilibrium ratio of 1:1 to the system. The ratio was chosen on the basis of the approximate stoichiometric equivalence of DGEBP-F and DGE-DHBP. 10-15 mg of the sample was weighed into a high pressure-sealed DSC pan and kept in the

refrigerator at 10 ^{o}C before performing the DSC measurements. A Perkin-Elmer DSC-7 apparatus was used. Isothermal experiments were conducted from 100^{o} to 160^{o}C at 10 K intervals for 250 minutes. Each sample was placed in a sample holder after the desired temperature was reached and then quenched to 20^{o}C. A second scan was conducted from 20 to 250^{o}C at the heating rate of 10 K/min to determine the glass transition temperature T_g and the residual heat, (if present).

Nonisothermal experiments were conducted from 20 to 250^{o}C at several heating rates: 1.5, 2.5, 5, 10, and 20 K/min. N_2 was used as the purge gas with the flow rate of 0.14 mL/min. The peak temperature for each heating rate was recorded.

4) Results

4.1 Curing kinetics

Exotherms obtained by DSC for the mixtures of DGEBP-F and MTHPA at several isothermal temperatures are presented in Figure 5.1. A diagram of the reaction rate as a function of curing time can be obtained with the assumption that the heat generated during cure is directly proportional to the rate of the reaction. The H_{tot} is calculated from the total area under the dynamic scan of the curing thermogram at 10 K/min. The corresponding value for the DGEBP-F + MTHPA system is 315 J/g. The diagram shows autocatalytic kinetic behavior from a nonzero initial reaction rate and sigmoid shape curves. The rate of reaction as a function of time for DGEBP-F and MTHPA is shown in Figure 5.2.

The calculated H_{tot} for DGE-DHBP + MTHPA and the blend system of DGEBP-F + DGE-DHBP is 338 and 364 J/g, respectively. Isothermal runs performed on DGE-DHBP and on the DGE-DHBP:DGEBP-F (1:1) blended sample mixed with the stoichiometric amounts of MTHPA are reported in Figures 5.3, and 5.4, respectively. The curing kinetics follows an autocatalytic model also in this case. As temperature increases, the time required for curing decreases, as expected.

A nonlinear least square method was used to determine the kinetic parameters (m, n, and k_2, see Eq.(5-4)) simultaneously without constraints [201] using Mathematica®. The uncatalyzed reaction rate was estimated from the intercept of the plot at t = 0. A comparison of reaction rates for cured systems is presented in Figure 5.5. They follow the Arrhenius behavior. k_1 for the blend was between that of both pure components while k_2 was lower than the values for pure components. There are significant differences in k_1 values between the two neat resins and the blend systems, with the blend value being much higher. This implies that there are differences in external catalysis mechanisms. However, the k_2 values of these systems are not much different since the reactivity and functionality groups of both epoxies are quite similar.

Figure 5.6 shows the comparison of the maximum isothermal reaction rate α_P and the reaction time t_p required to attain the maximum rate. Plots of reaction orders for all three systems are compared in Figure 5.7.

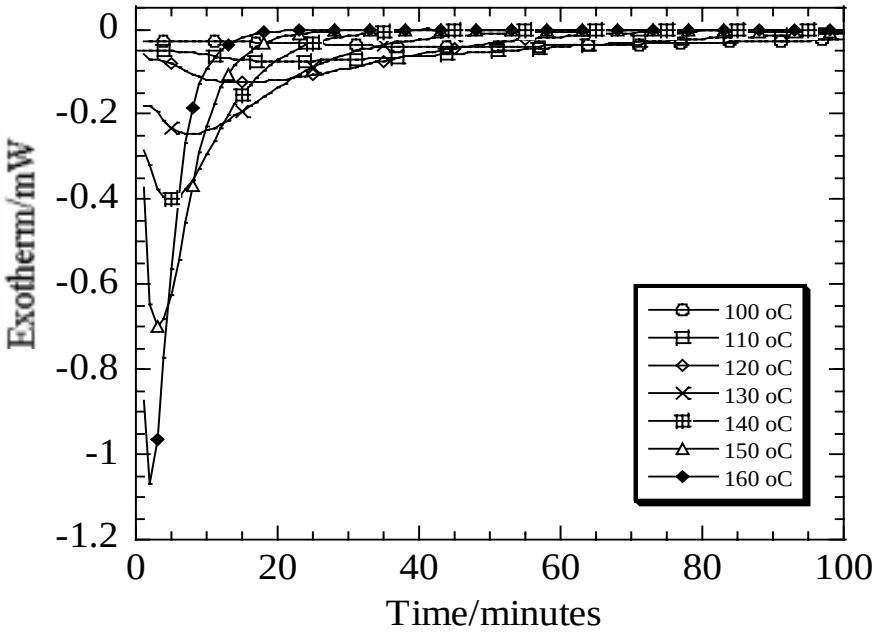

Figure 5.1 An exotherm of the isothermal measurement for the DGEBP-F system

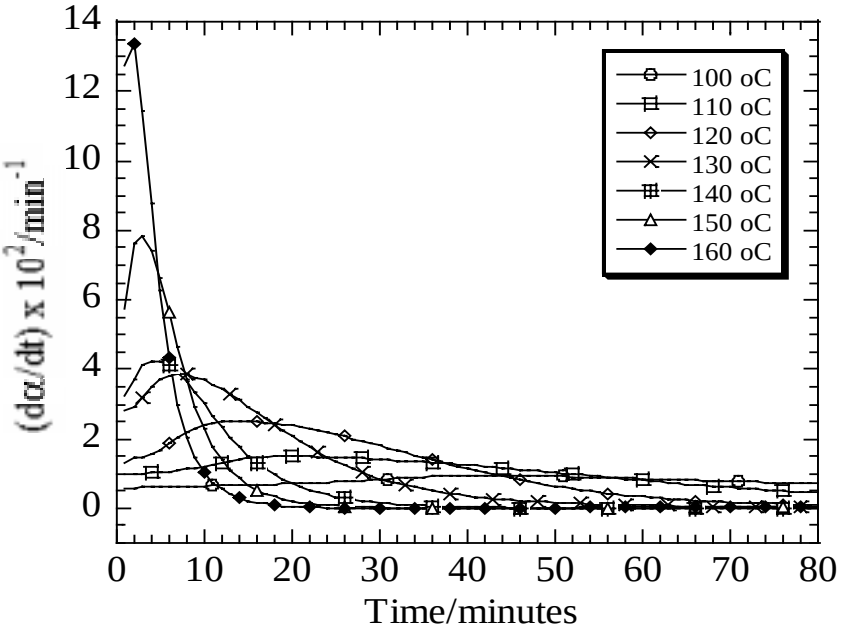

Figure 5.2 Rates of cure as a function of time for the DGEBP-F + MTHPA

There is no trend of m and n as a function of temperature, as previously observed by Khanna and Chanda [202] for curing of diglycidyl ester with anhydride. Table 5.1 shows the kinetic parameters for DGEBP-F, DGE-DHBP, and blends of DGEBP-F with DGE-DHBP. The activation energy for curing is obtained from the Arrhenius relationship. Two activation energies are obtained from the autocatalytic model, which represent both the uncatalyzed and catalyzed curing reactions.

The calculated kinetic parameters were confirmed by fitting the experimental data to the autocatalytic kinetic model, as shown in Figure 5.8, for the DGEBP-F system. Figure 5.9 presents a typical comparison between experimental and model results for DGE-DHBP systems. The maximum reaction rate was usually found between 20-40 % conversion. The model chosen shows a good fit with the experimental data in the initial stage of reaction and up to about 70 % conversion. Deviations are observed near the vitrification point; this is expected since the diffusion effect dominates the reaction at higher percentages of conversion.

The nonisothermal thermogram of DGEBP-F + MTHPA is shown in Figure 5.10 and a similar thermogram for DGE-DHBP in Figure 5.11. The peak at high heating rates shows the melting before curing reaction. The activation energy is calculated from the slope of the Kissinger and Ozawa relationship, as expressed in Figure 5.12 and 5.13. The activation energies obtained from the Kissinger method are higher than the values obtained from the Ozawa method. There is a small difference between the activation energies E_a calculated for these three systems, but they follow the same trend as the activation energies for the catalyzed reaction E_{a2} from isothermal kinetics - as displayed

in Table 5.2. The activation energy for the curing reaction of DGEBP-F + DGE-DHBP blend is lower compared with the other single component resin systems, indicating that the reaction kinetics of the mixed system are synergistic.

The differences in activation energies for isothermal and non-isothermal analysis for epoxy + anhydride systems have also been investigated by William and coworkers [203]. This has been attributed to the temperature range difference of curing between isothermal and non-isothermal methods. The chain-wise polymerization mechanisms of epoxies with anhydrides can be divided into three main steps including; initiation, propagation, and chain transfer steps. The tertiary amine base generates the active sites from anhydride and epoxide groups. These reactive groups react with epoxy and anhydride as growing chains. The chain transfer step occurs when the active centers are regenerated and growing chains are terminated. The E_a from non-isothermal analysis is usually higher than from isothermal measurements since the fitting of isothermal DSC is performed after an induction period.

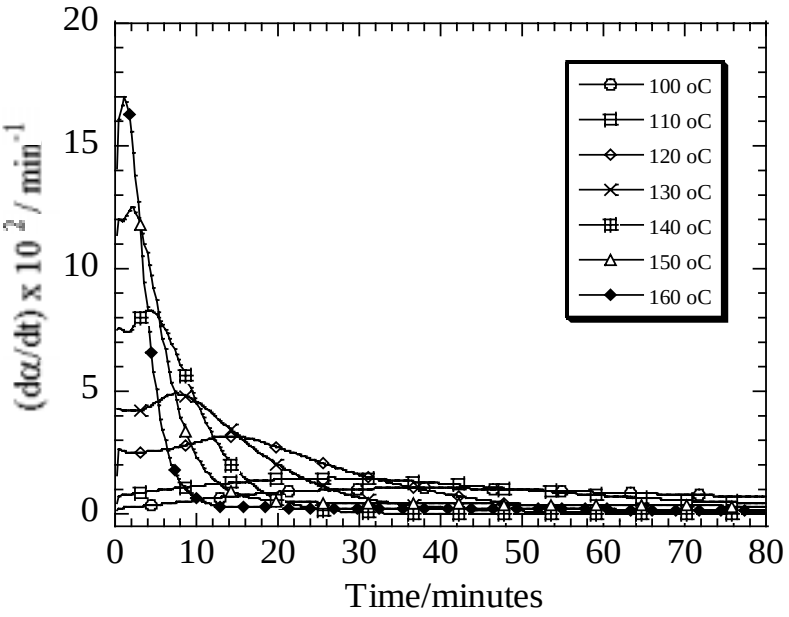

Figure 5.3 Rates of cure vs. time at several temperatures as a function of time for DGE-DHBP + MTHPA

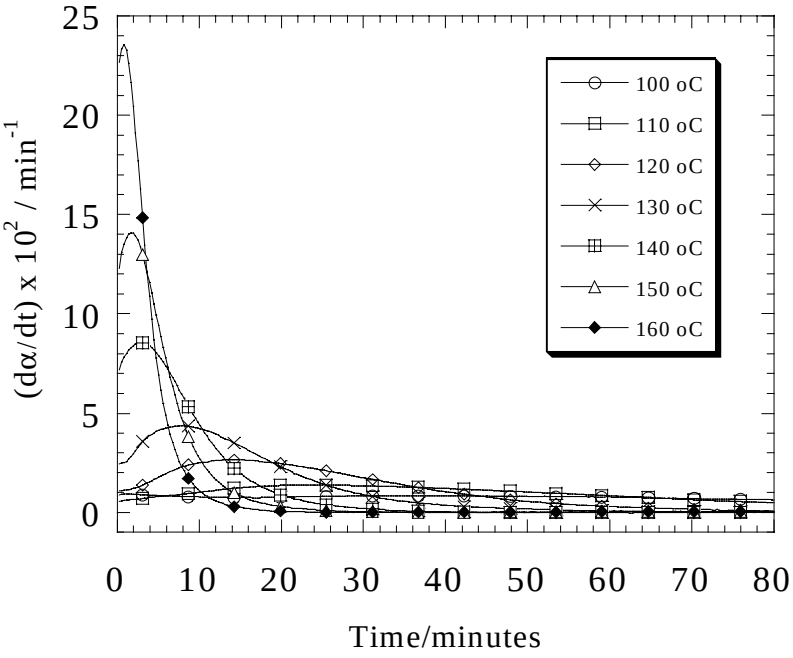

Figure 5.4 Rates of cure vs. time at several temperatures for blends of DGE-DHBP and DGEBP-F

Table 5.1 Comparison of kinetic parameters between DGEBP-F/ DGEHBP/ Blend of DGEBP-F & DGE-DHBP systems

Kinetic Parameters	DGEBP-F/MTHPA	DGE-DHBP/MTHPA	Blend of DGEBP-F & DGE-DHBP/MTHPA
k_1 (min^{-1})	$1.48x10^{7}exp(-8.08 \times 10^{7*}/RT)$ **r=0.9908	$1.52x10^{11}exp(-5.83 \times 10^{7*}/RT)$ r=0.9889	$2.98x10^{11}exp(-12.08 \times 10^{7*}/RT)$ r=0.9979
k_2 (min^{-1})	$2.63x10^{5}exp(-5.83 \times 10^{7*}/RT)$ r= 0.9871	$4.03x10^{6}exp(-6.88 \times 10^{7*}/RT)$ r=0.9548	$1.64x10^{6}exp(-5.66 \times 10^{7*}/RT)$ r=0.9929
α_P	$1.24x10^{6}exp(-6.78 \times 10^{7*}/RT)$ r=0.9850	$2.58x10^{8}exp(-8.78 \times 10^{7*}/RT)$ r=0.9885	$3.06x10^{8}exp(-8.90 \times 10^{7*}/RT)$ r=0.9970
t_p (min.)	$1.20x10^{-8}exp(-8.16 \times 10^{7*}/RT)$ r=0.9962	$1.97x10^{-11}exp(-10.66 \times 0^{7*}/RT)$ r=0.9822	$2.03x10^{-11}exp(-10.64 \times 10^{7*}/RT)$ r=0.9793
$m_{avg.}$	1.103	1.045	0.995
$n_{avg.}$	1.311	1.216	1.225
Ea_1	67.2 kJ/mol	48.4 kJ/mol	100.4 kJ/mol
Ea_2	48.4 kJ/mol	57.2 kJ/mol	47.0 kJ/mol

* J/kg•mol, ** r= correlation coefficient

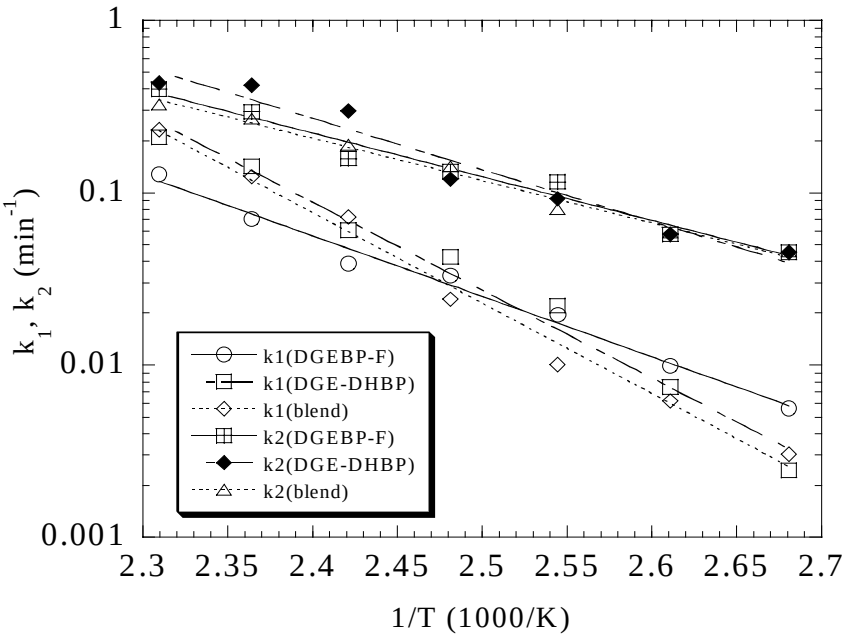

Figure 5.5 Comparison of reaction rates for DGEBP-F, DGE-DHBP, and blends of DGEBP-F with DGE-DHBP

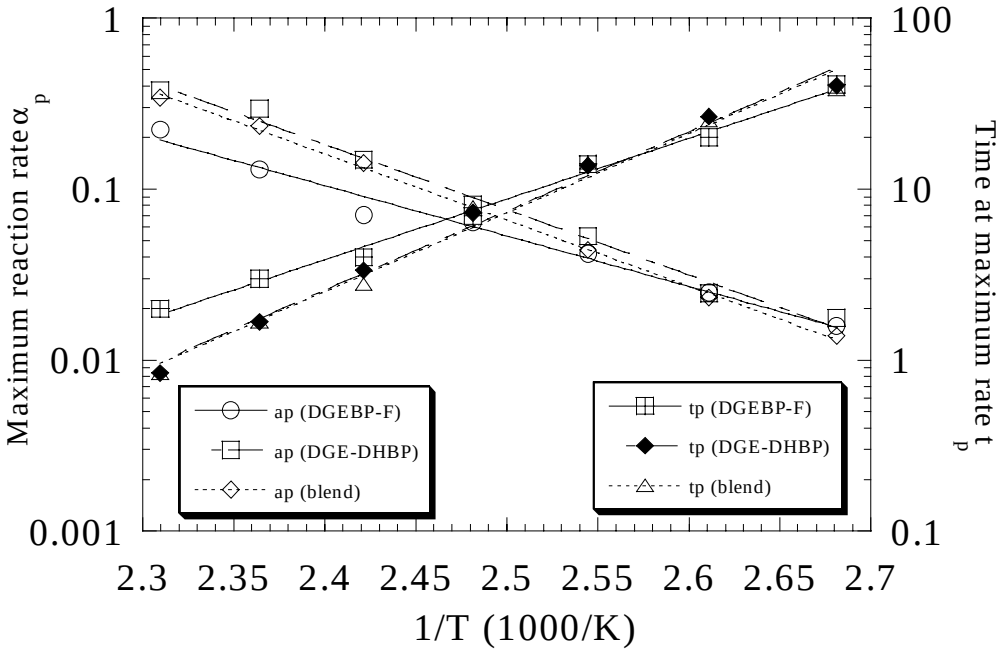

Figure 5.6 Comparison of maximum reaction rate α_p and time to attain maximum rate t_α for DGEBP-F, DGE-DHBP, and blends of DGEBP-F with DGE-DHBP

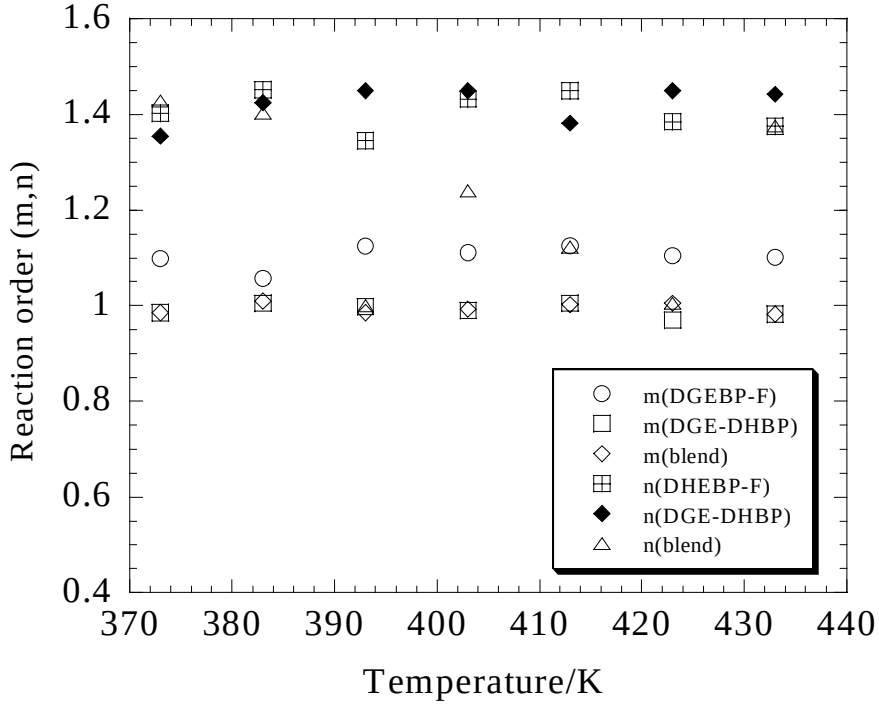

Figure 5.7 Comparison of reaction order (m, n) for DGEBP-F, DGE-DHBP, and blends of DGEBP-F with DGE-DHBP

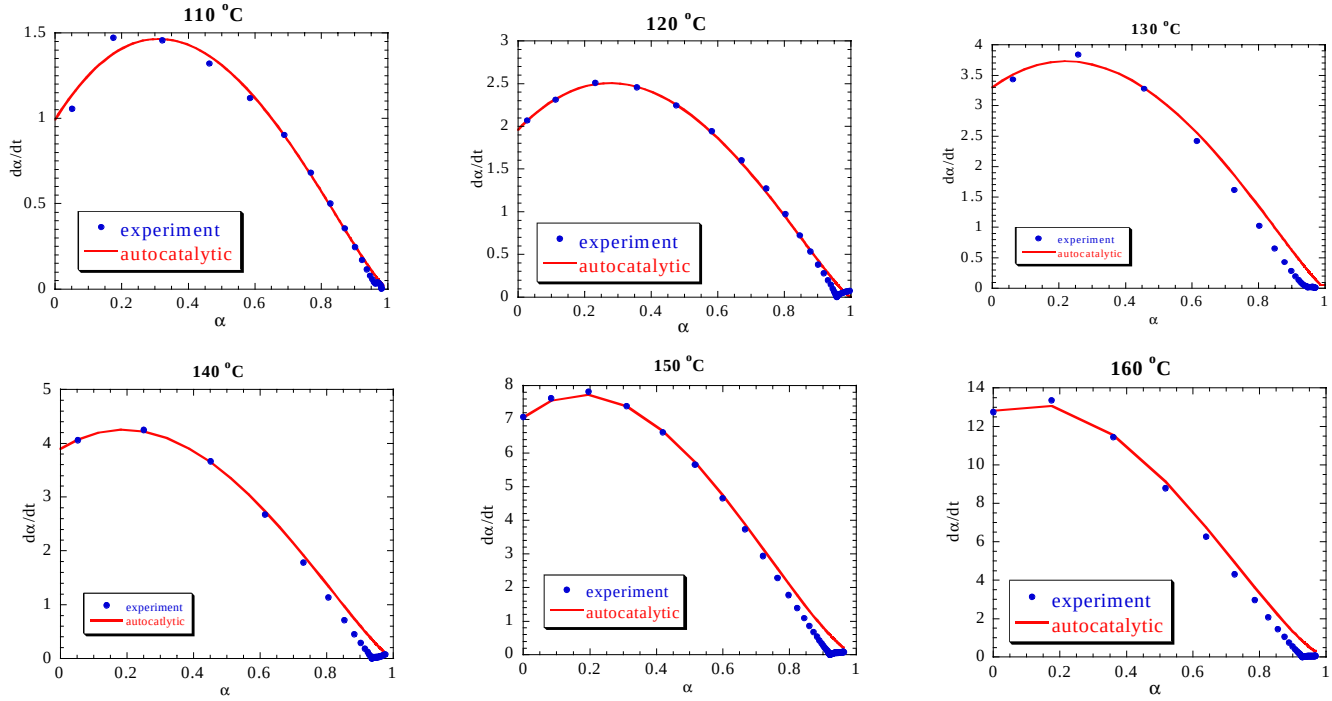

Figure 5.8 Comparison of experimental data with the autocatalytic model for DGEBP-F and MTHPA system

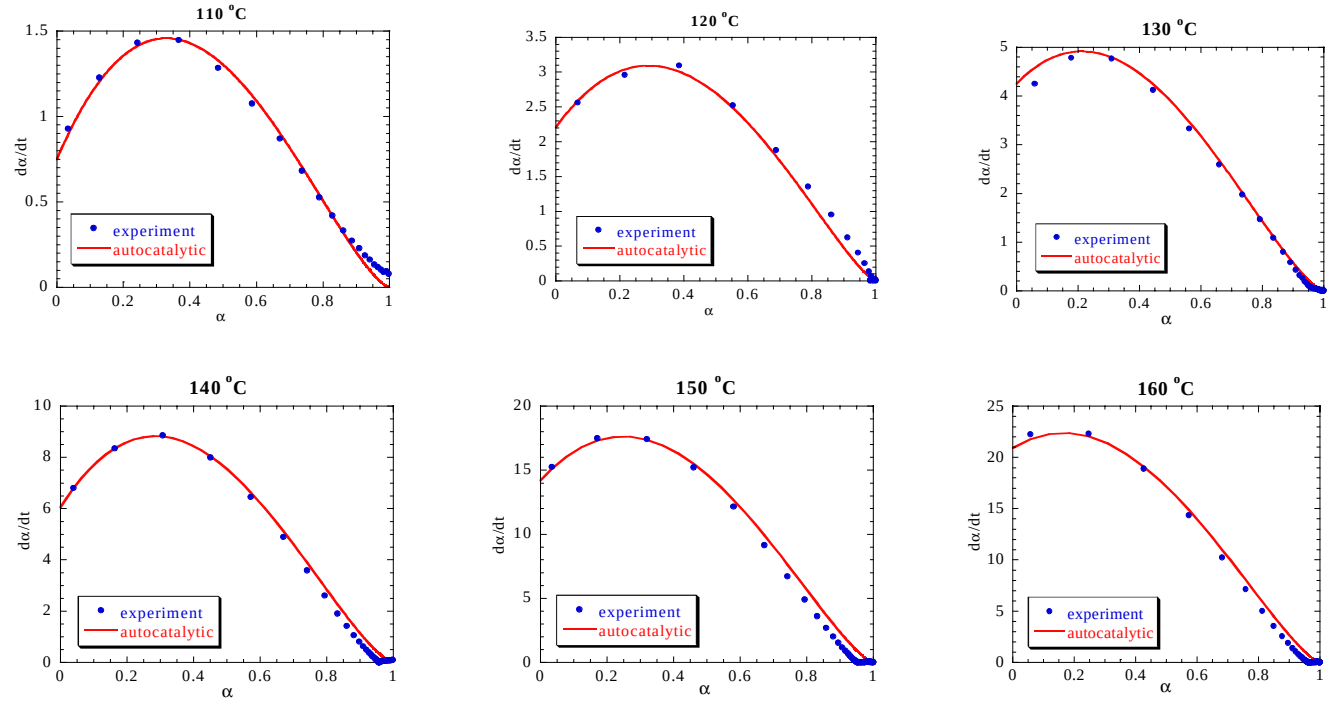

Figure 5.9 Comparison of experimental data with the autocatalytic model for DGE-DHBP and MTHPA system

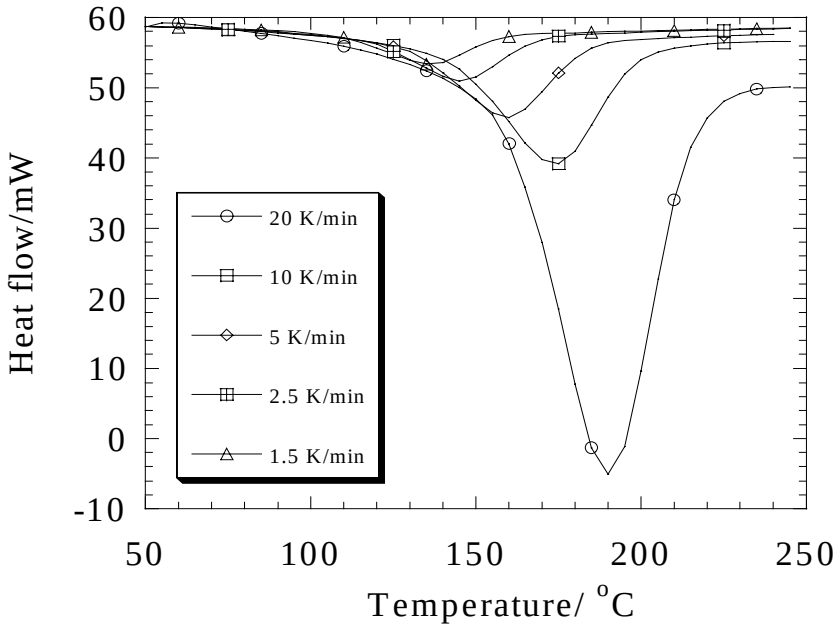

Figure 5.10 Dynamic thermograms for several heating rates of DGEBP-F + MTHPA

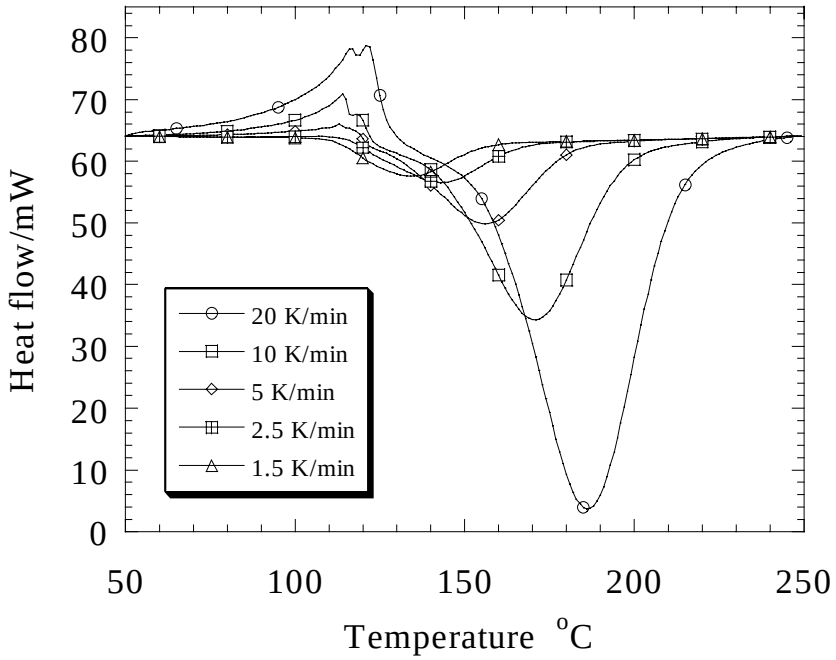

Figure 5.11 Dynamic thermograms for several heating rates of DGE-DHBP + MTHPA

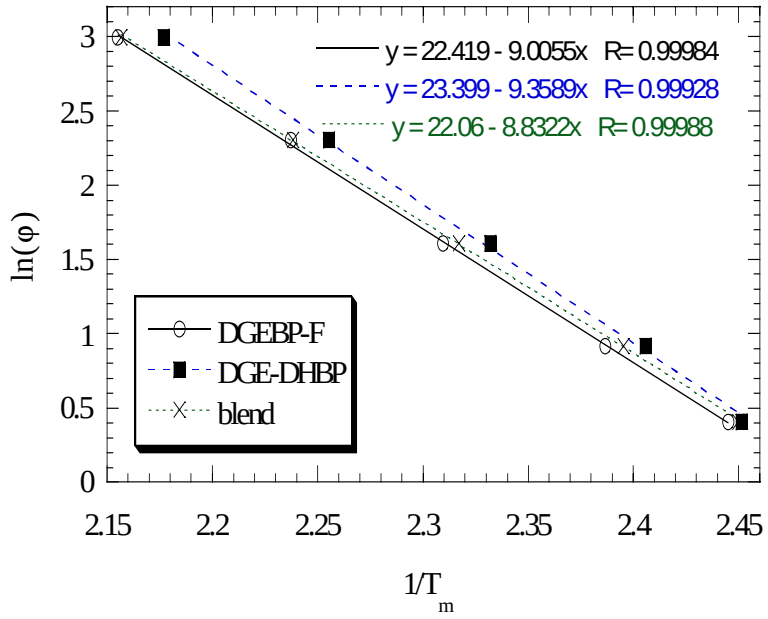

Figure 5.12 Comparison of data from multiple heating rates based on the Kissinger method for DGEBP-F, DGE-DHBP, and the 50:50 blend (DGEBP-F + DGE-DHBP)

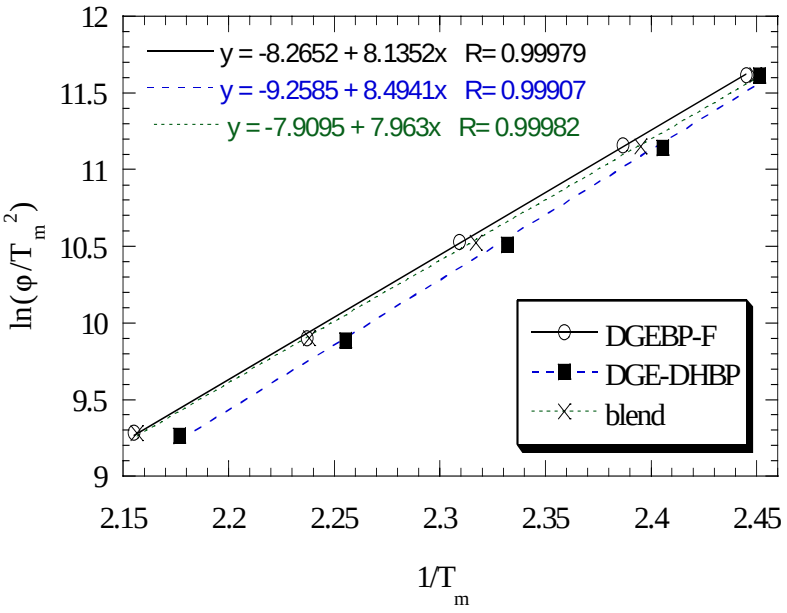

Figure 5.13 Comparison of data from multiple heating rates based on the Ozawa method for DGEBP-F, DGE-DHBP, and the 50:50 blend (DGEBP-F:DGE-DHBP)

Table 5.2 The nonisothermal data at different heating rates compared between DGEBP-F/ DGE-DHBP/ Blend of DGEBP-F & DGE-DHBP systems

Heating rate (K/min.)	Peak temperature (K)		
	DGEBP-F/MTHPA	DGE-DHBP/MTHPA	Blend (DGEBP-F/DGE-DHBP)
1.5	409	408	408
2.5	419	416	418
5	433	429	432
10	447	443	447
20	464	459	464
E_a (Kissinger method)	68.2 kJ/mol	70.6 kJ/mol	65.8 kJ/mol
E_a (Ozawa method)	71.2 kJ/mol	73.9 kJ/mol	69.8 kJ/mol

5) Concluding remarks

The presence of DGE-DHBP affects the kinetics of curing DGEBP-F, especially the activation energy of curing. The result of isothermal and non-isothermal kinetic model supports the same trend that the reaction kinetics of the mixed system are synergistic. The activation energy for the curing reaction of DGEBP-F + DGE-DHBP blend is lower compared with the other single component resin systems. There are significant differences in k_1 values between two neat resins and the blend systems, with the value for the blend being much higher. This implies that there are differences in external catalysis mechanisms. However, the k_2 values of these systems are not much different since the reactivity and functionality groups of both epoxies are quite similar.

The activation energy obtained from non-isothermal is higher than that from isothermal measurements since the fitting of isothermal DSC is performed after an induction period.

Effects of diffusion control and complicated reactions which retard the basic curing reaction are found in all systems after about 80 % conversion. The autocatalytic model does not take into account the effect of mobility retardation after the gelation point. Therefore, the curing rates calculated from the model are higher than the experimental values.

Curing both components *in situ* with the same curing agents is a processing advantage. Relatively small amounts of LC epoxy can be used as an additive to improve toughness of a non-LC epoxy for high performance applications.

CHAPTER 6

MISCIBILITY STUDIES

1) Introduction

In studies of the blend systems, one finds often the terms "*miscibility*" and "*compatibility*". A miscible polymer blend is created when the components are mixed at the molecular level, resulting in a single phase system. Properties of miscible blends represent an average of the components. For example, one glass transition temperature T_g which follows the weight average rule based on the Fox equation [204], is found. In contrast, the term compatible polymer blends is used to describe multiphase systems. Each phase is physically stable. Thus, multiple T_g values are observed in this system.

1.1 Thermodynamics of miscibility

The fundamental thermodynamic criteria which are necessary for the miscible system include: 1) Gibbs function of mixing must be negative [$\Delta G_m < 0$] and 2) the composition dependence of that function is positive [$(\partial^2 \Delta G_m / \partial \phi_2^2) > 0$] where ϕ_2 is the volume fraction of component 2. The relationship of ΔG_m and ϕ_2 indicates the phase behavior in that system. Figure 6.1 shows three possible phases in a binary polymer system. In case I, both criteria are fulfilled, and we have a miscible system. In case II, only the first criterion is satisfied. Thus, the partially miscible system exhibits a miscibility gap in the middle. In contrast, neither criteria are satisfied in case III which represents an immiscible system [205].

The diagram of temperature and phase for polymer mixtures is presented in Figure 6.2. With the variation of temperature, there is a change in liquid-liquid equilibrium phase boundaries. One might obtain the upper critical solution temperature UCST, case A) or lower critical solution temperature LCST, case B). The parameters which characterize the critical point are the critical temperature, T_c, and the critical composition ϕ_{2c}. The critical temperature, UCST, indicates the minimum temperature at which the two components will be miscible in all compositions while LCST indicates the opposite. The critical composition, ϕ_{2c} indicates a phase-inversion point. In the first region when $\phi_2 < \phi_{2c}$, the minor precipitating phase will be rich in component 2. On the other hand, the precipitating phase will be rich in component 1 when $\phi_2 > \phi_{2c}$ [206].

The *binodal* curve, as shown in Figure 6.2, divides the single-phase and two-phase regions and provides binodal points. At these points, we have equilibrium conditions and equal chemical potentials:

$$\mu_i \big| B = \mu_i \big| B' \tag{6-1}$$

where μ_i is the chemical potential of component i and can be represented as:

$$\mu_i = \left(\frac{\partial G}{\partial n_i}\right)\Big|_{T,P,nj\neq i} \tag{6-2}$$

Another condition is defined as the *spinodal* condition. The composition dependence of Gibbs function of mixing at S and S' points is equal to zero:

$$\left(\frac{\partial^2 \Delta G_m}{\partial \phi_2^{\,2}}\right) = 0 \tag{6-3}$$

In the region between the binodal and the spinodal there is the *metastable* condition. It is important to the mechanism and kinetics of phase separation [207].

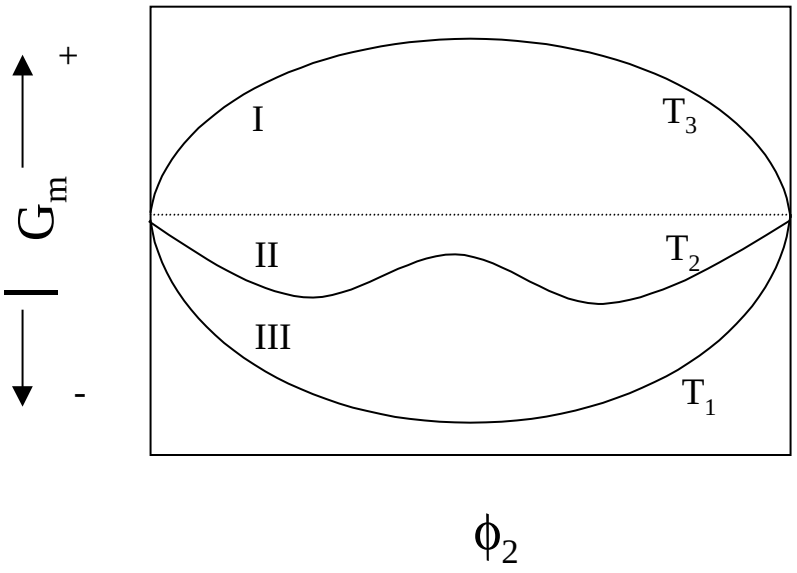

Figure 6.1 Schematic of three possible phases in a binary system (after [205])

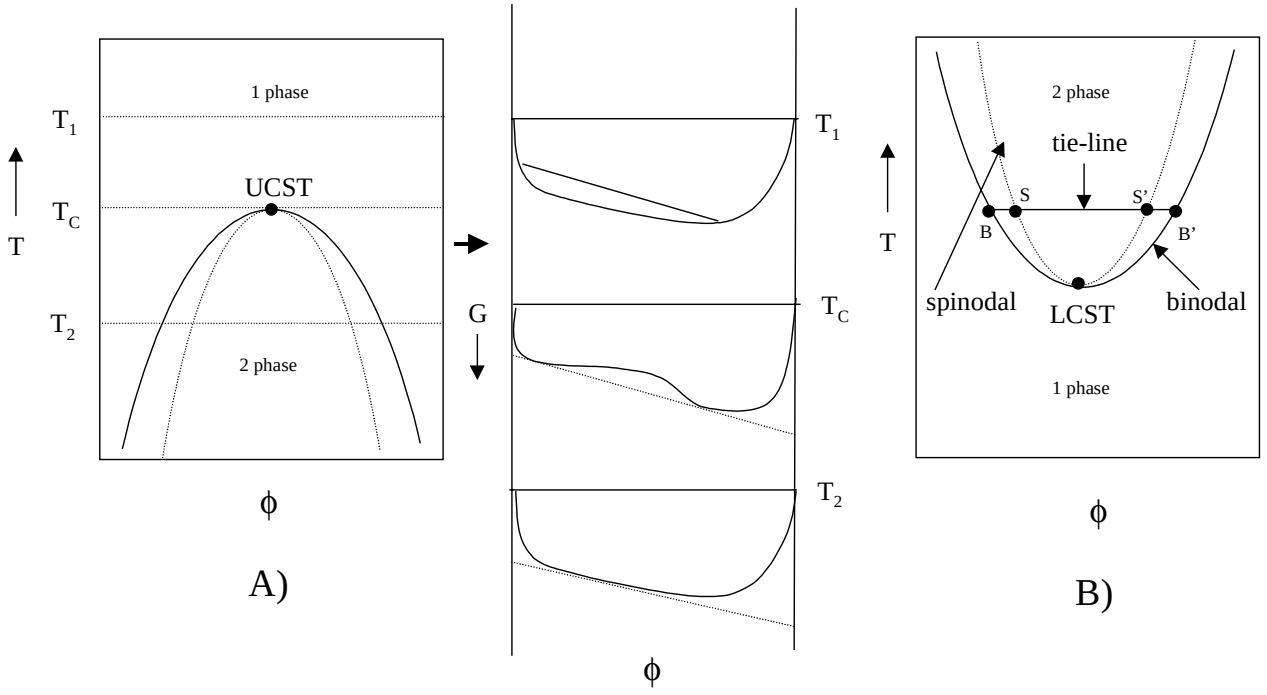

Figure 6.2 Schematic of temperature-phase diagram for A) upper critical solution temperature and its temperature dependence of free energy-composition relation, B) lower critical solution temperature.

The basic thermodynamic equation to describe miscibility can be established from the Gibbs function of mixing:

$$\Delta G_m = \Delta H_m - T\Delta S_m \tag{6-4}$$

where ΔH_m is the enthalpy change on mixing, ΔS_m is the entropy change on mixing and T is the absolute temperature. As mentioned earlier, the ΔG_m term has to be negative to fulfill the criteria of miscibility. Therefore, we need

$$\Delta G_m = \Delta H_m - T\Delta S_m < 0 \tag{6-5}$$

$$\Delta H_m < T\Delta S_m \tag{6-6}$$

Based on the lattice theory developed by Flory [208-209] and Huggins [210], the entropy change of mixing is given by:

$$\Delta S_m = -R(N_1 \ln \phi_1 + N_2 \ln \phi_2) \tag{6-7}$$

where N_i is the number of moles and R is the gas constant. The enthalpy change on mixing is:

$$\Delta H_m = RT\chi_{12} N_1 \phi_2 = BV_1 N_1 \phi_2 = (v_1 + v_2) B \phi_1 \phi_2 \tag{6-8}$$

where v_1 and v_2 are actual volumes of the components, V_1 is the molar volume of component 1, B is the interaction energy density, and χ_{12} is the interaction parameter or Flory-Huggins (F-H) chi parameter. The latter can be presented as:

$$\chi_{12} = \frac{BV_1}{RT} = \frac{z\Delta w_{12} N_A}{RT} = \frac{z\Delta w_{12}}{kT} \tag{6-9}$$

where N_A is the Avogado's number, z is the coordination number of the lattice and Δw_{12} is the energy for formation of an unlike contact pair. We have

$$\Delta w_{12} = w_{12} - \frac{(w_{11} + w_{22})}{2} \tag{6-10}$$

where w_{11}, w_{12} and w_{13} are the energies of the respective pair attractions. In the case of a non-polar systems, the energy of formation can be reduced to:

$$\Delta w_{12} = \frac{(w_{11}^{1/2} - w_{22}^{1/2})^2}{2} \tag{6-11}$$

From the previous assumption, the relationship of interaction parameter and Hildebrand's solubility parameter approach is expressed as:

$$\chi_{12} = \frac{V_1(\delta_1 - \delta_2)^2}{RT} \tag{6-12}$$

where δ_i is the solubility parameter of the component i.

1.2 Estimation of interaction parameter from solubility parameter

The use of the solubility parameter to study miscibility was described by Hilderbrand and Scott [211]. The solubility parameter was proposed to describe the enthalpy of mixing of nonpolar solutions. This approach was applicable only for the dispersive systems where the enthalpy of mixing is positive. The proposed relation is:

$$\Delta H_m = V\left(\left(\frac{\Delta E_1^V}{V_1}\right)^{1/2} - \left(\frac{\Delta E_2^V}{V_2}\right)^{1/2}\right)^2 \phi_1\phi_2 \tag{6-13}$$

where ΔE_i^v is the energy of vaporization of species I, V is the volume of the mixture and V_i is the molar volume of the species i. For low molecular weight materials, the solubility parameter can be measured from the energy of vaporization per unit volume as follows:

$$\delta = [\frac{\Delta E^v}{V}]^{1/2} \tag{6-14}$$

The solubility parameter describes the attractive interactions between molecules of material or the cohesion of the material. The value of δ^2 is known as the cohesive energy density (CED). The materials with higher δ require higher energy to disperse per volume.

Prausnitz et al. [212-213] introduced additionally permanent dipole and dispersion type interactions to the Hilderbrand solubility parameter. This helps to improve the agreement between calculation and experiment.

Hansen et al. included the dispersive, permanent dipole-dipole interactions, and hydrogen bonding constituents of the cohesive energy [214].

$$\delta^2 = \delta_d^2 + \delta_p^2 + \delta_h^2 \tag{6-15}$$

where δ_d is dispersive term, δ_p is the polar term, and δ_h is hydrogen bonding term. The Hansen solubility parameter provides often – but not always good agreement with the experimental results.

Advantages of the solubility parameter include the practical estimation of the universal parameters. Therefore, one can obtain compatible materials without performing the experiments. There are many applications of the solubility parameter concept including: the compatible matching of coating resins, the swelling study of cured elastomers, the study of polymer-polymer system [215], the polymer-binary [216], the copolymer [217], and the multicomponent system [218-221].

1.3 Group contribution methods

Group contribution methods have been widely used to estimate the solubility parameter [222]. Some research groups have reviewed this method and provided the table of group contribution for each functional group. This method was proposed by Small [223], Hoy [224], and van Krevelen [225]. The values from Small were obtained from measurements of the heat of vaporization. The parameters of Hoy were derived from vapor pressure measurements. Van Krevelen's values were obtained based on the cohesive energy of materials.

The assumption used in the group contribution techniques is based on the additive rule. Each functional group provides the additive contribution to the solubility parameter. Thus, the energy of vaporization is given by:

$$\Delta E_i^V = \sum_j n_j \Delta e_j \tag{6-16}$$

where Δe_j is the energy of vaporization contribution of group j and n_j is the number of groups of type j in the molecule. The solubility parameter is obtained as:

$$\delta = \left(\frac{\Delta E_i^V}{V_i} \right)^{1/2} = \left(\frac{\sum_j n_j \Delta e_j}{V_i} \right)^{1/2} \tag{6-17}$$

The molar attraction constant was defined by Small [223] as:

$$F_j = (\Delta E_{i,j}^V V_{i,j})^{1/2} \tag{6-18}$$

Therefore, the solubility parameter can be calculated by:

$$\delta_i = \left(\frac{\Delta E_i^V V_i}{V_i^2} \right)^{1/2} = \frac{\sum_j F_j}{V_i} = \frac{\rho_{ij} \sum_j F_j}{M_i} \tag{6-19}$$

where ρ_i is the polymer density and M_i is the molecular weight.

Coleman and coworkers [226] proposed the method to calculate the solubility parameter based on the molar volume V* and molar attraction constant P* obtained by the least square methods. This was calculated based on the data base complied by Daubert and Danner [227].

1.4 Evaluation of solubility parameter for thermoset system

Williams and coworkers [228] applied the Flory-Huggins (F-H) lattice model to study the phase separation of catalytically cured rubber-modified epoxy system during polymerization. The Gibbs function of mixing can be represented as:

$$\frac{\Delta G}{RTV} = \frac{\phi_1}{V_1}\ln\phi_1 + \frac{\phi_2}{V_2}\ln\phi_2 + \frac{\chi_{12}}{V_1}\phi_1\phi_2 \qquad (6\text{-}20)$$

where V_1 is the molar volume of component 1 at conversion p, $V_1 = \frac{(V_1)_o}{1-2p}$ $(V_1)_o$ is the initial molar volume of epoxy before polymerization, p is the extent of curing, V_2 is the molar volume of rubber and χ_{12} is the F-H interaction parameter.

There are three main assumptions for this study. First, the rubber is assumed to be inert with respective to the reactive epoxy. Therefore, the rubber has no effect on the curing kinetics parameters of the epoxy. Moreover, the reactivity of active sites is assumed to be equal. No effect from substitution and intermolecular reaction is involved in the reaction. Lastly, the interaction parameter is assumed to be constant for the entire reaction. This assumption is contradicted by the observation of Gales [229] who found that the interaction parameter changes as the curing reaction progresses.

The molecular weight of the system affects the entropy of mixing. As the molecular weight increases, the entropy of mixing becomes increasingly smaller until it becomes equal to zero as the molecular weight approaches infinity. Verchere and coworkers [230] studied the Temperature-phase diagram of CTBN rubber modified diglycidyl ether of bisphenol A (DGEBP-A) epoxy resin. The cloud point curves representing the equilibrium binodal curve as a function of molar mass was determined. As the molar mass increases, the curve shifts upwards. This indicates a reduction in miscibility between the epoxy and the rubber as the MW increases.

1.5 Methods to determine miscibility of polymer blends

There are a number of methods used to analyze the phase separation of polymer blends. In the first method, physical properties related to the extent of phase separation are measured. This includes the measurement of the glass transition temperature of blends by dynamic mechanical analysis, dielectric [231], dilatometric, or calorimetric techniques. The second method is to perform a direct measurement of the extent of phase separation from light scattering techniques [232], optical microscopy, scanning electron microscopy [233-234], or transmission electron microscopy [235].

2) Experiment

2.1 Sample Preparation

Pure components of DGEBP-F and blends of 10, 20, 30, 50, 80 and 100 % of DGE-DHBP by weight were prepared. The synthesized DGE-DHBP was dried and ground by mortar. Both epoxies were mixed in various concentrations and cured simultaneously with MTHPA at 120^{o}C for 2 hours, and at 170^{o}C for 1 hour under vacuum at 25 mm Hg.

2.2 Dynamic Mechanical Analysis (DMA)

Dynamic moduli and glass transition temperatures of the networks as a function of concentration of DGE-DHBP were investigated in the range of composition of 0, 10, 20, 30, 40, 50, 60, 80, and 100 % of pure DGE-DHBP with DGEBP-F cured with MTHPA at 120^{o}C for 2 hours, and postcured at 170^{o}C for 1 hour under vacuum. DMA measurements were performed on a Perkin Elmer DMA-7 apparatus using a three-point bending fixture. Measurements were run from 25-250 ^{o}C at the heating rate of 10 K/min at 1 Hz frequency. Nitrogen was the carrier gas, with the flow rate of 20 mL/min.

Secondary transitions of unmodified and modified samples were investigated by Rheometrics Dynamic Spectrometer RDS-IIe in the torsional mode. The constant strain amplitude was 1 % with the constant frequency of 10 radians/second. The experiments were performed from –150 to + 210^{o}C with the heating rate of 3^{o}C/min.

3) Results

3.1 Thermodynamics of miscibility

The solubility parameter was calculated based on the group contribution method recalculated by Coleman [226] as shown in Table 6.1. The calculated solubility parameter values of the four epoxy resins used are compared. The similar structure of these epoxies leads to the similarity of the solubility parameters. The closest values are found from the pair of DGE-DHBP and DGEBP-F which both have the same functionality, except that the functional groups are connected in different order. The carbonyl group in DGE-HHC increases the solubility parameter. The double bond in the DGE-DHMS structure results in a decrease of the solubility parameter compared with the DGE-DHBP system.

The similarity in solubility parameter for the DGE-DHBP and DGEBP-F leads to a high possibility of mutual dissolution of these two monomers. Moreover, the exothermic reaction during of epoxy curing also enhances the possibility of a miscible system. Molecular weight (MW) is another factor that affects the miscibility. The initial MW of epoxy resins used is shown in Table 4.1. The MW of epoxy increases as the reaction progresses. However, the exothermic conditions of curing reactions ensure the miscibility of these blends and is based on the basic idea from F-H theory for exothermic reactions. They predict that the condition of miscibility is always satisfied no matter how large the molecular weights. The miscibility observation will be confirmed from the detection of glass transition temperature of blends in the next section.

Table 6.1 The solubility parameter calculation by group contributions method

Structure	Functional group	V* cm^3/mol	F* $(cal\ cm^3)^{0.5}/mol$	δ $(cal/cm^3)^{0.5}$
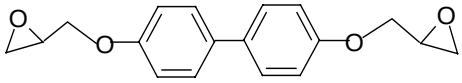 DGE-DHBP	$-CH_2-$	16.5	132	10.05
	>CH-	1.9	23	
	-O-	5.1	95	
	$-C_6H_5-$	75.5	735	
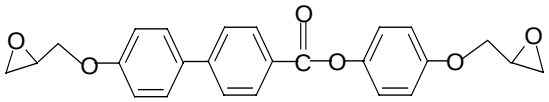 DGE-HHC	$-CH_2-$	16.5	132	10.45
	>CH-	1.9	23	
	-O-	5.1	95	
	-CO-	10.7	262	
	$-C_6H_5-$	75.5	735	
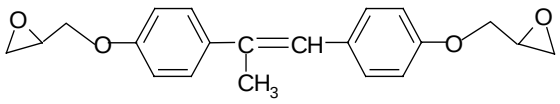 DGE-DHMS	$-CH_2-$	16.5	132	9.6
	>CH-	1.9	23	
	-O-	5.1	95	
	$-CH_3$	31.8	218	
	-CH=	13.7	113	
	$-C_6H_5-$	75.5	735	
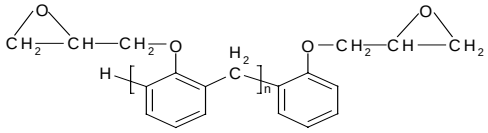 DGEBP-F	$-CH_2-$	16.5	132	9.92
	>CH-	1.9	23	
	-O-	5.1	95	
	$-C_6H_5-$	75.5	735	

3.2 Dynamic Mechanical Analysis

To determine the degree of miscibility of the coreacted monomers in the network, the glass transition temperature T_g was evaluated by means of DMA. T_g or α-transition of cured epoxy is the indication of rotational freedom in the segment between crosslinks [236]. Tan δ curves as a function of temperature determined for several concentrations of the DGE-DHBP system are shown in Figure 6.3. As the DGE-DHBP concentration increases, T_g also increases.

To estimate the degree of miscibility, the theoretical T_g of blended samples was calculated from the standard Fox equation as follows:

$$\frac{1}{T_g} = \frac{W_1}{T_{g1}} + \frac{W_2}{T_{g2}} \tag{6-21}$$

Here W_1 and W_2 are weight fractions of the respective components while T_{g1}, T_{g2} are the respective glass transitions of the components. Results indicate high miscibility across the composition range of blended samples. Moreover, the areas under tan delta and loss modulus curves, which represent the toughness of the material, are higher for low DGE-DHBP concentrations. Figure 6.4 presents the comparison of T_g obtained from DMA and DSC results as a function of DGE-DHBP concentration. The T_g values observed from DSC are lower than those from DMA but follow the same trend. As the DGE-DHBP concentration increases, a single intermediate T_g of the blended samples is observed. With reference to T_g's of the pure system, the T_g of the network increases with DGE-DHBP concentration.

Figure 6.5 shows the dynamic mechanical spectra of loss moduli for 0, 10, 30, 50, and 100 % DGE-DHBP. Two distinct peaks are observed at -80 and 110^{o}C, representing the β-transition and glass transition temperatures, respectively. The β-transitions of these samples can be assigned to side chain or pendant group movements. In epoxy systems, the β-relaxation transition is associated with $-CH_2CH(OH)CH_2O-$ segments of the cured molecule [229, 237]. The strength of the β-transition is related to the efficiency of epoxy in absorbing energy, as reflected in mechanical and acoustic properties [238-239]. As DGE-DHBP concentration increases, the β-peak tends to shift to lower temperatures. In contrast, the T_g of the blend tends to increase as DGE-DHBP concentration in the system increases. The T_g value obtained from DSC, DMA and RDS show the same trend, namely T_g increases as a function of DGE-DHBP concentration. However, the difference in values is small.

The effect of the curing conditions on dynamic mechanical properties are also compared. DGE-DHBP cured with MTHPA at 120 ^{o}C produced an isotropic phase while the nematic phase is found in curing the sample at 90 ^{o}C. The comparison shows that the isotropic sample has higher T_β. Its T_g is higher than for 0 %DGE-DHBP but is lower than for other compositions. The comparison of T_β and T_g values for each sample is presented in Table 6.6.

The dynamic modulus curves for cured epoxies consist of three main regions. The first is the glassy region which has a modulus value in the GPa range. In the transition region, there is a sudden drop of modulus from 10^9 to 10^7 Pa. The modulus in the rubbery

region (E'_R) is in the 10-20 MPa range. This region is constant for thermoset due to permanent bonding, The modulus value can quantify the crosslinking density. The relationship of E_R and crosslinking density has been studied based on the classical rubber elasticity [240]. Tobolsky [241] derived the relationship as follows:

$$E'_R = \frac{3\varphi dRT}{M_x} \tag{6-22}$$

The effect of dangling bonds is neglected. Therefore,

$$M_x = \frac{d}{\rho} \tag{6-23}$$

Thus, the relationship from (Eq. 4-12) is changed to:

$$E'_R = 3\varphi\rho RT = 3\varphi k_B T \tag{6-24}$$

where E'_R is the modulus in the rubbery state, φ is the front factor which is close to unity, d is the density, R is gas constant, k_B is Boltzman constant, T is temperature in degrees K, M_x is the molecular weight between crosslinks, and φ is the crosslinking density.

Table 6.2 shows the comparison of E'_R as a function of the DGE-DHBP concentration. The increase in modulus at the rubbery region as a function of the DGE-DHBP concentration is due to the effect of rigid molecules. Mesogenic units enhance the crosslink density of the coreacted network, especially in the condition that allows orientation of mesogenic units before complete curing.

For the DGE-DHBP sample, which was cured under isotropic conditions, the orientation was destroyed. Therefore, E'_R is of the same magnitude for the pure DGEBP-F sample. Cured DGE-DHBP under nematic conditions increases E'_R by 40 % compared with curing under isotropic conditions. For the network based on rigid units, modification

based on enthalpic deformations are required to modify the rubber elasticity theory. The finite extensibility of LC units affects the entropic response to the applied force. In the isotropic sample, there is no preferred direction, by definition. Thus, the crosslinks can move in all directions when force is applied. For nematic samples, the molecules are restricted in the direction perpendicular to the director. Therefore, the network can only move in an approximate direction parallel to the director.

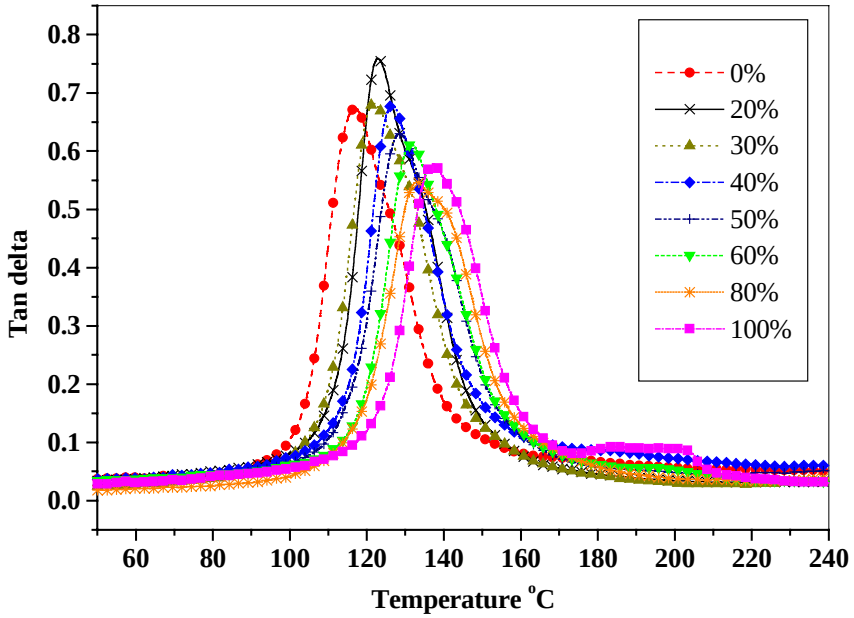

Figure 6.3 Comparison of tan delta results as a function of DGE-DHBP concentration obtained from DMA

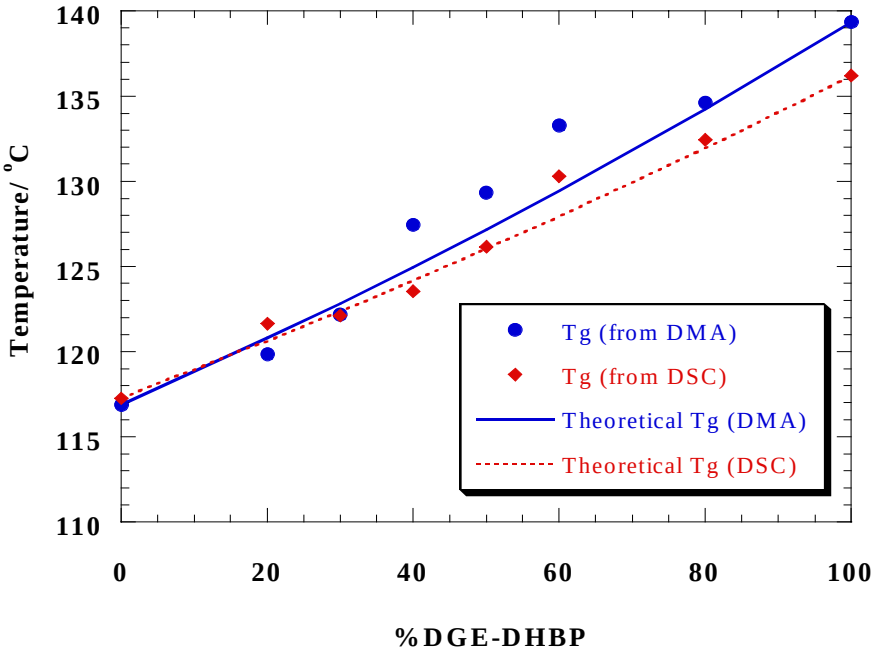

Figure 6.4 Comparison of experimental and theoretical T_g values obtained from DSC and DMA

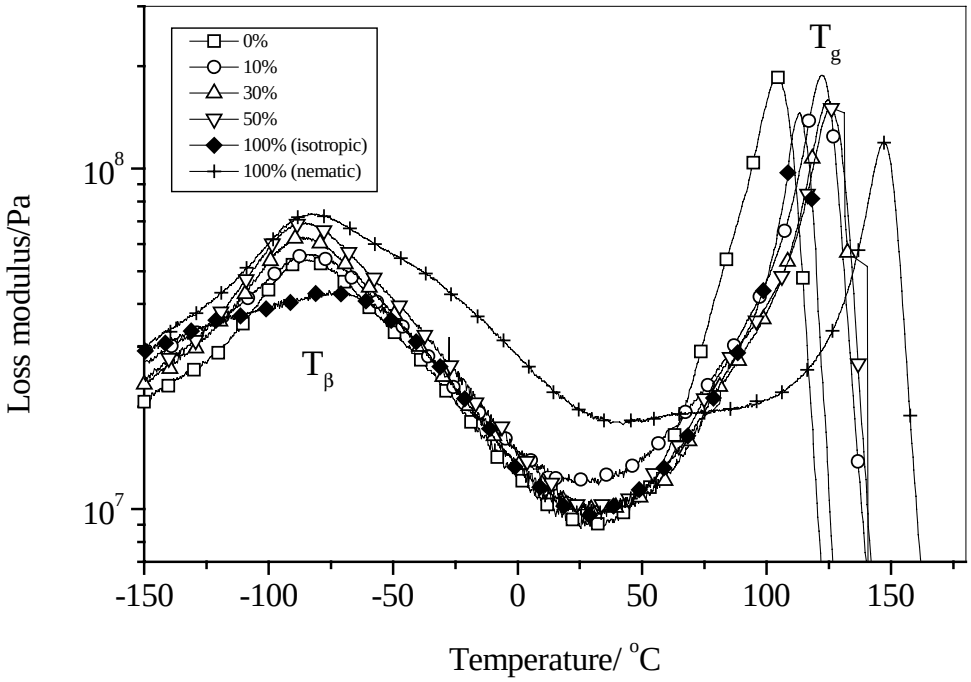

Figure 6.5 Comparison of loss modulus values for several DGE-DHBP concentrations and curing temperatures observed from RDS.

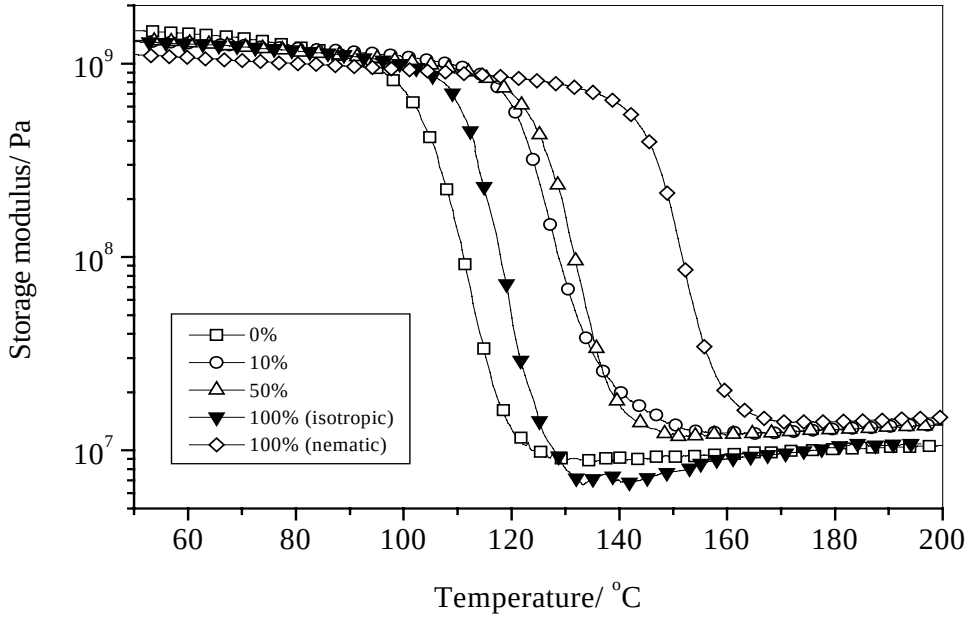

Figure 6.6 Comparison of storage modulus values for several DGE-DHBP concentrations observed from RDS.

Table 6.2 The comparison of T_β, T_g, loss modulus at room temperature and modulus at rubbery regions obtained from RDS

% DGE-DHBP	T_β (^oC)	T_g (^oC)	$E_{(T = 200\ ^oC)}$ (Pa)
0	-84.6	104.8	10.6×10^6
10	-84.0	122.1	13.7×10^6
30	-87.1	124.5	13.9×10^6
50	-85.5	125.9	13.6×10^6
100 (isotropic)	-75.7	113.2	10.6×10^6
100 (nematic)	-84.1	146.8	14.9×10^6

4) Conclusions

The solubility parameter was calculated based on the group contribution approach. The similarity in functional groups of DGE-DHBP and DGEBP-F causes closeness of the solubility parameters. As the curing reaction progresses, DGE-DHBP and DGEBP-F can dissolve in each other and form partial bridges. The high degree of miscibility results in a co-continuous phase morphology of blends. Therefore, the coreacted networks exhibit a single T_g across all compositions which scales with increasing DGE-DHBP concentration. Results show that for all compositions the glass transition temperature is increased relative to the pure epoxy components; hence, there is a potential for high temperature applications.

The dynamic mechanical study indicates a strong dependence of the secondary transition (T_β) of the nematic sample compared with the isotropic sample. This implies that the molecular motion of pendant groups in nematic LC epoxy is pronounced.

The increased modulus in the rubbery region as a function of DGE-DHBP concentration is explained in terms of the increased crosslink density for the mesogenic unit. Moreover, there is a 40% higher in E'_R for sample cured in the nematic phase compared with sample cured in the isotropic phase and is due to the extensibility of LC units. In the isotropic sample, there is no directionality of order. Thus, the crosslinks can move in all directions when force is applied. For nematic samples, the molecule is restricted in the perpendicular direction to the director. Therefore, the network can only move in the parallel direction to the director.

CHAPTER 7

MECHANICAL PROPERTIES OF EPOXY + LIQUID CRYSTALLINE EPOXY BLENDS

1) Introduction

The potential for using LCEs for improving the mechanical properties of epoxy matrices was recently examined by Sue et al. [130, 242] They utilized reactive groups of 4,4'-dihydroxy-α-methylstibine (DHAMS) blended with diglycidyl ether of 4,4'-dihydroxy-α-methylstibine (DGE-DHAMS) and cured with sulphanilamide as the matrix resins. Improved fracture toughness and modulus over a tough epoxy network resulted from the presence of liquid crystallinity. Blends of DGE-DHAMS with a phenolic novolac resin cured with sulphanilamide also show improved mechanical properties, even though the LC characteristics were not observed.

According to the capability of a thermotropic LC to reinforce thermoplastics, the anisotropic properties of LC are advantageous. In the interest of improving mechanical properties of the epoxy, the LCEs are chosen to modify the properties of epoxy resins because the inflexible building blocks between crosslink sites provide highly local molecular order within each domain. Moreover, the network provides enhancement in a transverse direction due to covalent crosslinking bonds. The self-reinforcing effect from the mesogenic units is the main interest for this research.

To study the effect of in situ curing of LCE with non-LC epoxy, the mechanical properties of materials are determined in both high speed and low speed testing. This chapter describes results of tensile, impact, and fracture toughness testing. The effects of

LCEs concentration, and the nature of mesogenic length of LCEs, are shown in section 3).

2) Experimental

2.1 Sample Preparation

2.1.1 Effect of LCEs concentration

Pure components of DGEBP-F and blends of 10, 20, 30, 50, 80 and 100 % of DGE-DHBP by weight were prepared. The synthesized DGE-DHBP samples were dried and ground by mortar. Both epoxies were mixed homogeneously in various concentrations and cured simultaneously with MTHPA at 120^{o}C for 2 hours, and post-cured at 170^{o}C for 1 hour under vacuum. All samples prepared for tensile, impact and fracture toughness tests were cured in the same way. At least 10 samples for each mechanical measurement were investigated.

2.1.2 Effect of the nature of mesogenic unit length of LCEs

The effect of mesogenic unit length was observed by comparing the mechanical properties of cured DGE-DHBP and DGE-HHC with MTHPA.

2.2 Tensile tests

Pure components and blends were prepared for tensile measurements according to the ASTM D5937-96 standard with the type 1A dog-bone shape (Figure 7.1). The tests were performed using a MTS testing machine with the 2000 lb load cell and 1 mm/min. crosshead speed. Strains were determined with the aid of a gauge extensometer. The

stress vs. strain curves were recorded to reveal their deformation as a function of each variation.

2.3 Impact tests

Impact measurements were measured with a Dynatup Impact Tester with 200 lb weight. Samples with a size of 12 x 60 x 4 mm^3 were prepared for Izod impact tests according to ASTM D5941-96. The 1.2 mm V-shaped sharp notch on each sample was cut as an initiator point and the natural crack generated by a fresh razor blade across the notch root (Figure 7.2). The impact strength was thus evaluated as a function of composition.

2.4 Fracture toughness

Fracture toughness was measured by the single notch procedure according to ASTM D5045-96. Sample specimen dimensions of thickness x length x width = 5 x 70 x 10 mm were prepared to ensure the state of plane strain at crack tips.

The samples with 0, 10, 20, 30, and 50 % DGE-DHBP were prepared for single edge notch bending (SENB). The cured samples were cut with a 45^o notch-cutting machine. The sharp notches were further cut with a diamond saw. The natural sharp crack was produced with a fresh razor blade. The sharp crack in all samples was prepared to ensure a valid result. The ratio of crack length, a, to the sample width, w, of samples was in the range of 0.45-0.55 to ensure the condition of plane strain (Figure 7.3). The three point bending test was performed on an MTS testing machine with the displacement rate of 1 mm/min with a suspension span of 50 mm at room temperature. The load-

displacement curves were used in calculations. The critical-stress-intensity factor, K_{IC}, and fracture energy, G_{IC}, values were obtained as functions of composition. K_{IC} is important to estimate the maximum load capacity while G_{IC} is for energy absorption.

The critical stress intensity in plane strain, K_{IC}, which represents the toughness of sample, is calculated as

$$K_{IC} = \frac{P}{B\sqrt{W}} f\left(\frac{a}{W}\right) \tag{7-1}$$

where P is peak load which represents the moment of crack extension, B is specimen thickness, W is specimen width, f(a/W) is the correction factor, and a represents the specimen crack length. The correction factor [243-244] is obtained from

$$f\left(\frac{a}{W}\right) = \frac{3\frac{S}{W}\sqrt{\frac{a}{W}}}{2\left(1+2\frac{a}{W}\right)\left(1-\frac{a}{W}\right)^{\frac{3}{2}}}\left[1.99 - \frac{a}{W}\left(1-\frac{a}{W}\right)\left\{2.15 - 3.93\left(\frac{a}{W}\right) + 2.7\left(\frac{a}{W}\right)^2\right\}\right] \tag{7-2}$$

The dimension of samples for valid K_{IC} values is as follows:

$$B, a, (W-a) > 2.5\left(\frac{K_{IC}}{\sigma_y}\right)^2 \tag{7-3}$$

where σ_y is the yield stress of the material.

The critical strain energy G_{IC} is calculated as

$$G_{IC} = \frac{(1-\nu^2){K_{IC}}^2}{E} \tag{7-4}$$

where ν is the Poisson ratio and E is the tensile modulus of the sample.

2.5 Double edge notch four point bending

The samples for double-notch four point bending (DN-4PB) were prepared following the method of Sue et al. [18, 245-246]. DN-4PB was performed to observe the characteristic crack tip of unmodified and modified epoxy samples compared with the cured LCEs. The sample specimen dimensions were thickness x length x width = 5 x 70 x 10 mm. Samples were prepared by curing the stoichiometric ratio of the epoxy and the curing agent in a vacuum oven. Double notches were cut with a diamond saw, followed by a fresh razor blade.

Figure 7.4 presents the configuration of a test specimen for double end-notch-4 point bending tests. The samples were tested by four-point bending using a MTS testing machine with cross-head speed of 0.5 mm/min until one section was broken. The section that did not break was used for the crack tip damage zone study. The small section in the middle section was cut perpendicular to the notch (Figure 7.5). The thin section was polished by 200 grit SiC paper, followed by 1 μm diamond paste with ethylene glycol. An optical microscope was used to observe the area around the crack tip.

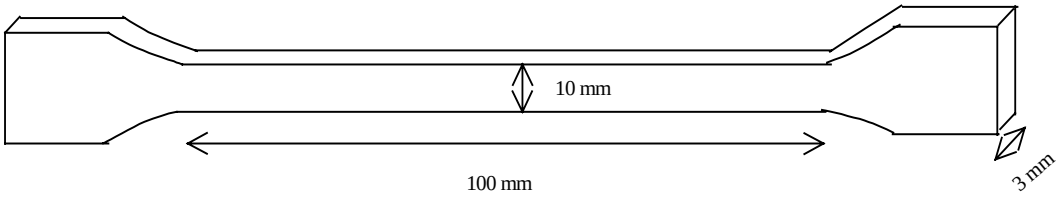

Figure 7.1 Configuration for tensile specimen testing

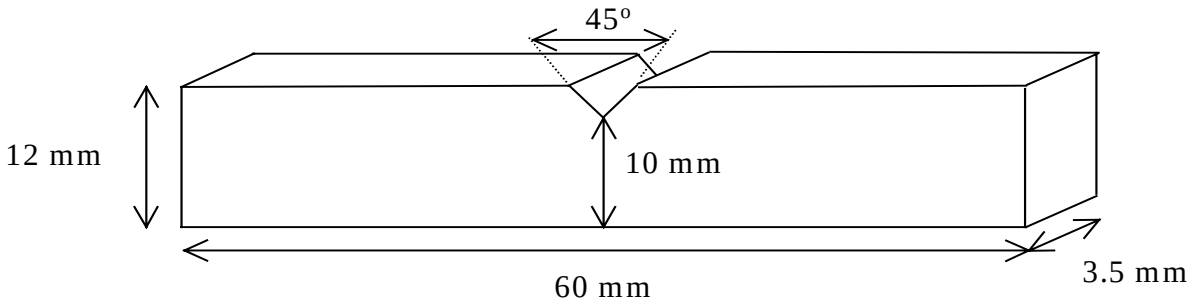

Figure 7.2 Configuration for impact specimen testing

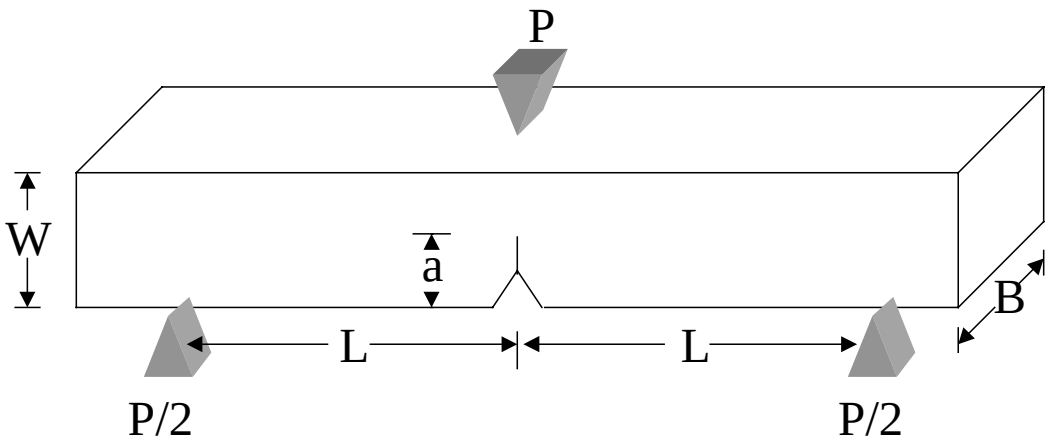

Figure 7.3 Configuration of the test specimen for single edge notch bending

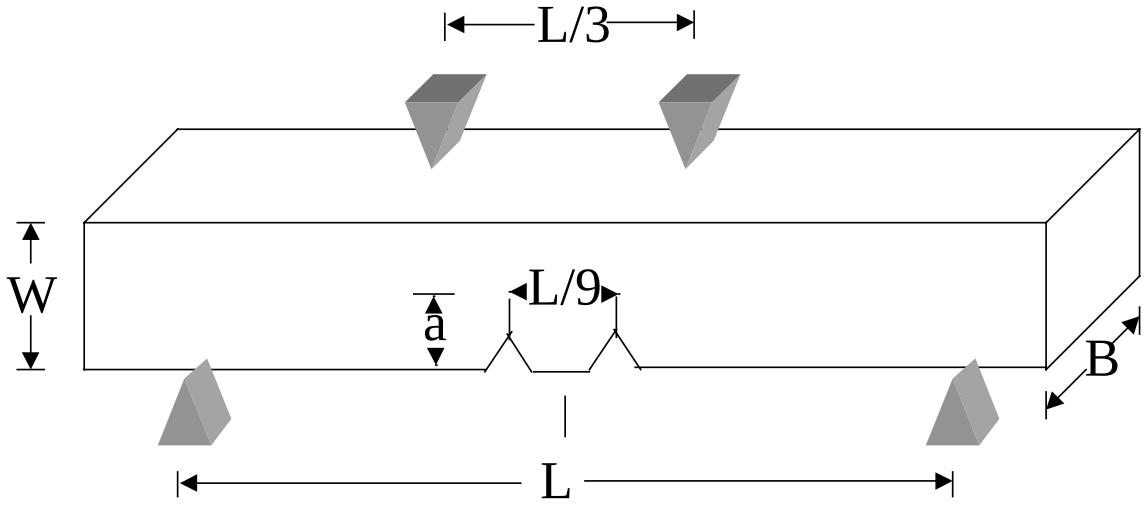

Figure 7.4 Configuration of the test specimen for double end-notch-4 point bending

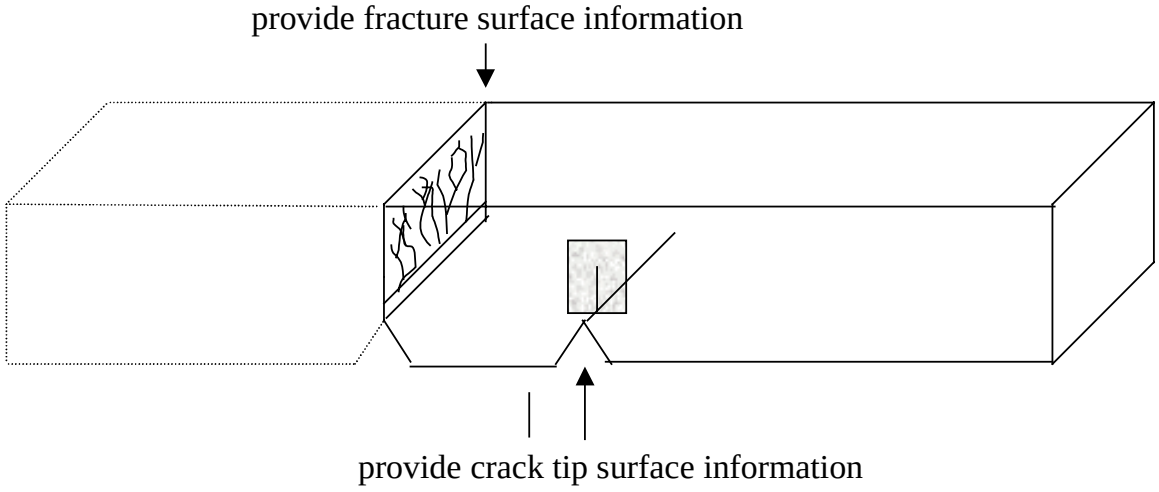

Figure 7.5 Information obtainable from double end-notch-4 point bending testing

2.6 Scanning Electron Microscopy

The morphologies of the fracture surfaces after tensile tests for each composition were observed using a JEOL T300 scanning electron microscope (SEM) at 15 kV accelerating voltage. Samples for each composition were cut to 2 mm heights. Each sample was mounted on a sample holder using an electrically conductive paint as an adhesive and coated with a thin gold layer by plasma sputtering to avoid a charging effect due to nonconductivity of the polymer.

3) Mechanical test results

3.1 Effect of LCEs concentration

Table 7.1 shows a summary of results from tensile, impact and fracture toughness tests as a function of DGE-DHBP concentration. The comparison of modulus, tensile strength, failure strain, and area under the stress-strain curve, which represent the toughness index or energy absorption, indicates an improvement of toughness as 10, and 20 % of DGE-DHBP is added. For each concentration of DGE-DHBP added, there is an improvement in both the modulus and yield strength. Selected stress vs. strain curves as a function of DGE-DHBP concentrations are presented in Figure 7.6. The deformation comprises a linear and a nonlinear region. For the 10 % DGE-DHBP sample a distinct yielding characteristics is found. Figure 7.7 shows the modulus of blends with two maxima, one around 10 % and the other about 50 % of DGE-DHBP, followed by a decreasing trend.

Thus, first we have the reinforcement of the non-LC phase by the presence of the rigid LC component. Then, we seem to exceed the θ limit, the concentration at which the LC component forms a second phase, the effect analyzed before in terms of the generalized statistical mechanical model of Flory [247] and also seen experimentally in thermoplastic PLCs [47, 248]. When the LC-rich phase is formed, the modulus initially decreases, but then increases as the consequence of the increasing LC concentration. Above 50 % of the LC component, the material becomes gradually brittle and the modulus decreases, an effect we have also seen in thermoplastics PLCs [249]. The results show improvement of tensile strength and failure strain at low concentrations of DGE-DHBP. However, the toughness index does not increase for samples containing more than 30 % by weight DGE-DHBP.

The comparison of impact strength or energy required to break the sample as a function of the DGE-DHBP concentration is illustrated in Figure 7.8. The results correspond to the toughness index result obtained from tensile tests and the areas under the loss modulus curves from DMA measurements. The impact strength curves show two maxima for DGE-DHBP concentrations below 50 % - and for the same reason. However, the second maximum occurs at a lower DGE-DHBP concentration than on the modulus diagram. This is a consequence of the higher sensitivity of impact testing to the brittleness introduced by the LC units.

The critical stress intensity in plane strain, K_{IC}, which represent the toughness of the sample, is reported in Figure 7.9 and Table 7.1. The K_{IC} values for blended samples increase as a function of % DGE-DHBP added, especially for 10 and 20 % DGE-DHBP.

However, the toughness decreases after 30 % DGE-DHBP has been added. The improvement in fracture toughness is due to the inhomogeneities of anisotropic rigid biphenyl functional groups in DGE-DHBP molecules. We found a two-fold increase in toughness when 20 % DGE-DHBP is blended with DGEBP-F. The fracture toughness improvement from this system is lower compared with thermoplastic modified epoxy and reactive rubber modified epoxy systems. Martinez [250] found a three-fold increase in K_{IC} for polysulfone-modified diaminodiphenyl methane cured diglycidyl ether of bisphenol A (DGEBP-A). However, there is difficulty in processing this material because of different viscosities of thermoplastics and the epoxy. Pearson [251] has reported that the incorporation of carboxyl terminated random copolymer of butadiene and acrylonitrile increases fracture toughness of this epoxy by a factor of three. However, some desirable intrinsic properties, including strength and stiffness of the modified materials, are lowered by the inclusion of elastomeric materials.

Fracture energies increase when DGE-DHBP is added to the pure DGEBP-F – as seen in Table 7.1. The value of G_{IC} doubles when 20 % DGE-DHBP is added.

Table 7.1: Comparison of mechanical properties from tensile, impact and fracture toughness test for each % DGE-DHBP

% DGE-DHBP	Tensile modulus (GPa)	Tensile strength (MPa)	Failure strain (%)	Toughness index	Impact strength (kJ/m^2)	Fracture toughness ($MPa/m^{1/2}$)	Fracture* energy (J/m^2)
0	2.51±0.21	59.46±6.57	3.42±0.82	1.25±0.50	0.83±0.11	1.03±0.09	294
10	2.88±0.15	69.29±0.74	4.93±1.24	2.54±0.92	1.18±0.13	1.65±0.16	556
20	2.62±0.12	62.38±6.04	3.35±0.74	1.31±0.52	1.00±0.12	2.31±0.15	802
30	2.89±0.26	62.55±8.59	3.14±0.80	1.28±0.56	1.05±0.10	1.71±0.04	441
50	3.18±0.22	64.36±3.35	2.61±0.45	1.04±0.16	0.77±0.08	1.56±0.20	681
80	2.57±0.16	62.34±3.93	3.35±0.54	1.26±0.32	0.94±0.09	-	-
100	2.59±0.19	49.68±4.11	2.42±0.22	0.68±0.11	0.75±0.11	-	-

* υ is assumed equal to 0.38

Note: All the deviation results (+/-) of mechanical properties are obtained from the standard deviation calculation

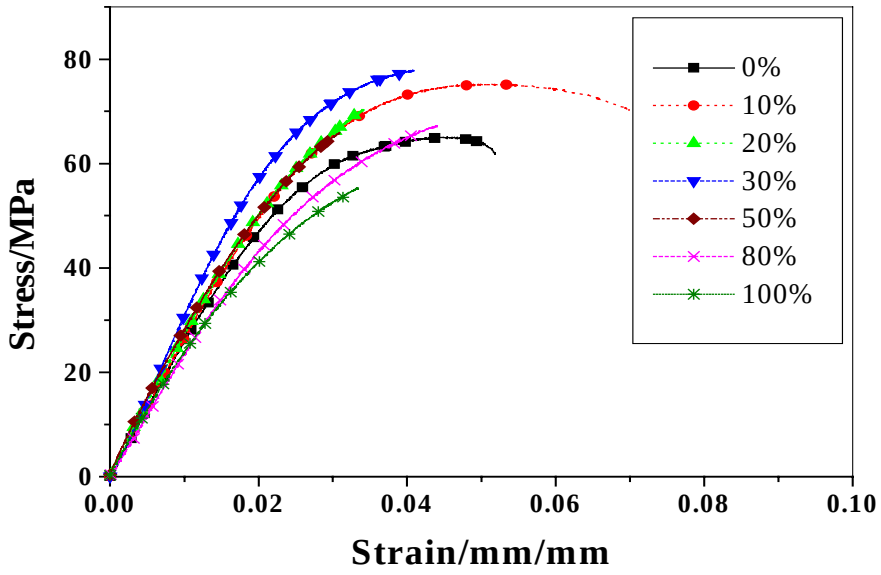

Figure 7.6 Stress vs. strain curves for several concentrations of the DGE-DHBP in DGEBP-F system

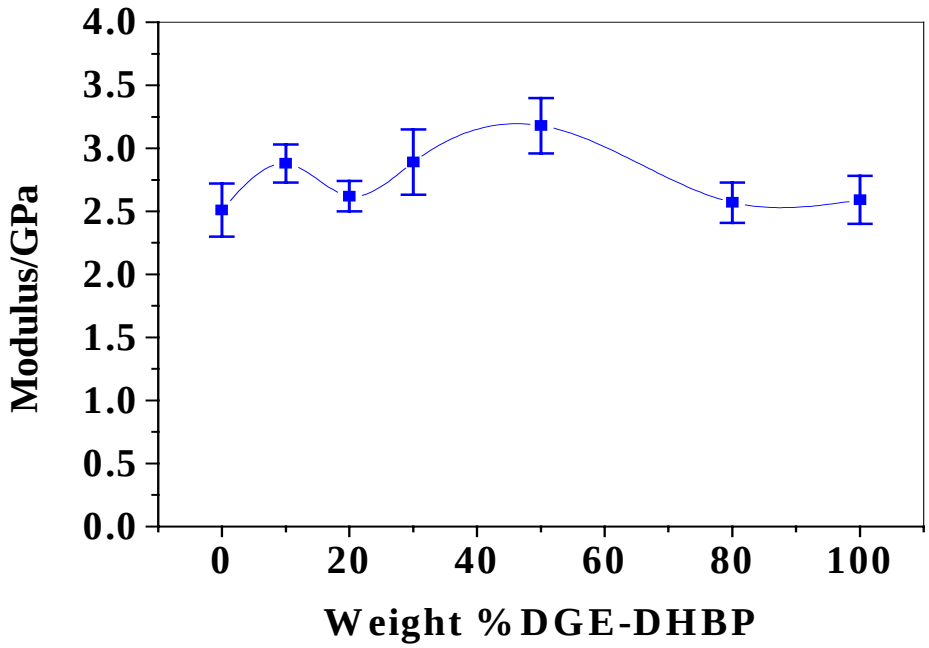

Figure 7.7 Comparison of modulus as a function of DGE-DHBP concentration

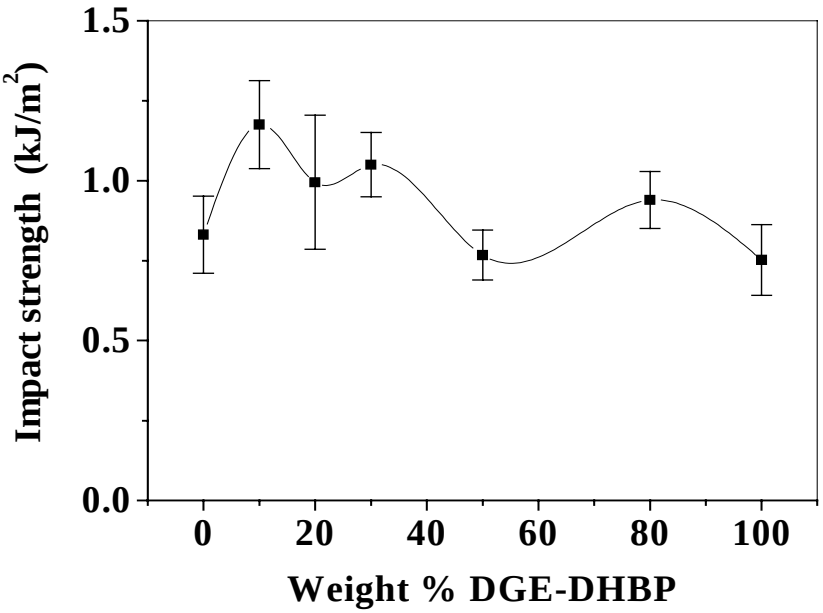

Figure 7.8 Comparison of impact strength as a function of DGE-DHBP concentration

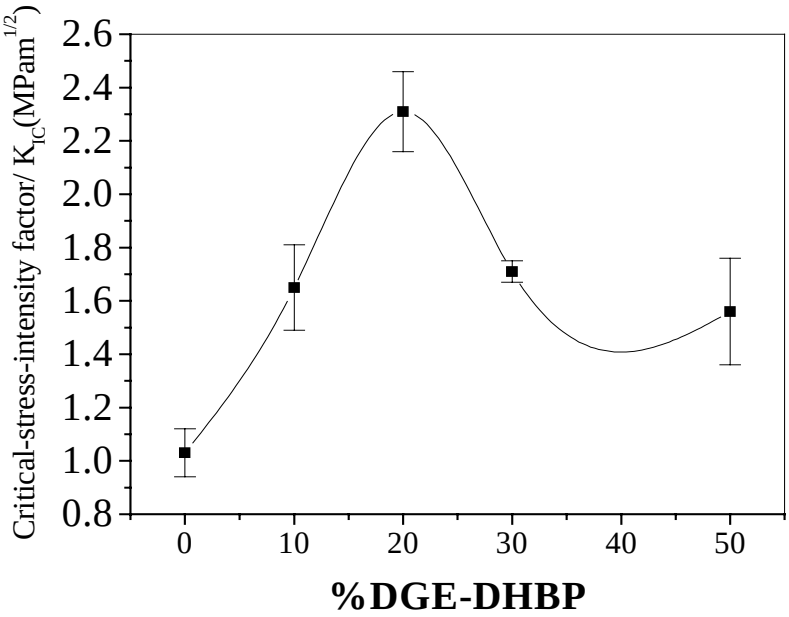

Figure 7.9 Comparison of critical-stress-intensity factor as a function of DGE-DHBP concentration

3.2 Effect of mesogenic unit length

The results of tensile and impact testing of DGE-HHC cured with MTHPA are reported in Table 7.2. Figure 7.10 presents the comparison of curves of stress vs. strain as a function of DGE-HHC concentration. The tensile strength increases monotonically with increasing concentration of DGE-HHC as does its modulus. However, the strain at failure tends to decrease as a function of the DGE-HHC concentrations. The results reflect the rigid reinforcement provided by the mesogenic units of DGE-HHC. The modulus increases by 36 % for 10 % DGE-HHC modified matrix compared with unmodified system. The tensile strength of the 10 % DGE-HHC system is 30 % higher than for the unmodified matrix. The failure strain is lower by 6 % compared with the unmodified sample when 10 % DGE-HHC is used as the modification. There is not much change for the tensile properties when more than 10 % DGE-HHC is added. Therefore, the concentration which provides the best modification is 10 % DGE-HHC.

The impact testing results, as a function of DGE-HHC concentration, are presented in Figure 7.11. The maximum impact strength is found for the 10 % DGE-HHC sample. The impact strength of the 10 % DGE-HHC is about three-fold larger compared with that of the unmodified sample.

The effect of mesogenic unit presence on impact strength in DGE-DHBP and DGE-HHC systems on impact strength is shown in Figure 7.12. DGE-HHC has a longer mesogenic unit length compared with DGE-DHBP (Table 4.1). The impact strength values for DGE-HHC are 3 times higher than for DGE-DHBP.

Table 7.2 Comparison of mechanical properties from tensile, impact for each % DGE-HHC

% DGE-HHC	Tensile modulus (GPa)	Tensile strength (MPa)	Failure strain (%)	Impact strength (kJ/m^2)
0	2.51±0.21	59.46±6.57	3.42±0.82	0.83±0.11
5	3.16±0.16	69.14±3.56	3.27±0.54	2.91±0.35
10	3.43±0.45	77.25±5.23	3.21±0.31	3.30±0.44
20	3.53±0.24	78.08±3.87	3.17±0.35	2.77±0.42

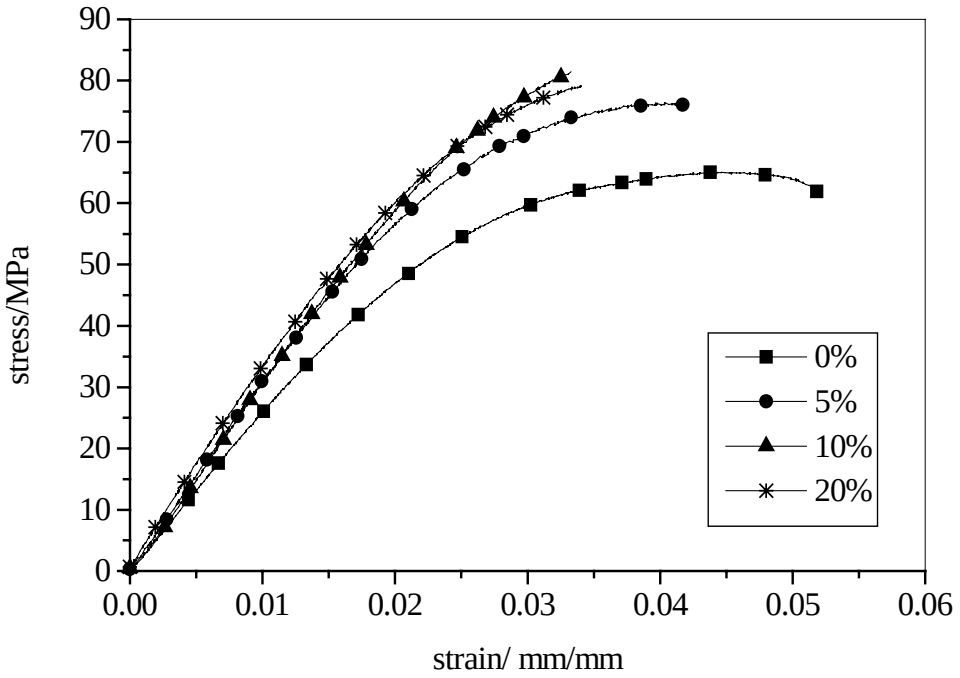

Figure 7.10 Stress vs. strain curves as a function of DGE-HHC concentration in the DGEBP-F system

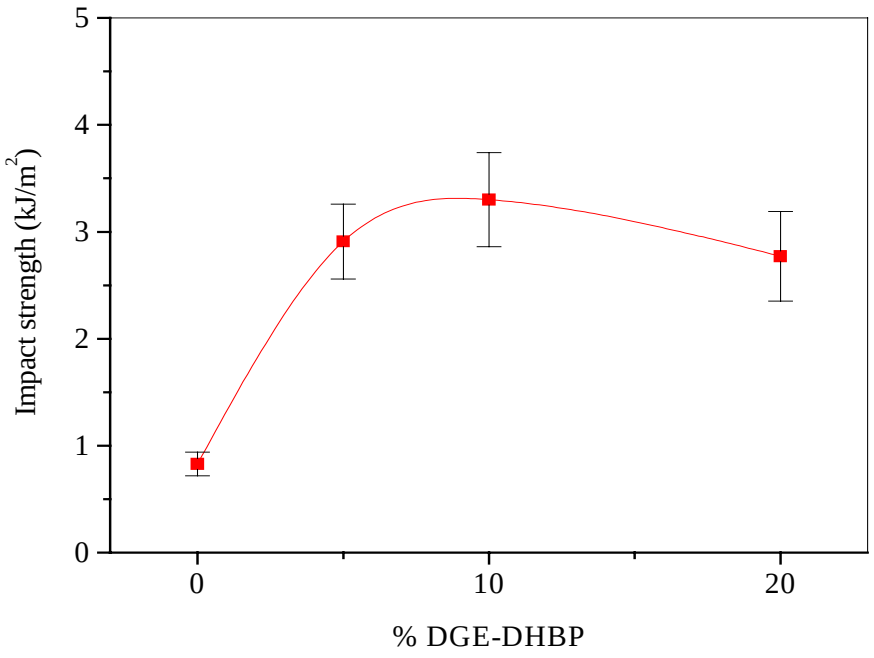

Figure 7.11 Comparison of impact strength as a function of DGE-HHC concentration

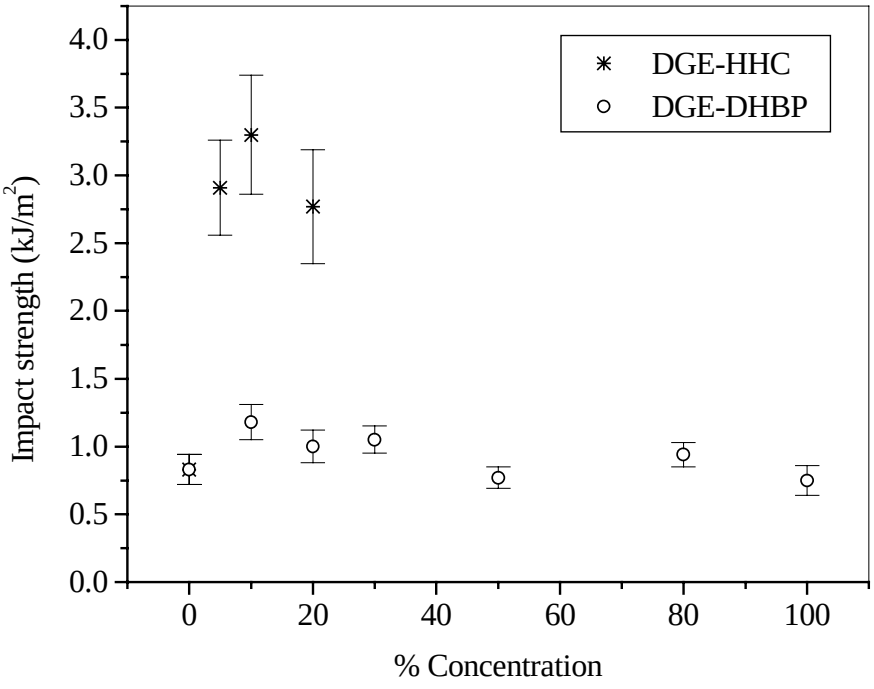

Figure 7.12 Comparison of impact strength as a function of DGE-DHBP and DGE-HHC concentrations in the systems containing DGEBP-F

4) Fractography

The fracture surfaces were investigated by a SEM for all compositions. Figure 7.13 represents the fracture surface of DGEBP-F while the respective surface of DGE-DHBP is shown in Figure 7.14. Typically three main regions are seen; namely initiation, propagation, and termination. Somewhat finer patterns are observed in Figure 7.14, reminiscent of those of Sue and coworkers [131] for their LC epoxies.

The comparison of fractography of pure DGEBP-F and the system containing 20 % DGE-DHBP is shown in Figure 7.15. We observed the river pattern where the multiple lines begin as a single line at the initiation point. The fracture surfaces of the tensile specimens for modified and unmodified systems exhibited marked differences in the area of rapid crack growth. Our micrographs do not show discontinuous fracture propagation observed by d'Almeida and Monteiro for their epoxies based on diglycidyl ether of bisphenol A and triethylene tetramine hardener [252]. However, they did not have a LC component and they introduced higher hardener concentrations. The main region, which reflects differences in toughness characteristics, is termination region. Figure 7.16 shows the fracture surface of the termination zone for the 20 % DGE-DHBP sample at high magnification. The stability of the crack growth regions varies with the DGE-DHBP concentration. Higher surface roughness is associated with the higher energy required to fracture the specimens. LC components introduce a deviation of crack propagation around the grain and lead to higher fracture toughness. The fracture surface of DGE-DHBP shows high roughness. However, the toughness observed is lower than expected. This is due to the large area of rapid crack propagation region as compared to initiation.

Large differences between the LC-containing materials and pure DGEBP-F are not observed for several reasons. First, both constituents are chemically similar epoxies. Second, significant interphase boundaries are known to be formed in interpenetrating polymer networks [253]. DSC [254] and DMA results show that a LC phase is formed during crosslinking, but partial bridging [255] is possible between a LC and a non-LC epoxy. The chemical structure of epoxies can be changed relatively easily during curing by variation of several parameters, including presence of nonreactive components. [3]

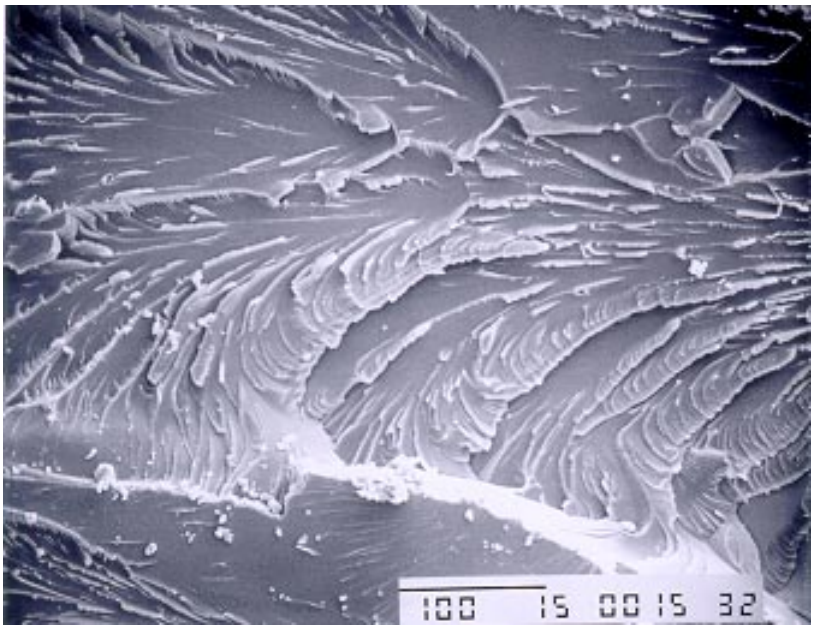

Figure 7.13 Fracture surface of DGEBP-F (scale: 100 μm)

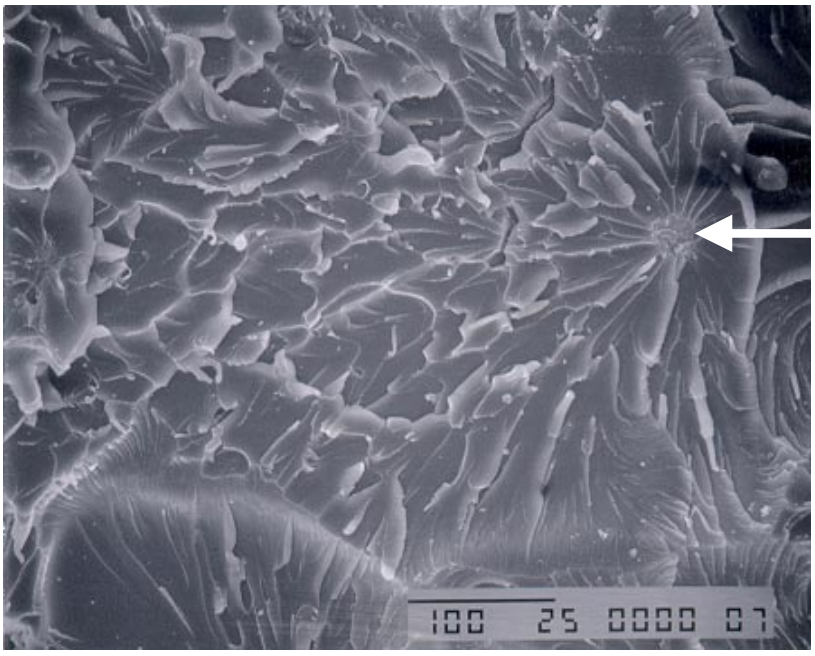

Figure 7.14 Fracture surface of DGE-DHBP (scale: 100 μm)

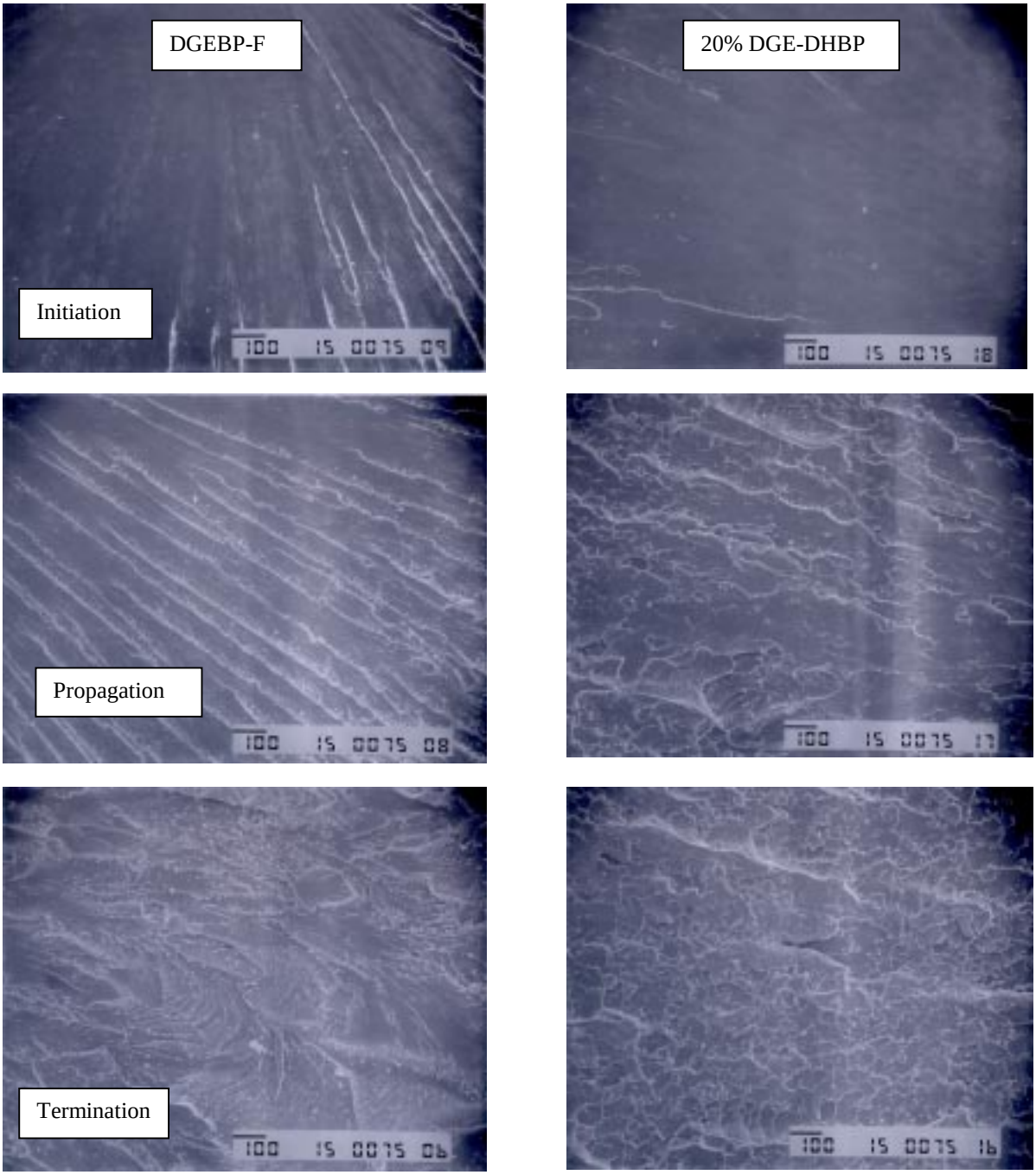

Figure 7.15 Comparison of fracture surfaces of pure DGEBP-F and the system containing 20 %DGE-DHBP (75x) (scale: 100 μm)

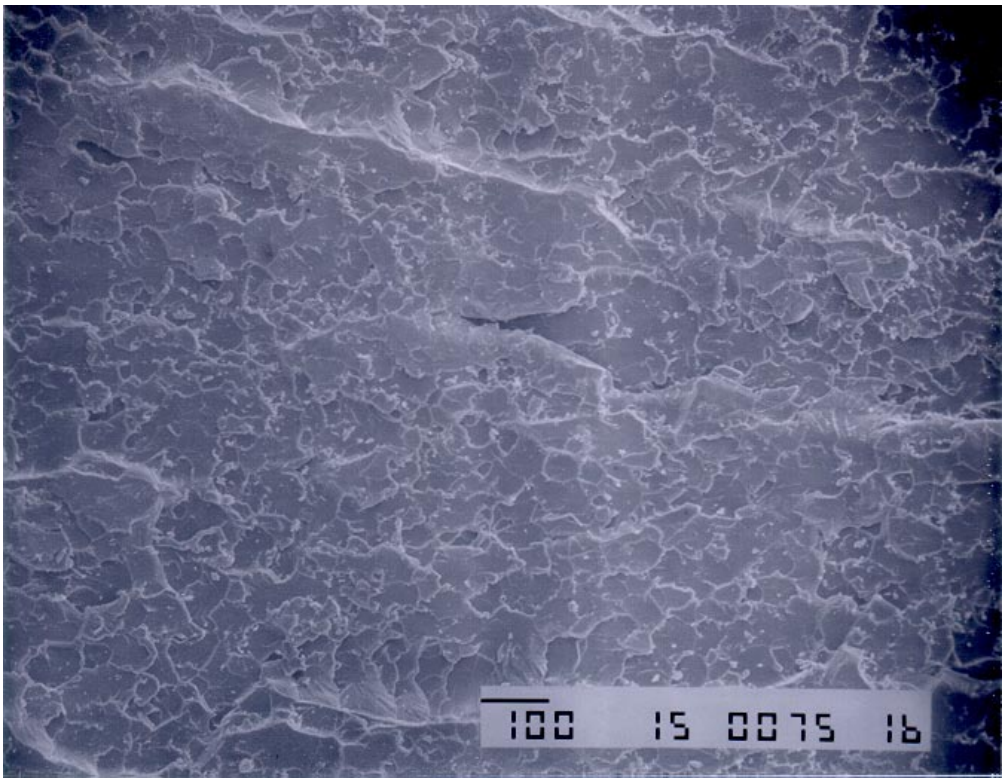

Figure 7.16 Fracture surface of termination zone of DGE-DHBP (scale: 100 μm)

5) Mechanism of crack formation.

The mechanical properties and morphology results reported in earlier section imply that there are differences in fracture mechanisms in unmodified and modified systems. This section is devoted to a study of these crack mechanisms. The mechanisms for cured LC epoxy and non-LC epoxies are compared, as shown in Figures 7.17 and 7.18. Figure 7.17 presents the optical micrograph of crack tip of DGE-DHBP and DAT. The mechanism is dominated by crack deflection and crack bridging. Arrows indicate the segmented crack which acts as a bridge to counteract crack propagation.

The main crack movement in DGEBP-F cured with MTPA is a straight line. This is an indication of brittle fracture. Some areas of crack bridging are observed. However, they are not dominant in affecting the fracture toughness.

The crack propagating mechanism for 10 % DGE-DHBP in DGEBP-F cured with MTHPA is presented in Figure 7.19. From the study as reported in section 3.1, the mechanical properties established that this concentration provided the highest improvement in strength. The main mechanism found in this case is crack deflection. This might be the effect of the mesogenic units distributed in the network. The fracture route follows along the LC edge so the deflection of crack in the sub-fracture surface zone is found.

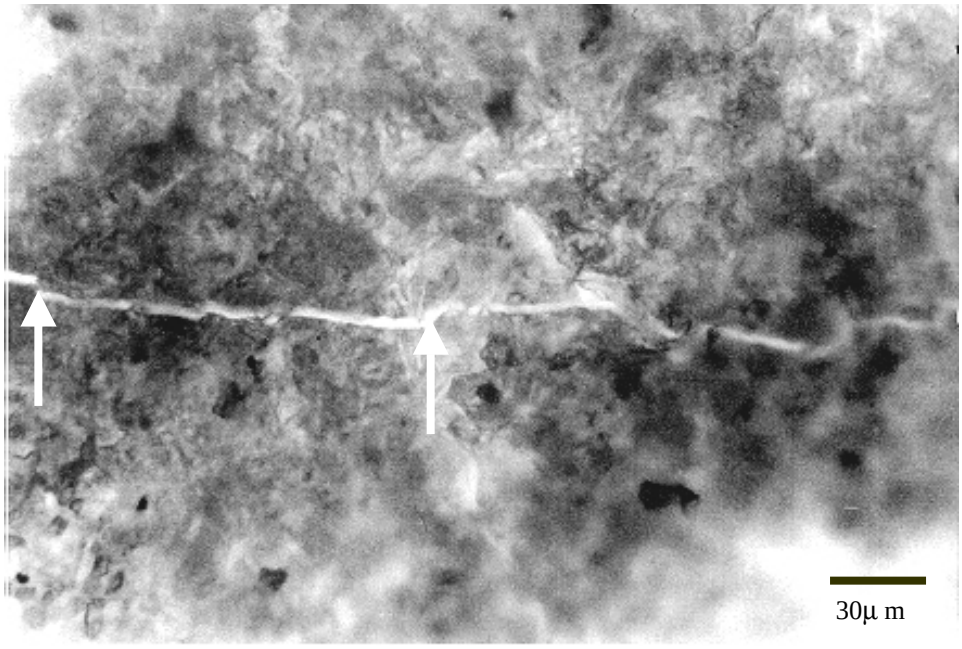

Figure 7.17 Optical micrograph of a crack obtained from cured DGE-DHBP with DAT. The arrows indicate the segmented crack which act like a bridge.

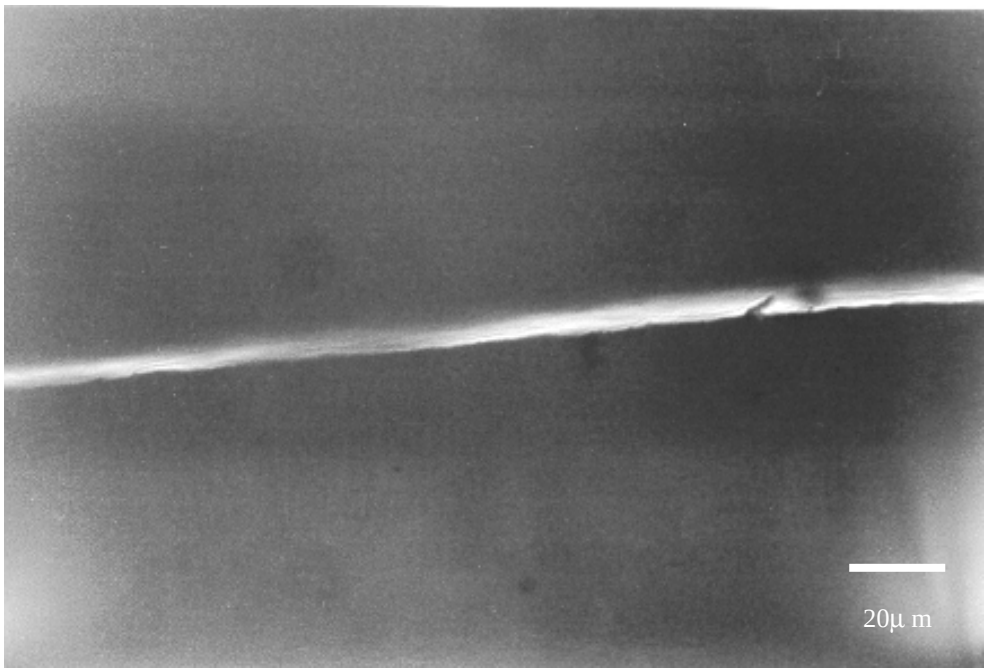

Figure 7.18 Optical micrograph of a crack area of cured DGEBP-F with MTHPA

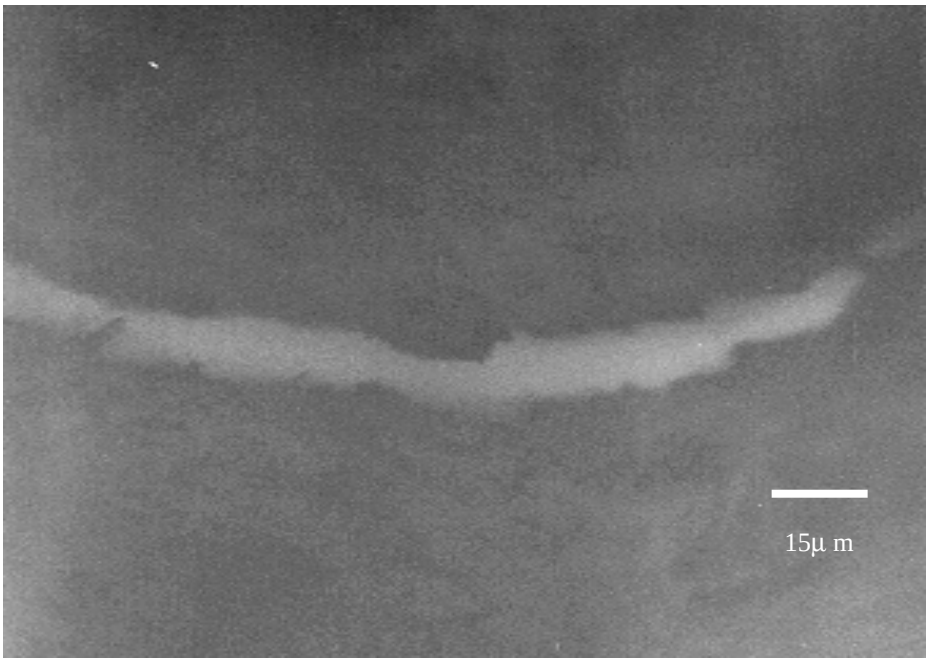

Figure 7.19 Optical micrograph of a crack area of cured 10% DGE-DHBP in DGEBP-F + MTHPA

6) Concluding remarks

The presence of DGE-DHBP enhances the toughness of the blended epoxy samples without decreasing the modulus of the sample - as observed by tensile and impact tests as well as reflected in the morphology observed from SEM pictures of fracture surfaces. The maximum in the toughness index at 10 % DGE-DHBP can be explained in terms of the disruption of epoxy network packing and creation of additional free volume. As discussed before, this happens below the θ limit of the orientation of the LC phase. However, a further increase of the DGE-DHBP concentration results in local formation of structure based on the added component. Thus, it is primarily the structure perturbation of the pure component which enhances toughness at low LC concentrations.

Higher mesogenic unit length causes an improvement of modulus and impact strength. The reinforcement from mesogenic units and partial bridging from LCE is more pronounced when longer rigid units are introduced. However, the increase in strength leads to a decrease in the strain at failure. Thus, longer mesogenic units apparently increase the brittleness of the material.

The study of the mechanism of crack propagation indicates that crack deflection and crack bridging are dominant in the case of DGE-DHBP cured with DAT. There is some fibril bridging which arrests crack propagation. The main mechanism of the 10% DGE-DHBP in DGEBP-F cured with MTHPA is crack deflection and curve fracture. The curve fracture increase the surface area of crack and introduce improve in toughness. This is the effect of the mesogenic units distributed in the network

CHAPTER 8

COMPOSITES OF MODIFIED EPOXY NETWORKS

1) Introduction

Composites are an important class of engineering materials with high performance properties. Composites are materials which combine two or more materials of different properties. Commonly, a strong and stiff component called the reinforcing element is embedded into a soft component (matrix). Composites have attractive properties due to synergistic contributions of their constituents.

Polymer matrix composites (PMCs) based on glass fibers have found numerous applications in modern engineering technology. They exhibit a combination of properties of the reinforcing element and the matrix, and have high strength-to-weight ratios. High performance polymer composites are expected to play an increasing role in the aerospace industry as airframe materials because of design flexibility. Directional strength or moduli can be achieved by orienting the fibers in a desired way to resist a load. This property cannot be found in isotropic materials such as metals and unreinforced materials. Moreover, PMCs can be combined with other structural components e.g. aluminum honeycombs or plastic foams as sandwich materials.

Epoxy matrix composites have many advantages, including superior mechanical properties, heat resistance, adhesion to many substrates, corrosion resistance, ease of processability and a relatively low cost. There is a high annual consumption of epoxies

for composite applications, including aerospace and spacecraft industries and electronic packaging applications.

Service in some applications of epoxy resins is limited in spite of these positive characteristics because of their brittleness. Even though glass fiber-reinforced epoxies show good performance, an improvement in fracture resistance is highly desirable for certain applications. There has been a rapid growth in recent years in the application of commingled polypropylene + glass fiber composites because of their combination of high performance, excellent resistance to most chemicals, and relatively low prices [256-257]. Treatment of glass fiber surfaces can be beneficial.

1.1 Composites performance

Composite performance is determined by 1) fiber; 2) matrix; and 3) fiber-matrix interfacial strength [258]. We shall discuss information concerning components related to this research.

1.1.1 Glass fibers

Glass fibers are widely used as reinforcing agents for structural and electrical applications because of superior tensile strength (high strength to weight ratio), and excellent thermal and corrosion stability. Outstanding dimensional stability is a benefit for many applications. Moreover, glass fibers have high dielectric strength and low dielectric constants, what make them suitable for electronic applications.

The mechanical performance of composites depends on the combined effect of the amount of reinforcement in the system and its spatial arrangement. The arrangement of fibers in the composite can be a continuous filament or a woven fabric, depending on

the applications. The relationship of composite strength to the fiber volume is presented in Figure 8.1. The strength is the highest in the case of a unidirectional arrangement where the glass loading ranges from 45 to 90 % by weight. The strength of bidirectional arrangement, for example woven fabrics, is in the middle range. The glass loading in this case is around 55 to 75 % by weight. Glass loading in a random arrangement is in the low range of 15 to 50 % by weight and leads to low strength [259]. The main applications of roving glass fiber is for pipes, rocket motor cases, and automobile bodies. Such materials can be processed by pultrusion, filament winding, and as continuous panels. Woven fabrics are typically used for aircraft structures, ordnance hardware, and tubing. Widely used processing methods include hand lay-up, and autoclave procedures.

1.1.2 Curing agents

Anhydride curing agents are widely used in laminates and casting applications since they are characterized by high ductility, excellent adhesion, and long pot life. Low viscosity epoxy resins with anhydride curing agents provide performance suitable for composites. Such curing agents have good mechanical properties and low shrinkage. Thus, the kinetics of curing by anhydrides is of interest for industrial applications. Amine bases are normally used as promoters for anhydride curing systems.

1.1.3 Interfacial bonding

Sufficient interface bonding is required to ensure effective load transmission from the matrix to the reinforcing phase. In case of weak adhesion or weakening from environment, the stress cannot be effectively transferred from fiber to fiber so the reinforcing action is not enabled. Many reinforcements are treated with coupling agents

to enhance the bonding. Typically, the coupling agents have dual functionalities that can bond both with the surface of the reinforcement and with the matrix [260].

The mechanisms which play an important role in fiber-matrix bonding include: 1) adsorption and wetting, 2) interdiffusion; 3) electrostatic attraction; 4) chemical bonding; and 5) mechanical adhesion [261].

1.1.3.1 Adsorption and wetting. The surface energies (γ) of components make their contributions mainly by van der Waals forces and affect wetting between the surfaces of the fibers and the resin. Wetting is strongly favored in cases of high surface energies and low interfacial energies. To obtain sufficient wetting, the surface energy of the fiber should be higher than that of the resin. For example, an epoxy resin (with $\gamma = 43$ mJ m^{-2}) can wet glass fiber (with $\gamma = 560$ mJ m^{-2}) easily, while this does not happen in the case of polyethylene fiber ($\gamma = 31$ mJ m^{-2}).

1.1.3.2 Interdiffusion and chemical reactions. Diffusion of molecules between the fibers and the matrix surface can enhance the adhesion between them. Many types of interdiffusion can promote adhesion of the interfaces including the diffusion of free chain ends. Entanglements of long chains can increase adhesive strength. Furthermore, the interdiffusion can lead to chemical reactions. The covalent bonds formed between the surfaces of fiber and matrix are strong and can enhance the adhesion. Carbon fibers can easily have surface reactions with organic groups, especially when the basal plane is exposed to resin.

1.1.3.3 Electrostatic attractions. The electrostatic charge difference between the fibers and matrix affect the interfacial bonding. This attraction is widely found for glass

fibers treated with silane coupling agents. The surface might be anionic or cationic, depending on the oxide in the glass and the pH of the aqueous solution. However, in some cases, electrostatic attraction is not the major adhesive bond in composites. The attraction can be reduced by using a polar solvent.

1.1.3.4 Mechanical adhesion. The interlock as the result of surface roughness can enhance fiber-matrix interconnections in the case of good wetting conditions. This effect is dominant in shear loading in contrast to tensile loading.

1.1.3.5 Residual stress. There are many sources of residual stress including: matrix deformation and phase transformation. The curing process of epoxy resins causes volume changes and creates residual stress. One of the widely found causes is thermal contraction during the cooling process. Normally, the fibers have lower thermal expansivity than the matrix. The stresses create compression in the fibers but tension in the matrix. Thus, the matrix contracts onto the fibers and compresses them.

1.2 Failure mechanism of composites

The failure mechanisms of PMCs are complicated and usually involve fiber breakage, fiber pull-out, matrix microcracking, or fiber-matrix interfacial failure. The type of damage and its growth depends on the type of the fiber, the matrix used and the processing procedure. After the initial failure mechanisms occur, they will propagate and cause catastrophic failure. Figure 8.2 shows examples of failure mechanisms of unidirectional reinforced composites.

1.3 Composite toughening

Although epoxy + glass fiber composite materials have high stiffness and high strength, they are brittle and show poor resistance to fracture. Therefore, researchers try to find effective methods to improve the fracture resistance and toughness of these composites, especially in applications in which one always encounters high loads and catastrophic failure might occur. Improvement of fracture toughness of epoxy resins through rubber or thermoplastic polymer additions has not translated directly into tougher composites. Therefore, the research in this area is still in progress.

2. Effect of glass fibers on curing kinetics

There are a few studies on the effect of the reinforcing component on epoxy curing kinetics. Mijovic [262] studied the effect of glass microspheres on curing kinetics of epoxies. Opalicki et al. [263] studied the effect of carbon fibers on epoxy curing kinetics. They found that the presence of reinforcing agents had a small effect on the kinetics.

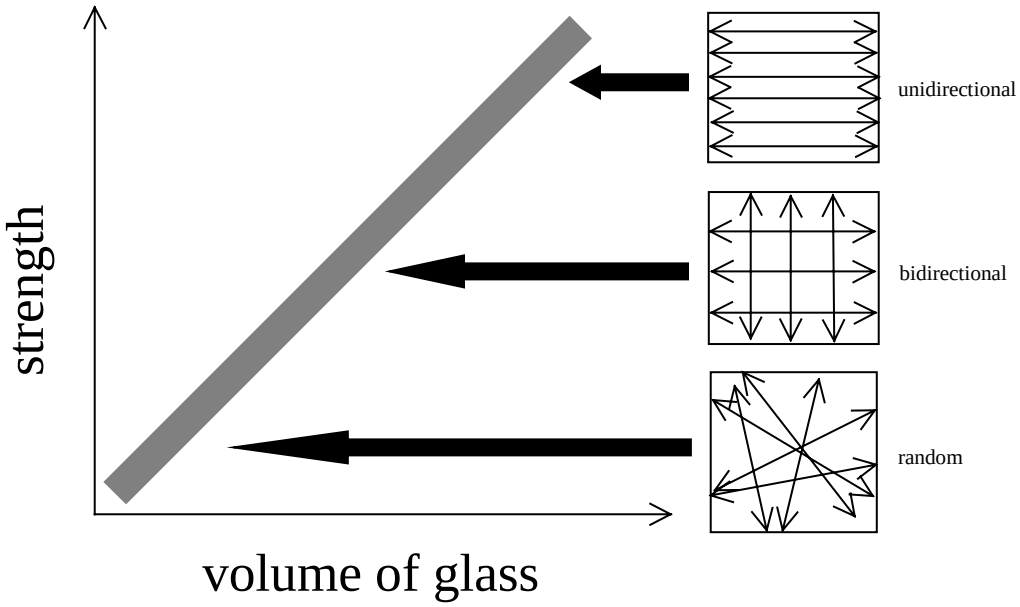

Figure 8.1 The relationship of the strength of composites to the arrangement of the reinforcement

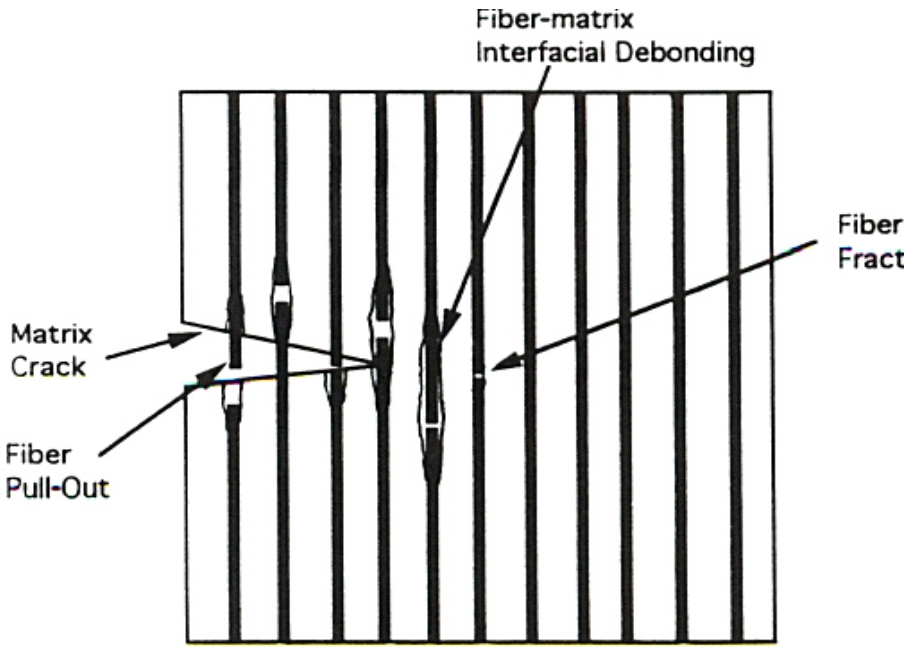

Figure 8.2 Modes of failure mechanisms of unidirectional reinforced composites.

3.1 Materials

The epoxy used in this study is a low viscosity diglycidyl ether of bisphenol F (DGEBP-F). The low viscosity epoxy is well suited for impregnation of the fibers - which should result in enhanced adhesion. The LCE which was chosen for blending with DGEBP-F is DGE-DHBP. Methyltetrahydro-phthalic anhydride (MTHPA) pre-catalyzed by benzyl triethyl ammonium chloride (BTEAC) is the curing agent.

Three sets of experiments were performed and compared: neat resin, aminosilane-treated plain weave glass fiber (GF) (Twintex woven roving 324-3B), and the hybrid maleated polypropylene (PP) + balanced glass mat (TPP6024CNO) with 68 % by weight glass fiber; both kinds of glass fiber materials were supplied by Vetrotex CertainTeed, Wichita Falls, TX.

3.2 Calorimetric measurements

The epoxy and curing agent were mixed in the stoichiometric ratio according to the weight equivalence. Both woven glass fibers and polypropylene + glass fibers were ground and 10 % by weight added to the resin mixtures. Each 10-15 mg sample was inserted into a high pressure sealed DSC pan and kept in the refrigerator to prevent the curing reaction.

A Perkin-Elmer differential scanning calorimeter (model DSC-7, power compensated, operating on UNIX platform) was used to investigate the kinetics of curing in isothermal and dynamic experiments. The isothermal runs were made to cover the range of processing temperatures between 100 and 160^{o}C in 10^{o}C increments. The DSC sample chamber was allowed to equilibrate at each isothermal temperature for 5 minutes.

Then each sample was introduced into the sample holder. The data acquisition was started after the temperature reached equilibrium. The sample was run for an extent of time and then quenched to 20^{o}C. The second scan was run from 20 to 250^{o}C at the heating rate of 10 K/min to detect the glass transition temperature (T_g) and determine residual heat.

The nonisothermal experiments were conducted from 20 to 250^{o}C at several heating rates, namely 1.5, 2.5, 5, 10, and 20 K/min. Nitrogen was used as the carrier gas with a flow rate of 1.3 kPa/min. High purity indium was used to calibrate the DSC before performing the experiments.

3.3 Mechanical Testing

3.3.1 Sample Preparation

3.3.1.1 Compression samples

Pure components of DGEBP-F and blends of 5, 10, 20, 30 and 50 % of DGE-DHBP by weight were prepared as matrices for GF samples. The synthesized DGE-DHBP was dried and ground with a mortar. Both epoxies were mixed in the proportions indicated and cured simultaneously with MTHPA.

Composites were prepared using six layers of woven fibers by hand lay-up techniques. The woven fibers were wet with the matrix and cured in an aluminum mold under 2500 Pa pressure in a vacuum oven. The cure schedule for both neat resin and GF sample was 120^{o}C for 2 hours, and then 170^{o}C for 1 hour under vacuum The percentage of fibers in the composites was in the range from 60 to 65 %. Plaques obtained were cut

into strips and polished for each testing. All samples prepared for tensile, impact and four-point bending tests were obtained using the same cure schedule.

3.3.1.2 Pultrusion samples

Pultrusion samples were prepared by pultruding 28 strands of glass fibers through a resin bath with the pulling speed of 26.67 cm/min. Prior to pultrusion the liquid crystalline epoxy was blended into the non-LC epoxy. The resin was mixed at 2500 rpm speed with the temperature of the heating zone set at 227 ^{o}C. Figure 8.3 is the schematic of the pultrusion process. The amount of glass fibers in the pultruded samples is in the range of 85-87 % as determined by thermogravimetric analysis (TGA).

3.3.2 Tensile tests

Tensile measurements on reinforced samples were made to compare moduli and mechanical performance. Tensile tests were performed with a MTS testing machine with the 20,000 lb load cell with 5 mm/min. crosshead speed. The composite samples were prepared according to ASTM D3039-95a with the dimensions of width (w) x length (l) x depth (d) = 25 x 100 x 4.8 mm.

3.3.3 Four point bending tests

Four-point bending tests were performed on a MTS testing machine according to ASTM D790-96a. The sample dimension of width (w) x length (l) x depth (d) = 12 x 100 x 4.8 mm. The force was applied with the position according to the l/d ratio of 16/1. The rate of cross-head speed used was 2.2 mm/min.

3.3.4 Impact tests

Impact testing was performed with a Dynatup Impact Tester with a 200 lb weight. Composite coupons were used for Izod tests. Samples, each with the dimension 60 x 12 x 4 mm^3, were prepared according to the ASTM D5941-96 standard for neat resins. The 1.2 mm sharp notch on each sample was precisely cut as an initiator point and the crack generated by a fresh razor blade cut across the notch root. Unnotched glass fiber reinforced samples were prepared following ASTM D4812-93.

3.3.5 End notch flexure tests

The most common failure in laminated composites is interlaminar fracture or delamination. The interlaminar fracture toughness of composites in the shear mode was determined by end notch flexure (ENF) tests. The ENF geometry can produce pure shear loading at the delamination crack tip. Interlaminar fracture toughness in mode II was measured as a function of concentration of DGE-DHBP. Samples with dimensions of 25 x 120 x 4 mm with Al foil as the crack starter at mid plane were prepared. The starter crack length (a) was 25 mm. The schematic of the sample for ENF is shown in Figure 8.4.

Based on the beam theory and the notation in Figure 8.5, displacement at the central loading point δ is obtained as follows [264-265]:

$$\delta = \frac{\Delta_{AB} + \Delta_{BC} + \Delta_{CD}}{2} \tag{8-1}$$

The elastic compliance C which is defined as the displacement δ divided by applied load P is

$$C = \frac{2L^3 + 3a^3}{8E_f Wh^3} \tag{8-2}$$

where L is the half-span length, a is crack length, E_f is flexural modulus, W is the width of the specimen, and h is half of the thickness of the composite.

The strain energy release rate of ENF is defined as:

$$G = \frac{P^2}{2W}\frac{dC}{da} \tag{8-3}$$

The critical strain energy release rate can be derived as:

$$G_{IIC} = \frac{9a^2P^2}{16E_f W^2 h^3} = \frac{9P^2Ca^2}{2W(2L^3 + 3a^3)} \tag{8-4}$$

3.3.6 Scanning Electron Microscopy

The fracture surfaces, after tensile tests on the pultrusion samples, were observed using a JEOL scanning electron microscope (SEM). Fracture samples for each composition were cut to 2 mm. Each sample was mounted on a sample holder, using an electrically conductive paint as an adhesive, and coated with a thin layer of gold by sputtering.

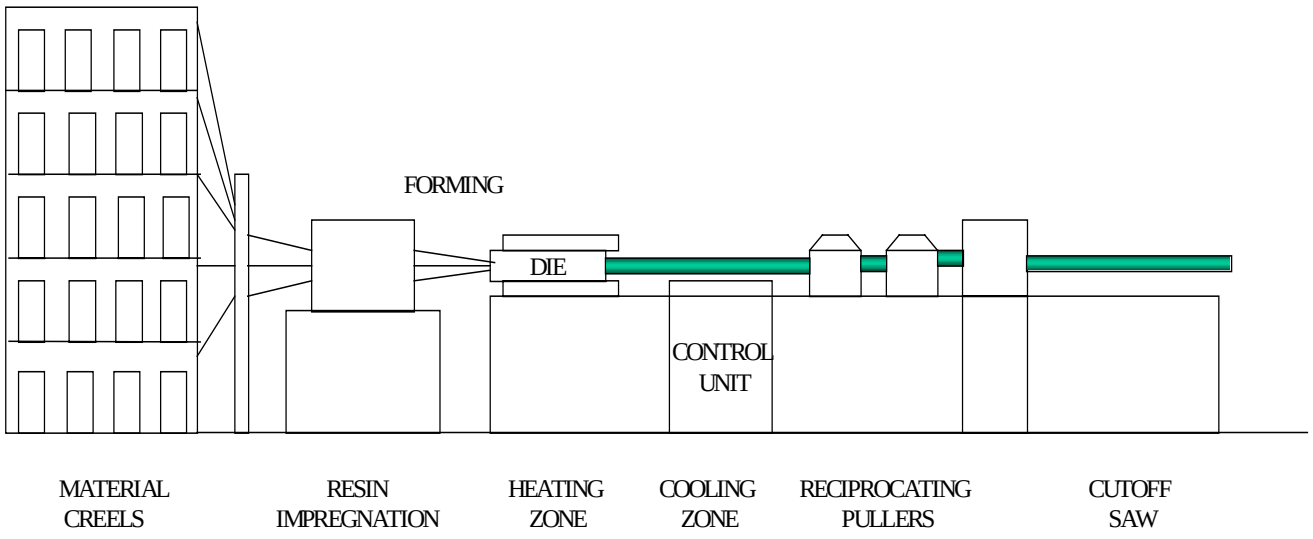

Figure 8.3 Schematic of pultrusion processing

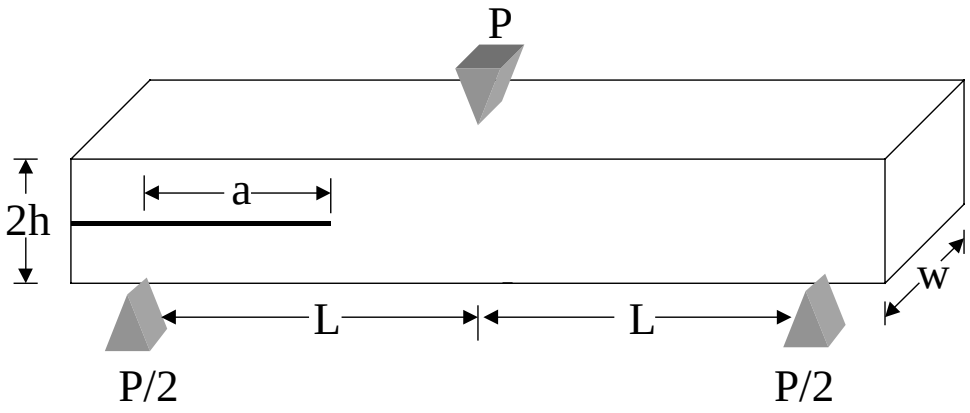

Figure 8.4 Configuration of test specimens for end notch flexural testing

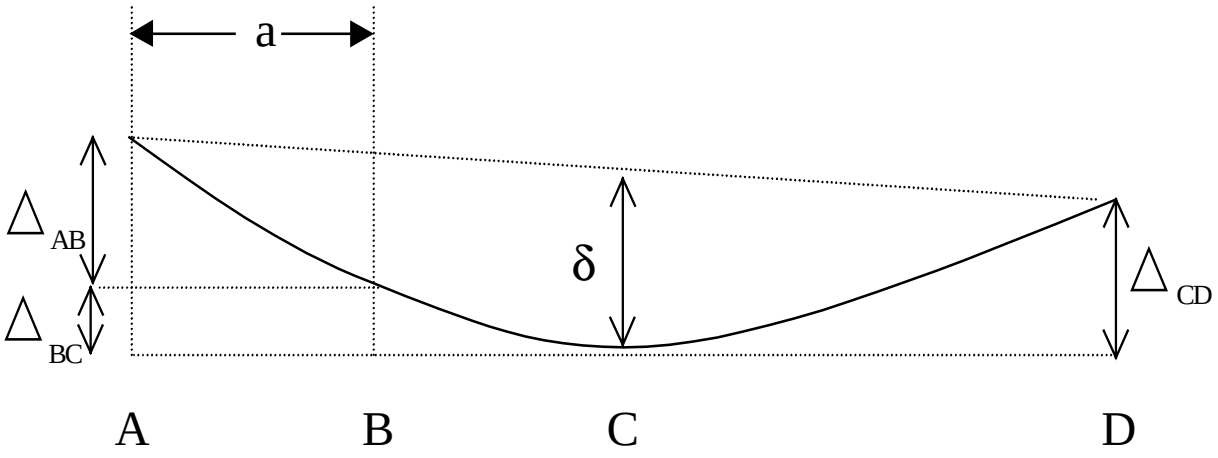

Figure 8.5 Configuration of ENF samples used in the calculation of displacement

4. Results

4. 1 Isothermal and non-isothermal calorimetric results

Results of several isothermal DSC runs performed on DGEBP-F and MTHPA are shown in Chapter 5. Figures 8.6 and 8.7 show respectively exotherms for the system with glass fibers, and the PP + glass fiber system. As already noted in Chapter 5, the heat released during cure is assumed to be directly proportional to the rate of reaction and so one obtains the reaction rate as a function of time for our three systems. All thermograms show autocatalytic kinetic behavior starting from a nonzero initial reaction rate.

The kinetic parameters, m, n, and k_2 were determined using the nonlinear least square regression technique of Marquardt [266]. The maximum isothermal reaction rate α_P and the reaction time t_p required to attain the maximum rate have been calculated as a function of temperature.

Figure 8.8 exhibits the comparison of k_1 and k_2 for the neat resin, the glass fibers and the PP + glass fiber systems. Compared to the neat resin, the presence of glass fibers and of PP + glass fibers affects k_1 only slightly. As for k_2, the neat resin and the resin + PP commingled with glass fibers exhibit quite similar values and practically the same temperature dependence. By contrast, glass fibers increase k_2 values significantly. This indicates that the maleated PP serves to decrease k_2.

An increase in the α_p and t_p parameters for the maleated PP hybrid fibers is also observed, as shown in Figure 8.9. The time required to cure the neat resin to achieve the maximum reaction rate is higher than for glass-fiber-reinforced systems; the difference increases with the temperature increase.

The overall reaction order is in the range between 2.4-2.5 and is in agreement with the study by Montserrat and coworkers [267]. They studied curing kinetics of diglycidyl ether of bisphenol A (DGEBP-A) with methytetrahydrophthalic anhydride (MTHPA). Our reaction order is 1.4 with respect to the unreacted functional groups (n) while it is 1 with respect to the reacted functional groups (m).

Table 8.1 shows kinetic parameters for the three systems. The activation energy for curing is obtained from the Arrhenius relationship. From the autocatalytic model, one obtains two activation energies which pertain to the uncatalyzed and catalyzed curing reactions. As expected from the results displayed in Figure 8.9, the activation energy of the glass fiber reinforced system is lower than for the other two systems.

The reaction rates $d\alpha/dt$ for the three systems, for each system at several temperatures, experimental and those calculated from the autocatalytic kinetic model, are shown in Figures 8.10 and 8.11. The maximum reaction rate is usually found between 20 – 40 % conversion. The model chosen shows a good fit to the data in the middle stage of reaction up to about $\alpha = 0.8$ conversion. Deviations are observed near the vitrification point since the diffusion effect dominates the reaction at higher percentages of conversion. At low conversion stages, up to $\alpha \approx 0.25$, we also observe deviations from the autocatalytic model, especially for the glass fiber reinforced system.

The activation energies of curing, obtained from the Kissinger and Osawa relationship for all three systems, are compared in Table 8.2. Some differences between the activation energies E_a calculated for different systems are seen. E_a obtained from the

glass fiber reinforced system is lower than for the neat resin while E_a obtained for the PP + glass fiber reinforced system is higher than for the neat resin system.

From isothermal results, E_{a2} obtained from k_2 represents the activation energy for the catalyzed reaction mechanism, while E_{a1} corresponds to the uncatalyzed reaction. Both energies show the same trend, namely the lowest values for the glass fiber containing system, intermediate values for the neat resin, and the highest values for the PP-containing system. We noted differences in numerical values between the two methods as well as the fact that parameters from *isothermal* experiments differentiate better the materials from one another.

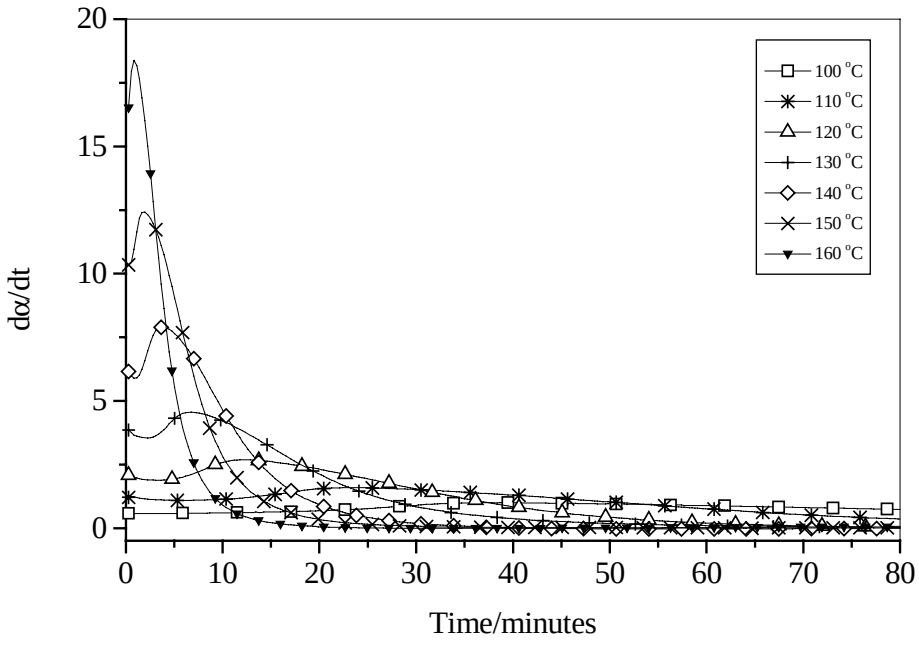

Figure 8.6 Rates of cure as a function of time for the glass-fiber reinforced system for several temperatures

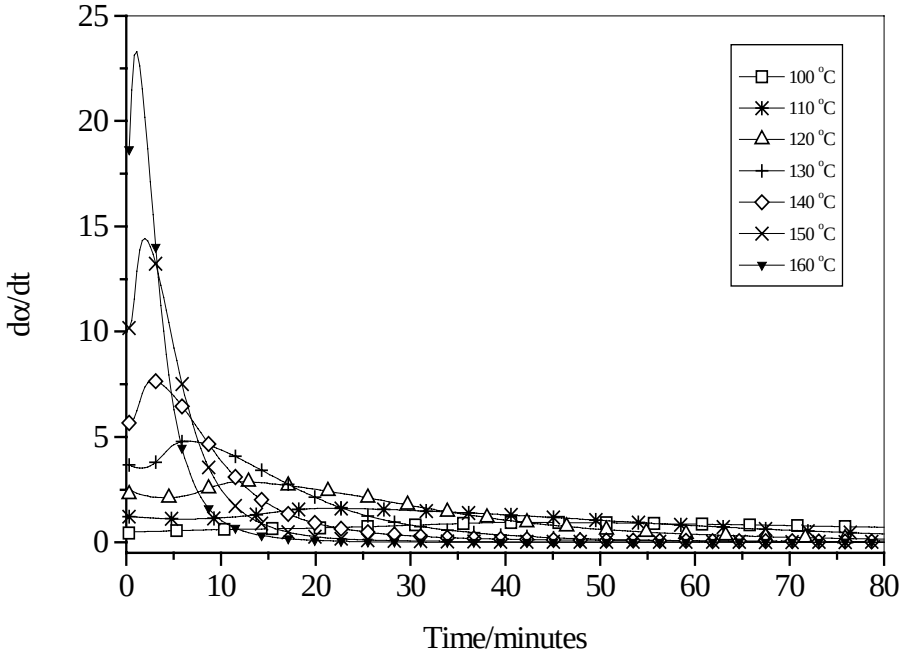

Figure 8.7. Rates of cure as a function of time for the polypropylene + glass fiber system for several temperatures

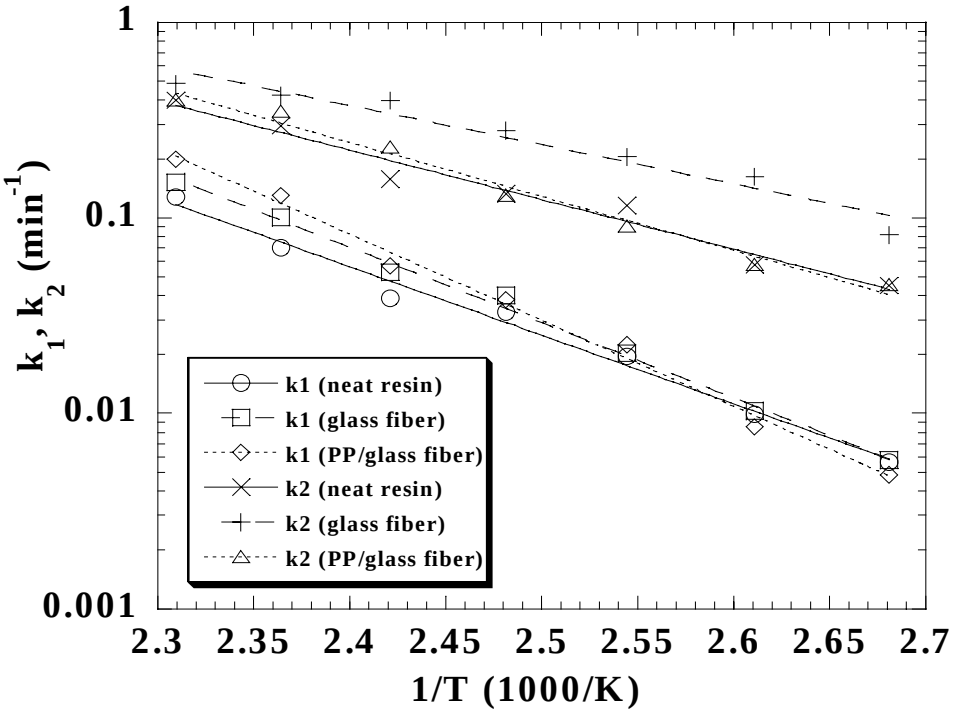

Figure 8.8 Comparison of the reaction rates in the neat resin, glass fiber reinforced, and polypropylene + glass fiber systems

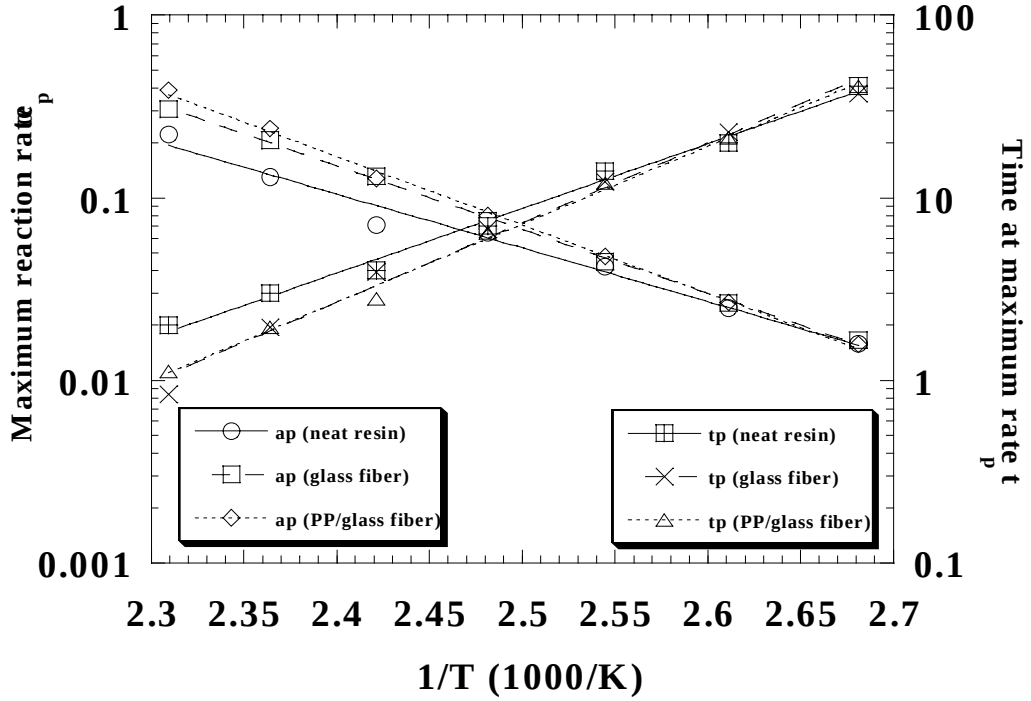

Figure 8.9 Comparison of the maximum reaction rates α_p and times at the maximum rate t_p

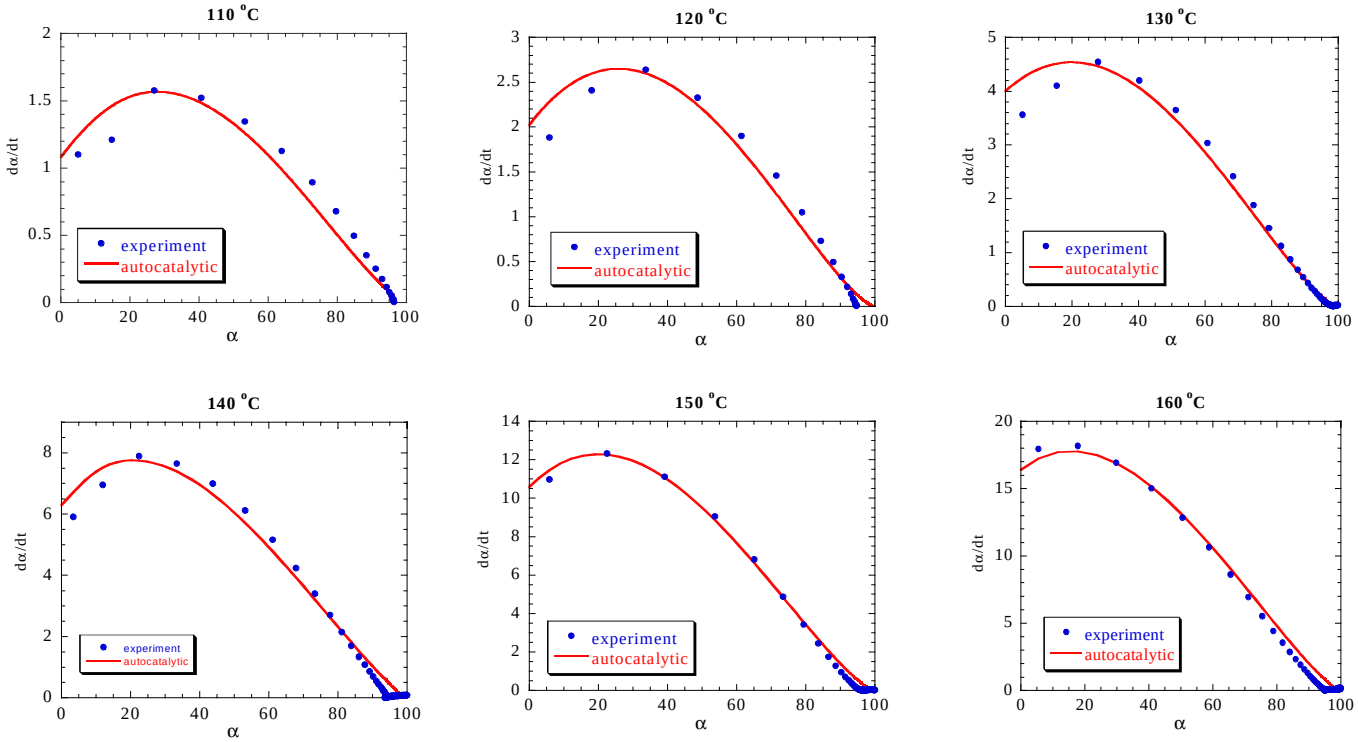

Figure 8.10 Comparison of experimental data with the autocatalytic model for DGEBP-F and MTHPA with glass fibers

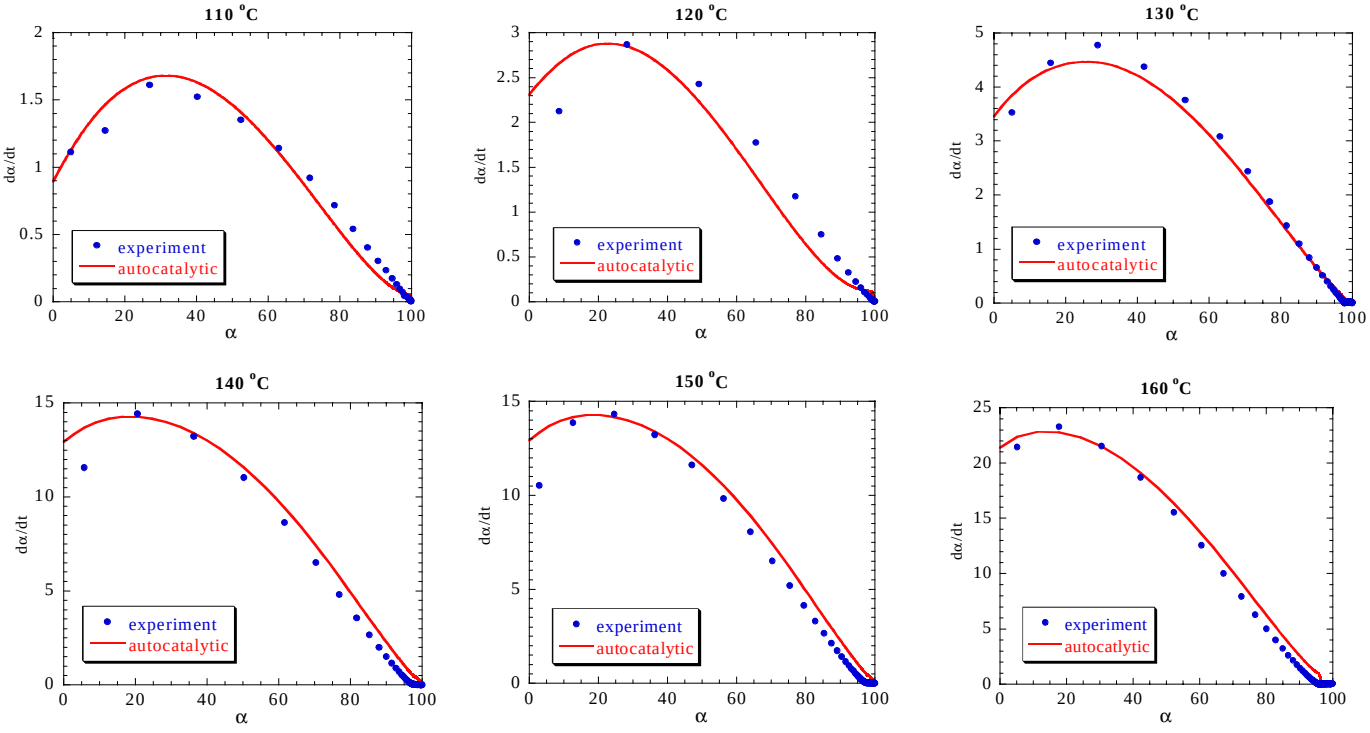

Figure 8.11 Comparison of experimental data with the autocatalytic model for DGEBP-F and MTHPA with polypropylene + glass fibers

Table 8.1: Comparison of kinetic parameters between neat resin, glass fiber and polypropylene + glass fiber reinforced systems

Kinetic Parameters	DGEBP-F+MTHPA	Neat Resin + Glass fibers	Neat Resin + PP + Glass fibers
k_1 (min^{-1})	$1.48x10^7 exp(-8.08 \times 10^7/RT)$ r = 0.9908	$1.23x10^8 exp(-8.87 \times 10^7/RT)$ r = 0.9974	$3.03x10^9 exp(-10.14 \times 10^7/RT)$ r = 0.9956
k_2 (min^{-1})	$2.63x10^5 exp(-5.83 \times 10^7/RT)$ r = 0.9871	$2.43x10^4 exp(-4.61 \times 10^7/RT)$ r = 0.9670	$1.08x10^6 exp(-6.38 \times 10^7/RT)$ r = 0.9848
α_p (min^{-1})	$1.24x10^6 exp(-6.78 \times 10^7/RT)$ r = 0.9850	$3.58x10^7 exp(-8.04 \times 10^7/RT)$ r = 0.9992	$1.69x10^8 exp(-8.64 \times 10^7/RT)$ r = 0.9986
t_p (min)	$1.20x10^{-8} exp(8.16 \times 10^7/RT)$ r = 0.9962	$9.49x10^{-11} exp(10.03 \times 10^7/RT)$ r = 0.9922	$1.54x10^{-10} exp(9.83 \times 10^7/RT)$ r = 0.9992
$m_{avg.}$	1.103	1.144	1.003
$n_{avg.}$	1.311	1.422	1.429
Ea_1	67 kJ/mol	74 kJ/mol	84 kJ/mol
Ea_2	48 kJ/mol	38 kJ/mol	53 kJ/mol

- J/kg•mol

Table 8.2: Nonisothermal data at several heating rates for the neat resin, resin + glass fiber, and resin + polypropylene + glass fibers systems

Heating rate (K/min.)	Peak temperature (K)		
	DGEBP-F + MTHPA	Resin + Glass fibers	Resin + PP + Glass fibers
1.5	409	409	409
2.5	419	418	419
5	433	432	429
10	447	447	446
20	464	464	463
E_a (Kissinger method)	68.2 kJ/mol	66.9 kJ/mol	68.6 kJ/mol
E_a (Ozawa method)	71.2 kJ/mol	70.5 kJ/mol	72.1 kJ/mol

4.2. Mechanical Testing

4.3.1 Comparison of effect of glass fiber and polypropylene/glass fiber

Results of tensile measurements for neat resins and reinforced samples are shown in Table 8.3. Modulus, tensile strength and failure strain are compared. Tensile properties of the epoxy resin are highly improved by glass fiber reinforcement - as expected. We note an 18 times higher elastic modulus and a fourfold increase in tensile strength. A slight decrease is observed in the strain at failure of the reinforced system compared to that of the neat resin. In turn, compare now the GF system to the GF + PP system. The former seems to have better mechanical properties. However, these values are not comparable since the amount of GF in the GF + PP system is 32 % lower than in the GF mat. Therefore, normalized mechanical values with respect to the normalized density of resin and concentration of glass fibers in the sample are shown in Table 8.4. Modulus values for the GF + PP system are comparable to the GF system. The tensile strength of the GF + PP system is lower than that for the pure GF system. The effect of PP is to increase the failure strain compared to the neat resin and GF systems. This improvement is related to the yielding behavior of PP. The GF + PP composites have a 42 % higher failure strain than GF composites.

Impact measurement results are presented in Table 8.3. The impact strength of the GF-reinforced composite is almost 400 times higher than for the neat resin. The normalized impact strength of the PP + GF samples are about 4 % higher than those of the GF system. (see Table 8.4)

Table 8.3: Comparison of mechanical properties between neat resin, glass fiber and polypropylene + glass fiber systems.

system	Modulus (GPa)	Tensile strength (MPa)	Failure strain (%)	Impact strength (kJ/m^2)
Neat resin	2.51 ± 0.21	59.5 ± 6.6	3.12 ± 0.82	0.83 ± 0.11
Epoxy + woven glass mat	47.3 ± 4.5	256 ± 17.4	2.78 ± 0.14	346.6 ± 19.7
Epoxy + balanced PP + GF mat	34.6 ± 4.2	171 ± 9.3	2.90 ± 0.11	263.2 ± 17.8

Table 8.4: Comparison of ratio of mechanical properties to normalized density between neat resin, glass fiber and polypropylene + glass fiber systems.

System	Normalized density, ρ (g/cm^3)	Modulus/ρ ($GPa/g{\cdot}cm^{-3}$)	Tensile strength/ρ ($MPa/g{\cdot}cm^{-3}$)	Failure strain/ρ ($\%/g{\cdot}cm^{-3}$)	Impact strength/ρ ($kJ{\cdot}m^{-2}/g{\cdot}cm^{-3}$)
Neat resin	1.25	2.01 ± 0.17	47.6 ± 5.28	2.50 ± 0.66	0.66 ± 0.09
Epoxy + woven glass	1.84	25.7 ± 2.45	139 ± 9.46	1.51 ± 0.08	188.4 ± 10.7
Epoxy + balanced PP	1.35	25.7 ± 3.12	127 ± 6.9	2.15 ± 0.08	195.4 ± 13.2

4.3.2 Effect of LCE concentration on the composites performance

4.3.2.1 Compression samples

In chapter 7, the tensile properties of neat resin were studied. The modulus, tensile strength, and failure strain are improved when 10-30 % of DGE-DHBP is added. However, the tensile strength and elongation at break tend to decrease as more than 30 % DGE-DHBP is added. The improvement found in the epoxy matrix is not retained in the corresponding glass fiber composites. The selected stress vs. strain relationship for 0 to 30 % DGE-DHBP for composite samples is shown in Figure 8.12. The tensile test results for the reinforced samples are shown in Table 8.5. The modulus, tensile strength and failure strain are compared. Comparing the unmodified matrix in the glass fiber system to DGE-DHBP modified sample, the latter shows lower modulus. However, an improvement is found in tensile strength. The tensile strength of the 5 % DGE-DHBP system is about 20 % higher than for the unmodified system. The increase in tensile strength is not found when more than 20 % DGE-DHBP is added.

The flexural measurement indicates that a low DGE-DHBP concentration increases flexural modulus and flexural strength. Figure 8.13 shows the comparison of load vs. displacement curves for flexural tests as a function of the DGE-DHBP concentration. The four-point bending results, as a function of DGE-DHBP concentration, are shown in Figure 8.14. The flexural modulus and rupture strength are improved when less than 10 % DGE-DHBP is used in the modified matrix. The flexural strength increases by 16 % when 5 % DGE-DHBP is added to the matrix. The flexural modulus of the 5 % DGE-DHBP system is about 14 % higher than that of 0% DGE-

DHBP. Moreover, the samples from the modified matrix exhibit non-catastrophic failure instead of the catastrophic failure found for the non-modified sample. The yielding behavior of load is found after the major break for all modified matrix samples.

Impact test results are presented in Table 8.6. The impact strength of the GF-reinforced composite show the same trend as the result for the neat resin. The impact strength increases as the DGE-DHBP concentration in the epoxy matrix increases. The peak result is found when 10 % DGE-DHBP is added to the matrix. The impact strength of the epoxy, modified with 10 % DGE-DHBP, is improved by 54 % compared with the unmodified epoxy.

Interlaminar fracture toughness in the mode II was measured as a function of the concentration of DGE-DHBP. The load-displacement curve for ENF, as a function of DGE-DHBP, is shown in Figure 8.16. As expected, there is a linear increase of load vs. displacement up to the non-linear load point (P_{NL}). The nonlinear elastic behavior is found for all compositions from point P_{NL} to P_{max} (maximum load). The unstable crack growth occurs after the maximum load point.

The comparison of load-displacement, as a function of the DGE-DHBP concentration, is presented in Figure 8.17. The highest performance is observed when 5 % DGE-DHBP is added to modify the matrix. The relationship of interlaminar fracture energies (G_{IIC}) of the composite, as a function of the DGE-DHBP concentration, is shown in Table 8.7. The fracture energy, at the onset of non-linear crack growth ($G_{IIC}(NL)$), increases from 1.03 kJ/m^2 for unmodified system to 1.66kJ/m^2 for 5% DGE-DHBP. The value of G_{IIC} at the maximum load was calculated. The $G_{IIC}(max)$ increased from 1.16

kJ/m^2 for modified resin to 2.06 kJ/m^2 for the 5 % DGE-DHBP modified sample. This value of G_{IIC}(NL) is suitable for industrial applications.

4.3.2.2 Pultruded samples

The modified matrix for glass fiber composites shows a dominant improvement in impact strength that found in both pultrusion and compression samples. However, the pultrusion samples show overall higher tensile, flexural and impact strength compared with the compression molded samples. The strength of composites is related to the amount of glass fibers in the system and arrangement of glass fibers. The strength of composites increases directly in relation to the amount of glass fiber. There is almost 87 % fiber weight fraction in the pultrusion samples while the fraction of glass fibers in compression samples is about 55 %. The mechanical testing of pultrusion samples was performed along the fiber direction where the glass fibers support the applied load.

The tensile modulus and flexural modulus of the pultrusion samples is about 4 times higher than compression samples. The impact strength for the pultrusion samples is about 3 times higher than the compresion samples. There is 48 % increase in impact strength of 10 % DGE-DHBP for pultrusion samples compared with the unmodified system.

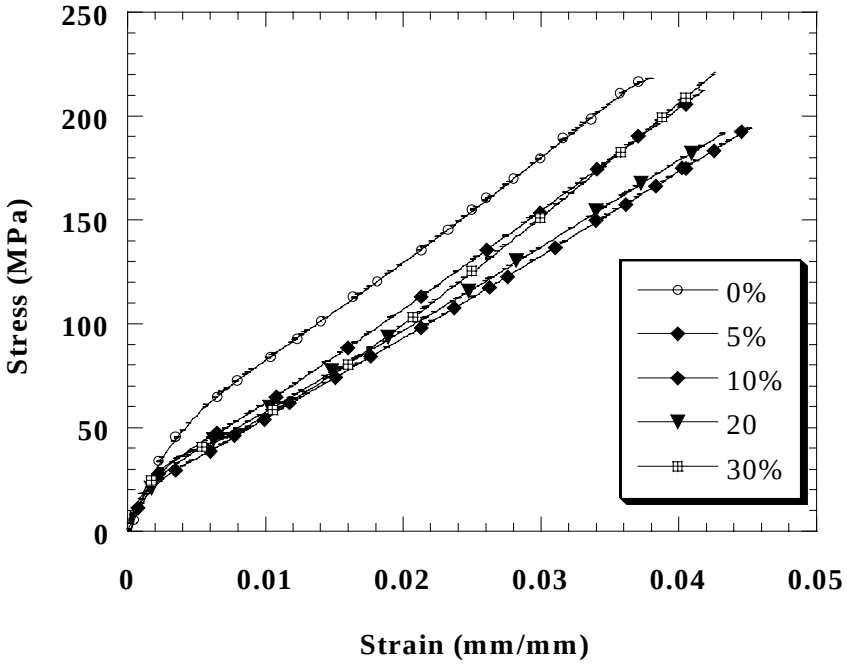

Figure 8.12 Stress vs. strain relationship as a function of DGE-DHBP concentration

Table 8.5 Comparison of tensile properties as a function of DGE-DHBP on modified composites

DGE-DHBP	Modulus (GPa)	Tensile Strength (MPa)	Failure Strain (%)
0%	8.54±0.5	219.8±21.5	6.7±0.1
5%	7.53±0.4	262.0±12.5	7.7±0.3
10%	8.05±0.8	278.7±14.4	7.3±0.4
20%	7.70±0.2	279.0±14.7	6.9±0.1
30%	7.54±0.6	215.6±11.0	7.0±0.2
50%	6.70±0.1	197.6±11.8	7.3±0.5

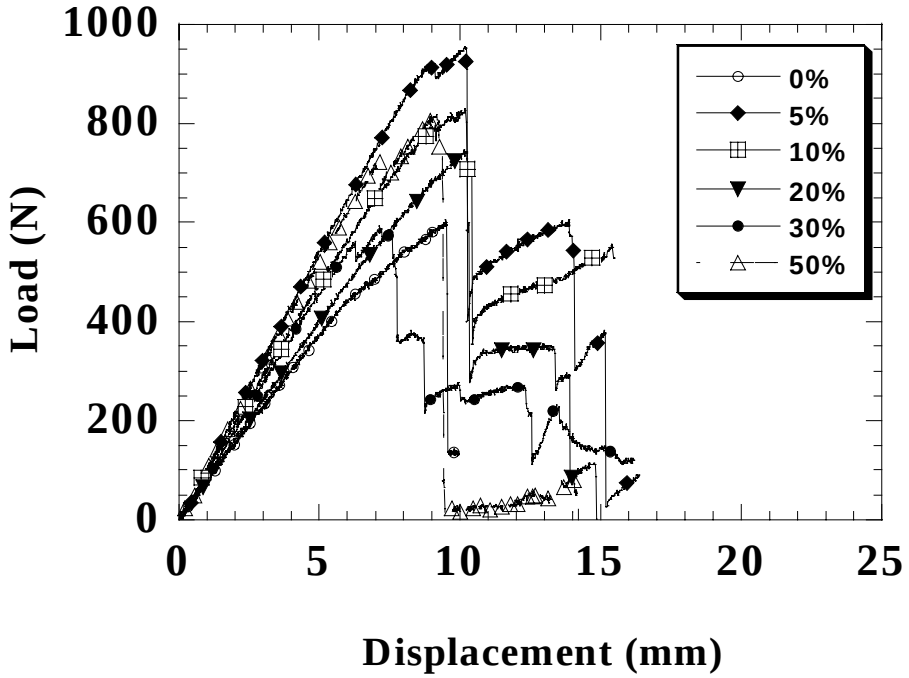

Figure 8.13 Comparison of load-displacement curves for flexural test as a function of DGE-DHBP

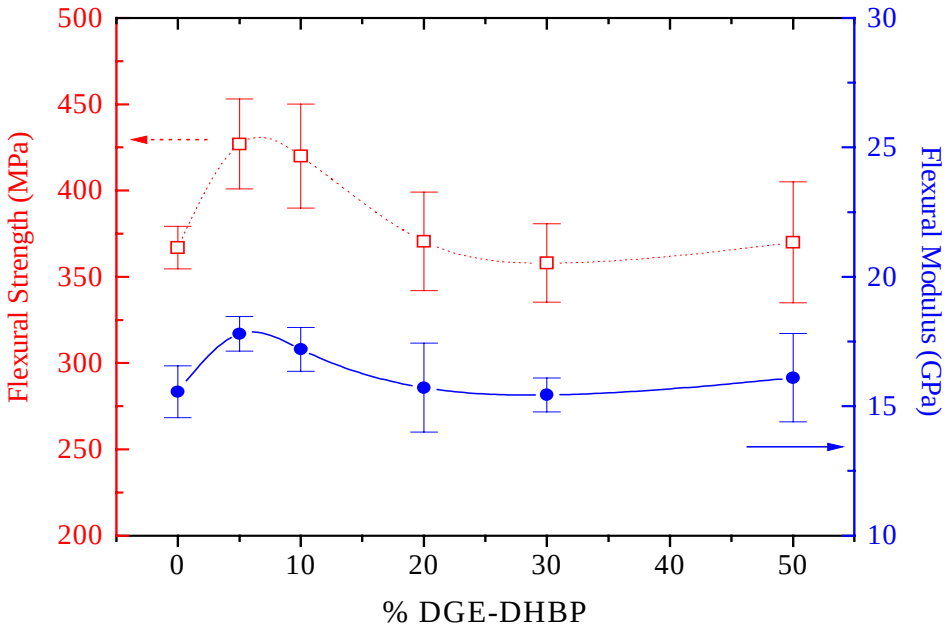

Figure 8.14 Comparison of flexural strength and flexural modulus for glass fiber containing samples as a function of DGE-DHBP concentration

Table 8.6 Comparison of impact properties as a function of DGE-DHBP

% DGE-DHBP	Impact strength (kJ/m^2)	Maximum load (kN)
0	103.9 ± 35.1	0.93+0.01
5	136.2 ± 21.3	1.09+0.08
10	160.8 ± 25.4	1.32+0.12
20	161.6 ± 12.5	1.12+0.08
30	151.9 ± 20.9	1.08+0.10

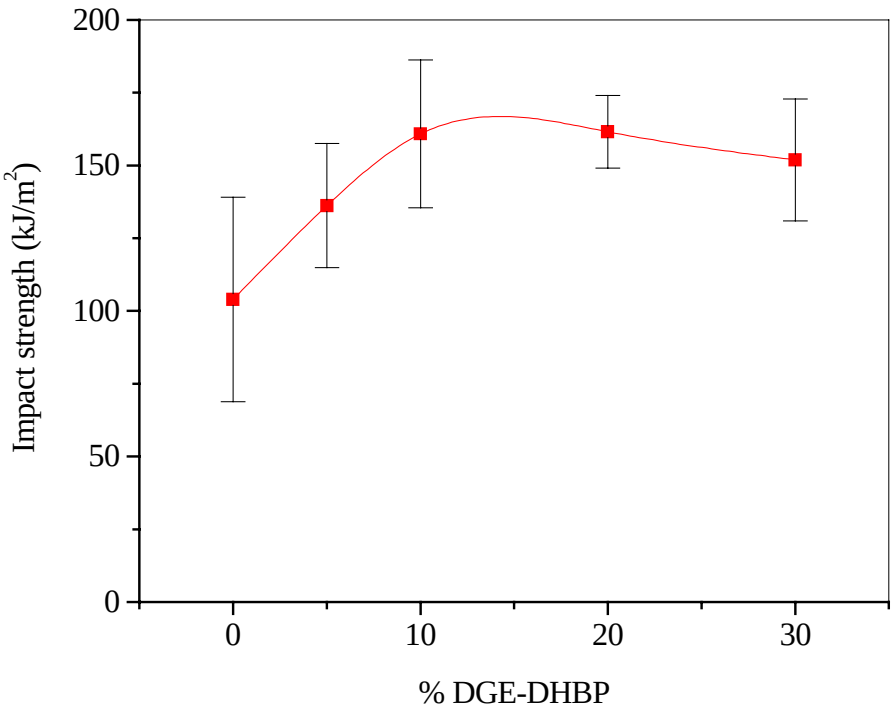

Figure 8.15 Comparison of impact strength as a function of DGE-DHBP concentration for modified composites

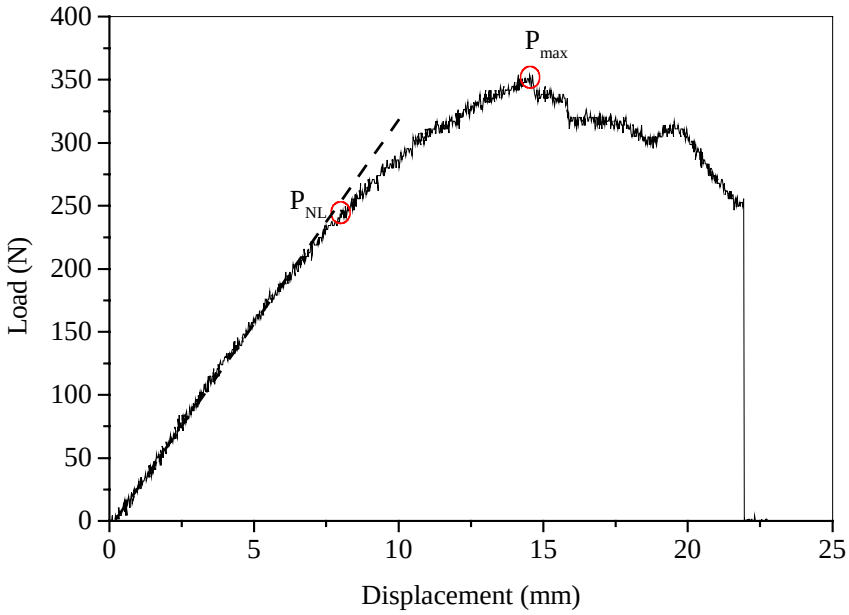

Figure 8.16 A typical load-displacement curve for the ENF fracture test

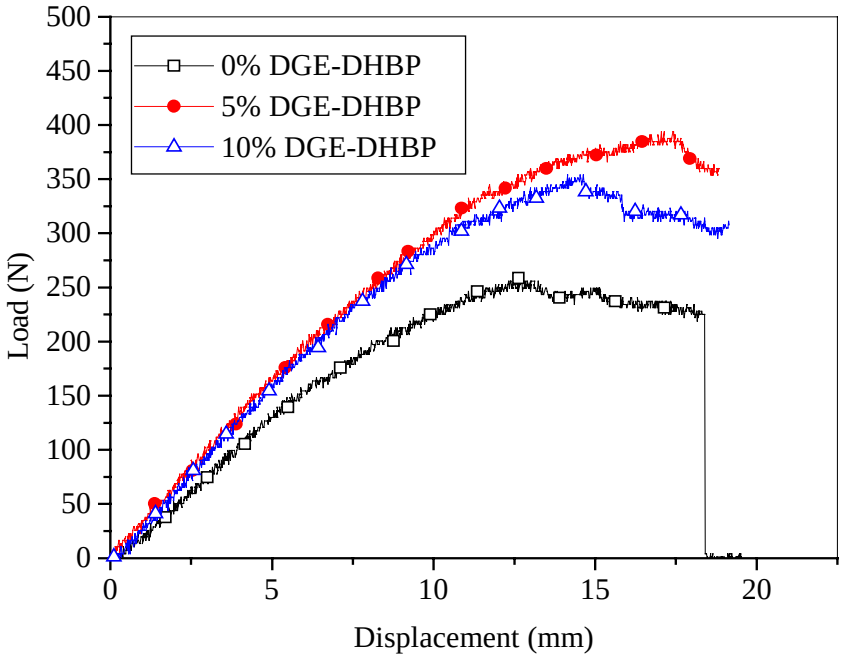

Figure 8.17 Comparison of load-displacement curves for ENF fracture tests for several concentrations

Table 8.7 Comparison of interlaminar fracture toughness at non-linear point (G_{IIC} (NL)) and at maximum load point (G_{IIC} (max)) as a function of DGE-DHBP concentration

% DGE-DHBP	G_{IIC} (NL) (kJ/m^2)	G_{IIC} (max) (kJ/m^2)
0	1.03±0.29	1.16±0.13
5	1.66±0.29	2.11±0.24
10	1.24±0.33	1.38±0.31

Table 8.8 Comparison of mechanical properties of pultrusion and laminate samples.

	Pultrusion		Laminate	
Mechanical Properties	0%DGE-DHBP	10% DGE-DHBP	0%DGE-DHBP	10% DGE-DHBP
Tensile : Modulus (GPa)	32.5±0.4	41.1±0.8	8.5±0.5	8.05±0.8
Flexural : Modulus (GPa)	67.2±2.2	66.7±2.1	15.6±1.0	17.8±0.9
Impact : Strength (kJ/m^2)	354.3±7.2	526.1±61.2	103.9±35.1	160.8.3±25.6
Fiber weight fraction	87%	87%	55%	55%

4.4. Morphologies

The SEM images of the unmodified glass fiber composites are shown in Figures 8.18 and 8.19. The images of modified glass fiber composites are shown in Figures 8.20 and 8.21. The longitudinal direction of glass fibers for the pultruded composites after tensile testing is shown. The better adhesion is found in the DGE-DHBP modified epoxy system. Better adhesion between glass fibers and the matrix is one of the important factors which can enhance the mechanical properties of composite materials. This observation explains the enhancement of mechanical properties of the DGE-DHBP modified DGEBP-F matrix.

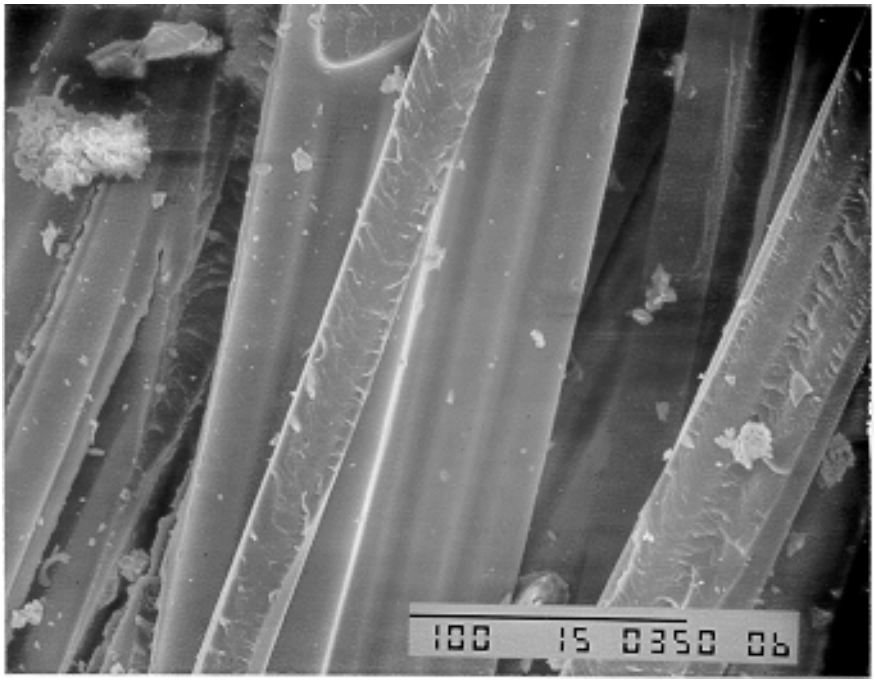

Figure 8.18 SEM micrograph of the unmodified epoxy matrix (350X)

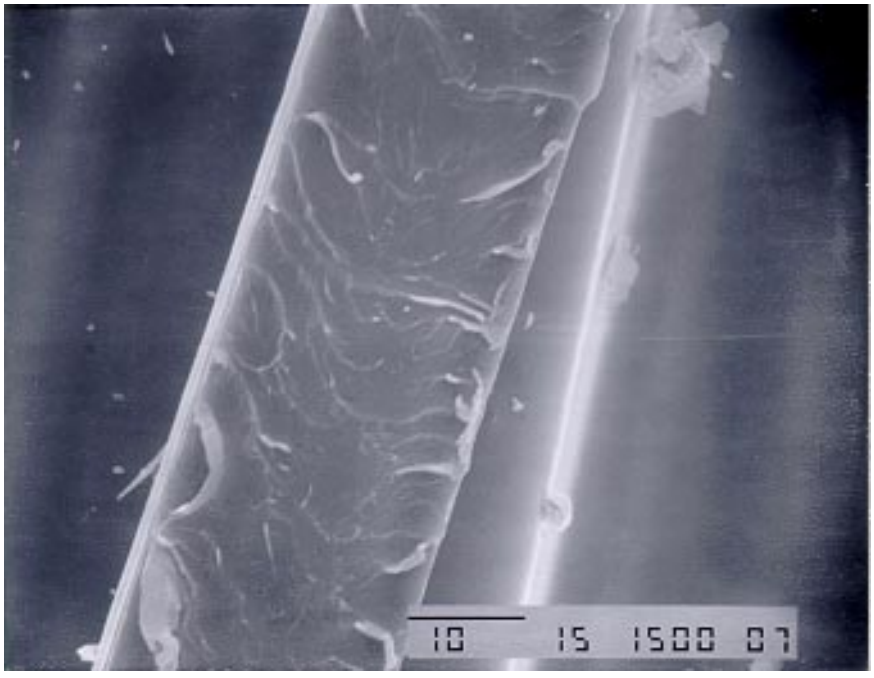

Figure 8.19 SEM micrograph of the unmodified epoxy matrix (1500X)

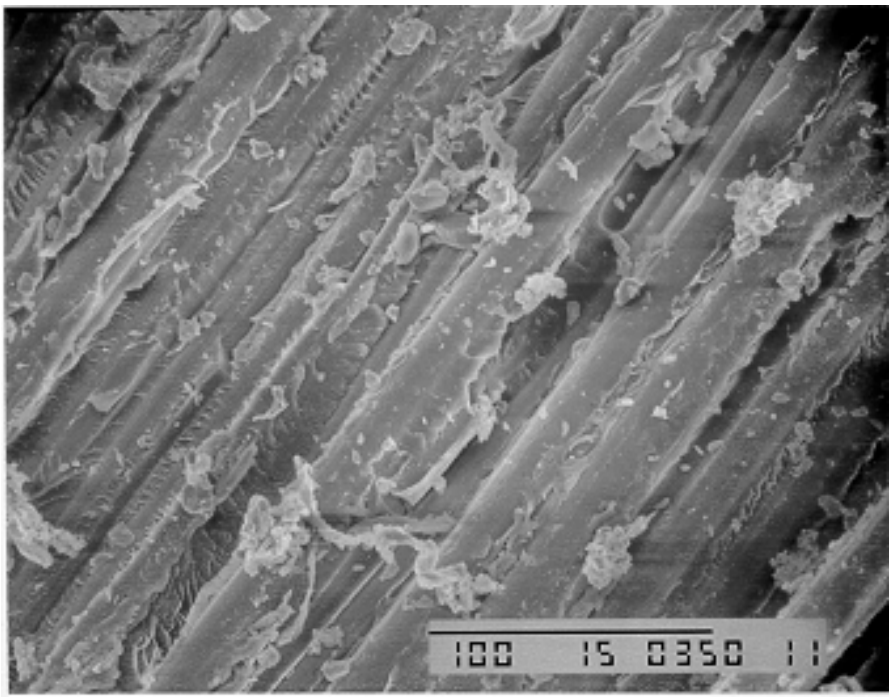

Figure 8.20 SEM micrograph of 10 % DGE-DHBP modified epoxy matrix (350X)

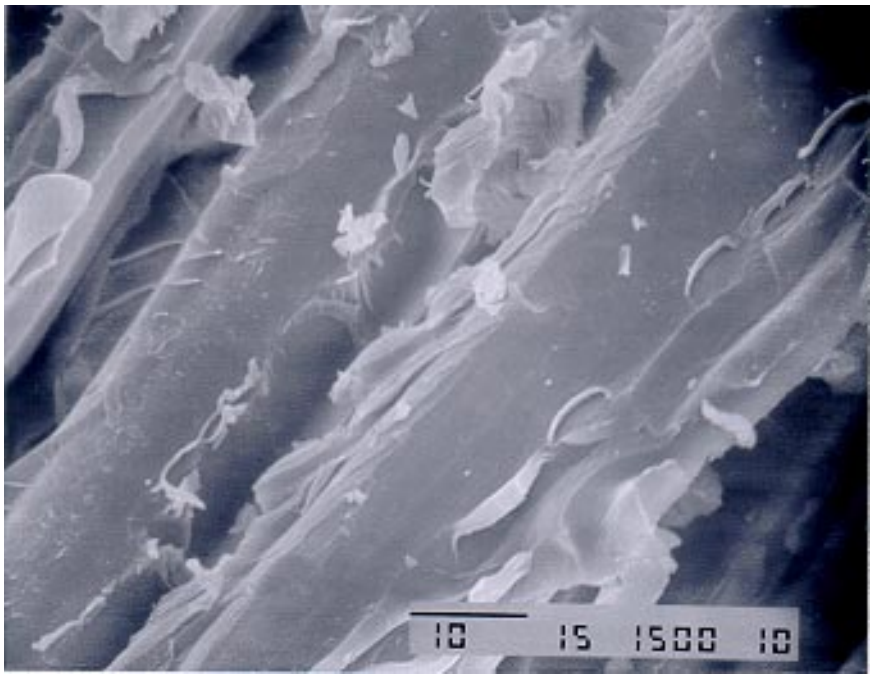

Figure 8.21 SEM micrograph of 10 % DGE-DHBP modified epoxy matrix (1500X)

5) Discussion

The kinetic parameters obtained from the isothermal DSC data show the presence of glass fibers has a certain - although not very large effect on the epoxy cure kinetics. We observed increases in reaction rates along with decreased times required to reach the maximum reaction rate. The glass fibers have been treated with an amine silane coupling agent to improve adhesion between the glass and epoxy matrix. We infer that the amine groups on the glass fiber substrate react with the glycidyl groups of the epoxy resin. However, since only low concentrations of amine silane coupling agents are used, we do not consider their effects on the curing kinetics.

The polypropylene + glass fiber component has been introduced into the thermoset system to increase flexibility - as seen from an increase in the strain to failure. The maleated PP fibers increase the time to cure and reduce the reaction rate compared to the glass system.

Mechanical performance of the hybrid polypropylene + glass fiber composites is comparable to glass fiber composites. Moreover, a significant improvement in failure strain and impact strength is observed in the case of polypropylene + balanced glass mat composites, while the density is lower than for pure glass fiber reinforced composites.

6) Conclusions

DGE-DHBP enhances toughness of the blended epoxy samples without decreasing the modulus of the samples - as observed by tensile and impact tests. Moreover, the results do not show adverse effects such as decreasing T_g. Improving the mechanical properties of epoxy resins is also found in composite material properties. The largest improvements are for low concentrations of DGE-DHBP in the DGEBP-F based systems. The improvement in modified epoxy matrices is also found in the composites – as seen in impact, flexural testing, and fracture toughness. Moreover, the samples with modified matrices indicate non-catastrophic failure, instead of the catastrophic failure seen in unmodified samples. The decrease in tensile properties observed in modified matrices also support other mechanical properties. The improvements observed in the composites are related to better adhesion between the glass fibers and the modified epoxy matrix. This is reflected in the morphology seen in the SEM micrographs of the fracture surfaces.

The dominant improvement which is found in both pultrusion and compression samples is the impact strength. However, the pultrusion samples show overall higher tensile, flexural and impact strength compared with the compression molded. The strength of composites is related to the amount of glass fibers in the system and the arrangement of glass fibers. There is about 87 % fiber weight fraction in pultrusion samples while the fraction of glass fibers in compression samples is about 55 %. The mechanical testing of pultrusion samples was performed along the fiber direction where the glass fibers strongly support the load applied.

CHAPTER 9

SUMMARY AND FUTURE WORK

Summary

1) Epoxy resins support many crucial applications in engineering technology. However, their brittleness has excluded them from certain applications. There are three popular routes to toughening epoxy resin which are the incorporation of reactive rubber particles, modification of thermoplastic polymers, and incorporation of rigid inorganic particles. The existence of rubber particles successfully improves the fracture toughness of epoxy. However, the improvement has a detrimental effect on the modulus and glass transition temperature. In case of thermoplastic toughening, the difficulty in processing was found due to the difference in viscosity of thermoset and thermoplastic.

The toughening strategy in this research is the use of liquid crystalline epoxies (LCEs). Successful toughening was achieved at low concentrations of LCEs in the reacting systems. The mesogenic units and partial bridging improve the toughness. Improvement is also found for the modulus. However, the toughness increase is smaller compared with that obtained from rubber particle modification.

2) LCEs are capable of forming LC phases during curing. Three types of LC epoxy resins are chosen include:

2.1) Digylcidyl ether of 4,4’-dihydroxybiphenol (DGE-DHBP).

2.2) Digylcidyl ether of 4-hydroxyphenyl-4”-hydroxybiphenyl-4’-carboxylate (DGE-HHC)

2.3) Digylcidyl ether of 4,4'-dihydroxy-α-methylstilbene (DGE-DHMS).

For monomer LCEs, the structures consist of different lengths of mesogenic units which are endcapped with glycidyl groups. The similar characteristic of these LCEs is the para-substituents benzene rings which are elongated. These mesogenic units can arrange parallel to one another in case that the proper curing condition is controlled. Moreover, the end reactive groups can react further with a curing agent and form three-dimensional networks with lock-in molecular order.

DGE-DHBP was chosen due to the similarity in functional group with non-LC base epoxy (DGEBP-F) used in this research. The second LCE, DGE-HHC, was chosen because the longer in mesogenic unit length and the broad LC phase stability region. These two LCEs were used to blend with non-LC and their mechanical properties were measured. For DGE-DHMS, this LCE was chosen as the standard for LCE. Their properties have been readily characterized by some researchers [160-161].

3) The addition of LCEs affects the kinetics of curing non-LC epoxies, especially the curing activation energies. Effects of diffusion control and complicated reactions which retard the basic curing reaction are found in all systems after about 80 % conversion. The autocatalytic model does not take into account the effect of mobility retardation after the gelation point. Therefore, the curing rates calculated from the model at higher conversions are higher than the experimental values.

4) The coreacted networks exhibited a single T_g across all compositions - which scales with increasing the DGE-DHBP concentration. The results show the glass transition temperature is increased relative to the pure epoxy components for all

compositions. Hence there is a potential for high temperature applications. The result of miscible system was related to the similarity in solubility parameters between the DGEBP-F and DGE-DHBP.

5) Four main parameters affecting the physical and mechanical properties of final modified epoxy were studied and compared.

5.1) Effect of LCEs concentration

The maximum in toughness is found when small concentrations of LCE are added, generally not higher than 20 %. The maximum toughness obtained at 10 % DGE-DHBP can be explained in terms of the disruption of the epoxy network packing, creating additional free volume. A further increase of the DGE-DHBP concentration results in local formation of a second structure based on the added component. Thus, it is primarily the structure perturbation of the pure component which enhances toughness at low LC concentrations.

5.2) Effect of curing temperature and time

TTT diagram of cured LCEs have been obtained by using polarized optical microscope and X-ray diffractometry. The TTT diagram of LCEs also shows S-shaped as well as the diagram of non-LCEs. In case of LCEs, this diagram provides the phase stability information of the anisotropic phases. The molecular interaction between epoxy and curing agent as well as the thermal perturbation affect the shape of TTT diagram. Only in the extent range of curing condition that provides the balance of LC anisotropy. Therefore, the range of temperatures at which one cure LCE should be controlled to obtain the desirable final cured properties.

Moreover, the curing time should be sufficient to allow the LC domain formation. The LC domain formation during curing is controlled by the nucleation-growth mechanism. Therefore, a large and perfect LC domain might be formed when the proper curing condition is established.

5.3) Effect of mesogenic unit length

The effect of increased mesogenic unit length is an improvement of the modulus and impact strength. In other words, the reinforcement from mesogenic units and partial bridging from LCE is more pronounced when longer rigid length is introduced. However, the increase in strength leads to a decrease in strain at failure.

5.4) Effect of curing agents

The choice of curing agents affects the final LC phase texture. Anhydride curing agents provides a higher probability for a crosslinking reaction compared with the chain extension reaction and causes a lower stability of LC phase formation. In contrast, tetra-functional amines provide the opportunity of chain extension to the product and might enhance the LC phase stability. Moreover, the asymmetrical functionality of curing agents apparently strengthen the LC phase stability.

6) The improvement in modified epoxy matrices is also found in composites – as seen in impact, flexural testing, and toughness. The samples with modified matrices exhibit non-catastrophic failure instead of the catastrophic failure seen in unmodified samples. The improvements observed in the composite are related to better adhesion between glass fibers and the modified epoxy matrix and is reflected in the morphology seen in the SEM pictures of fracture surfaces.

7) The mechanical improvement for composites is found in both pultrusion and compression samples. However, the pultrusion samples show overall higher tensile, flexural and impact strength compared with the compression molded. This can be explained in term of the amount of glass fibers in the system and the arrangement of glass fibers. Normally, the strength of composites increases directly in relation to the amount of glass fiber. There is about 87 % fiber weight fraction in pultrusion samples while the fraction of glass fibers in compression samples is about 55 %. The mechanical testing of pultrusion samples was performed along the fiber direction where the glass fibers strongly support the load applied.

Future work

There are several directions for future research which can be derived from this work. Some practical suggestions can be formulated as follows:

1) More study would be worthwhile to maximize the reinforcing effect of liquid crystalline epoxy resin; a theoretical model of phase separation could be formulated. The thermodynamic analysis based on the lattice model to study the miscibility of blends by cloud point measurement should be studied.

2) The degree of orientation of the LC phase of cured epoxy can be controlled by the application of either mechanical, electrical or magnetic fields. The effect of magnetic and electric fields to align the mesogenic unit alignment on mechanical properties of epoxy + liquid crystalline epoxy blend will further generate a new approach to develop material for anisotropic applications.

3) The properties of cured LCEs can be tailored depending on the chosen structure of epoxy and curing conditions. Mechanical properties at low temperatures (< 0 ^{o}C) should be completed for low temperature applications

4) The application of LCEs and coreacted LCEs + epoxy as the matrix for high performance composite applications is a possibility, given the good interfacial adhesion between glass fibers and LCEs

REFERENCES

[1] Rosen SL. Fundamental Principles of Polymeric Materials. New York: Wiley 1993.

[2] Hess M, and Kosfeld R, in Salamone JC Editor. Polymeric Materials Encyclopedia. Boca Raton, FL: CRC Press 1996.

[3] Bazyliak L, Bratychak M, and Brostow W. Mater Res. Innovat. 1999;3:132; Bazyliak L, Bratychak M, and Brostow W. Mater Res. Innovat. 2000;3:218.

[4] Bowden PB. The Physics of Glassy Polymers, Howard RN, Ed. NY Wiley 1973.

[5] Treloar, LRG. The Physics of Rubber Elasticity, Oxford: Claredon Press 1975.

[6] Bhowmick AK, and Stephens HL. Handbook of Elastomers; New Development and Technology; Marcel Dekker Press 1988.

[7] Arends CB. Polymer toughening, NY: Marcell Dekker, Inc. 1996.

[8] Kirshenbaum SL. Rubber-Modified Thermoset Resins, C.K. Riew, Ed. American Chemical Society pp 163 1984.

[9] Riew CK. Rubber-toughened plastics. Advances in Chemistry Series 222, ACS 1989.

[10] Riew CK, and Kinloch AJ. Toughening Plastics I. Advances in Chemistry Series 233, ACS 1993.

[11] Riew CK, and Kinloch AJ. Toughening Plastics II. Advances in Chemistry Series 252, ACS 1996.

[12] Klempner D, Sperling LH, and Utracki LA. Interpenetrating Polymer Networks, Advanced in Chemistry Series 239, ACS 1994.

[13] Sperling LH. Interpenetrating Polymer Networks and Related Materials, New York: Plenum Press 1981.

[14] Prakash NA, Liu YM, Jang BZ, and Wang JB. Polymer Composites, 1994;15:479.

[15] Kinloch AJ, and Young RJ. Fracture Behavior of Polymers. New York: Elsevier Applied Science 1985.

[16] Sultan JN, and McGarry FJ. Polymer Eng. & Sci. 1973;13:29.

[17] Parker DS, Sue HJ, Huang J, and Yee AF. Polymer 1990; 31:2267.

[18] Sue HJ. Polymer Eng. & Sci. 1991;31:275.

[19] Girard-Reydet E, Sautereau H, Pascaut JP, Keates P, Navard P, Thollet G, and Vigier G. Polymer 1998; 39:2269.

[20] Bauer RS, Ed. Epoxy Resin Chemistry II, Adv. Chem. Ser., # 221, ACS, Washington, D.C. 1984.

[21] Ho TH, Wang CS. J. Appl. Polymer Sci. 1993;50:477.

[22] Buner IR, Rushford IL, Rose WS, Hunston DL, and Riew CK, J. Adhesion 1982;13:242.

[23] Pearson RA, and Yee AF. J. Appl. Polymer Sci. 1992;48:1051.

[24] Kirshenbaum SL. Rubber-Modified Thermoset Resins, C.K. Riew, Ed. American Chemical Society, 1984. p 163.

[25] Kunz SC, Sayre JA, and Assink RA. Polymer 1987;23:1897.

[26] Han X, Yun Z, and Guo F. Mat. Res. Soc. Symp. Proc. 1992;274:11.

[27] Bucknall CB, and Partridge IK. Polymer 1983;24:639.

[28] Diamont I, and Moulton RJ. SAMPE Int. Symp. 1984;29:422.

[29] Raghava RS. J. Polymer Sci. Phys. 1987;25:1017.

[30] Recker HG, Allspach T, Altstadt V, Folda T. Heckmann W, Ittemann P. Tesch H, and Weber T. SAMPE Quart. 1989;21:46.

[31] Hedrick JL, Yilgor I, Jurek M, Hedrick JC, Wilkes GL, and McGrath JE. Polymer 1991;32:2020.

[32] Min BG, Stachurski ZH, and Hodgkin JH. J. Appl. Polymer Sci. 1993;50:1511.

[33] Collings PJ. Liquid Crystals, NJ:Princeton University Press 1990 pp. 24-34.

[34] Onsager L. Ann. N.Y. Acad. Sci. 1949;51:627.

[35] Flory PJ. Proc. Royal Soc. 1956;234A:73.

[36] Robinson C. Trans. Faraday Soc. 1956;52:571.

[37] Cottis SG, Economy J, and Novak BE. US Patent 3,637,593:1972.

[38] Hsiao BS, Shaw MT, and Samulski ET. Macromolecules 1988;21:543.

[39] Brostow W. Polymer 1990;31:979; Brostow W. in Physical Properties of Polymer Handbook, Mark JE, Ed. American Institute of Physics Press, Woodbury NY, 1996, Chap. 33.

[40] Collyer AA. Rheology and Processing of Liquid Crystal Polymers, Acierno AD and Collyer AA. Eds. Chapman & Hall 1996.

[41] Berry JM, Brostow W, Hess M, and Jacobs GD. Polymer 1998;39:4081.

[42] Brostow W, Faitelson EA, Kamensky MG, Korhov VP, and Rodin YP. Polymer 1999;40:1441.

[43] Brostow W, and Walasek J. J. Chem. Phys. 1996;105:4367.

[44] Brostow W, Hibner K, and Walasek J. J. Chem. Phys. 1998;108:6484.

[45] Demus D. Z. Chem.1975;15:1.

[46] Kulichikhin VG, Plate NA. Polymer Sci. 1991;33:1.

[47] Brostow W, Hess M, Lopez B, and Sterzynski T. Polymer. 1996;37:1551.

[48] Brostow W, Sterzynski T, and Triouleyre S. Polymer. 1996;37:1561.

[49] La Mantia FP. Thermotropic Liquid Crystal Polymer Blends, Technomic Publishing 1993

[50] Husman G, Helminiak T, Adams W, Wiff D, and Benner C. Am. Chem. Soc. Symp. Ser. 1980;132:203.

[51] Hwang WF, Will RD, Benner CL, and Helminiak TE. J. Macromol. Sci. Phys. 1983;B22:231.

[52] Friedrich K, Hess M, and Kosfeld R. Makromol. Chem. Symp. 1988;16:251.

[53] Misra A, Tendolkar A, and Sharma SK. Abstract Paper 194 ACS Meeting New Orleans 1987:337.

[54] Weiss RA, Wansoo H, and Nicolais L. Polymer Eng. & Sci. 1987;27:689.

[55] Kulichkhin VG, Vasil'eva OV, Litvinov IA, Parsamyan IL, and Platé NA. Dokl. Akad. Nauk SSSR 1989;309:1161.

[56] Bilizard KG, and Baird DG. Polymer Eng. & Sci. 1987;27:653.

[57] Pracella M, Dainelli D, Galli G, and Chiellini E. Makromol. Chem. 1986;187:2387.

[58] Paci M, Barone C, and Magagnini PL. J. Polymer Sci. Phys. 1987;25:1595.

[59] Bouligand Y, Cladis PE, Liebert L, and Strzelecki L. Mol. Cryst. Liq. Cryst. 1974;25:233.

[60] Clough SB, Blumstein A, and Hsu EC. Macromolecules 1976;9:123.

[61] Mitchell GR, Davis FL, and Ashman A. Polymer;1987;28:639.

[62] Broder DJ, Finkelmann H, and Kondo K. Macromol. Chem. 1988;189:185.

[63] Broer DJ, Mol GN, and Challa G. Makromol. Chem. 1989;190:19.

[64] Hikmet RAM, and Broer DJ. Polymer 1991;32:1627.

[65] Broer DJ, Mol GN, and Challa G. Makromol. Chem. 1991;195:59.

[66] Anderson A, Gedde UW, and Hult A. Polymer 1992;33:4014.

[67] Broer DJ, and Mol GN. Polymer Eng. & Sci. 1991;31:1627.

[68] Hikmet RAM, Zwerver BH, and Broer DJ. Polymer 1992;33:89.

[69] Dhein R, Meier HM, Müller HP, and Gipp R, Germany Offen 3622613 A1:1988.

[70] Earls JD, and Hefner RE. Jr. European Pat. Appl. 379057 A2:1990.

[71] Hefner RE.Jr, and Earls JD. European Pat. Appl. 475238 A2:1990.

[72] Eirchmeyer S, Müller HP, and Karbach A. European Pat. Appl. 445401 A2:1991.

[73] Melissaris AP, and Litt MH. Macromolecules 1994; 27:2675.

[74] Melissaris AP, Sutter JK, Litt MH, Scheiman DA, and Scheiman M. Macromolecules 1995;28:860.

[75] Douglas EP, Langlois DA, and Benicewicz BC. Chem. Mater. 1994;6:1925.

[76] Bayclay GG, Ober CK, Papathomas KI, and Wang DW. Macromolecules 1992;25:2947.

[77 Körner H, and Ober CK. Polym. Mater. Sci. Eng. Prepr. ACS 1995;73:456.

[78] Mormann W, and Zimmerman J. Macromol. Symp. 1995;93:97.

[79] Wang YH, Hong YL, Yang FS, and Hong JL. Polym. Mater. Sci. Eng. Prepr. ACS 1994;71:678.

[80] Aharoni SM, and Edwards SF. Macromolecules 1989:22:3361.

[81] Aharoni SM, Murthy NS, Zero K, and Edwards SF. Macromolecules 1990;23:2533.

[82] Aharoni SM Macromolecules 1991;24:235.

[83] Markoski LJ, Walker KA, Deeter GA, Spilman GE, Martin DC, and Moore JS. Chem. Mater. 1993;5:248.

[84] Caruso U, Pragliola S, Roviello A, and Sirigu A. Macromolecules 1993;26:221.

[85] Aharoni SM. Macromolecules 1991;24:4286.

[86] Finkelmann H, Kock HJ, and Rehage G. Makromol. Chem. Rapid Commun. 1981;2:317.

[87] Schätzle J, Kaufhold W, and Finkelmann H. Makromol. Chem. 1989;190:3269.

[88] Carfagna C, Amendola E, and Giamberini M. J. Mater. Sci. Lett. 1994; 13:126.

[89] Carfagna C, Amendola E, and Giamberini M. Composite Structures 1994;27:37.

[90] Barclay GG, and Ober CK. Progr. Polymer Sci. 1993;18:899.

[91] Muller HP, Gipp R, and Heine H. U.S. Patent 4,764,581:1988.

[92] Earls JD, Hefner RE, and Puckett PM. U.S. Patent 5,218,062:1993.

[93] Giamberini M, Amendola E, and Carfagna C. Mol. Cryst. Liq. Cryst. 1995;266:9.

[94] Weiss R, and Ober CK. Editors. Liquid Crystalline Polymers: Chemistry, Structure and Properties, Washington DC:American Chemical Society 1990.

[95] Carfagna C, Amendola E, Giamberini M, Hakemi H and Pane S. Polymer Inter. 1997;44:465.

[96] Carfagna C, Amendola E, and Giamberini M. Progr. Polymer Sci. 1997;22:1607.

[97] Carfagna C, Amendola E, Giamberini M, and Hakemi H, Pane S. Polymer Inter. 1997;44:465.

[98] Barclay GG, McNamee SG, Ober CK, Papathomas KI, and Wang DW. J. Polymer Sci. Chem. 1992;30:1845.

[99] Carfagna C, Nicolas C, Amendola E, Carfagna C, Jr. , and Fillippov AG. J. Appl. Polymer Sci. 1992;44:1456.

[100] Griffith AA. The Phenomena of Rupture and Flow in Solids. Philosophical Transactions, Series A 1992; 221:163.

[101] ASTM standard D 5045-96.

[102] Herz J, Reiss-Husson F, Rempp P, and Luzzati V. J. Polymer Sci. C 1964;1275.

[103] Blumstein A, Blumstein RB, and Vanderspurt TH. J. Colloid & Interface Sci. 1969;31(2):236.

[104] Strzelecki L, and Leibert L. Bull. Soc. Chem. France 1973:597.

[105] Clough SB, Blumstein A, and Hsu EC. Macromolecules 1976;9(1):123.

[106] Finkelmann H, Koch HJ, and Rehage G. Makromol. Chem. Rapid Commun. 1981;2:317.

[107] de Gennes PG. C.R. Acad. Sci. B 1975;B281:101.

[108] de Gennes PG. Polymer Liquid Crystals. Eds. Ciferri A, Krigbaum WR and Meyer RB, Academic Press: New York, 1982 p.115-131.

[109] Warner M, Gelling KP, and Vilgis TA. J. Chem. Phys. 1988;88:4008.

[110] Warner M. Side Chain Liquid Crystal Polymers, Ed. McArdle CB, Chapman and Hall: New York, 1989, pp.7.

[111] Finkelmann H, Kock HJ, Gleim W, and Rehage G. Makromol. Chem. Rapid Commun. 1984;5:287.

[112] Hammerschmidt K, and Finkelmann H, Makromol. Chem. 1989;190:1089.

[113] Zentel R, and Benalia M. Makromol. Chem. 1987;188:665.

[114] Barnes NR, Davis FJ, and Mitchell GR. Mol. Cryst. Liq. Cryst. 1989;168:13.

[115] Jpn. Kokai Tokkyo Koho Jp 58.206.597 (83,206,579) :1983.

[116] Dhein R, Meier HR, Müller HP, and Gipp R. Germany Offen. 3622613 A1:1988.

[117] Dhein R, Müller HP, Meier HR, and Gipp R. U.S. Patent 4,762,901:1988.

[118] Müller HP, Gipp R, and Heine H. U.S. Patent 4,764,581:1988.

[119] Earls JD, and Hefner Jr, RF. European Patent Appl. 379,057 A2:1990.

[120] Earls JD, and Hefner Jr, RF. European Patent Appl. 475,238 A2:1990.

[121] Broer DJ, Finkelmann H, and Kondo K. Makromol. Chem. 1988;189:185.

[122] Broer DJ, Finkelmann H, and Kondo K. Makromol. Chem. 1989;190:3201.

[123] Broer DJ, Finkelmann H, and Kondo K. Makromol. Chem. 1989;190:2255.

[124] Broer DJ, Lub J, and Mol GN. Macromolecules 1993;26:1244.

[125] Onada S, Yano S, Tsunashima K, and Inoue T. Polymer 1996;37:1925.

[126] Barclay GG, McNamee SG, Ober CK, Papathomas K I, and Wang DW. J. Polymer Sci. Chem. 1992;30:1845.

[127] Shiota A, and Ober CK. J. Polymer Sci. Chem. 1996;34:1291.

[128] Grebowicz JS. Macromol. Symp. 1996;104:191.

[129] Szczepaniak P, Warchalowska M, Rejdych J, Leszczynska I, and Rudnik E. J. Polymer Sci. Phys. 1998;36:21.

[130] Sue HJ, Earls JD, and Hefner RE. J. Mater. Sci. 1997;32:4031.

[131] Sue HJ, Earls JD, and Hefner RE. J. Mater. Sci. 1997;32:4039.

[132] Sue HJ, Earls JD, Hefner RE, Villarreal NI, Garcia-Meitin EI, Yang PC, Cheatam CM, and Plummer CG. Polymer 1998;39:4707.

[133] Lin Q, Yee AF, Sue HJ, Earls JD, and Hefner RE. J. Polymer Sci. Phys. 1997; 35:2363.

[134] Carfagna C, Amendola E., Giamberini M, Filippo AG, and Bauer RS. Liquid Crystals 1993; 13:571.

[135] Guthrie J, Morton A, and Nield E. Surf. Coat. Int. 1993;75: 212.

[136] Carfagna C, Amendola E, and Giamberini M. Composites Struct. 1994;27:37.

[137] Giamberini M, Amendola E, and Carfagna C. Mol. Cryst. Liq. Cryst. 1995;266:9.

[138] Barclay GG, McNamee SG, Ober CK, Papathomas KI, and Wang DW. J. Polymer Sci. Chem. 1992;30:1831.

[139] Amendola E, Carfagna C, Giamberini M, and Pisaniello G. Macromol. Chem. & Phys. 1995;196:1577.

[140] Lin Q, Yee AF, Earls JD, Hefner Jr., RE, and Sue HJ. Polymer 1994;35:2679.

[141] Mormann W, Zimmermann J, and Irle C. Polymer Prepr. ACS 1993;34(2):704.

[142] Carfagna C, Amendola E, and Giamberini M. J. Mater. Sci. Lett. 1994;13:126.

[143] Carfagna C, Amendola E, and Giamberini M. Macromol. Chem. & Phys. 1994;195:2307.

[144] Mallon JJ, and Adams PM. J. Polymer Sci Chem. 1993;31:2249.

[145] Jahromi S, Lub J, and Mol GN. Polymer 1994;35:622.

[146] Jahromi S, and Mijs W. Mol. Cryst. Liq. Cryst. Sci. Technol. :Sect. A. 1994; 250:209.

[147] Jahromi S, Kuipers WAG, Norder B, and Mijs WJ. Macromolecules 1995;28:2201.

[148] Koscielny B, Pfitzmann A, and Fedtke M. Polymer Bull. 1994;32:529.

[149] Sadafule DS, Raghuraman RN, Navale NG, Kumbhar CCG, and Panda SP. J. Macromol. Sci. Chem. 1988;A25:121.

[150] Bellamy LJ, The Infrared Spectra of Complexes Molecules, Vol I and II, Chapman and Hall, London 1980.

[151] Hefner Jr. RE, Earls JD, and Puckett PM. US Patent 5,266,660:1993.

[152] Brostow W. Science of Materials 2nd Ed., Robert E. Krieger Publishing Company, Malabar, FL 1985.

[153] Warner M, Gelling KP, and Vilgis TA. J. Chem. Phys. 1988;88:4008.

[154] Gillham JK, and Glandt CA. Characterization of Thermosetting Epoxy System using Torsional Pendulums in Chemistry and Properties of Crosslinked Polymers, Labana SS, Ed. Academic Press Inc., 1977 pp.495.

[155] Gillham JK. The Role of the Polymeric Matrix in the Processing and Structural Properties of Composites Materials, Seferis JC. and Nicolias L, Ed. 1983 pp 127.

[156] Aronhime MT, and Gillham JK. Time Temperature Transformation (TTT) Cure Diagram of Thermosetting Polymeric Systems in Advance in Polymer Science 78, Dusek K, Ed. Springer-Verlag Berlin Heidelberg 1986.

[157] Gillham JK. Polymer Eng. & Sci. 1986;26:1429.

[158] Nam JD, and Seferis JC. Carbon 1992;30:751.

[159] Kirchmeyer S, Karbach A, Muller HP, Meier HM, and Dhein R, International Conference on Crosslinked Polymers, Proceedings of the Conference, 1990 pp.167-176.

[160] Lin Q, and Yee AF. Polymer 1994;35(2):2679.

[161] Ortiz C, Kim R, Rodighiero E, Ober CK, and Kramer EJ. Macromolecules 1998;31:4074.

[162] R. F. Fisher, J. Polymer Sci. 1960;44:155.

[163] Y. Tanaka, and H. Kakiuchi, J. Macromol. Sci. Chem., 1996;A1:307.

[164] Byrne CA, Hagnauer GL, and Schneider NS. Polymer 1983; 24:206.

[165] Mijovic J, Fishbain A, and Wijaya J. Macromolecules 1992;25:979

[166] Harrod JF J. Appl. Polymer Sci. 1962;6:s63.

[167] Harrod JF. J. Polymer Sci. 1963;1A:385.

[168] Moacanin J, Cizmecioglu M, Tsay F, and Gupta A. Org. Coat Plast. Chem. 1982;47:587.

[169] Morgan RJ, and Mones ET. J. Appl. Polymer Sci. 1987;33:999.

[170] Shechter L, Wynbtra J, and Kurkjy RE. Ind.& Eng. Chem. 1956;48:94.

[171] Shechter L Wynbtra J, and Kurkjy RE. Ind. & Eng. Chem. 1957;49:1107.

[172] Dusek K, and Bleha M. J. Polymer Sci. Chem. 1977;15:2393.

[173] Riccardi CC, and William RJJ. J. Appl. Polymer Sci. 1986;32:3445.

[174] Simon SL, and Gillham JK. J. Appl. Polymer Sci. 1994;53:709.

[175] Smith IT. Polymer 1961;2:95.

[176] Laird RM, and Parker RE. J. Chem. Soc. 1961;83:4277.

[177] Eastham AM, de B. Darwent B, and Beaubien PE. Can. J. Chem. 1951;29:575.

[178] Eastham AM, and de B. Darwent B. Can. J. Chem. 1951;29:585.

[179] Morgan RJ. J. Mater. Sci. 1985;12:1.

[180] Rogers MG. J. Appl. Polymer Sci. 1972;16:1953.

[181] Meston SA, and Morris CEM. Makromol. Sci. Rev. in Makromol. Chem. & Phys. 1984; C24:117.

[182] Sojka SA, and Moniz WB. J. Appl. Polymer Sci. 1976;20:1977.

[183] Rabek JF. Experimental Methods in Polymer Science, John Wiley: Chichester 1980.

[184] Mertzel E, and Koenig JL. Adv. Polymer Sci. 1986;75:92.

[185] Lee H. and Neville K. Handbook of Epoxy Resins, New York: McGraw Hill 1976 pp 4-35-4-56.

[186] Hadad DK, Epoxy Resins, Chemistry and Technology 2nd Ed, Ed. May CA, New York: Marcel Dekker 1988a pp 1111-1123.

[187] Bidstrup WW, and Senturia SD. Polymer Eng. & Sci. 1989;29:290

[188] Macoski CW. Brit. Polymer 1985;17:239.

[189] Verchére D, Sautereau H, Pascault JP, Riccardi CC, Moschier SM, and Williams RJJ. J. Appl. Polymer. Sci. 1990;38:725.

[190] Mijovic J, and Lee CH. J. Appl. Polymer Sci. 1989;38:2155.

[191] Aronhime AT, and Gillham JK. Adv. Polymer Sci. 1986;78:83.

[192] Yousefi A, Lafleur PG, and Gauvin R. Polymer Composites 1997;18:157.

[193] Prime RB. Thermal Characterization of Polymeric Materials, Volume 2. Turi EA. Ed., New York:Academic Press 1997.

[194] Lau S. ACS Symp. Ser. 1992;496.

[195] Kamal MR. Polymer Eng.& Sci. 1974;14:231.

[196] Kamal MR, and Sourour S. Polymer Eng.& Sci. 1973;13:59.

[197] Ozawa T. Bull. Chem. Soc. Jpn. 1965;38:1881.

[198] Ozawa T. J. Therm. Anal. 1970;2:301.

[199] Doyle CD. Anal. Chem. 1961;33:77.

[200] Kissinger HE. Anal. Chem. 1957;29:1702.

[201] Marquardt DN. J. Soc. Ind. Appl. Math. 1963;11:431.

[202] Khanna U, and Chanda M. J. Appl. Polymer Sci.1993;49:319.

[203] Riccardi CC, Dupuy J, and Williams RJJ. J. Polymer Sci. Phys. 1999;37:2799.

[204] Fox TG. Bull. Am. Phy. Soc. 1956;1:123.

[205] Paul DR, and Barlow JW. J. Macromol. Sci. Chem. 1980;C18:109.

[206] Keskkuka H. Polymer Compatibility and incompatibility: Principles and Practice, Šolc K. Ed. Michigan: MMI Press. 1982.

[207] Olabisi O, Robeson LM, and Shaw MT. Polymer- Polymer Miscibility. New York: Academic Press 1979.

[208] Flory PJ. J. Chem. Phys. 1942;10:51.

[209] Flory PJ. Principles of Polymer Chemistry, Cornell University Press 1953.

[210] Huggins ML. J. Am. Chem. Soc. 1942;64:1712.

[211] Hilderbrand J, and Scott R. The Solubility of Non-Electrolytes 3rd Ed. New York: Reinhold 1949.

[212] Harris HG, and Prausnitz JM. Ind. Eng. Chem. Fund. 1969;8:180.

[213] Blanks RF, and Prausnitz JM. Ind. Eng. Chem. Fund. 1964;3(1):1.

[214] Burrell H. Polymer Handbook 2nd Ed. Brandrup J. and Immergut EH. Eds. New York: Wiley-Interscience 1975.

[215] Shaw MT. J. Appl. Polm. Sci. 1974;18:449.

[216] Piccarolo S, and Titomanilo G. Ind. Eng. Chem. Pro. Des. Dev. 1982;22:146.

[217] Schneier B. Polym. Lett. 1972;10:245.

[218] Rigbi Z. Polymer 1978;19:1229.

[219] Shell Chemicals, Solubility Parameters 2nd Ed. Tech. Bull. ICS 1978;(X)/78/1.

[220] Shell Chemicals, Solvent System Design Tech. Bull. ICS 1978;(X)/78/2.

[221] Froehling PE, and Hillegers LT. Polymer 1981;22:261.

[222] Bunn CW. J. Polym. Sci. 1955;16:323.

[223] Small PA. J. Appl. Chem. 1953;3:71.

[224] Hoy KJ. J. Paint Technol. 1970;42:76.

[225] Van Krevelen PW. Properties of Polymers, Amsterdam: Elsevier 1972 pp135.

[226] Coleman MM, Serman CJ, Bhagwagar DF, and Painter PC. Polymer 1990;31:1187.

[227] Daubert TE, and Danner RP. Data Compilation: Tables of Properties of Pure Compounds. New York: American Institute of Chemical Engineering 1989.

[228] William RJJ, Borrajo J, Adabbo HE, and Rojas AJ. Rubber Modified Thermoset Resins, Riew CK, and Gilliam JK. Eds. Advances in Chemistries Series 208. Washington DC: ACS 1976 pp.195.

[229] Homes AH, Ph.D. Dissertation, Texas A&M 1992.

[230] Verchere D, Sautereau H, Pascault JP, Moschiar SM, Ricardi CC, and Williams RJJ. Polymer 1989;30:108.

[231] Gillham JK, Glandt CA, and McPherson CA. Chemistry and Properties of Crosslinked Polymers, New York:Academic Press 1977.

[232] Hyun D, and Kim SC. Polymer Eng. & Sci. 1991;31:289.

[233] Visconti S, and Marchessault RH. Macromolecules 1974;7:913.

[234] Boisserie C, and Marchessault RH. J. Polymer Sci. Phy. 1977;15:1211.

[235] Verchere D, and Pascault JP. J. Appl. Polymer Sci. 1990;41:467.

[236] Ting RY. Epoxy Resins : Chemistry and Technology, May CA. Ed. New York: Marcel Dekker, Inc. 1988

[237] Kline DE. J. Polymer Sci. 1960;47:237.

[238] McCrum N, Williams B, and Read G. Anelastic and Dielectric Effects in Polymerics Solids, New York: Dover 1991.

[239] Menard KP. Dynamic Mechanical Analysis : A Practical Introduction, CRC Press 1999.

[240] Nielson IE. Mechanical Properties of Polymer and Composites. New York: Mercel Dekker 1975.

[241] Tobolsky AV. Properties and Structure of Polymer. New York: John Wiley 1960.

[242] Carfagna C, Nicolais C, Amendola E, Carfagna C, Jr., and Filippov AG. J. Appl. Polymer Sci. 1992;44:1456.

[243] Tada H, Paris PC, and Irwin GR. The Stress Analysis of Cracks Handbook. 2nd Ed. St. Louis: Paris Productions, Inc. 1985.

[244] Anderson TL. Fracture Mechanics Fundamental and Applications, FL: CRC Press 1995.

[245] Sue HJ, Pearson RA, Parker DS, Huang J, and Yee AF. Polymer Preprints. ACS 1988;29:147.

[246] Sue HJ, and Yee AF. J. Mater. Sci. 1993;28:2951.

[247] Blonski S. Brostow W, Jonah DA, and Hess M. Macromolecules 1993;26:84.

[248] Brostow W, Hess M, and Lopez BL, Macromolecules 1994; 27:2262.

[249] Brostow B, Dziemianowicz TS, Romanski J, and Werber W. Polymer Eng. & Sci. 1988;28:785.

[250] Martinez I, Martin MD, Eceiza A, Oyanguren P, and Mondragon I. Polymer 2000;41:1027.

[251] Bagheri R, Williams MA, and Pearson RA, Polymer Eng. & Sci. 1997;37:245.

[252] D'Almeida JRM, and Monteiro SN, J. Polymer Eng. 1998;18:235.

[253] Song M, Hourston DJ, and Schafer F-U. Polymer 1999;40:5773.

[254] Punchaipetch P, Ambrogi V, Giamberini M, Brostow W, Carfagna C, and D'Souza NA. Polymer, 2000;41: to be published.

[255] Lee JY, Jang J, Hong SM, Hwang SS, and Kim KU. Polymer 1999;40:3197.

[256] Thomason JL, and Scholenberg GE. Composites 1994; 25**:** 197.

[257] Karger-Kocsis J. Polypropylene Structure, Blends and Composites, Chapman & Hall, London 1995.

[258] Mallick PK. Fiber Reinforced Composites, Dekker, New York 1993.

[259] Mettes DG. Handbook of Fiberglass and Advanced Plastics Composites. Ed. Lubin G. Van Nostrand Reinhold Company, New York 1969.

[260] Plueddeman EP, Interfaces in Polymer Matrix Composites, Academic Press, New York 1974.

[261] Hull D, and Clyne TW. An Introduction to Composites Materials. Cambridge University Press, New York 1996.

[262] Mijovic J., J. Appl. Polymer Sci. 1986; 31:1177.

[263] Opalicki M, Kenny JM, and Nicolais L. J. Appl. Polymer Sci. 1996; 61:1025.

[264] Russell AJ, and Street KN. Progress in Science and Engineering of Composites Ed. Hayadhi T, Kawata K, and Umekawa S. ICCM-IV, ASM International, Tokyo 1982 p. 279.

[265] Russell AJ, and Street KN. Moisture and Temperature Effects on the Mixed-Mode Delamination Fracture of Unidirectional Graphite/Epoxy ASTM STP 876, 1985 p. 349.

[266] Marquardt DN, J. Soc. Ind. Appl. Math. 1963; 11:431.

[267] Montserrat S, Flaqué C, Pagès P, and Málek J. J. Appl. Polymer Sci.,1995; 56: 1413.